L'origine de l'émission électromagnétique de haute énergie dans l'environnement des trous noirs supermassifs

Francesco Ursini

Francesco Ursini. L'origine de l'émission électromagnétique de haute énergie dans l'environnement des trous noirs supermassifs. Phénomènes cosmiques de haute energie [astro-ph.HE]. Université Grenoble Alpes; Università degli studi Roma Tre, 2016. Français. NNT : 2016GREAY062 . tel-01589295

HAL Id: tel-01589295
https://theses.hal.science/tel-01589295

Submitted on 18 Sep 2017

ROMA TRE
UNIVERSITÀ DEGLI STUDI

Communauté
UNIVERSITÉ Grenoble Alpes

THÈSE

Pour obtenir le grade de

DOCTEUR DE LA COMMUNAUTÉ UNIVERSITÉ GRENOBLE ALPES

preparée dans le cadre d'une cotutelle entre la *Communauté Université Grenoble Alpes* et l'*Università degli Studi Roma Tre*

Spécialité : **Astrophysique et Milieux Dilués**

Arrêté ministériel : le 6 Janvier 2005 - 7 Août 2006

Présentée par

Francesco URSINI

Thèse dirigée par **Pierre-Olivier PETRUCCI**
et codirigée par **Giorgio MATT**

préparée au sein de l'**Institut de Planétologie et d'Astrophysique de Grenoble** et de l'**Università degli Studi Roma Tre - Dipartimento di Matematica e Fisica**
et de l'**Ecole Doctorale de Physique**

Constraining the high-energy emission sources in the environment of supermassive black holes

Thèse soutenue publiquement le **28 Octobre 2016**,
devant le jury composé de :

M.me Claudine KAHANE
Professeur, IPAG/UGA, Présidente
M. René GOOSMANN
Maître de conférences, OAS/UNISTRA, Rapporteur
M.me Paola GRANDI
Professeur adjoint, INAF-IASF/UNIBO, Rapporteur
M.me Alessandra DE ROSA
Chercheur, INAF-IAPS, Examinateur
M. Julien MALZAC
Chercheur, IRAP, Examinateur
M. Pierre-Olivier PETRUCCI
Chercheur, IPAG, Directeur de thèse
M. Giorgio MATT
Professeur, UNIROMA3, Co-Directeur de thèse

Contents

Part I

Introduction

Chapter 1

Active Galactic Nuclei: observational properties and basic physics

Contents

1.1 What are AGNs?

The electromagnetic emission of most galaxies is essentially due to stars. A non-negligible contribution is usually due to the reprocessing of stellar radiation by the interstellar medium, which is composed of gas and dust. Therefore, a “normal” galaxy, such as the Milky Way, mostly emits optical/UV and infrared radiation. A small fraction of the total energy output is emitted in the X-ray band, owing to supernova remnants and accreting binary systems with a compact object, like a neutron star or a black hole (e.g., Fabbiano 1989). H II regions are responsible for weak emission lines, mostly in the optical/UV spectrum.

However, many galaxies have a much broader spectral energy distribution (SED), ranging from the radio band up to X-rays and gamma-rays. The fraction of these so-called *active galaxies* is roughly 10 percent, the precise value depending upon environment and redshift (e.g., Brandt & Alexander 2015). The broad SED of active galaxies, and in particular their peculiar high-energy emission, is due to a very bright and compact central region, called *Active Galactic Nucleus* (AGN). I show in Fig. 1.1 the average energy distribution of active galaxies compared with a normal one (for further details, see Elvis

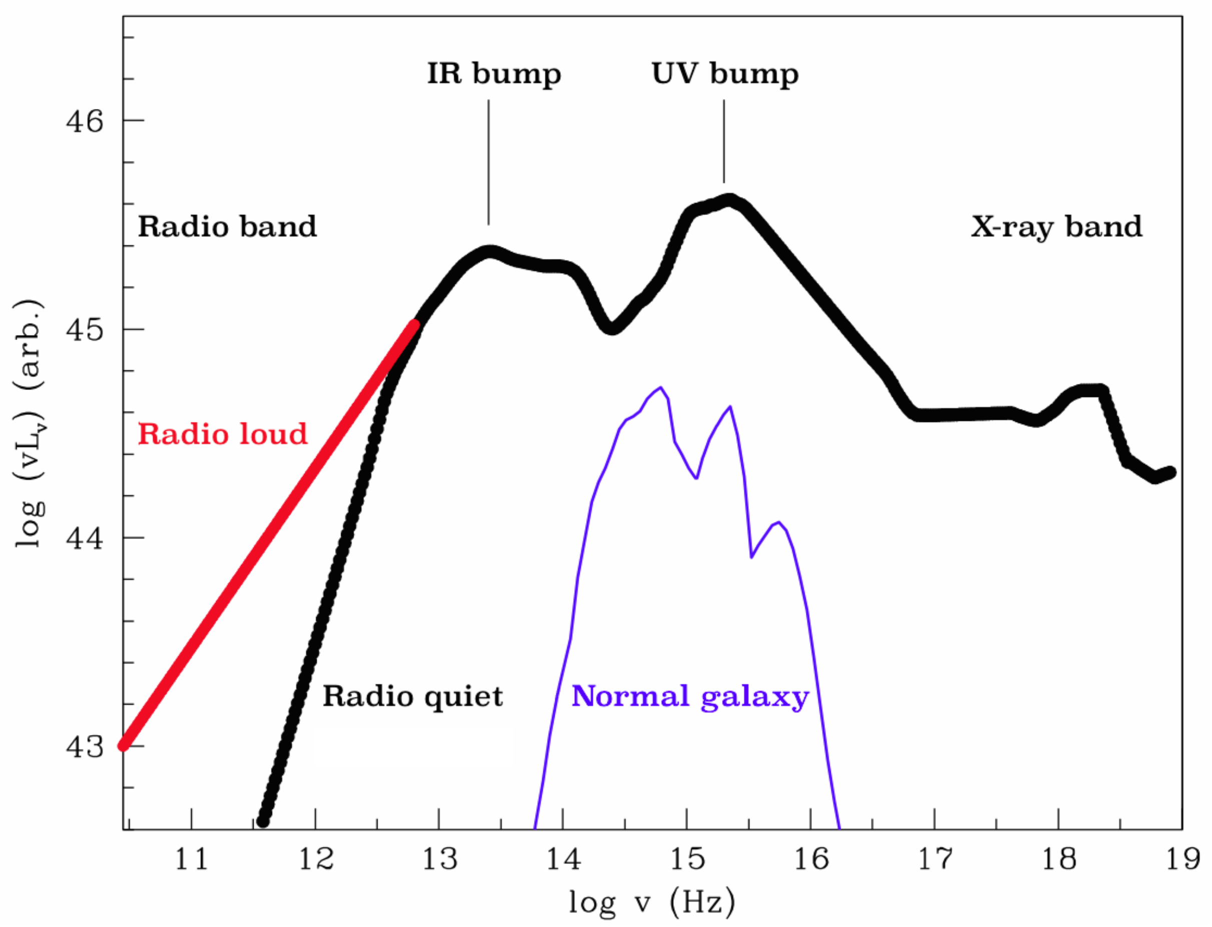

Figure 1.1 – Comparison of energy distributions between active and normal galaxies, loosely based on Elvis et al. (1994).

et al. 1994). The SED of an AGN can be decomposed into at least four main components, which I will further discuss in the following: (i) the primary emission in the optical/UV band; (ii) the infrared continuum, which is due to thermal emission from dust heated by the primary UV radiation; (iii) the high-energy continuum, which is due to reprocessing of the primary optical/UV emission by hot gas; (iv) the radio emission, due to synchrotron radiation, which can be relatively strong (*radio-loud* AGN) or weak (*radio-quiet* AGN).

In addition to the broad, non-stellar energy distribution, AGNs also exhibit strong emission lines in their spectra, which in fact led to the discovery of this class of objects. In 1943, Carl Seyfert identified a class of spiral galaxies with a bright core and showing strong, high-ionization emission lines in their optical spectra (Seyfert 1943). Furthermore, the line profiles were found to be broader than the lower-ionization emission lines seen in the spectra of most “normal” galaxies. I show in Fig. 1.2 the optical/UV spectrum of NGC 5548, one of the AGNs in the original Seyfert sample. These optical properties became the defining characteristics of what we now call *Seyfert galaxies*, the earliest identified and most numerous class of AGNs. Today, we refer to Seyfert galaxies with or without detected broad lines as *type 1* and *type 2* Seyferts, respectively (Bassani et al. 1999). The optical lines of Seyfert 2s, despite the lack of broad components, indicate a higher ionization than that observed e.g. in H II regions (e.g., Veilleux & Osterbrock 1987; Ho 2008, see also Fig. 1.3).

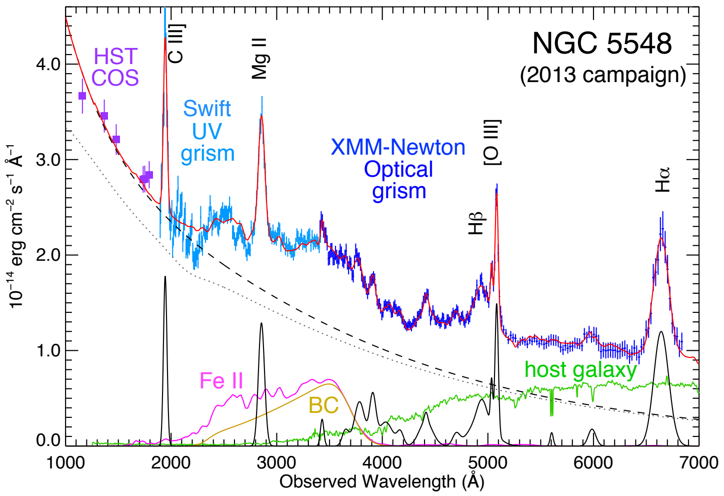

Figure 1.2 – Average optical/UV spectrum of the AGN in NGC 5548, from a multi-satellite campaign in 2013 (adapted from Mehdipour et al. 2015, see Chapter 4). The best-fit model is shown in red. The dashed black curve is the underlying continuum (the dotted curve is corrected for reddening). The emission lines are shown at the bottom. The feature in magenta is the "small blue bump": blended Fe II lines + Balmer continuum (in yellow, due to H recombination to $n = 2$). The contribution from the host galaxy is shown in green.

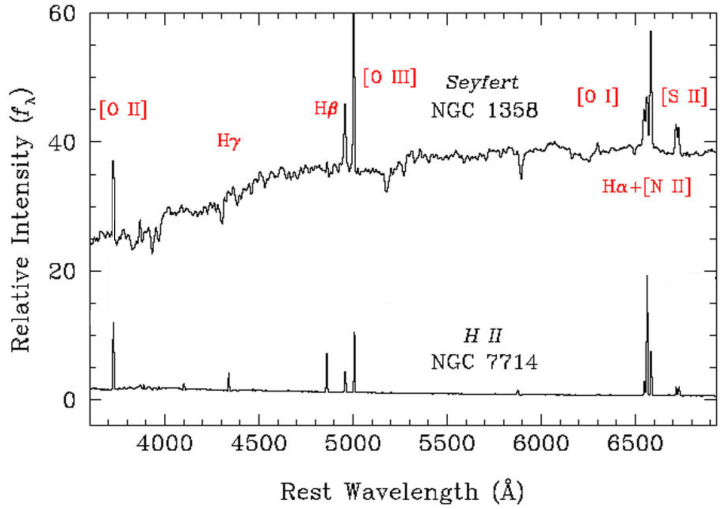

Figure 1.3 – Optical spectrum of the active nucleus in the Syfert 2 galaxy NGC 1358, compared with the H II nucleus in NGC 7714 (adapted from Ho 2008).

Another important feature of AGNs is their strong and fast variability at all wavelengths. If a source varies coherently, the emitting region must be causally connected. Then, the observed variability time-scale translates to an upper limit of the source size based on light-travel time. AGNs are found to be variable on all observable time-scales, from decades down to a few hours (e.g., Ulrich et al. 1997). Then, roughly speaking, the maximum size of the emitting region of an AGN should not exceed a few light days, as also indicated by microlensing analysis (e.g. Morgan et al. 2010). But the average luminosity of an AGN is of the order of $10^{45} - 10^{46}$ ergs s^{-1}. Therefore, an AGN is able to produce more power than an entire galaxy within a region that is about the size of our Solar System.

In summary, the spectrum of an AGN cannot be a superposition of stellar spectra. It rather requires a completely different emission mechanism. According to the present understanding, this mechanism is the accretion of matter onto a supermassive black hole.

1.2 The central engine of AGNs

Accretion of matter onto a compact object can provide a very efficient mass to energy conversion, which is needed to explain the AGN huge power emitted within a small region. Let us start with some simple order-of-magnitude estimates (for a more detailed discussion, see e.g. Frank et al. 2002). The gravitational potential energy released by the accretion of a mass m onto a body of mass M and radius R_* is

$$\Delta E = \frac{GMm}{R_*} \tag{1.1}$$

where G is the gravitational constant. If this energy is converted into radiation, for example by heating, the luminosity output is

$$L = \frac{GM\dot{M}}{R_*} \tag{1.2}$$

where $\dot{M}$ is the accretion rate. Clearly, the efficiency of this process depends on the compactness of the accreting object, namely the ratio M/R_*. Let us rewrite eq. 1.2 introducing the gravitational radius, $R_G = GM/c^2$:

$$L = \frac{R_G}{R_*}\dot{M}c^2 \equiv \eta\dot{M}c^2 \tag{1.3}$$

where η represents the efficiency of the conversion of rest-mass energy into radiation. The maximum efficiency is reached by the most compact objects, such as neutron stars ($R_* \sim 10$ km) and black holes. Although the definition of R_* for a black hole is not obvious, it is customary to use the radius of the innermost stable circular orbit. This is the smallest circumference along which free particles may stably orbit around a black hole. The existence of such a lower limit is a general relativistic effect. The detailed calculations, involving the determination of the geodesics of the Kerr metric, can be found in all classic textbooks on general relativity (Misner et al. 1973; Wald 1984; Straumann 2004). For our discussion, it is useful to remind that $\eta \simeq 0.06$ for a Schwarzschild black hole, and $\eta \simeq 0.31$ for a maximally rotating black hole (spin parameter $a = 0.998$; see Thorne 1974)[1]. With such a high efficiency, an accretion rate of $0.1-1\ M_\odot$/yr is enough to produce a luminosity of the order of $10^{45} - 10^{46}$ ergs s^{-1}. For this simple estimate to be physically consistent, however, the luminosity should be less than the Eddington limit, which occurs when the outward radiation pressure equals the inward gravitational attraction. Mathematically, $L \leq L_{\rm Edd}$ must hold, where

$$L_{\rm Edd} \simeq 1.3 \times 10^{45} \left(\frac{M}{10^7 M_\odot}\right) \text{ ergs s}^{-1}. \tag{1.4}$$

Therefore, the AGN emission can be explained by accretion of matter, with a rate of at least a significant fraction of a solar mass per year, onto a black hole having a mass of roughly $10^6 - 10^{10}\ M_\odot$, i.e. a supermassive black hole.

---

[1] In the ideal case $a = 1$, η would reach 0.42.

1.2.1 The accretion disc

Let us now consider the accretion of matter onto a black hole in a bit more detail. If the infalling matter has some angular momentum with respect to the black hole, it will prevent free fall. In order to actually fall onto the black hole, the matter must get rid of most of its angular momentum. Then, there must be en effective mechanism for transporting the angular momentum outward. This is what happens in an accretion disc: dissipative processes (collisions of fluid elements, shocks, viscosity) convert part of the energy of the bulk orbital motion into heat, which is partly radiated away and lost. Then, the gas will sink deeper into the gravitational well and lose angular momentum, spiralling down towards the black hole. However, the total angular momentum cannot change, because we are assuming gravity to be the only external force. Rather, the angular momentum is transported outwards by the torques exerted by the viscous forces (for a more detailed discussion, see Frank et al. 2002, Chap. 4).

Before delving into further details, we can qualitatively predict the radiation spectrum we expect from an accretion disc around a black hole. If we simply assume that the disc emits as a blackbody, we can estimate its luminosity as

$$L \simeq 2\pi R^2 \sigma_{\rm SB} T^4 \tag{1.5}$$

where R is the disc radius, $\sigma_{\rm SB}$ is the Stefan-Boltzmann constant and T is the temperature. If we also assume that $L \sim L_{\rm Edd}$ and $R \sim R_G$, namely most of the luminosity is released in the inner part of the disc, we find a temperature

$$T \simeq 5 \times 10^5 \left(\frac{M}{10^8 M_\odot}\right)^{-1/4} \text{ K}. \tag{1.6}$$

The more massive the black hole, the cooler the accretion disc. Translating into an energy via the Boltzmann constant $k_{\rm B}$,

$$k_{\rm B} T \simeq 40 \left(\frac{M}{10^8 M_\odot}\right)^{-1/4} \text{ eV}. \tag{1.7}$$

In other words, the emission of an accretion disc around a supermassive black hole peaks in the UV band. For a solar-mass black hole, the emission peaks in the X-ray band. This estimate, despite its crudeness, qualitatively explains the UV bump seen in AGNs and the X-ray emission of the (much lower-mass) galactic black hole binaries (e.g., Remillard & McClintock 2006).

1.2.2 The Shakura-Sunyaev model

Let us look more closely at the physical structure and properties of the accretion disc. If the matter flow is vertically confined close to the orbital plane, the disc can be considered as geometrically thin, i.e. not far from a two-dimensional flow. The laws governing the physics of a thin accretion disc around a compact object (not necessarily a black hole) are, in principle, relatively simple to state. Essentially, the structure of the disc is determined by the conservation of mass, angular momentum and energy and by the vertical hydrostatic equilibrium. The thin disc structure was investigated by Shakura and Sunyaev in a fundamental paper (Shakura & Sunyaev 1973; see also Pringle & Rees 1972).

A general relativistic version of the model was given in Novikov & Thorne (1973), with further extensions and corrections in subsequent works (see, e.g., Abramowicz & Fragile 2013, and references therein). The Shakura-Sunyaev model uses a few extra assumptions that make the set of equations algebraic, and also linear in different radial ranges. In particular, the disc is assumed to be in steady state and the rotation is assumed to be Keplerian. Moreover, the kinematic viscosity ν is assumed to have a simple form (the so-called "alpha viscosity prescription"):

$$\nu = \alpha c_s H \tag{1.8}$$

where c_s is the sound speed, H is the half thickness of the disc and $0 < \alpha < 1$ is a numeric constant. This equation derives from the hypothesis that turbulence is the main source of viscosity. Then, $\nu \sim \lambda v_t$ where λ is the correlation length of turbulence and v_t is the mean turbulent speed. Assuming that $v_t < c_s$, and that $\lambda \lesssim H$, eq. 1.8 is found.

A remarkable result of the Shakura-Sunyaev model is the energy flux radiated from a disc surface unit, i.e. a ring at a radius R, per unit time:

$$F(R) = \frac{3GM\dot{M}}{8\pi R^3}\left[1 - \left(\frac{R_*}{R}\right)^{1/2}\right] \tag{1.9}$$

where the accretion rate $\dot{M}$ is constant because of the mass conservation. The radiated flux, then, does not depend on the viscosity. If the vertical energy transport is radiative, the energy flux through the surface has the same form as that of a stellar "gray" atmosphere:

$$F(R) = \frac{4\sigma_{\rm SB} T_c^4(R)}{3\tau(R)} \tag{1.10}$$

where $T_c(R)$ is the central disc temperature and $\tau(R)$ is the vertical optical depth. Both quantities, in general, depend on the radius and their values are found by solving the Shakura-Sunyaev equations. However, a particular solution can be easily derived by assuming that the disc is optically thick in the vertical direction. In other words, we just set $\tau \gg 1$ and neglect the radial dependence. Then, each element of the disc radiates roughly as a blackbody with an effective temperature $T(R)$, so that

$$F(R) = \sigma_{\rm SB} T^4(R). \tag{1.11}$$

Using eq. 1.9 and 1.11, we find

$$T(R) = \left\{\frac{3GM\dot{M}}{8\pi R^3 \sigma_{\rm SB}}\left[1 - \left(\frac{R_*}{R}\right)^{1/2}\right]\right\}^{1/4}. \tag{1.12}$$

At large radii, where $R \gg R_*$, we have

$$T \simeq 3.7 \times 10^5 \left(\frac{M}{10^8 M_\odot}\right)^{-1/2} \left(\frac{\dot{M}}{1\, M_\odot/\mathrm{yr}}\right)^{1/4} \left(\frac{R}{R_G}\right)^{-3/4} \mathrm{K}. \tag{1.13}$$

The characteristic temperature of the disc is therefore 10^5 K, in rough agreement with eq. 1.6. Interestingly, eq. 1.13 does not differ much from a more accurate solution of the Shakura-Sunyaev equations, at least at large radii (Frank et al. 2002). In particular, $T(R) \propto R^{-3/4}$ is valid and can be used to find the spectrum of the disc.

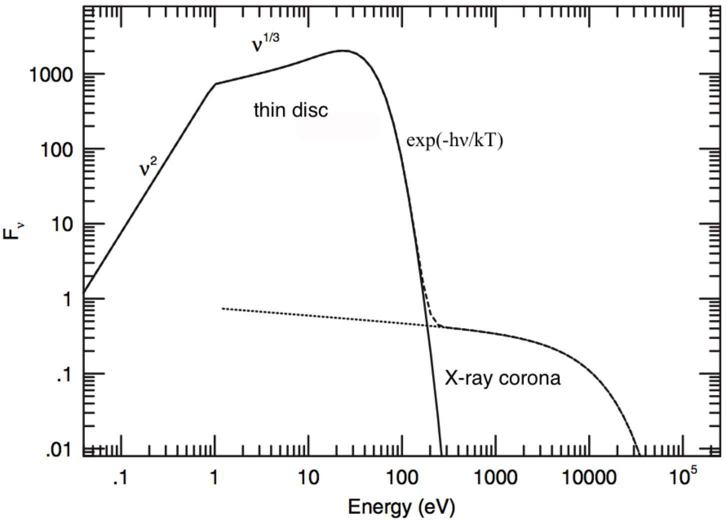

Figure 1.4 – Schematic view of the spectrum emitted by a thin accretion disc (adapted from Netzer 2006). The disc spectrum peaks in the UV/soft X-ray band, while the X-ray emission is explained by a different region, the so-called corona (see Chapter 2).

Using the blackbody assumption, the spectrum emitted by an element of the disc is given by Planck's law. The spectral radiance is thus

$$B_\nu[T(R)] = \frac{2h\nu^3}{c^2}\frac{1}{\exp[h\nu/k_\mathrm{B}T(R)]-1}. \tag{1.14}$$

The monochromatic luminosity emitted by the disc is found by integrating over the radius, i.e.

$$L_\nu = \int_{R_\mathrm{in}}^{R_\mathrm{out}} B_\nu[T(R)]\, 2\pi R\, \mathrm{d}R = \frac{4\pi h\nu^3}{c^2}\int_{R_\mathrm{in}}^{R_\mathrm{out}} \frac{R}{\exp[h\nu/k_\mathrm{B}T(R)]-1}\,\mathrm{d}R \tag{1.15}$$

where R_in is the inner radius and R_out the outer radius. At low energies, $h\nu \ll k_\mathrm{B}T$, the Planck function is approximated by the Rayleigh-Jeans form and $L_\nu \propto \nu^2$. At high energies, $h\nu \gg k_\mathrm{B}T$, the integrand assumes the Wien form and the resulting spectrum is dominated by the decaying exponential term $e^{-h\nu/k_\mathrm{B}T}$. For intermediate energies, it can be shown that approximately $L_\nu \propto \nu^{1/3}$ (e.g., Frank et al. 2002). Finally, the flux observed at a distance D by an observer whose line of sight is inclined by an angle i with respect to the disc is $F_\nu = L_\nu \cos i / D^2$. A schematic view of the spectrum is given in Fig. 1.4. Clearly, the accretion disc alone is not enough to explain the X-ray emission of an AGN, because the disc spectrum peaks in the UV/soft X-ray band and then has a rapid turnover. The hard X-rays must originate from reprocessing of the disc emission in a hotter region, which is called corona in analogy with the solar one. We will see the details of X-ray production in Chapter 2.

1.2.3 Other disc models

The Shakura-Sunyaev model is regarded as a standard model for the accretion disc around a compact object. However, many other models have been proposed, in particular relaxing the hypothesis of geometrical thinness. For example, at high accretion rates the temperature and hence the radiation pressure in the disc can become large enough to "inflate" the disc, which cannot be regarded as thin anymore.

To be more precise, we should analyse the vertical structure of the disc. A hidden assumption of virtually all disc models is that the mass contained in the disc is small compared with the mass of the accreting object, thus the self-gravity of the disc can be neglected. Let us write the hydrostatic equilibrium equation along the vertical z-axis, for a fluid element in the disc, which "floats" at an angle θ out of the plane:

$$\frac{\mathrm{d}P}{\mathrm{d}z} = -\rho \frac{GM \sin\theta}{R^2} \tag{1.16}$$

where P is the pressure and $\rho = \rho(R, z)$ is the local density. In general, we should consider P as the sum of the gas pressure and of the radiation pressure. If the former component dominates, we simply have $P = \rho c_s^2$ where c_s is the isothermal sound speed. Moreover, $\sin\theta \simeq z/R$ if the disc is thin. Then, eq. 1.16 becomes:

$$\frac{\mathrm{d}\rho}{\mathrm{d}z} = -\rho z \frac{GM}{c_s^2 R^3}. \tag{1.17}$$

The equation has the simple solution

$$\rho(R, z) = \rho(R, 0) \exp\left(-\frac{z^2}{H^2}\right) \tag{1.18}$$

where $H = c_s\sqrt{R^3/GM} = c_s/\Omega_{\mathrm{K}}$, Ω_{K} being the Keplerian angular velocity. The thin disc condition can be stated as $H \ll R$, which is equivalent to $c_s \ll v_{\mathrm{K}}$ i.e. the local Keplerian velocity must be highly supersonic. But the sound speed increases with temperature, which increases with the accretion rate. This is an indication that, at high accretion rates, the thin disc approximation is likely to break down.

The main types of accretion disc models beyond Shakura-Sunyaev (Abramowicz & Fragile 2013) are the so-called slim discs (e.g., Abramowicz et al. 1988), thick discs (or "polish doughnuts"; see, e.g., Paczyńsky & Wiita 1980), and radiatively-inefficient accretion flows (RIAFs; Narayan & Yi 1994, 1995). Slim and thick discs are normally associated with large accretion rates. They are inefficient radiation emitters, as the accretion timescale is shorter than the time that photons need to diffuse and reach the disc surface. In other words, the photons are trapped in the accretion flow and captured by the black hole before they can escape. RIAFs have instead very low accretion rates, and a low radiation efficiency as well. If the accretion rate is low, the surface density of the disc can become so low that Coulomb interactions are not sufficient to maintain thermal coupling between ions (mostly protons) and electrons. Then, the two types of particles will have two different temperatures. Protons, being much more massive, carry most of the gravitational energy, while the radiative energy losses are mostly due to electrons. But since protons are thermally decoupled from electrons, they are advected into the black hole transporting much of the gravitational energy with them. In other words, the energy is mostly dissipated by advection of the hot, virialized protons rather than by radiation from the cold electrons. RIAFs are thus very hot but inefficient emitters. Indeed, slim or thick discs are "radiation-trapped" (i.e. they have a long radiative diffusion time), while RIAFs are intrinsically inefficient (i.e. they have a long cooling time). However, in all these models, advection is the main cooling mechanism, so they are commonly referred to as advection-dominated accretion flows (ADAFs).

To summarize, the ADAF/slim or thick discs are "cold" and optically thick, similar in this respect to thin discs, and can be useful to model high-luminosity, high-accretion rate objects (e.g., Mineshige et al. 2000). ADAF/RIAFs are "hot" and optically thin, and adequate to describe low-luminosity, low-accretion rate sources (for a review, see Yuan & Narayan 2014). One of the most intriguing applications of RIAFs is perhaps the explanation of the broad-band emission from the Galactic Center in terms of an "underfed" supermassive black hole (Narayan et al. 1995). Furthermore, RIAFs are invoked to interpret the emission from low-luminosity AGNs, as we will see in Chapter 5.

Further disc models have been proposed, to take into account ejection as well as accretion, such as jet emitting discs (JED) in the context of X-ray binaries (Ferreira et al. 2006). This model envisages an outer standard accretion disc down to a transition radius, and an inner magnetized accretion disc driving an electron-positron jet.

1.3 AGN classification and the unified model

Besides the general properties I outlined so far, AGNs display a wide variety of observational features at different wavelengths. The AGN taxonomy is rich, including Seyferts 1 and 2, different kinds of radio galaxies, and high-luminosity objects. As we have seen in sec. 1.1, the first AGNs were identified by Carl Seyfert in 1943 as peculiar nearby spiral galaxies. Then, in 1963, Maarten Schmidt identified a *quasar* (quasi-stellar radio source) for the first time. This was the bright radio source 3C 273, that was associated with a 13th magnitude stellar object thanks to a series of lunar occultation observations (Hazard et al. 1963). Then, its redshift could be determined from the optical spectrum, resulting in $z = 0.158$ (Schmidt 1963). This discovery was a real breakthrough, as the implied comoving distance was 2 billion light years, making 3C 273 the most distant object known at the time, even though this was not immediately and easily accepted (Weedman 1976). In the mid-1970s, it was realized that quasars and Seyferts were connected and probably different manifestations of the same phenomenon (Rowan-Robinson 1977). Today, it is well established that quasars are a high-luminosity version of Seyfert galaxies, where the nucleus is so bright ($L > 10^{45}$ ergs s^{-1}, up to 10^{49} ergs s^{-1}) that it can outshine the host galaxy.

Apart from luminosity, the optical and radio properties of AGNs are diverse and give rise to different empirical classifications, although most of them can be described by a unified model. I will briefly describe the most important observational differences between classes of AGNs.

1.3.1 Optical spectra: the line-emitting regions

In sec. 1.1 we have also seen that the optical spectra of Seyferts can be roughly divided into two classes: type 1, showing both broad and narrow emission lines, and type 2, showing narrow lines only. This classification can be generalized to all AGNs, quasars included. Type 1 spectra are characterized by broad, permitted (i.e., recombination) emission lines (hydrogen Lyman and Balmer series, H II, Mg II, C IV and so on). The large line widths from Doppler broadening, of the order of thousands of km s^{-1}, imply that the line-forming regions are moving at high velocities. The narrow lines, both permitted and forbidden, originate in low-density gas, i.e. low enough that collisional de-excitation does not occur. Such lines (including e.g. [O II], [O III], [N I], [N II], [S II]) have widths of hundreds of km s^{-1}.

According to the present understanding, there is no fundamental difference between type 1 and type 2 AGNs, meaning that the central engine is the same. The observational differences can be simply explained by assuming the presence of two different line-emitting regions. The narrow lines are emitted in a "narrow-line region" (NLR), while the broad lines originate from a "broad-line region" (BLR). Then, in type 1 AGNs we see the emission from both the BLR and the NLR, while in type 2 AGNs we see the NLR only.

There are also sources showing intermediate properties between type 1 and 2. In particular, narrow-line Seyfert 1 galaxies (NLS1s; Osterbrock & Pogge 1985) are AGNs showing broad lines which are actually narrower (500–1500 km s^{-1}) than the typical broad lines in Seyfert 1s. The reasons for this peculiarity are not fully understood (e.g. Pogge 2011). NLS1s could be Seyfert 1s in their early life (Grupe et al. 1999), with relatively small black hole masses (Grupe & Mathur 2004) and very high accretion rates (Grupe et al. 2010). Then, the smaller black hole mass might imply lower velocities of the matter in the BLR, thus relatively smaller widths of the broad lines.

Some constraints on the physical parameters of the BLR and NLR can be derived from emission-line diagnostics (for a detailed discussion, see e.g. Osterbrock 1989). The lack of forbidden lines from the BLR implies that they are collisionally de-excited, i.e. the electron density is higher than the critical densities for collisional de-excitation of the strong forbidden lines observed from the NLR. For example, the critical density of [O III] $\lambda\lambda$4959+5007 is $\sim 10^8$ cm^{-3}, which is generally accepted as a lower limit of the BLR electron density. An upper limit to the electron density of the BLR can be derived from the commonly observed semi-forbidden line C III] λ1909, whose critical density is $\sim 10^9$ cm^{-3}. For the NLR, where forbidden lines are seen, the density should not exceed a few $\times 10^5$ cm^{-3}. An estimate of the NLR electron temperature can be derived from the ratios of emission lines with different upper levels, like [O III] and [S II] lines. The temperature value is usually $10,000 - 20,000$ K, corresponding to the photoionization equilibrium.

The size and location of BLR and NLR can be deduced from the line variability and reverberation lags with respect to the continuum (e.g., Peterson et al. 2004) or via spectroscopy and photoionization modelling (e.g., Wandel et al. 1999). In particular, the reverberation technique has been successfully applied to the BLR in a number of AGNs, with typical inferred distances of about $10 - 100$ light days from the central source (e.g., Peterson 2006). The NLR, by contrast, is much less variable, making it unviable to use reverberation mapping. Indeed, the NLR is found to be at kpc scales with photoionization techniques, albeit with large uncertainties (e.g., Bennert et al. 2006).

1.3.2 The unified model

Why there is no broad-line emission in type 2 AGNs? Either they have no BLR at all, or it must be somehow hidden from our sight. Historically, the first strong evidence of the presence of a BLR in a type 2 AGN has been the discovery of broad optical lines in the polarized spectrum of the Seyfert 2 NGC 1068 (Antonucci & Miller 1985). This means that the BLR emission is obscured by an absorbing medium, and scattered into our line of sight from material located at larger distances. The reflected spectrum is relatively weak, but still detectable thanks to its high degree of polarization ($\sim 16\%$, while the direct light is essentially unpolarized). Moreover, such a polarization indicates that the absorber should have more or less a toroidal structure, to prevent scattering in a large range of angles and polarization to be washed out. The size of such an obscuring torus should of the order of parsecs, i.e. enough to obscure the BLR, but not the NLR.

According to the standard unified model, type 1 and 2 AGNs are intrinsically the

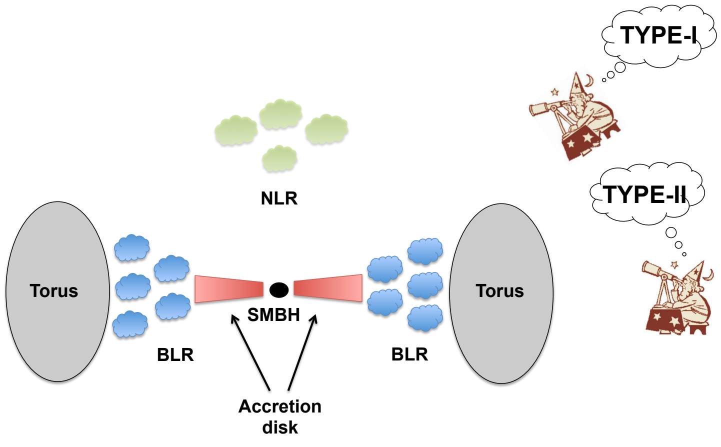

Figure 1.5 – Schematic view of an AGN in the light of the standard unification model. The difference between type 1s and 2s is due to the different orientation (`http://www.isdc.unige.ch/~ricci/Website/Active_Galactic_Nuclei.html`).

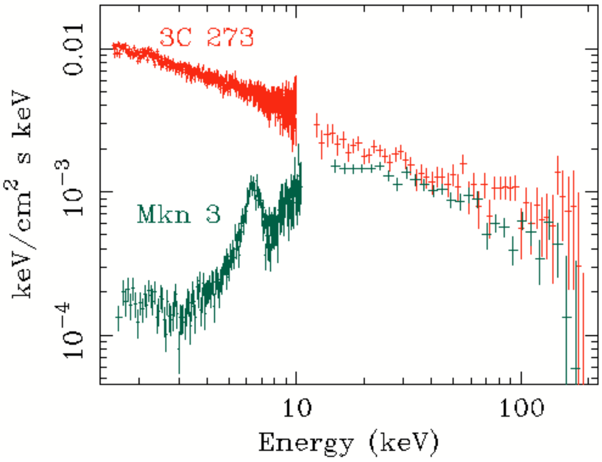

Figure 1.6 – X-ray spectra of the type 1 quasar 3C 273 and of the Seyfert 2 Mkn 3, taken with *BeppoSAX* (Bassani et al. 1999). The spectral energy distributions are similar in the hard X-rays above 10 keV, but very different at lower energies, because of a photoelectric cut-off in Mkn 3, which is typical of type 2 AGNs.

same class of objects, and their differences are only due to a different orientation relative to the obscuring torus (see Antonucci 1993 for an early review, and Bianchi et al. 2012a for a more recent one). A type 2 AGN is seen approximately edge-on, so that it appears hidden by the torus, while a type 1 AGN is seen approximately face-on or at low angles to the torus axis (see Fig. 1.5).

The unified model provides also an explanation for the difference observed in the X-ray spectra of type 1 and type 2 AGNs (see Fig. 1.6). Type 1s usually exhibit an X-ray continuum that is phenomenologically well described by a power law, as we will see in more detail in Chapter 2. The X-ray spectra of type 2s are instead much weaker at low energies, below 1-2 keV. This is easily explained by the presence of the obscuring torus, which causes photoelectric absorption of soft X-rays, the cut-off energy depending on the column density of the absorber. For example, column densities below $\sigma_{\mathrm{T}}^{-1} \simeq 1.5 \times 10^{24}$ cm^{-2} (where σ_{T} is the Thomson cross-section) produce a photoelectric cut-off between 1 and 10 keV, and such sources are said to be Compton-thin. Higher column densities can absorb the X-ray emission up to tens of keV, and such sources are called Compton-thick.

There are also evidences of the existence of "true" type 2 sources, i.e. completely lacking a BLR (e.g. Bianchi et al. 2012a,b). Such sources are found to be low-luminosity and weakly accreting. This can be explained theoretically, e.g. if the BLR arises from instabilities in the inner, radiation pressure-dominated region of the disc, that disappears at low accretion rates (Nicastro 2000) or if it is embedded in a disc wind (Elitzur & Ho 2009).

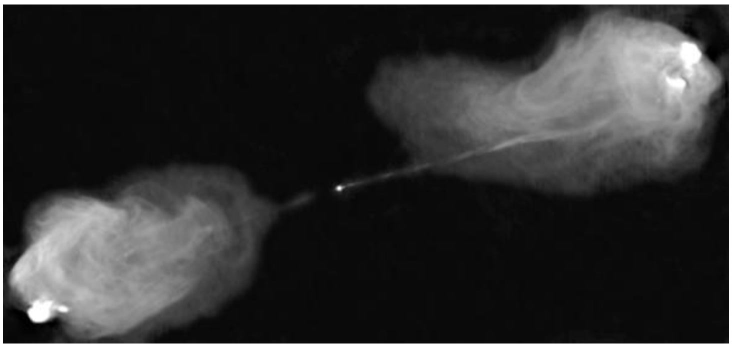

Figure 1.7 – Radio image at 5 GHz of the radio galaxy Cygnus A taken by VLA (`http://images.nrao.edu/261`; Carilli & Barthel 1996).

1.3.3 Radio classification

Roughly 10-20% of AGNs are radio-loud, meaning that they have a ratio of radio-to-optical flux above 10 (Kellermann et al. 1989). The emission of radio galaxies is characterized by a powerful and diffuse radio emission, which can be extended up to 100 kpc-scale regions, i.e. even beyond the host galaxy itself. Generally, radio-loud AGNs are known to exhibit bipolar jets launched from the nucleus, producing radio through gamma-ray emission that is relativistically beamed along the jet axes. At greater distances, larger-scale structures, called radio lobes, are sometimes observed. The radio lobes are thought to be produced by the interaction of the jet with the surrounding medium. One of the best example is Cygnus A, a very powerful radio source showing two narrow jets terminating in extended radio lobes (see Fig. 1.7). The radio continuum emission in radio-loud AGNs is thought to be synchrotron radiation, i.e. emission from relativistic electrons moving in a magnetic field (Sect. 2.1.2). Part of the synchrotron photons will undergo inverse Compton scattering (Sect. 2.1.3) by the electrons (synchrotron self-Compton), reaching X-ray and gamma-ray energies.

Radio-loud AGNs are classified according to their optical properties and to their radio morphology (for a review, see Urry & Padovani 1995). The type 1s, i.e. the radio-loud counterpart of Seyfert 1s, are called broad-line radio galaxies (BLRGs) or radio-loud quasars, depending on the luminosity. Analogously, the radio-loud counterpart of Seyfert 2s are called narrow-line radio galaxies (NLRGs). Following the work of Fanaroff & Riley (1974), radio galaxies are divided into two morphology and radio power subclasses: the low-luminosity Fanaroff-Riley (FR) I and the high-luminosity FR II. FR Is are more compact and their radio luminosity peaks near the nucleus, while FR IIs exhibit well-separated radio lobes with bright outer edges. When jets are observed, they are more collimated in FR IIs. Cygnus A, for example, is a classical FR II. Finally, a small number of radio-loud AGNs have unusual spectral characteristics, most likely related to a small viewing angle to the line of sight (Urry & Padovani 1995). These are called blazars, and are characterized by high luminosity and very rapid variability. This class includes the BL Lacertae (BL Lac) objects, which lack strong optical emission or absorption lines, and flat-spectrum radio quasars (FSRQs), which show strong and broad optical emission lines. The basic idea of unified schemes, i.e. that most observational differences are due to a different orientation, is thus suitable to describe radio-loud as well as radio-quiet AGNs (see Fig. 1.8).

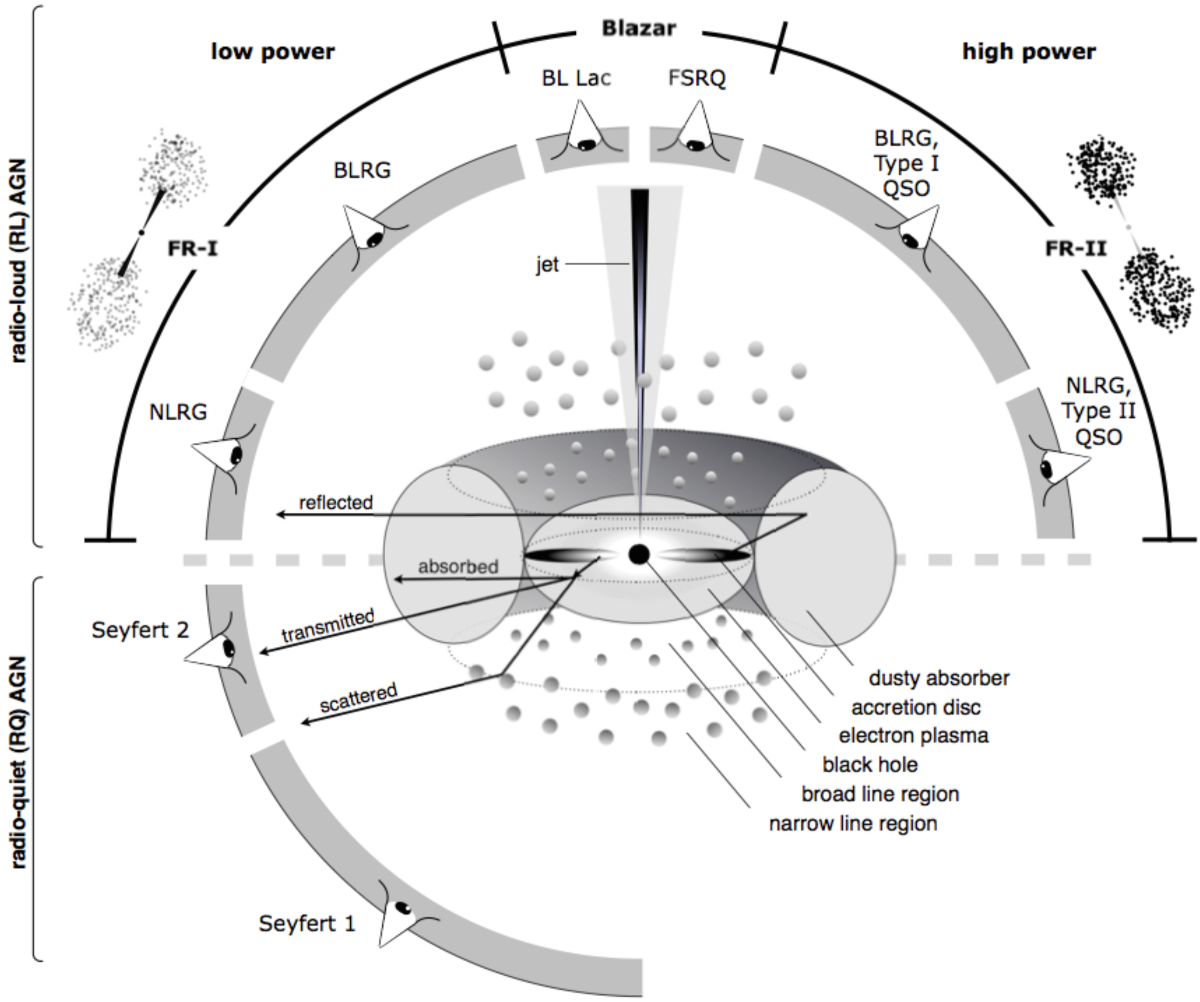

Figure 1.8 – Unified scheme for radio-loud and radio-quiet AGNs (adapted from Beckmann & Shrader 2012).

Chapter 2

The X-ray emission of AGNs

Contents

2.1 Radiative processes

In this section, I will review the most important radiative processes that are believed to take place in AGNs, focusing on the X-ray production. I will thus discuss Bremsstrahlung, synchrotron emission and inverse Compton scattering. In particular, the latter process is thought to explain the primary X-ray emission of AGNs and will be discussed in more detail. A comprehensive introduction on the theory of radiative processes can be found in the classic textbook by Rybicki & Lightman (1979).

2.1.1 Bremsstrahlung

Bremsstrahlung ("braking radiation") is radiation due to the acceleration of a charged particle by the Coulomb field of another charged particle. It is also called free-free emission, because the radiating particle is in a free state both before and after the interaction. If the two interacting charged particles are identical, the emitted radiation is small[1]. Therefore, electron-electron and ion-ion collisions are generally unimportant in cosmic plasmas, while electron-ion interactions represent the most relevant case. Given the difference of mass, the acceleration of electrons is much larger than that of ions, and it thus produces most of the Bremsstrahlung emission.

A detailed treatment of Bremsstrahlung would require quantum electrodynamics, because this process can produce photons with energies comparable to that of the emitting particle. However, an essential understanding can be derived from classical radiation theory. Quantum corrections are usually introduced in the form of Gaunt factors of order unity (Rybicki & Lightman 1979).

The power emitted by an electron deflected by the electric field of an ion can be qualitatively estimated as follows. Let us consider an electron passing by an ion having a charge Ze, with velocity v and impact parameter (i.e. minimum approach) b. The electron will experience an acceleration due to the Coulomb force

$$a \simeq \frac{Ze^2}{m_\mathrm{e} b^2} \tag{2.1}$$

and therefore, from the Larmor formula, the emitted power will be

$$P = \frac{2e^2a^2}{3c^2} \simeq \frac{2Z^2e^6}{3m_\mathrm{e}^2c^3b^4}. \tag{2.2}$$

The maximum power corresponds to the minimum impact parameter, which cannot be arbitrarily small because of the uncertainty principle:

$$b_\mathrm{min} \simeq \frac{\hbar}{m_\mathrm{e} v}. \tag{2.3}$$

Then,

$$P_\mathrm{max} \simeq \frac{2Z^2m_\mathrm{e}^2v^4e^6}{3c^3\hbar^4}. \tag{2.4}$$

To find the spectrum, we should use the generalized Larmor formula:

$$P = \frac{2|\ddot{\mathbf{d}}|^2}{3c^2} \tag{2.5}$$

where $\mathbf{d}$ is the dipole vector. Since $\ddot{\mathbf{d}} = -e\,\mathbf{a}$, it is easy to go into the frequency space by taking the Fourier transform and find $\hat{\mathbf{d}}(\omega)$. Then, the total emitted energy will be

$$E = \int_{-\infty}^{+\infty} P(t)\,\mathrm{d}t = \frac{2}{3c^2}\int_{-\infty}^{+\infty} |\ddot{\mathbf{d}}(t)|^2\,\mathrm{d}t = \frac{8\pi}{3c^2}\int_0^{+\infty} \omega^4\,|\hat{\mathbf{d}}(\omega)|^2\,\mathrm{d}\omega. \tag{2.6}$$

---

[1] This is simply due to the conservation of momentum (which implies null acceleration of the electric dipole moment) and angular momentum (which implies null acceleration of the magnetic dipole moment). Thus the first non-zero contribution comes from the electric quadrupole moment.

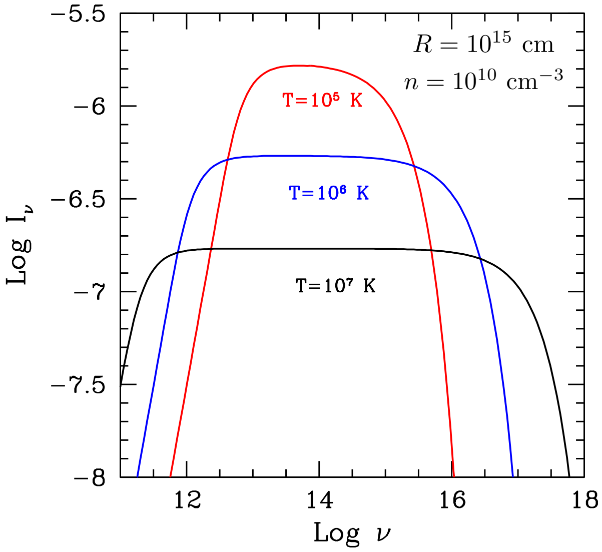

Figure 2.1 – Thermal Bremsstrahlung intensity for different temperatures (adapted from Ghisellini 2013). The spectrum is flat, with a high-energy cut-off due to the finite interaction time and a low-energy cut-off due to self-absorption.

Therefore, the spectrum is

$$\frac{\mathrm{d}E}{\mathrm{d}\omega} = \frac{8\pi}{3c^2}\,\omega^4\,|\hat{\mathbf{d}}(\omega)|^2. \tag{2.7}$$

The interaction occurs within a characteristic time-scale $\tau \simeq b/v$. Therefore, frequencies $\omega \gg 1/\tau$ do not contribute to the emission and we expect $\hat{\mathbf{d}}(\omega) = 0$ in the high-frequency limit. Indeed, the detailed calculation shows that the spectrum from a single collision is approximately flat up to a cut-off at high frequencies (for the details, see Rybicki & Lightman 1979):

$$\frac{\mathrm{d}E(b)}{\mathrm{d}\omega} = \begin{cases} \dfrac{8Z^2e^6}{3\pi c^3 m_\mathrm{e}^2 v^2 b^2} & \text{if } b \ll v/\omega, \\ \\ 0 & \text{if } b \gg v/\omega. \end{cases} \tag{2.8}$$

The above result is valid for a single electron colliding with an ion, but it can be extended to the more relevant case of many electrons travelling in a medium. If n_e is the electron density and v their (fixed) speed, the incident flux of electrons is $n_e v$. The element of area is $2\pi b\,\mathrm{d}b$ around each ion. If n_i is the ion density, the emitted power per unit volume per unit frequency is found to be (Rybicki & Lightman 1979):

$$\frac{\mathrm{d}E(v,\omega)}{\mathrm{d}\omega\mathrm{d}V\mathrm{d}t} = \frac{16Z^2e^6}{3c^3m_\mathrm{e}^2 v}\,n_i\,n_e\,\ln\left(\frac{m_\mathrm{e}v^2}{\hbar\omega}\right). \tag{2.9}$$

To derive the above equation, the electrons are assumed to have a fixed velocity, which is of course a simplified case. In astrophysical plasmas, a more useful application is that of thermal Bremsstrahlung, namely when the particle velocity distribution is Maxwellian: $f(v) \propto v^2\exp(-mv^2/2k_\mathrm{B}T)$ where T is the temperature. To find the thermal Bremsstrahlung emission, we thus need to integrate eq. 2.9 over $f(v)$. The limits of integration are (v_min, ∞) where $m_\mathrm{e}v_\mathrm{min}^2/2 = h\nu$ in order to create one photon with energy $h\nu$. Then,

$$\frac{\mathrm{d}E(T,\omega)}{\mathrm{d}\omega\mathrm{d}V\mathrm{d}t} = \frac{\displaystyle\int_{v_\mathrm{min}}^{\infty}\frac{\mathrm{d}E(v,\omega)}{\mathrm{d}\omega\mathrm{d}V\mathrm{d}t}v^2\exp\left(-\frac{m_\mathrm{e}v^2}{2k_\mathrm{B}T}\right)\,\mathrm{d}v}{\displaystyle\int_0^{\infty} v^2\exp\left(-\frac{m_\mathrm{e}v^2}{2k_\mathrm{B}T}\right)\,\mathrm{d}v} \tag{2.10}$$

and the integral can be solved analytically. The final result is

$$\frac{\mathrm{d}E(T,\omega)}{\mathrm{d}\omega \mathrm{d}V \mathrm{d}t} \simeq 6.8 \times 10^{-38}\, Z^2\ n_i\, n_e\, T^{-1/2}\, e^{-h\nu/k_\mathrm{B}T}\, \mathrm{ergs\ s^{-1}\ cm^{-3}\ Hz^{-1}}. \tag{2.11}$$

where n_i, n_e are in units of cm^{-3} and T is in Kelvin. The thermal Bremsstrahlung spectrum is flat up to an exponential cut-off occurring at $h\nu \sim k_\mathrm{B}T$. The total emitted power per unit volume is found by integrating over frequency:

$$\frac{\mathrm{d}E(T)}{\mathrm{d}V \mathrm{d}t} \simeq 1.4 \times 10^{-27}\, Z^2\ n_i\, n_e\, T^{1/2}\, \mathrm{ergs\ s^{-1}\ cm^{-3}}. \tag{2.12}$$

Therefore, the power density scales with $n_e^2 T^{1/2}$ (assuming $n_i \sim n_e$). The cooling time can be evaluated as the ratio between the energy density of the thermal electrons, i.e. $(3/2) n_e k_\mathrm{B} T$, and the power density:

$$t_\mathrm{B} \simeq 2 \times 10^{11}\, n_e^{-1}\, T^{1/2}\, \mathrm{s}. \tag{2.13}$$

The above calculations are valid only in the optically thin case, namely when the emitted photons escape without interacting with the free electrons. However, in the more general case, we should take into account self-absorption. Since we are dealing with thermal radiation, i.e. emitted by matter in thermal equilibrium, the absorption coefficient can be found using the Kirchhoff law (Rybicki & Lightman 1979):

$$\alpha_\nu^{ff} \simeq 3.7 \times 10^{8}\, Z^2\, n_i\, n_e\, T^{-1/2}\, \nu^{-3} (1 - e^{-h\nu/k_\mathrm{B}T})\, \mathrm{cm}^{-1}. \tag{2.14}$$

When $h\nu \gg k_\mathrm{B}T$ (Wien regime), $\alpha_\nu^{ff} \propto \nu^{-3}$. When $h\nu \ll k_\mathrm{B}T$ (Rayleigh-Jeans regime), $\alpha_\nu^{ff} \propto \nu^{-2}$. Then, the free-free absorption is larger at lower frequencies, and smaller at higher frequencies. Therefore, the Bremsstrahlung spectrum has not only a high-energy cut-off, but also a low-energy cut-off due to self-absorption (see Fig. 2.1).

2.1.2 Synchrotron

When charged particles move in a magnetic field, they are continuously accelerated by the Lorentz force. For non-relativistic velocities (*cyclotron* radiation), the frequency of emission is simply that of gyration, namely $\omega_B = qB/mc$ where q is the charge, m is the mass and B is the magnetic field. In other words, this process results in line emission (or absorption). The quantization of cyclotron motion gives rise to a Hamiltonian almost identical to that of the harmonic oscillator. The particle can thus occupy only specific energy levels (the so-called Landau levels) spaced by $\hbar\omega_B$. Cyclotron absorption lines in the X-ray band (tens of keV) have been observed in a number of X-ray pulsars, allowing to constrain their strong magnetic field (e.g., Walter et al. 2015).

For relativistic velocities (*synchrotron* radiation), the frequency spectrum is more extended and complex. First, the frequency of the rotation becomes $\omega_B = qB/\gamma mc$, thus it depends on velocity. The acceleration, which is perpendicular to the velocity vector, has a magnitude $a = \omega_B v_\perp$ where $v_\perp$ is the velocity projected onto the plane normal to the magnetic field. The power emitted by the particle spiralling round the magnetic field is given by the Larmor formula. Since $\omega_B \propto m^{-1}$ and $P \propto a^2 \propto \omega_B^2$, we have $P \propto m^{-2}$, namely the power scales with the inverse square of the mass and electrons will be much more effective than protons, at least for a given velocity. We can thus focus on electron synchrotron emission. The Larmor formula results in:

$$P = \frac{2}{3}\, c\, r_0^2\, \gamma^2\, \beta_\perp^2\, B^2 \tag{2.15}$$

where $r_0 = e^2/m_\mathrm{e}c^2$ is the classical electron radius. For electrons with an isotropic velocity distribution, the formula can be easily averaged over all angles, for a given β. The mean square transverse velocity will simply be two-thirds of β^2. Finally,

$$P = \frac{4}{3}\, c\, \sigma_\mathrm{T}\, \gamma^2\, \beta^2\, U_B \tag{2.16}$$

where $\sigma_\mathrm{T} = 8\pi r_0^2/3$ is the Thomson cross section and $U_B = B^2/8\pi$ is the magnetic energy density. Plugging in numbers,

$$P \simeq 1.1 \times 10^{-15}\, \gamma^2\, \beta^2\, B^2\, \mathrm{ergs\ s^{-1}}. \tag{2.17}$$

The characteristic time-scale τ of synchrotron radiation, or the "lifetime" of an electron with initial energy $E = \gamma m_\mathrm{e} c^2$, can be evaluated as $\tau \sim E/P$. Assuming $\beta \simeq 1$, we find

$$\tau \simeq \frac{25}{\gamma B^2}\, \mathrm{G^{-2}\, yrs}. \tag{2.18}$$

For example, an electron with $\gamma = 1000$ would have a synchrotron lifetime of 8 ks in the vicinity of the accretion disc of an AGN with $B = 10$ gauss (e.g. Martí-Vidal et al. 2015). In the radio lobes of a radio-loud AGNs, instead, the magnetic field is likely of the order of 10^{-5} gauss (Croston et al. 2005) and the same electron would have a cooling time of 250 million years.

If we now wish to determine the synchrotron spectrum, we shall start from the typical emitted frequency. We cannot evaluate this typical frequency as the inverse of the typical lifetime, because of two important effects seen by a distant observers. First, the relativistic beaming effect implies that the emitted radiation is concentrated in a narrow cone of semi-aperture $1/\gamma$. Then, the photons are emitted towards the observer during a time $\Delta t_e \simeq 2/\gamma\omega_B$ i.e. shorter than the rotation period. Additionally, the observer sees an even shorter pulse, because of Lorentz contraction of the electron's path: $\Delta t_o = \Delta t_e(1-\beta) \simeq \Delta t_e/2\gamma^2$. Then, the typical time is

$$\Delta t_o = \frac{1}{\gamma^3 \omega_B}. \tag{2.19}$$

It is the inverse of this time that must be taken as the typical synchrotron frequency:

$$\omega_s = \gamma^3 \omega_B = \gamma^2 \frac{eB}{m_\mathrm{e} c}. \tag{2.20}$$

The fact that the pulses of radiation are confined to short time intervals means that the observed spectrum is spread over a broad frequency range. A more careful treatment (Rybicki & Lightman 1979) shows that the spectrum peaks at ω_c, the so-called critical frequency:

$$\omega_c = \frac{3}{2}\, \omega_s \sin\alpha = \frac{3\gamma^2 eB \sin\alpha}{2 m_\mathrm{e} c} \tag{2.21}$$

where α is the angle between velocity and magnetic field. Approximately,

$$\nu_c = \omega_c/2\pi \simeq 4 \times 10^6 \, \gamma^2 \, B \, \mathrm{G}^{-1} \, \mathrm{Hz}. \tag{2.22}$$

For $\gamma \sim 10^3$ and $B \sim 10^{-5}$ gauss, we have $\nu_c \sim 100$ MHz i.e. synchrotron emission at radio frequencies. The relativistic jets observed in radio-loud AGNs (see Chapter 1) are powerful radio synchrotron sources. However, at higher velocities such as $\gamma \sim 10^7$, the critical frequency is in the X-ray band. Perhaps the most famous case of an X-ray synchrotron source is the Crab Nebula (e.g., Bühler & Blandford 2014), but also in radio-loud AGNs the synchrotron process likely plays an important role (e.g., Landt et al. 2008).

For a detailed calculation of the spectrum, we should find the electromagnetic field produced by the electron during its helical motion and transform it into the observer's frame. It can be shown that the power spectrum is (Rybicki & Lightman 1979)

$$P(\omega) = \frac{\sqrt{3} e^3 B \sin\alpha}{2\pi m_\mathrm{e} c^2} F(x) \tag{2.23}$$

where $x = \omega/\omega_c$, $F(x) = x \int_0^\infty K_{5/3}(y) \, \mathrm{d}y$ and $K_{5/3}$ is the modified Bessel function of order 5/3, peaking at $x \simeq 0.29$ i.e. $\omega \simeq 0.29\omega_c$.

However, even without taking into account the precise form of $F(x)$, we can draw some interesting results. First, the whole dependence on the electron energy is contained in the ratio ω/ω_c. In other words, no factor of γ appears in the power spectrum, except for that contained in $\omega_c \propto \gamma^2$. Let us now consider the emission from a set of relativistic electrons. We can assume their velocity distribution to be a power law, i.e. the number density of electrons with velocities between γ and $\gamma + \mathrm{d}\gamma$ is $N(\gamma)\,\mathrm{d}\gamma = N_0 \gamma^{-p}\,\mathrm{d}\gamma$. This is the kind of distribution observed for galactic cosmic rays, which can be theoretically explained by the Fermi acceleration mechanism (for a review, see e.g. Blandford & Eichler 1987). To find the total power radiated per unit volume per unit frequency, we just need to integrate $P(\omega)$ over the distribution:

$$\frac{\mathrm{d}E(\omega)}{\mathrm{d}\omega \mathrm{d}V \mathrm{d}t} = N_0 \int_{\gamma_\mathrm{min}}^{\gamma_\mathrm{max}} P(\omega) \gamma^{-p} \, \mathrm{d}\gamma \propto \int_{\gamma_\mathrm{min}}^{\gamma_\mathrm{max}} F(\omega/\omega_c) \gamma^{-p} \, \mathrm{d}\gamma. \tag{2.24}$$

Changing the variable to $x = \omega/\omega_c$ and recalling that $\omega_c \propto \gamma^2$,

$$\frac{\mathrm{d}E(\omega)}{\mathrm{d}\omega \mathrm{d}V \mathrm{d}t} \propto \omega^{-(p-1)/2} \int_{x_\mathrm{min}}^{x_\mathrm{max}} F(x) x^{(p-3)/2} \, \mathrm{d}x. \tag{2.25}$$

where the limits of integration depend on γ_min and γ_max. If these limits are sufficiently wide, we can approximate $x_\mathrm{min} = 0$ and $x_\mathrm{max} = \infty$, so that the integral becomes constant. Then,

$$\frac{\mathrm{d}E(\omega)}{\mathrm{d}\omega \mathrm{d}V \mathrm{d}t} \propto \omega^{-(p-1)/2} \tag{2.26}$$

namely the spectrum is described by a power law of the form $\omega^{-\alpha}$, where the spectral index α is related to the particle distribution spectrum p:

$$\alpha = \frac{p-1}{2}. \tag{2.27}$$

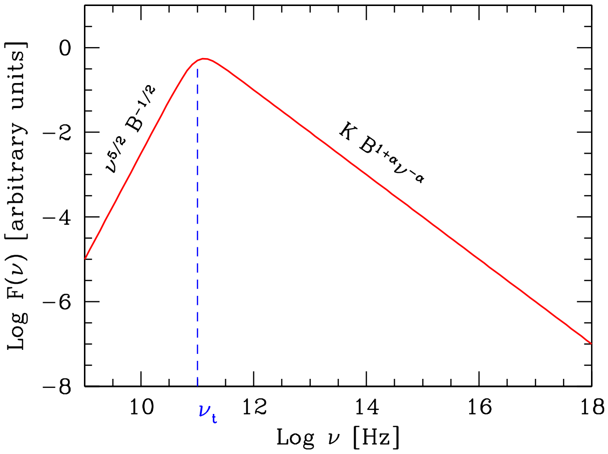

Figure 2.2 – The synchrotron spectrum from a partially self-absorbed source (adapted from Ghisellini 2013).

Therefore, a power law electron distribution produces a power law photon spectrum, and the two spectral indices are related to each other. Then, by measuring α we have a measurement of p. Typically, $\alpha \simeq 0.5 - 1$ thus $p \simeq 2 - 3$.

Like for thermal Bremsstrahlung, we should take into account self-absorption. The difference is that, in the case of synchrotron, we mostly have to deal with a power law (i.e. non-thermal) particle distribution. Then, the Kirchhoff law is not valid and we have to use the more fundamental Einstein relations for emission and absorption. The absorption coefficient is found to be (Rybicki & Lightman 1979)

$$\alpha_\nu \propto \nu^{-(p+4)/2}. \tag{2.28}$$

For $p = 2$, we have $\alpha_\nu \propto \nu^{-3}$. Therefore, self-absorption occurs at low frequencies and produces a low-frequency cut-off in the spectrum (see Fig. 2.2).

2.1.3 Inverse Compton scattering

Compton scattering is the inelastic scattering of photons by electrons. This process conserves the photon number, but it can strongly affect the incident spectrum. When the energy of the scattering photon is much smaller than the rest-mass energy of the electron, there is no significant energy transfer and the process is essentially elastic. This is called Thomson scattering, and it can be described in terms of classical electrodynamics by approximating the photon as a continuous electromagnetic wave. In the more general case, the process is not elastic because of the recoil of the electron. Referring to Fig. 2.3, the initial 4-momenta of the photon and of the electron are respectively

$$k_i^\mu = \frac{1}{c}(h\nu_i, h\nu_i, 0, 0) \qquad p_i^\mu = (m_\mathrm{e} c, 0, 0, 0). \tag{2.29}$$

The final 4-momentum of the photon is

$$k_f^\mu = (h\nu_f, h\nu_f \cos\theta, h\nu_f \sin\theta, 0) \tag{2.30}$$

while for the electron we have some p_f^μ which we do not need to write down, as we can simply use $|p_f|^2 = m_\mathrm{e}^2 c^2$. The 4-momentum conservation yields

$$k_i^\mu + p_i^\mu = k_f^\mu + p_f^\mu \Rightarrow |p_f|^2 = |k_i + p_i - k_f|^2. \tag{2.31}$$

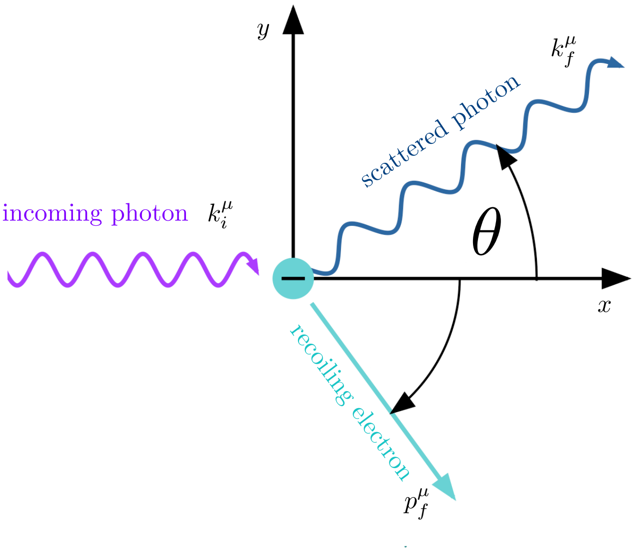

Figure 2.3 – Sketch of Compton scattering: a photon with initial 4-momentum k_i^μ collides with a static electron. After the collision, the photon will have a 4-momentum k_f^μ and the electron will recoil with a 4-momentum p_f^μ.

After some calculations, we obtain the final energy of the photon as a function of the initial energy and of the scattering angle:

$$h\nu_f = \frac{h\nu_i}{1 + \dfrac{h\nu_i}{m_\mathrm{e}c^2}(1-\cos\theta)}. \tag{2.32}$$

This relation is most easily written in terms of wavelengths:

$$\lambda_f - \lambda_i = \lambda_\mathrm{C}(1-\cos\theta) \tag{2.33}$$

where λ_C is the Compton wavelength:

$$\lambda_\mathrm{C} = \frac{h}{m_\mathrm{e}c} \simeq 0.024\,\text{Å}. \tag{2.34}$$

The photon undergoes an energy loss due to electron recoil, which is negligible only if $\lambda \gg \lambda_\mathrm{C}$, i.e. $h\nu \ll m_\mathrm{e}c^2$. This process, where the photon loses energy, is called *Compton scattering*. The cross-section of this process, i.e. the ratio between the scattered power and the incident flux, is given by the quantum-mechanical Klein-Nishina formula (see, e.g., Rybicki & Lightman 1979). Contrary to the classical Thomson cross-section, the Klein-Nishina formula depends on the photon energy. For low energies ($h\nu \ll m_\mathrm{e}c^2$), it reduces to the Thomson cross-section, while for high energies the cross-section falls rapidly ($\sigma \propto 1/h\nu$).

The above calculations are valid for a static electron. But if the electron is moving in the observer's frame, the photon can actually gain energy rather than lose it. In the latter case, the process is called *inverse Compton scattering*. To analyse this mechanism, we have to perform two Lorentz transformations: first from the observer's frame to the electron's frame, where eq. 2.32 holds, and then back to the original frame. Let S be the observer's frame, and S' the electron's frame. The electron is moving with a relativistic velocity $\boldsymbol{\beta}$ in S, and the photon (with initial energy E_i) is propagating in a direction forming an angle Θ_i with $\boldsymbol{\beta}$. Transforming to S' we just have the Doppler effect:

$$E_i' = E_i\gamma(1-\beta\cos\Theta_i). \tag{2.35}$$

The photon energy in S' after the Compton scattering is given by eq. 2.32. We assume that the initial photon energy in S' is much less than $m_\mathrm{e}c^2$, i.e. $\gamma E_i \ll m_\mathrm{e}c^2$ so that we can approximate eq. 2.32 as

$$E'_f \simeq E'_i \left[1 - \frac{E'_i}{m_\mathrm{e}c^2}(1-\cos\theta)\right] \simeq E'_i. \tag{2.36}$$

Finally, transforming back to S:

$$E_f = E'_f \gamma(1+\beta\cos\Theta'_f). \tag{2.37}$$

Neglecting for the moment the angle dependencies, we find a simple result: the energies of the photon before scattering in S, in S', and after scattering in S are in the approximate ratios $1 : \gamma : \gamma^2$. The net effect is thus to boost the photon energy by a factor of γ^2, which can be very high. When the intermediate photon energy γE_i is comparable with $m_\mathrm{e}c^2 = 511$ keV, the quantum mechanical Klein-Nishina corrections become important, reducing the probability of scattering. On the other hand, the intermediate photon energy can be as high as ~ 100 keV, thus resulting in very high final energies. Anyway, from the conservation of energy, the limit on the energy gain for the photon is $\gamma m_\mathrm{e}c^2$.

Let us now consider the case of an isotropic distribution of photons. Averaging the above equations over angles, it can be shown (Rybicki & Lightman 1979) that the total emitted power is

$$P = \frac{4}{3}\, c\, \sigma_\mathrm{T}\, \gamma^2\, \beta^2\, U_{ph} \tag{2.38}$$

where U_{ph} is the initial photon energy density. Remarkably, this is the same expression as the synchrotron power (eq. 2.16), except for the presence of U_{ph} instead of the magnetic energy density U_B. Indeed, also the synchrotron process can be understood as if a given energy flux cU_B was scattered by the electron (with the Thomson cross section). Therefore, we have the general result

$$\frac{P_\mathrm{IC}}{P_\mathrm{sync}} = \frac{U_{ph}}{U_B} \tag{2.39}$$

i.e. the losses due to inverse Compton and to synchrotron emission are in the same ratio as the photon energy density and the magnetic energy density.

To obtain the power emitted by a distribution of electrons, we must integrate eq. 2.38 over their energy distribution. For example, the total power from a thermal plasma of non-relativistic electrons ($\gamma \simeq 1$, $\langle\beta^2\rangle \simeq 3k_\mathrm{B}T/m_\mathrm{e}c^2$) of number density $n_e = \mathrm{d}N_e/\mathrm{d}V$ is

$$\frac{\mathrm{d}P_\mathrm{tot}}{\mathrm{d}V} = \frac{4k_\mathrm{B}T}{m_\mathrm{e}c^2}\, c\, \sigma_\mathrm{T}\, U_{ph}\, \frac{\mathrm{d}N_e}{\mathrm{d}V}. \tag{2.40}$$

In other words, the incident power $c\sigma_\mathrm{T}U_{ph}$ is scattered by $\mathrm{d}N_e$ electrons to give the power $\mathrm{d}P_\mathrm{tot}$. This implies that, for each scattering event, the average fractional energy gain of the photons is $4k_\mathrm{B}T/m_\mathrm{e}c^2$, minus the energy that is lost because of electron recoil:

$$\frac{\Delta E}{E} = \frac{4k_\mathrm{B}T - E}{m_\mathrm{e}c^2}. \tag{2.41}$$

Clearly, the photons gain energy only if the electron temperature is high enough, i.e. $4k_\mathrm{B}T > E$. We can also estimate the cooling time of this process as the ratio of the energy density of the electrons, i.e. $(3/2)n_e k_{\rm B}T$, to $\mathrm{d}P_{\rm tot}/\mathrm{d}V$:

$$t_{\rm IC} = \frac{3m_{\rm e}c}{8\sigma_{\rm T}U_{ph}} \simeq \frac{1.6\times10^7\ \text{s ergs cm}^{-3}}{U_{ph}}. \tag{2.42}$$

Calculating the spectrum of inverse Compton is conceptually analogous to what we have seen so far. We can start from a mono-energetic photon distribution, transform it from the observer's frame to the electron's frame, compute the scattering, and then transform back to the observer's frame. Then, the total spectrum from a set of photons scattering off a set of electrons is found by averaging over the actual distributions of photons and electrons. For example, in the case of a mono-energetic beam of photons scattering off a non-thermal, power law distribution of relativistic electrons with index p, the scattered spectrum is a power law with index $\alpha = (p-1)/2$, i.e. exactly the same as for synchrotron (Rybicki & Lightman 1979). However, this approach is only useful to calculate the spectra in the case of photons undergoing a single scattering. To give a complete description, we need to take into account multiple scatterings.

First, we define a *Compton parameter* y, which measures the average energy gain of photons in crossing a plasma. The Compton parameter is simply the average fractional energy change per scattering $\Delta E/E$, multiplied by the mean number of scatterings. For a plasma with optical depth τ, the number of scatterings is of the order of $\tau^2+\tau \simeq \max(\tau,\tau^2)$. Then,

$$y = \frac{\Delta E}{E}\times\max(\tau,\tau^2). \tag{2.43}$$

If $y \gtrsim 1$, the incident photon energy and spectrum will be significantly altered. For non-relativistic electrons in thermal equilibrium, $\Delta E/E$ is given by eq. 2.41. In the case $E \ll 4k_{\rm B}T$, i.e. when photons gain much energy at the expense of the electrons, $\Delta E/E \simeq 4k_{\rm B}T/m_{\rm e}c^2$ and

$$y_{\rm th,nr} = \frac{4k_{\rm B}T}{m_{\rm e}c^2}\times\max(\tau,\tau^2). \tag{2.44}$$

In a medium of optical depth $\tau \gg 1$, each photon will scatter $\sim \tau^2$ times before escaping. Then, from the very definition of y, the final energy of the emerging photons will be on average

$$E_f = E_i\, e^y. \tag{2.45}$$

When $E_f = 4k_{\rm B}T$, the photons stop gaining energy: the process has saturated.

For relativistic electrons with $\gamma \gg 1$, we have $\Delta E/E = (4/3)\gamma^2$ (e.g. from eq. 2.38). On average, $\langle\gamma^2\rangle = \langle(E/m_{\rm e}c^2)^2\rangle \simeq 12(k_{\rm B}T/m_{\rm e}c^2)^2$. In the end,

$$y_{\rm th,r} = \left(\frac{4k_{\rm B}T}{m_{\rm e}c^2}\right)^2\times\max(\tau,\tau^2). \tag{2.46}$$

The process of multiple scattering of a photon by a thermal distribution of electrons is called *thermal Comptonization*. I now briefly overview different physical regimes of Comptonization, referring to Rybicki & Lightman (1979) and Pozdnyakov et al. (1983) for an extensive discussion.

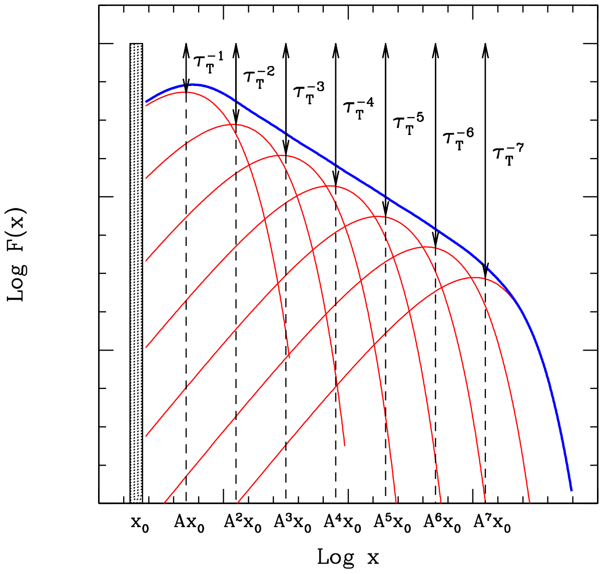

Figure 2.4 – Comptonization spectrum for small optical depth (as a function of $x \equiv h\nu/k_\mathrm{B}T$). A power law stems out from the superposition of all the scattering orders (adapted from Ghisellini 2013).

Small optical depth: Let $A_1 = \Delta E/E$ be the amplification of the photon energy for a single scattering. If $\tau < 1$, we have $y = A_1\tau$. After the first scattering, a fraction τ of the photons undergoes an energy increase by a factor A_1. After k scatterings, the energy of τ^k photons is increased by a factor of A_1^k, until the average photon energy is comparable with the temperature and further scatterings cannot increase the photon energy anymore. It can be shown that the emerging spectrum, i.e. the sum of all the scattering orders (see Fig. 2.4), has a power law shape: $F_\nu \propto \nu^{-\alpha}$, where

$$\alpha = -\frac{\ln\tau}{\ln A_1} = -\frac{\ln\tau}{\ln y - \ln\tau}. \tag{2.47}$$

When $\tau \ll 1$ and $A_1 \gg 1$, namely there are a few scatterings with a high energy gain, the spectrum will have a bumpy shape instead of being a power law.

Large optical depth: In this case, we must solve the Boltzmann equation for Compton scattering, i.e. the kinetic equation describing the evolution of the photon density $n(\omega)$ in the phase space due to the scattering. For isotropic homogeneous radiation, the equation can be generically written as (Rybicki 2003):

$$\frac{1}{c}\frac{\partial n}{\partial t} = n_e\,\sigma_\mathrm{T}\,(-n + e) \tag{2.48}$$

where, in the right-hand side, the term $-n$ accounts for extinction and the term $e = e(\omega, t)$ accounts for the scattered emission. The appropriate scattering term was found by Kompaneets (1957), in the hypotheses that the photon energy is $h\nu \ll m_\mathrm{e}c^2$, and that the thermal electrons are non-relativistic, $k_\mathrm{B}T \ll m_\mathrm{e}c^2$. For astrophysical applications, we must take into account the photon input and escape, i.e. we should include a source term $Q(x)$ and a diffusion term which depends inversely on the mean number of scatterings. The modified Kompaneets equation is (e.g. Liedahl 1999):

$$\frac{\partial n}{\partial t_c} = \frac{k_\mathrm{B}T}{m_\mathrm{e}c^2}\frac{1}{x^2}\frac{\partial}{\partial x}\left[x^4\left(\frac{\partial n}{\partial x} + n + n^2\right)\right] + Q(x) - \frac{n}{\max(\tau, \tau^2)}. \tag{2.49}$$

where $x \equiv h\nu/k_{\rm B}T$ and $t_c \equiv (n_e\sigma_{\rm T}c)t$ is the time measured in units of the mean time between scatterings. $Q(x)$ describes the number density of input photons produced per unit Compton time. The equation can be solved analytically making some simplifying assumptions. In particular, let us assume $n \ll 1$ and $Q(x) = 0$ at the typical energies of the Comptonized spectrum, i.e. the source only emits low-energy photons. Moreover, if we look for a steady-state solution, the time derivative is null. Finally,

$$\frac{y}{4}\frac{\partial}{\partial x}\left[x^4\left(\frac{\partial n}{\partial x}+n\right)\right] - nx^2 = 0 \tag{2.50}$$

where we introduced the Compton parameter y (eq. 2.44). For $x \gg 1$, an approximate solution is the Wien law: $n(x) \propto e^{-x} \Rightarrow I_\nu \propto \nu^3 e^{-x}$ i.e. we have an exponential cut-off at high energies, above $k_{\rm B}T$. When $x \ll 1$, the term in n can be neglected and the solution is a power law: $n \propto x^m$ with

$$m = -\frac{3}{2} \pm \sqrt{\frac{9}{4}+\frac{4}{y}}. \tag{2.51}$$

The emerging spectrum is also a power law: $I_\nu \propto \nu^{3+m}$, i.e. $I_\nu \propto \nu^{-\alpha}$ where

$$\alpha = -\frac{3}{2} \mp \sqrt{\frac{9}{4}+\frac{4}{y}}. \tag{2.52}$$

The negative root is appropriate for $y \gg 1$ (saturated Comptonization). In this case $m = 0$ and $\alpha = -3$, i.e. we have the low-energy tail of the Wien spectrum. The positive root is appropriate for $y < 1$, so that we have a power law with $\alpha > 1$ up to the high-energy cut-off.

2.2 The X-ray spectrum of AGNs

The X-ray emission of AGNs extends over three decades of energy, from the Galactic absorption cut-off at ~ 0.1 keV up to several hundreds of keV. The hard X-ray spectrum above 2 keV is well described by a power law with spectral index $\alpha \sim 1$ (eq. 2.52), i.e. the monochromatic flux is $F_\nu \propto \nu^{-\alpha}$. Equivalently, the photon flux per unit energy is $F_E \propto E^{-\Gamma}$ where $\Gamma \equiv 1+\alpha$. The photon index Γ is more commonly used in X-ray astronomy.

The primary, power law-like emission can be modified by different processes, such as Compton reflection from the accretion disc or more distant material, and absorption from surrounding gas, both neutral and ionized. In particular, the X-ray spectra of AGNs commonly show a high-energy bump peaking at ~ 30 keV and an iron Kα fluorescence line at 6.4 keV, which are both interpreted as effects of reprocessing of the primary radiation in matter close to the black hole (e.g. Lightman & White 1988; Matt et al. 1991). Moreover, a smooth rise in the spectrum is often observed below 1-2 keV, above the extrapolated high-energy power law (e.g. Bianchi et al. 2009a). The origin of this so-called soft excess is currently a matter of debate (e.g. Done et al. 2007). The main features of the X-ray spectrum are shown in Fig. 2.5 and are discussed in more detail below.

2.2.1 Primary continuum: thermal Comptonization

Observations with different X-ray satellites (such as *GINGA, ASCA, XMM-Newton*) show that the photon index of the AGNs spectra commonly ranges between 1.5 and 2,

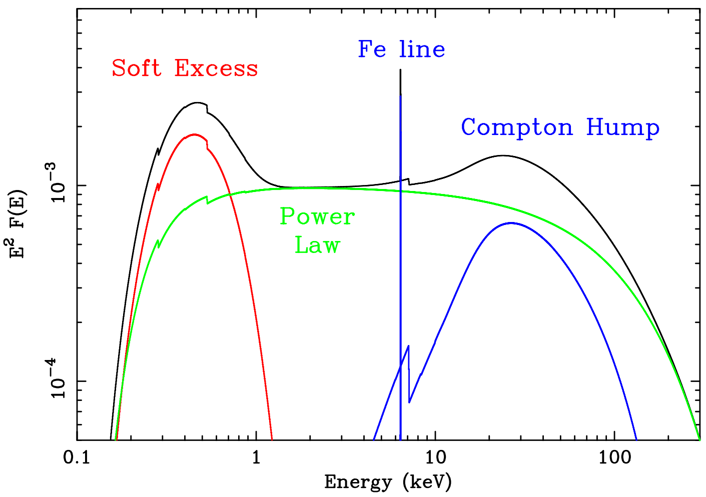

Figure 2.5 – Model X-ray spectrum of an unobscured AGN (black line) with the main components: the primary power law with a high-energy cut-off (green), the Compton reflection hump with iron $K\alpha$ line (blue), and the soft excess (red). Galactic absorption decreases the flux below 0.3 keV. Adapted from Fabian (2006).

both for Seyferts (e.g., Nandra & Pounds 1994; Bianchi et al. 2009a) and for quasars (e.g., Piconcelli et al. 2005). Radio-loud sources tend to have lower values of Γ, i.e. a flatter spectrum (e.g., Grandi et al. 2006). Moreover, a high-energy cut-off around ~ 100 keV has been found in several sources, thanks to high-energy data from *BeppoSAX* (e.g., Perola et al. 2002), *INTEGRAL* (e.g., Malizia et al. 2014), and, more recently, *NuSTAR* (see e.g. Fabian et al. 2015 and Marinucci et al. 2016, and references therein).

As we have seen in Sec. 2.1.3, thermal Comptonization of soft photons by hot electrons produces a power law spectrum with a high-energy cut-off, roughly corresponding to the temperature of the plasma. This mechanism thus explains the shape of the observed X-ray spectra of AGNs, if we assume the presence of a hot region where the optical/UV photons emitted from the accretion disc are Comptonized. As we have seen in Chapter 1, this region is called corona. A priori, thermal Bremsstrahlung might also be important, but generally it is much less efficient than Comptonization in high-luminosity compact sources. This can be seen by comparing the cooling times, as the shortest time corresponds to the dominant process (e.g. Fabian et al. 2015). On the other hand, synchrotron emission is likely important in radio-loud sources, where strong jets are observed. Their flatter spectrum is thought to be due to synchrotron self-Compton emission, namely inverse Compton scattering of the radio-synchrotron photons by the electrons in the jet (e.g. Ghisellini et al. 1985; Reeves & Turner 2000).

The analysis of the X-ray spectrum of AGNs can yield informations on the physical parameters of the corona, in particular its temperature ($T \sim 10^8 - 10^9$ K from the cut-off energy) and optical depth. However, the coronal geometry is uncertain. It could be a slab "sandwiching" the accretion disc, or a sphere, or a "patchy" medium made of blobs (see Fig. 2.6). In any case, as a crude sketch, we may think of a geometrically thick, small optical depth corona lying above the geometrically thin, optically thick accretion disc. Part of the optical/UV photons from the disc are Comptonized in the hot corona and become X-rays. Since this process cools the corona, there must be some other mechanism that heats the corona, in order to maintain a high enough temperature. This energy source could be the dissipation of magnetic flux through reconnection (e.g. Di Matteo 1998). I will review different models of the hot corona in Sect. 2.4.

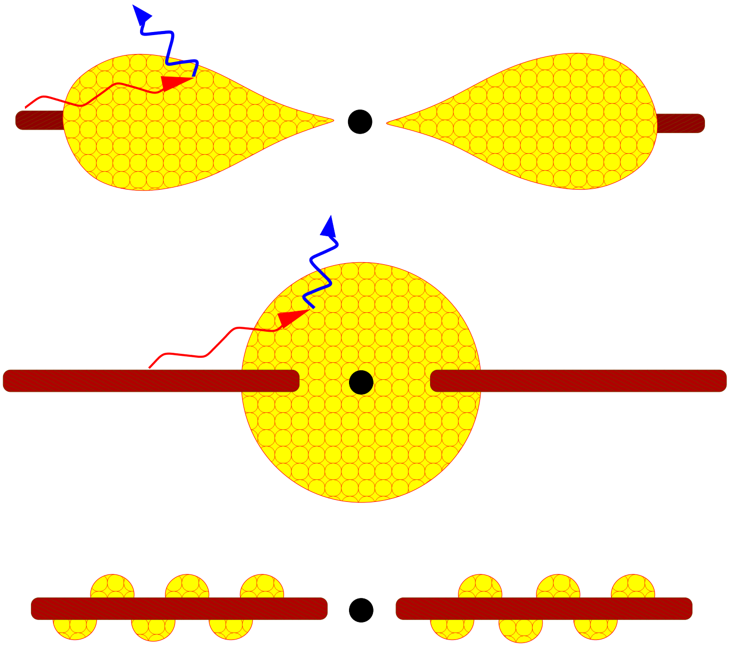

Figure 2.6 – Sketches of different geometries for the hot Comptonizing corona of an AGN (adapted from Reynolds & Nowak 2003).

2.2.2 Compton reflection and iron Kα line

The primary emission can be reflected, namely Compton scattered by surrounding gas. If the reflecting material is Compton-thick, i.e. it has a column density $N_{\rm H} > 1.5 \times 10^{24}$ cm^{-2}, the incident spectrum will undergo a significant reflection. On the other hand, if the material is Compton-thin, much of the incident radiation will escape without interacting. The accretion disc itself can be an effective reflector, but also the Compton-thick torus assumed in the unified model could scatter a significant fraction of the primary X-ray radiation (e.g. Ghisellini et al. 1994).

Let us discuss the possible results of the reprocessing by Compton-thick matter. An X-ray photon can be either Compton scattered by the electrons, or photoelectrically absorbed by a neutral atom or ion, if its energy is above the threshold for the relevant atomic transition. For photoionization, the K-shell ($n = 1$) has the largest cross-section. Following K-shell photoionization, the resulting ion can de-excite in two ways, namely fluorescence and Auger effect. In the first case, an L-shell ($n = 2$) electron drops into the K-shell and its energy is radiated as a Kα line photon. In the second case, the same energy is transferred to another L-shell electron, which is then ejected. The fluorescent yield (i.e. the probability that de-excitation occurs via fluorescence rather than Auger effect) is an increasing function of the atomic number. Since iron has the highest cosmic abundance among the heavier metals (e.g. Lodders 2003), the Fe Kα line at 6.4 keV is usually the strongest (e.g. Matt et al. 1997; Fabian et al. 2000, see also Fig. 2.7).

Concerning Compton scattering, the primary X-ray power law illuminating a slab of Compton-thick matter produces a continuum peaking at ~ 30 keV, with a cut-off at 4-5 keV due to photoelectric absorption (e.g. Magdziarz & Zdziarski 1995). The reflection efficiency can be measured by the so-called reflection fraction $\mathcal{R}$, namely the ratio between the reflected flux and the direct flux that an observer receives. For an isotropic source above an infinitely extended disc, $\mathcal{R} = 1$ i.e. half of the photons emitted by the source reach the observer directly, while the other half are reflected from the disc. Then, $\mathcal{R}$ can be considered as a proxy of the solid angle Ω subtended by the reflector, because

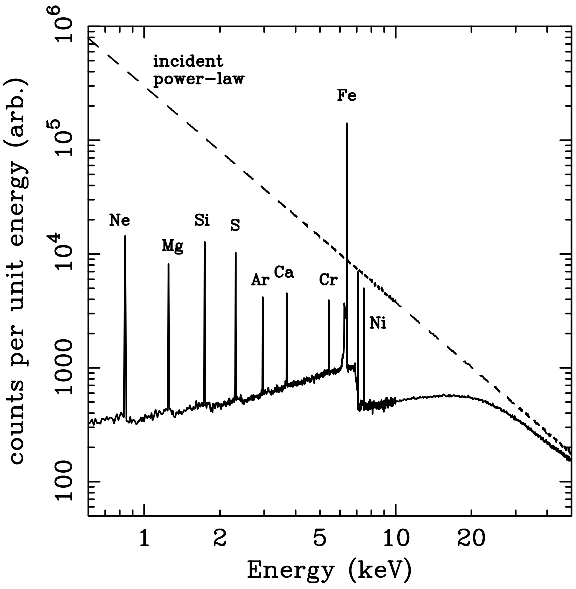

Figure 2.7 – Monte Carlo simulation of X-ray reflection from a neutral semi-infinite slab (Reynolds 1996). The dashed line shows the incident continuum, and the solid line shows the reflected spectrum integrated over all angles.

in general $\mathcal{R} = \Omega/2\pi$ (Magdziarz & Zdziarski 1995). However, this geometrical relation could be different for a distant reflector, i.e. other than the disc (e.g. Malzac & Petrucci 2002). Finally, the reflection efficiency would be less for Compton-thin material, and $\mathcal{R}$ cannot be interpreted as a covering factor in this case (e.g. Murphy & Yaqoob 2009).

Several calculations of X-ray reflection spectra have been performed in the literature, because this is an important effect to take into account when modelling the spectra of AGNs. Such calculations include reflection both from cold (i.e. neutral) matter (e.g. George & Fabian 1991a; Matt et al. 1991; Magdziarz & Zdziarski 1995; Nandra et al. 2007; Murphy & Yaqoob 2009) and from ionized matter (e.g. Ross & Fabian 1993; Matt et al. 1993; Zycki et al. 1994; Matt et al. 1996; Ross & Fabian 2005; García & Kallman 2010; García et al. 2013, 2014). The simplest and most used geometry is that of a semi-infinite, plane-parallel slab of constant density, but different configurations have been explored, such as reflection from a torus (Murphy & Yaqoob 2009) and from a finite-size disc (García et al. 2014). The main geometrical parameters characterizing the observed spectrum emerging from a reflector are the inclination angle and the location and geometry of the primary source (see also Sect. 2.4.3). In the case of a disc, the inner/outer radii are also important. Moreover, the physical conditions of the gas, such as the chemical composition and the ionization level, strongly affect the spectrum. The ionization parameter is usually defined as

$$\xi \equiv \frac{4\pi F_X}{n} \tag{2.53}$$

where F_X is the illuminating X-ray flux and n is the number density of the gas. When $\xi \lesssim 100$ ergs s^{-1} cm, the matter is in the “cold” regime, where the metals are neutral or weakly ionized, and a significant Fe Kα line at 6.4 keV is produced. At higher ionization levels, Fe Kα lines from Fe XXV and Fe XXVI (at 6.67 keV and 6.966 keV respectively) can be observed. However, when $\xi \gtrsim 10^4$ ergs s^{-1} cm, the material is too ionized to produce any atomic signature (see Fig. 2.8).

The Fe Kα line represents a powerful diagnostics to probe the innermost regions of an AGN. This line is intrinsically narrow, but the observed energy profile is shaped by both

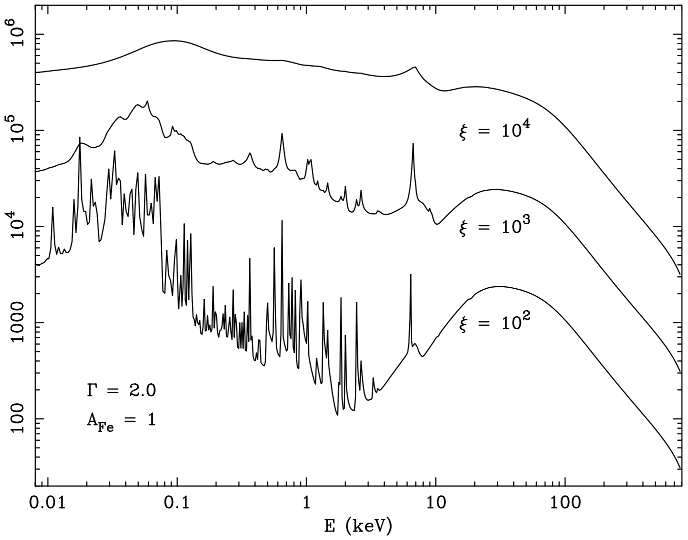

Figure 2.8 – Reflected spectra for three values of the ionization parameter ξ, in units of ergs s^{-1} cm (Ross & Fabian 2005). Besides the Fe Kα fluorescence line, the lower-ionization spectrum shows a forest of soft X-ray emission lines due to radiative recombination of different ions.

special relativistic (i.e. Doppler shift) and general relativistic (i.e. gravitational redshift and light bending) effects. If the line is produced within a few gravitational radii from the black hole, it can appear dramatically broadened and skewed to low energies, resulting in a characteristic profile (e.g. Fabian et al. 1989). The strongest effect is expected for a maximally rotating black hole, as the inner radius of the disc can extend down to 1.23 R_G (Laor 1991, see also Fig. 2.9). The first clear observation of such a broadened line has been in the Seyfert 1 MCG –6-30-15, with *ASCA* data (Tanaka et al. 1995). Broad line profiles (full width at half maximum of $\sim 5 \times 10^4$ km s^{-1}) are observed in a number of sources (e.g. Nandra et al. 2007). An alternative model has been proposed, in which the line profile is shaped by absorption, rather than by relativistic effects (Miller et al. 2008). However, a correlation between a relativistically broadened Fe Kα line and a Compton reflection bump has been found in the Seyfert 2 NGC 1365, using broad-band observations with *XMM-Newton* and *NuSTAR* (Risaliti et al. 2013; Walton et al. 2014). This observation supports the relativistic reflection scenario. Finally, if the broad line profile is interpreted as being due to relativistic effects, it is possible to constrain the inner radius of the disc and the spin of the black hole. From such spectroscopic analyses, there are indications that a significant number of supermassive black holes are rapidly spinning ($a > 0.9$; see Reynolds 2013, and references therein).

2.2.3 Soft excess

The soft excess is an extra, featureless emission below 1-2 keV, with respect to the extrapolated power law observed at higher energies (see Fig. 2.10). It has been found for the first time in the Seyfert 1 Mrk 841 with *EXOSAT* data (Arnaud et al. 1985), and it is commonly seen in the X-ray spectrum of AGNs (e.g. Walter & Fink 1993; Bianchi et al. 2009a). However, its physical origin is still uncertain and debated.

The soft excess is usually well fitted by a blackbody component with a temperature of 0.1-0.2 keV, which is unrelated to the X-ray luminosity or the black hole mass (Gierliński & Done 2004; Bianchi et al. 2009a) and too high to be explained as emission from a standard Shakura-Sunyaev disc. The constancy of the temperature could indicate an origin from atomic processes. If the disc is ionized, the soft excess could be due to the reprocessing of the primary continuum, such as recombination continuum and line

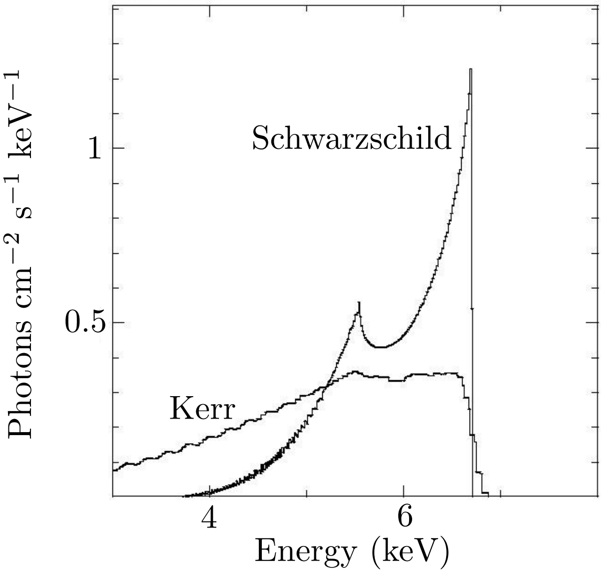

Figure 2.9 – Comparison of relativistic Fe Kα line profiles from an accretion disc around a Schwarzschild black hole and a maximally rotating (Kerr) black hole (adapted from Fabian et al. 2000).

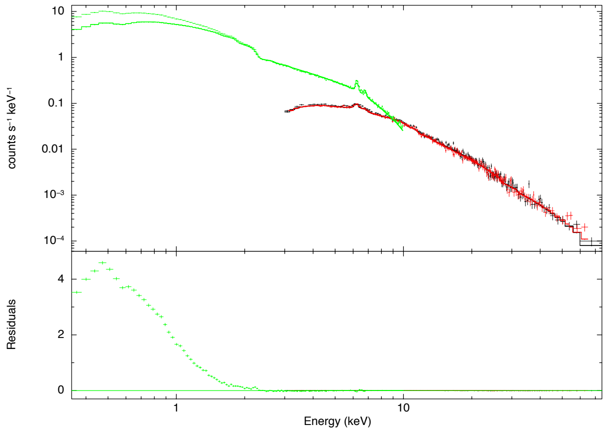

Figure 2.10 – The soft excess observed in the Seyfert 1 Ark 120 (Matt et al. 2014). The plot shows the *NuSTAR* 3–79 keV spectra (in black and red) and the best-fitting model extrapolated to the *XMM-Newton*/pn 0.3–10 keV spectrum (in green).

emission following photoionization (e.g. Ross & Fabian 1993). In particular, given the smooth and featureless shape of the soft excess, a scenario based on relativistic reflection can explain this component as the blending of many, relativistically blurred soft X-ray emission lines (e.g. Crummy et al. 2006; Cerruti et al. 2011; Walton et al. 2013).

A different explanation for the soft excess is thermal Comptonization by a warm, optically thick medium (see, e.g., Magdziarz et al. 1998; Petrucci et al. 2013; Boissay et al. 2014; Matt et al. 2014), which could be the upper layer of the accretion disc (e.g. Janiuk et al. 2001; Czerny et al. 2003; Różańska et al. 2015) or even the disc itself (Done et al. 2012). This scenario would naturally explain the observed correlation of the soft excess with the optical/UV luminosity (e.g. Walter & Fink 1993). In particular, this model has been tested for the Seyfert 1 Mrk 509, using data from a long multiwavelength campaign (Kaastra et al. 2011). In that case, Mehdipour et al. (2011) found a correlation between the optical/UV and soft ($<$ 0.5 keV) X-ray flux, but no correlation between the optical/UV and hard ($>$ 3 keV) X-ray flux. The spectral modelling indicated the presence of a "warm" corona with temperature $kT \sim 1$ keV and optical depth $\tau \sim 15$, responsible for both the optical/UV emission and the soft X-ray excess (Mehdipour et al. 2011; Petrucci et al. 2013, see also Fig. 2.11). I will return to this campaign in Chapter 3.

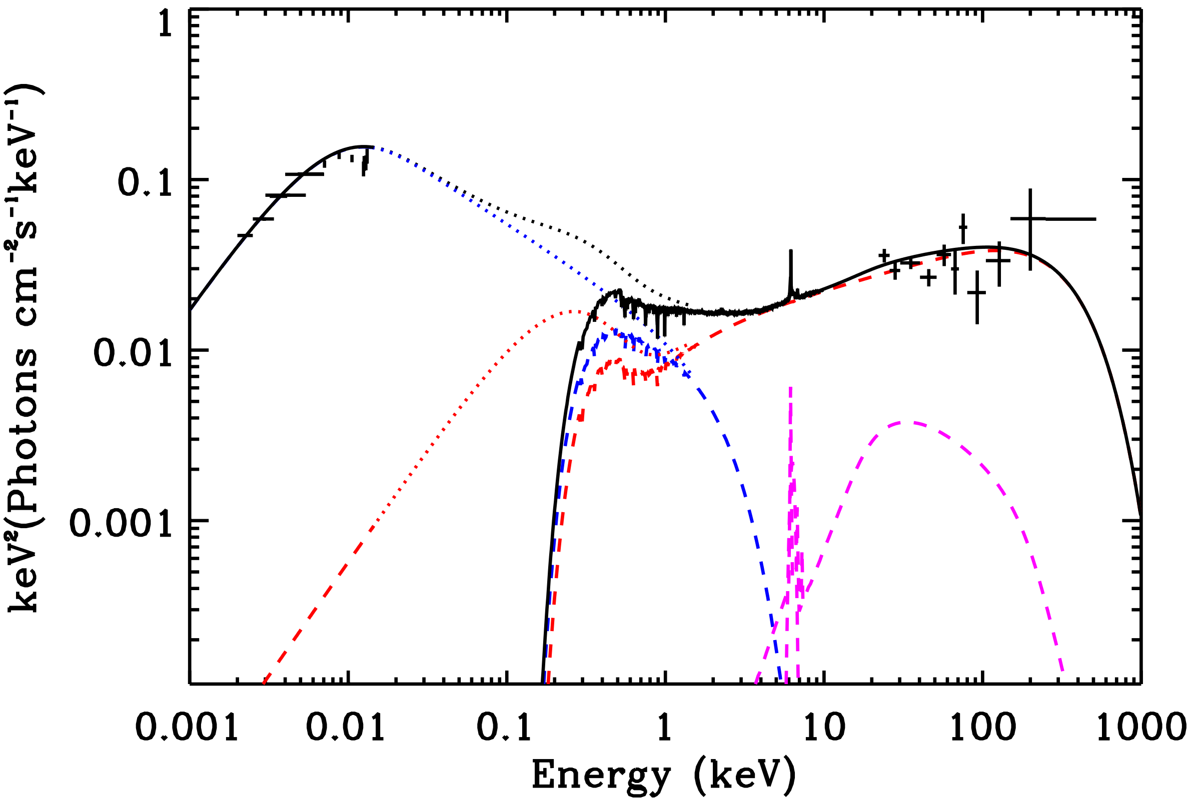

Figure 2.11 – Best-fit model of the UV/X-ray spectrum of Mrk 509 (Petrucci et al. 2013). The data (from *HST, FUSE, XMM-Newton, INTEGRAL*) are the black crosses. The solid black line is the best-fit model including absorption. The dashed lines are the different spectral components: the hot corona emission (in red), the warm corona emission (in blue), the reflection component (in magenta). The dotted lines are the corresponding components, but absorption-free.

2.2.4 Absorption

The X-ray emission of AGNs is often modified by absorption, both ionized and neutral, by complex structures surrounding the central engine.

The warm absorber: High-ionization absorbers (the so-called warm absorbers) produce significant absorption lines on $\sim 50\%$ of type 1 AGN spectra (e.g. Crenshaw et al. 2003b), both in the UV and in the soft X-ray band. These features are usually blueshifted with respect to the systemic velocity of the sources, indicating that the warm absorbers are outflowing with typical velocities of 10^2-10^3 km s^{-1}. The absorbing medium can be modelled by an outflowing shell in photoionization equilibrium (e.g. Kaastra et al. 2000). Such ionized outflows are commonly found to be multiphase, i.e. they often span a broad range in velocity and in ionization in a given source (for a review, see Costantini 2010). In local Seyferts, the absorption lines are usually narrow (full width at half maximum $\sim 10^2$ km s^{-1}, e.g. Kaastra et al. 2000). In about 15% of optically selected quasars, broad absorption lines (width of $\sim 10^4$ km s^{-1}) are also observed (Hamann & Sabra 2004; Knigge et al. 2008). The appearance of such outflows could be determined by orientation effects (Elvis 2000).

The variability time-scale of absorption lines can, in principle, be used to measure the distance of the warm absorber from the ionizing source (e.g. Crenshaw et al. 2003b). Searching for such a variability on short time-scales is one of the main motivations for conducting multiwavelength (UV/X-rays) monitoring campaigns of AGNs (Mrk 509, see Kaastra et al. 2011; NGC 5548, see Kaastra et al. 2014 and Chapter 4). Constraining the location of the warm absorbers is crucial to estimate their mass outflow rate and kinetic luminosity, and to evaluate their potential impact on the host galaxy (e.g. Crenshaw & Kraemer 2012).

Besides the UV and soft X-ray absorption features, highly blueshifted iron K-shell absorption lines around 7 keV have been detected in the X-ray spectra of several AGNs, indicating absorption from mildly relativistic outflows with velocities up to $\sim 0.4c$ (e.g. Tombesi et al. 2010, and references therein). These are the so-called ultra-fast outflows (UFOs). Warm absorbers and UFOs could be parts of the same, large-scale outflow, where the UFOs are likely launched from the inner accretion disc and the warm absorbers at larger distances, such as the outer disc or the torus (Tombesi et al. 2013).

Cold absorption: Neutral absorption can substantially modify the X-ray spectrum, especially suppressing the observed soft X-ray flux. As we have seen in Chapter 1, type 2 spectra are strongly affected by photoelectric absorption by dust and gas, which can be explained by the presence of an obscuring torus at parsec scales. However, there are observational evidences that such a torus cannot be a simple, homogeneous structure (e.g. Matt 2002). First, time variability of X-ray absorption, i.e. variability of the absorbing column density, is ubiquitous among nearby Seyfert 2 galaxies, on time-scales ranging from a few months to a few years (Risaliti et al. 2002). Variability on shorter time-scales (days or hours) has been found in a number of sources (e.g. NGC 4388, Elvis et al. 2004; NGC 4151, Puccetti et al. 2007; NGC 1365, Risaliti et al. 2009; NGC 7582, Bianchi et al. 2009b). The X-ray appearance of some sources can even switch from Compton-thick to Compton-thin (e.g. Matt et al. 2003), or vary from an absorbed type 2 spectrum to an unobscured state (NGC 1365, Walton et al. 2014). These findings suggest that the torus has a complex and clumpy structure, such as a set of outflowing clouds launched from the accretion disc (e.g. Elitzur & Shlosman 2006; Nenkova et al. 2008). Moreover, evidence for fast variability due to cold absorption has been found also in type 1 AGNs, namely sources that are generally unobscured (e.g. Mrk 766, Risaliti et al. 2011; ESO 323-G77, Miniutti et al. 2014). Such discrete absorption events, or “eclipses”, are due to clouds of neutral or mildly ionized gas crossing the line of sight, possibly located in the BLR (see also Markowitz et al. 2014; Torricelli-Ciamponi et al. 2014). In extreme cases, unabsorbed type 1 sources can switch to an obscured state (H0557-385, Coffey et al. 2014; NGC 5548, Kaastra et al. 2014). In particular, I will discuss in Chapter 4 the unexpected behaviour observed during a long campaign on NGC 5548, which is part of this thesis work.

2.3 Variability

AGNs are commonly observed to be variable at all wavelengths. The variations appear to be aperiodic and of variable amplitude. Such random variability is often referred to as “noise”, in the sense that it is the result of a stochastic process. In particular, strong and fast variability is usually observed in the X-rays, both in flux and spectral shape. Such a variability is a hallmark of AGNs, and of historical importance to rule out alternatives to supermassive black holes as their central engine (e.g. Elliot & Shapiro 1974). Indeed, the most rapid variability can be of the order of minutes, implying a very compact source (for a review, see Mushotzky et al. 1993). If the variability time-scale is t, the size of the source must be roughly

$$r \lesssim ct \simeq \frac{t}{50\,\mathrm{s}} \left(\frac{M}{10^7 M_\odot}\right) R_G. \tag{2.54}$$

Variability is in commonly described in terms of the power spectral density (PSD), which is the product of the Fourier transform of the light curve and its complex conjugate. This represents the amount of variability power P as a function of Fourier frequency f (i.e. the inverse of the time-scale). The PSD of AGNs is usually well parametrized by a power law: $P(f) \propto f^{-\alpha}$, with $\alpha = 1-2$ over time-scales of hours to months (e.g. Vaughan et al. 2003, and references therein). This kind of spectrum, where $\alpha > 1$, is usually called "red noise", as opposed to white noise (which has a flat PSD, being uncorrelated in time). The availability of very long (up to several years) light curves from observatories such as *RXTE* have led to the discovery of frequency breaks in the PSD. Indeed, a typical PSD of an AGN is characterised by a slope $\alpha \simeq 2$ at high frequencies (i.e. short time-scales), flattening to a slope $\alpha \simeq 1$ at low frequencies (i.e. long time-scales). The break frequency generally corresponds to a few days time-scale, but it can be up to a few months (e.g. Edelson & Nandra 1999; Markowitz et al. 2003b; McHardy et al. 2004; Sobolewska & Papadakis 2009). Such breaks in the PSD are also observed in stellar-mass Galactic X-ray binaries, but with much smaller time-scales, of fractions of seconds. Indeed, the PSD break time-scale is found to increase proportionally with the black hole mass, and to decrease with increasing accretion rate (McHardy et al. 2006). This is considered a strong support for the scale invariance of accreting black hole systems, leading to the suggestion that AGNs are a scaled-up version of Galactic black holes (McHardy et al. 2006). The physical origin of the PSD break time-scale is not fully understood, however it might be associated with the inverse Compton cooling time (Ishibashi & Courvoisier 2012). Indeed, the Compton cooling time t_{IC} is inversely proportional to the radiation density U_{ph} (eq. 2.42), which, at distance R from the input source, is

$$U_{ph} = \frac{L_s}{4\pi R^2 c} \tag{2.55}$$

where L_s is the soft luminosity. From eq. 1.3, we can assume that $L_s = \eta \dot{M} c^2$. Then, expressing the distance R in units of the gravitational radius, we explicit the dependence on the mass, finding the simple result:

$$t_{\mathrm{IC}} \propto \frac{M^2}{\dot{M}} \tag{2.56}$$

which matches the empirical relationship between variability time-scale, black hole mass, and accretion rate (McHardy et al. 2006).

Another estimator for the variability, especially useful for short data sets, is the so-called normalized excess variance (e.g. Nandra et al. 1997; Vaughan et al. 2003). This is essentially the variance of the light curve after subtracting the contribution from measurement errors. The square root of this quantity is called the fractional root mean square variability amplitude (or just fractional variability, F_{var}). The only difference is that F_{var} is a linear statistic, so it can be expressed in percentage terms. The excess variance is found to correlate with the black hole mass and with the accretion rate (e.g. using *XMM-Newton* light curves, see Ponti et al. 2012). Therefore, AGNs seem to have universal variability properties, once rescaled for the black hole mass and accretion rate.

Besides the flux variability, also spectral variability is commonly observed in AGNs. The photon index is found to correlate with the characteristic frequency in the PSD, when normalised to the black hole mass (Papadakis et al. 2009). This implies a link between the spectral and timing properties of AGNs, which could be driven by the accretion rate. Moreover, the spectrum is usually found to be softer, i.e. with a lower Γ, when the flux is higher (e.g. Sobolewska & Papadakis 2009; Soldi et al. 2014). This softer-when-brighter behaviour can be explained as an effect of Comptonization, since an increase in the soft input photon luminosity, due for example to an increasing accretion rate, would result in a more efficient Compton cooling of the corona. A lower coronal temperature would in turn produce a softer spectrum. However, at least part of the spectral variability could be produced by different effects, rather than being just intrinsic. Variable absorption (see Sect. 2.2.4) could produce variations of the observed flux and of the spectral shape, even if the source is not intrinsically varying. The reflection component (see Sect. 2.2.2) can also produce variations in the observed spectrum, when in combination with a variable (in flux) primary continuum (e.g. Ponti et al. 2006; Miniutti et al. 2007).

Finally, another characteristic of the spectral-timing properties of the X-ray variability is the existence of time lags between different X-ray energy bands. The spectra of AGNs often show a delay of the hard X-ray variations (above 2 keV) with respect to soft X-rays (below 1-2 keV), the so-called hard lags (e.g. Papadakis et al. 2001; Vaughan et al. 2003; McHardy et al. 2004). Such hard lags are commonly larger on longer time-scales, and at higher energies. The hard lags are also seen in X-ray binaries, and are generally interpreted in terms of propagation of mass accretion rate fluctuations in the disc (e.g. Kotov et al. 2001; Arévalo & Uttley 2006). However, also soft lags have been detected in a number of sources, meaning that the soft X-ray variations lag behind the hard X-ray variations. The first detection of a soft lag (between the 0.3–1 and 1–4 keV bands) was reported in the NLS1 1H 0707-495 (Fabian et al. 2009; Zoghbi et al. 2010), and interpreted as a signature of relativistic reflection (Sect. 2.2.2) which responds to continuum changes after the light-crossing time from the source to the reflecting region. The characteristic time-scales of the soft lags are generally short (~ 100 s), and correlated with the black hole mass (De Marco et al. 2013).

2.4 The “hot” corona

I now focus on the theoretical models that have been proposed to describe the hot, Comptonizing corona that is thought to be responsible for the X-ray emission in AGNs. Let us summarize the main observational facts that must be explained: (i) the size of the X-ray emitting region must be small ($\sim$ a few gravitational radii), as indicated by the fast variability, and also by microlensing studies (e.g. Chartas et al. 2009; Morgan et al. 2012); (ii) the observed spectrum in the hard X-rays is described by a power law, with $\Gamma = 1.5 - 2$ for Seyfert galaxies, and with a high-energy cut-off; (iii) the X-ray source should be relatively close to the inner disc, at least in sources showing relativistic reflection features and/or soft lags.

2.4.1 Thermal Comptonization in plasma clouds

A basic treatment of thermal Comptonization with applications to cosmic X-ray sources was given in a seminal paper of Sunyaev & Titarchuk (1980), where the steady-state Kompaneets equation was solved in the case of a cloud of plasma with different geometries (spherical, disc, cylinder) illuminated by a soft photon source (homogeneous or inhomogeneous). This approach was later extended, with the calculation of the angle distribution and polarization of the Comptonized radiation (Sunyaev & Titarchuk 1985), and taking into account relativistic effects (Titarchuk 1994). The solution describes a balance between photon injection, thermal Comptonization and photon escape. Treating photon diffusion in the cloud, the distribution $P(t)$ of the photons over the escape time is obtained. Then, assuming a given input spectrum $I_0(\nu, t = 0)$, the solution of the Kompaneets equation leads to the Comptonized spectrum $I(\nu, t)$. The stationary spectrum of the escaping radiation is then

$$F(\nu) = \int_0^\infty I(\nu, t) P(t) \, \mathrm{d}t. \tag{2.57}$$

$P(t)$ depends both on the geometry and on the optical depth of the plasma, and the effect of Comptonization depends on the temperature as well. Therefore, the resulting spectrum depends on the optical depth and temperature of the plasma, and a large range of power law spectral indexes can be reproduced by choosing the right parameters. However, the observation that the spectral shape of AGNs is rather uniform led to the suggestion that the spectrum is determined by some universal mechanism, such as an interplay between the accretion disc and the corona (Haardt & Maraschi 1991, see below).

2.4.2 The two-phase model

The inner region of an AGN is essentially composed of two phases, namely a hot, optically thin, X-ray emitting corona located above a cold, optically thick, UV-emitting accretion disc. Haardt & Maraschi (1991, 1993) developed a model in which these two phases are coupled: the cold phase (i.e. the disc) provides the soft photon input for Comptonization in the hot phase (i.e. the corona), and part of the hard, Comptonized emission from the corona contributes to the heating of the cold phase. To a first approximation, the geometry of the system can be assumed to be plane-parallel, where the two phases are two homogeneous and isothermal layers. Haardt et al. (1994) developed a more detailed model of a non-uniform, "patchy" corona consisting of several blobs.

The basic reasoning is as follows. Let P_G be the total gravitational power, a fraction f of which is dissipated in the corona and keeps it "hot". This heating power is re-emitted via Comptonization, so we have a Compton luminosity $L_h = f P_G$. The remaining gravitational power, i.e. a fraction $(1 - f)$ of P_G, is dissipated in the accretion disc. The total luminosity emitted by the corona can be written as AL_s, where L_s is the soft luminosity from the disc and A is some amplification factor due to Comptonization. The amplification factor can be theoretically calculated by energetic and geometric considerations. The energetics of the disc/corona system was discussed in detail by Petrucci et al. (2013), see their appendix B. I will summarize their calculations, which will be useful in the following (see Chapter 7).

First, since Comptonization conserves the number of photons, there is a relation between the seed soft photon luminosity entering and cooling a corona and the observed

Comptonized luminosity. Let $n_{\rm obs}$ be the observed photon rate of the Comptonized spectrum. By conservation, n_{obs} is equal to the sum of the seed photons crossing the corona without being scattered $n_{s,0}$ and of the photons which are scattered and emitted "upward" (i.e. towards the observer) $n_{c,up}$. If the corona has an optical depth τ, and the total seed photon rate is n_s, we can write

$$n_{s,0} = n_s e^{-\tau} \tag{2.58}$$

$$n_{c,up} = \frac{1}{2} n_s (1 - e^{-\tau}) \tag{2.59}$$

where the factor 1/2 is valid if the Comptonization process is isotropic, i.e. half of the Comptonized photons are emitted "downward" (back to the disc) and half upward. Then,

$$n_{obs} = n_{s,0} + n_{c,up} = \frac{1}{2} n_s (1 + e^{-\tau}). \tag{2.60}$$

Therefore,

$$n_s = \frac{2n_{obs}}{1 + e^{-\tau}}. \tag{2.61}$$

Then, if $\tau \ll 1$, $n_s \simeq n_{obs}$ (only a few photons are Comptonized) while if $\tau \gg 1$, $n_s \simeq 2n_{obs}$. Now, let us consider the power emitted by the corona. The corona total power L_{tot} is the sum of the seed luminosity L_s and the heating power L_h:

$$L_{tot} = L_h + L_s. \tag{2.62}$$

Now, both L_s and L_h can be decomposed as the sum of upward and downward luminosities. The upward part of L_s, namely $L_{s,u}$, is given by the sum of the seed photons which cross the corona without being scattered, and of the seed photons which are scattered upward. The downward part of L_s, namely $L_{s,d}$, is given by the seed photons which are scattered downward. Therefore,

$$L_h = L_{h,u} + L_{h,d} = 2L_{h,u} \tag{2.63}$$

$$L_s = L_{s,u} + L_{s,d} = \left[L_s e^{-\tau} + \frac{1}{2} L_s (1 - e^{-\tau}) \right] + \frac{1}{2} L_s (1 - e^{-\tau}) \tag{2.64}$$

where the first equation is simply due to the assumed isotropy of the Comptonization process. The second equation is analogous to eq. 2.58 and 2.59. The observed luminosity is given by the sum of the upward luminosities:

$$L_{obs} = L_{s,u} + L_{h,u}. \tag{2.65}$$

Now, from eq. 2.63, 2.64 and 2.65, we can derive L_h:

$$L_h = 2L_{obs} - L_s (1 + e^{-\tau}) \tag{2.66}$$

and from eq. 2.62, we have

$$L_{tot} = 2L_{obs} - L_s e^{-\tau}. \tag{2.67}$$

If $\tau \ll 1$, $L_{tot} \simeq 2L_{obs} - L_s$ while if $\tau \gg 1$, $L_{tot} \simeq 2L_{obs}$.

Finally, we can derive the amplification factor $A = L_{tot}/L_s = (L_h + L_s)/L_s$. The radiative equilibrium of the source of seed photons (i.e. the disc) implies another expression for L_s, where we introduce the intrinsic emission of the disc $L_{s,intr}$:

$$L_s = L_{s,intr} + L_{s,d} + L_{h,d} = L_{s,intr} + \frac{1}{2} L_s (1 - e^{-\tau}) + \frac{1}{2} L_h. \tag{2.68}$$

Dividing by L_s, we have

$$\begin{aligned} 1 &= \frac{L_{s,intr}}{L_s} + \frac{1}{2} - \frac{e^{-\tau}}{2} + \frac{L_h}{2L_s} \\ \Rightarrow \frac{L_h}{L_s} &= 1 + e^{-\tau} - 2\frac{L_{s,intr}}{L_s}. \end{aligned} \tag{2.69}$$

Then, for the amplification factor we have

$$A = 1 + \frac{L_h}{L_s} = 2 + e^{-\tau} - 2\frac{L_{s,intr}}{L_s}. \tag{2.70}$$

In the limiting case of a passive accretion disc, we have $L_{s,intr} = 0$: all the gravitational power is dissipated in the corona ($f = 1$). In other words, the disc itself does not intrinsically emit radiation, but rather reprocesses and re-emits (as soft emission) the hard radiation from the corona. For an optically thin corona above a passive disc, we find $A = 3$, while $A = 2$ for an optically thick corona.

More generally, let η be the fraction of the Compton luminosity emitted towards the disc (i.e. η quantifies the anisotropy of the Compton process; $\eta = 1/2$ for isotropic emission) and let a be the disc albedo, i.e. the disc absorbs a fraction $(1 - a)$ of the hard radiation. The energy balance between the disc and an optically thin corona results in the following equation for A (Haardt & Maraschi 1991):

$$A = 1 + \frac{f}{1 - f[1 - (1 - a)\eta]}. \tag{2.71}$$

In the limits $a = 0$ and $f = 1$, and assuming $\eta = 1/2$ (i.e. isotropic emission), we recover $A = 3$.

Finally, we know that the Comptonized spectrum has a power law shape:

$$I(E) = I(E_0)\left(\frac{E}{E_0}\right)^{-\alpha}. \tag{2.72}$$

Assuming that the soft emission is close to a blackbody (which peaks at $\sim 3k_\mathrm{B}T$), the soft luminosity can be approximated as $L_s \simeq I(E_0)E_0$, while the Compton (or heating) luminosity is

$$L_h = \int_{E_\mathrm{min}}^{E_\mathrm{max}} I(E)\,\mathrm{d}E. \tag{2.73}$$

The extremes of integration are $E_\mathrm{min} \simeq E_1$, namely the energy of the once-scattered photons, and $E_\mathrm{max} \simeq 3k_\mathrm{B}T$, where T is the coronal temperature. Moreover, $E_1 = A_1E_0$, where A_1 is the average gain in a single scattering. In the end, we find an equation for the heating/cooling ratio, thus another expression for A, now depending on the spectral shape (Haardt & Maraschi 1991):

$$A - 1 \simeq \frac{1}{1-\alpha}\left[\left(\frac{3k_\mathrm{B}T}{E_0}\right)^{1-\alpha} - (A_1)^{1-\alpha}\right]. \tag{2.74}$$

The spectral index α is a function of the optical depth and temperature (see Sect. 2.1.3). In particular, $\alpha = -\ln\tau/\ln A_1$ when $\tau < 1$ (eq. 2.47). Haardt & Maraschi (1991) found an iterative solution of eq. 2.74. The main result is that α is always between 1.1 and 1.4

(corresponding to Γ between 2.1 and 2.4), when $f = 1$, for a large range of optical depth and temperature values. In other words, the optical depth and temperature of the corona adjust in order to keep a constant heating/cooling ratio, i.e. a constant amplification factor, which is mostly set by geometry. Independent numerical simulations confirm this behaviour. In particular, Beloborodov (1999), applying the Comptonization code of Coppi (1992), found empirical relations between the photon index in the 2–10 keV range and both the Compton parameter y and the amplification factor A:

$$\Gamma \simeq \frac{9}{4} y^{-2/9} \tag{2.75}$$

$$\Gamma \simeq \frac{7}{3} A^{-0.1}. \tag{2.76}$$

The empirical relation 2.75 is not far from the theoretical prediction of eq. 2.52. These results show that, even with $f = 1$, which gives the hardest spectra, the expected photon index is generally larger than the observed values (i.e. 1.5–2). Moreover, the model of Haardt & Maraschi (1991) predicts nearly equal UV and X-ray luminosities, although a different angular distribution of the hard photons with respect to the soft ones can give rise to larger soft-to-hard ratios (Haardt & Maraschi 1993). In any case, the model predicts a tight correlation between the X-ray and UV fluxes.

Haardt et al. (1994) further developed the two-phase model by relaxing the assumptions on geometry. Indeed, the corona might have a patchy structure, because of the formation of magnetic loops in which the energy is stored and then dissipated through reconnection. In this case, only a fraction of the accretion power is released in the hot phase, which is composed of active blobs. The disc, instead of being passive, can contribute to most of the UV luminosity as in the standard, Shakura-Sunyaev model. Being non-uniformly illuminated, the disc reprocesses the X-ray radiation in "hot spots" where the thermalized radiation is re-emitted in the far UV/soft X-ray band. This reprocessed emission, then, can be identified with the observed soft X-ray excess. This model predicts a correlation between the hard X-ray Comptonized photons and the soft reprocessed photons, in particular when the X-ray and UV luminosities are similar (Haardt et al. 1994, 1997). The variability of the observed emission can be due to variations of the accretion rate or to stochastic variations of the number of active blobs.

Such Comptonization models have been successfully tested on Seyfert 1s (e.g. Petrucci et al. 2000, 2001), providing estimates of the temperature ($k_{\mathrm{B}}T \sim 100 - 200$ keV) and of the optical depth ($\tau \sim 0.1$) of the hot corona. I will further discuss this point in Chapter 3 and following.

2.4.3 The lamp-post model

The lamp-post geometry is a simplified configuration of the disc-corona system, where the corona is assumed to be a point-like X-ray source located on the symmetry axis of the disc (Fig. 2.12; see also Matt et al. 1991; Martocchia & Matt 1996; Henri & Petrucci 1997; Petrucci & Henri 1997). This model has been used especially to explore the properties of the reflection continuum and the iron line (e.g. Martocchia et al. 2000). For example, the lamp-post scenario can explain self-consistently the properties of the Compton reflection and of the relativistic iron line in sources such as MCG –6-30-15 (Martocchia et al. 2002).

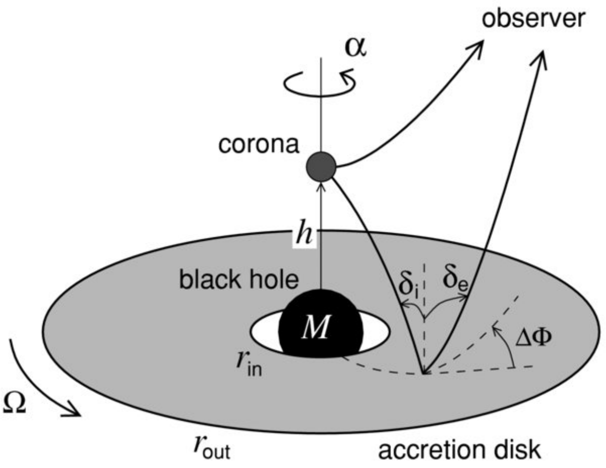

Figure 2.12 – The lamp-post geometry: the primary, point-like X-ray source is located on the axis of the black hole at height h, illuminating the accretion disc. The observer sees the primary radiation and the reflection component, both distorted by light bending. Figure from Dovčiak et al. (2011).

As we have seen in Sect. 2.2.2, very broad and redshifted Fe Kα lines indicate that the reflecting material extends down to a few gravitational radii from the black hole (e.g. Tanaka et al. 1995; Fabian et al. 2009). However, the variability behaviour of fluorescence lines can be puzzling. Generally, the Fe Kα line (either broad or narrow) and continuum emission do not appear to correlate with each other (e.g. Markowitz et al. 2003a). Even in the well studied MCG –6-30-15, no clear correlation is seen between the relativistic line and the primary continuum (Fabian et al. 2002). This could be at odds with a line originating in the innermost region of the disc, which should be close to the primary X-ray source. However, Miniutti & Fabian (2004) found that the primary and reflected fluxes can either be correlated, anticorrelated or uncorrelated, because of light bending in the proximity of the black hole. In the lamp-post model of Miniutti & Fabian (2004), the primary X-ray source has a ring-like geometry, because it is assumed to rotate around the axis, and emits isotropically in its rest frame. The source is located above the accretion disc at a radial distance of a few gravitational radii from the black hole, and at a variable height above the equatorial plane. The model includes the relativistic beaming of the primary emission as well as general relativistic effects. The height is a crucial parameter, because it determines the strength of light bending. Indeed, if the source moves along the rotation axis, the observed flux can vary even if the intrinsic luminosity is constant. Light bending can boost the continuum as seen by the innermost region near the black hole, and reduce at the same time the flux emitted towards the observer. However, the illumination of the inner part of the disc will not be greatly affected, because part of the bent X-ray radiation will be lost over the event horizon. This results in a nearly constant (or weakly varying) reflection component, while the observed primary emission drops substantially with decreasing height (Miniutti & Fabian 2004; see also Niedźwiecki & Życki 2008).

The lamp-post geometry is currently used in detailed models for the calculation of reflection spectra (e.g. Dauser et al. 2013a; García et al. 2014; Niedźwiecki et al. 2016). The observed spectrum and variability can thus be interpreted taking into account the effects of strong gravity near the black hole. In this geometry, the sources showing reflection-dominated spectra (e.g. 1H 0707-495, Zoghbi et al. 2010; IRAS 13224-3809, Chiang et al. 2015) seem to require very compact sources, located close to the black hole. In particular, the most extreme spectrum seen from 1H 0707-495 would require a source lying within 1 gravitational radius of the event horizon of a rapidly spinning black hole (Fabian et al. 2012). However, as pointed out by Dovčiak & Done (2015, 2016), the source must also be large enough to intercept sufficient seed photons to produce the hard X-ray Comptonized continuum. According to Dovčiak & Done (2015, 2016), the intrinsic X-ray luminosity of 1H 0707-495 should be very high ($L_X \sim 2L_{\mathrm{Edd}}$) in the lamp-post scenario, requiring a source size of at least 10 gravitational radii. This point will be further discussed in Chapter 8.

2.4.4 Compactness and pair production

I end up this section with a brief overview of the possible role of pair production in the corona. Electron-positron pair production from photon-photon collisions can be important in compact and luminous sources, when photons are energetic enough. The compactness parameter is usually defined as (e.g. Guilbert et al. 1983):

$$l = \frac{L}{R}\frac{\sigma_{\mathrm{T}}}{m_{\mathrm{e}}c^3} \tag{2.77}$$

where L is the luminosity and R is the radius (assuming a spherical source). This is a useful quantity to express the optical depth for pair production $\tau_{\gamma\gamma}$. We have $\tau_{\gamma\gamma} \sim n_\gamma \sigma_{\gamma\gamma} R$, where n_γ is the photon density and $\sigma_{\gamma\gamma}$ is the photon-photon pair production cross section. The photon density is $n_\gamma \sim U_{\mathrm{rad}}/E_\gamma \sim L/(4\pi R^2 c \cdot m_{\mathrm{e}}c^2)$. The cross-section $\sigma_{\gamma\gamma}$ is a function of the incident photon energies, having a maximum value of $\sim 0.2\sigma_{\mathrm{T}}$ (e.g. Ghisellini 2013). Finally,

$$\tau_{\gamma\gamma} \sim \frac{l}{20\pi}. \tag{2.78}$$

Therefore, when the compactness parameter is $l \gtrsim 60$, the optical depth exceeds unity and a significant fraction of the source luminosity is channelled into pairs.

In the case of thermal Comptonization in a hot corona, we can define a compactness l_h corresponding to the heating power L_h. For the soft photon source, we have a compactness l_s corresponding to the soft luminosity L_s. The ratio l_h/l_s is determined by the spectral characteristics (spectral index and temperature; see Sec. 2.4.2 and Ghisellini & Haardt 1994). Moreover, the values of l_h and l_s can be completely determined considering pair balance, reasoning as follows (Ghisellini & Haardt 1994). If the compactness is small, an increase in the heating power leads to an increased temperature. But when the temperature reaches $\sim 2m_{\mathrm{e}}c^2$ (i.e. ~ 1 MeV), pair production becomes significant, and it increases the number of particles. Then, the total energy is shared among more particles, thus the temperature starts decreasing as the heating (and l_h) increases. In other words, the increased luminosity increases the number of pairs rather than the temperature. At equilibrium, pair balance is reached, i.e. pair production and destruction occur at the same rate. For a given compactness, there is a maximum allowed temperature, and for a given temperature there is a maximum compactness allowing pair equilibrium. Then, there is a one-to-one relationship between the compactnesses l_s and l_h and the spectral characteristics.

Interestingly, in a pair-dominated plasma, an increase in the "cooling" (i.e. the soft luminosity), for a constant heating, produces an increase in the plasma temperature rather than a decrease. This is because more cooling implies a decrease of the temperature, thus a decrease of pair production and less particles sharing the energy. When pair balance is reached, the final temperature is actually higher (Ghisellini & Haardt 1994; Ghisellini 2013).

For low values of l_h, the contribution of pairs is negligible. However, l_h can be > 60 and up to a few hundreds in some sources (Done & Fabian 1989; Fabian et al. 2015).

Indeed, recent results on the temperature and compactness measured in AGNs suggest that these parameters roughly follow the relation imposed by pair balance (Fabian et al. 2015; see also the analysis of Mrk 509 by Petrucci et al. 2013). This in turn suggests that pair production/annihilation might play an important role in determining the physical parameters of the corona and thus the spectral properties of AGNs.

Chapter 3

Motivation and overview of this thesis

Contents

I will now introduce this thesis work, which is discussed in detail in Part II. First, I will review a number of open issues related to the physics of AGNs, and in particular to their high-energy emission. Then, I will outline the goals of this thesis and present the main body of the dissertation, including both published and ongoing works.

3.1 Some open questions on the physics of AGNs

As we have seen in the previous chapters, according to the present understanding, AGNs are powered by an accretion disc around a supermassive black hole, which emits mostly in the optical/UV band (Sect. 1.2). The X-ray emission, at least in radio-quiet Seyferts, is likely due to thermal Comptonization of disc photons by a hot corona located close to the disc (Sect. 2.4). This explains the observed power-law shape of the hard X-ray spectrum, as well as the presence of a high-energy cut-off, which is seen in a number of sources (Sect. 2.2.1). The reprocessing of the primary X-ray emission by the disc or more distant material gives rise to features like a Fe Kα emission line and a Compton bump peaking at ~ 30 keV (Sect. 2.2.2). The X-ray spectrum of many AGNs shows also a soft excess, i.e. a smooth rise below 1 keV above the extrapolated high-energy power law, whose origin is still uncertain (Sect. 2.2.3). Beyond this picture, several fundamental questions are still open, as I summarize below.

3.1.1 The geometrical and physical parameters of the hot corona

The observations indicate that the hot, X-ray-emitting corona is compact and most likely located in the inner part of the accretion flow (e.g. Reis & Miller 2013, see also Sect. 2.4). However, we still lack good constraints on the coronal temperature and optical depth for most sources. The geometry of the disc/corona system is also unknown, the size and location of the corona being a matter of debate: is the corona a slab, or a spherical cloud, or a more complex region? Is it continuous, or is it a patchy medium made out of several blobs? Is it very small, as assumed in the lamp-post geometry, or extended?

3.1.2 The nature of the soft excess

This component is commonly interpreted as either an effect of relativistically blurred reflection, or Comptonized emission by a warm, optically thick plasma (Sect. 2.2.3). In the latter case, such a warm corona would be responsible for both the optical/UV and the soft X-ray emission. This might have important consequences on our understanding of the central engine of AGNs. For example, Magdziarz et al. (1998) assumed the presence of a warm corona to explain the UV/soft X-ray spectrum of NGC 5548, suggesting that this medium is a transition region between the cold outer disk and a hot inner flow. Petrucci et al. (2013), instead, suggested that the warm corona is the upper layer of the accretion disc in Mrk 509.

3.1.3 The origin of the reflection component

A number of sources show features of relativistically blurred reflection from the very inner part of the accretion disc, within a few gravitational radii from the black hole (Sect. 2.2.2). However, these features are not ubiquitous and, in many cases, the reflection component seems to originate from distant material, such as the outer part of the disc, or the torus at pc scales. In other sources, the reflection component is weak or even absent. This might indicate that, in some sources, the standard accretion disc is truncated at some radius, with the inner region perhaps replaced by a different kind of accretion flow, such as a Compton-thin RIAF (Sect. 1.2.3). Constraining the reflection component potentially gives us important informations, but it requires separating its contribution from the primary X-ray continuum, which is not always straightforward.

3.2 Goals and strategy

To answer to the questions raised above, we need to study the broad-band (UV to hard X-rays) spectrum and variability of AGNs in detail and on adequate time-scales, in order to model consistently and simultaneously all the spectral components (e.g. Nandra et al. 1998). The approach based on multiple, broad-band observations was proven particularly successful by a multiwavelength campaign on the Seyfert 1 Mrk 509 (Kaastra et al. 2011; Mehdipour et al. 2011; Petrucci et al. 2013). This 1-month monitoring consisted of ten observations with *XMM-Newton* and *INTEGRAL*, giving the opportunity to analyse the optical/UV to hard X-ray emission of the source. Petrucci et al. (2013) found the hard X-ray continuum to be well described by a Comptonized spectrum produced by a hot ($kT_e \sim 100$ keV), optically thin ($\tau \sim 0.5$) corona, likely located in the very inner part

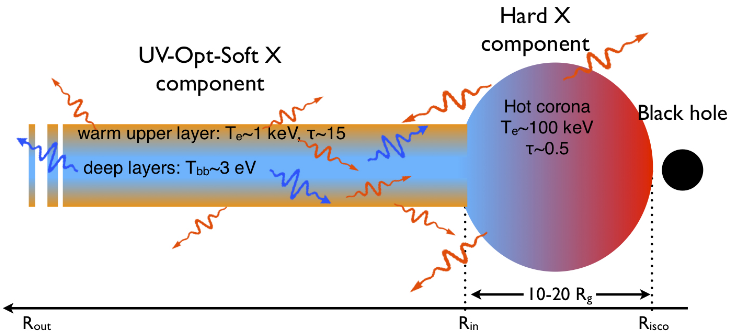

Figure 3.1 – Geometry of the accretion flow in Mrk 509 (from Petrucci et al. 2013). The hot, optically thin corona produces the hard X-ray emission, and is located in the inner part of the accretion flow. The warm, optically thick corona produces the optical/UV up to soft X-ray emission, and it extends over a large part of the accretion disc.

of the accretion flow. Mehdipour et al. (2011), studying the optical to X-ray variability, found a correlation between the optical/UV and soft (< 0.5 keV) X-ray flux, but no correlation between the optical/UV and hard (> 3 keV) X-ray flux. This result suggested the presence of a second, warm corona, responsible for the soft excess as well as the optical/UV emission. Indeed, Petrucci et al. (2013) found the UV/soft X-ray spectrum to be well fitted by a warm Comptonization component, produced by a corona with a temperature of ~ 1 keV and an optical depth of ~ 15 (see also Fig. 2.11). Moreover, Petrucci et al. (2013) estimated the amplification ratio A for this warm plasma to be close to the theoretical prediction for a slab corona lying above a passive disc (i.e. $A \simeq 2$, Sect. 2.4.2). The temperature of the soft seed photons was found to be different for the warm and hot coronae, indicating a different radial location. The tentative sketch of this two-corona model is shown in Fig. 3.1.

This thesis work is aimed at scrutinizing the high-energy emission of AGNs, through a detailed spectral analysis of high-quality UV/X-ray data. The approach of this work is twofold, being based both on new observations from *NuSTAR*, *XMM-Newton* and other X-ray satellites, and on archival data bases. While the detailed study of single sources allows us to build and constrain self-consistent physical models (as for Mrk 509), the analysis of large samples gives us insights into the average properties of AGNs. In the first chapters of Part II (Chapters 4, 5 and 6) I will present the data analysis of three sources, namely NGC 5548, NGC 7213 and NGC 4593. In the last chapters (Chapters 7 and 8) I will discuss two ongoing projects based on the data analysis and numerical simulations of a large sample of sources.

3.2.1 NGC 5548, NGC 7213, NGC 4593

The three sources analysed in this thesis are all nearby, X-ray-bright Seyfert 1 galaxies. However, each of them shows interesting peculiarities.

NGC 5548 (Chapter 4) has been the object of a long, multiwavelength campaign in 2013. Surprisingly, the spectrum of this archetypal Seyfert 1 appeared strongly absorbed in both the UV and X-rays. This obscuring event was attributed to an accretion disc wind (Kaastra et al. 2014). My main contribution to this campaign has been the analysis of the high-energy data from *XMM-Newton*, *NuSTAR* and *INTEGRAL*, which enabled a detailed study of the high-energy spectrum (Ursini et al. 2015a).

NGC 7213 (Chapter 5) is a low-luminosity and weakly accreting AGN. I analysed the first ever *NuSTAR* observation of this source, carried out in 2014 (Ursini et al. 2015b). This peculiar AGN does not show evidence for a Compton-reflected continuum nor for a high-energy cut-off, suggesting the presence of a very hot corona and a truncated accretion disc, perhaps replaced by a RIAF.

NGC 4593 (Chapter 6) was selected to perform a joint *XMM-Newton*/*NuSTAR* monitoring on a time-scale of a few days, made in early 2015 (PI: P.-O. Petrucci), to characterize its spectral and variability behaviour. The source showed a remarkable variability in flux and spectral shape, indicating significant variations in the geometry and/or physics of the accretion flow on relatively short time-scales (Ursini et al. 2016a,b).

3.2.2 The CHEESES sample

The project CHEESES (which stands for Constraining the High-Energy Emission Sources in the Environment of Supermassive black holes, just like the title of this thesis) is based on the spectral analysis of a large sample of AGNs with archival *XMM-Newton* data (Chapter 7). Although this is a work in progress, I will present and discuss some interesting results, in particular concerning the possibility that the UV/soft X-ray emission is generally due to a warm corona covering a nearly passive disc.

Finally, I will present numerical simulations with a fully relativistic code (Dovčiak & Done 2015, 2016), with the goal of constraining the size and location of the hot corona in the lamp-post geometry (Chapter 8). This ongoing work is also based on the CHEESES sample. The preliminary results point to a compact hot corona which can be quite close to the event horizon of the central black hole.

Part II

Constraining the high-energy emission sources in AGNs

Chapter 4

Anatomy of the AGN in NGC 5548

Contents

During 2013, the Seyfert 1 NGC 5548 has been the object of a long, multiwavelength observational campaign (PI: J. Kaastra, at SRON). The main goal of this program has been the study of the ionized outflow (the warm absorber: see Sect. 2.2.4).

AGNs show significant amounts of ionized gas outflowing from the central black hole, producing X-ray and UV absorption. The balance between accretion and ejection could affect the co-evolution of the supermassive black holes and their host galaxies (see the review by King & Pounds 2015, and references therein). In order to study the kinematics, distance and physical conditions of such outflows in detail, high-resolution UV data and high-quality X-ray spectra are both needed. In general, photoionized gas is characterized by the ionization parameter $\xi = L/(nr^2)$ where L is the ionizing luminosity, n is the density and r is the distance to the ionizing source. The distance is clearly an important parameter, because it may carry information on the launching mechanism (e.g. MHD winds from the accretion disc, or thermal winds from more distant matter such as the torus). L and ξ are directly measured, while the density can be inferred from the UV absorption troughs (e.g. Arav et al. 2008) or, for the bulk of the X-ray absorber, from the variability of ξ as a function of L (the delay of the variations being determined by the ionization/recombination time-scale, which is inversely proportional to n; e.g. Kaastra et al. 2012).

In the following, I will present an overview of the campaign on NGC 5548 and of the most important result, namely the unexpected observation of a fast outflow, different from the warm absorber and never seen before in this source. In Sect. 4.2 I will discuss the specific contribution of this thesis to the campaign.

4.1 The 2013 multiwavelength campaign

4.1.1 NGC 5548: an archetypal Seyfert 1

NGC 5548 is a bright and nearby active galaxy, hosting a supermassive black hole of 3.2×10^7 solar masses (Pancoast et al. 2014) and lying at a redshift of $z = 0.017$ (de Vaucouleurs et al. 1991). It was one of the catalogued objects in the seminal work of Seyfert (1943). Being one of the X-ray brightest (2–10 keV flux of $2 - 5 \times 10^{-11}$ ergs s^{-1} cm^{-2}) and most luminous (2–10 keV luminosity of $1 - 3 \times 10^{44}$ ergs s^{-1}) Seyfert 1s, it is one of the best studied AGNs. Moreover, NGC 5548 was the first object in which narrow X-ray absorption lines from warm absorbers were discovered, from *Chandra* high-resolution spectra (Kaastra et al. 2000). In past years, the source was observed by several X-ray observatories, such as *ROSAT* and *CGRO* (Magdziarz et al. 1998), *BeppoSAX* (Petrucci et al. 2000), *XMM-Newton* (Pounds et al. 2003) and *Suzaku* (Liu et al. 2010). The broad-band spectrum was always found to be consistent with that of a typical, unobscured Seyfert 1.

NGC 5548 was selected to conduct a deep monitoring to investigate the structure of the outflow, constrain its distance and study the nature of the continuum emission.

4.1.2 Timeline and overview of the campaign

The campaign on NGC 5548 was conducted from May 2013 to February 2014, involving eight observatories (Mehdipour et al. 2015, see Fig. 4.1). The core of the campaign consisted of a series of 12 observations with *XMM-Newton*, from June to August 2013, with two later observations in December 2013 and February 2014. Six *XMM-Newton* exposures were taken simultaneously with *HST*, five with *INTEGRAL* (the last one in February was not strictly simultaneous, but close in time), and three with *NuSTAR*. During the campaign and beyond, there was also a continuous monitoring with *Swift*. Three *Chandra* observations were taken in September 2013, one of them being simultaneous with *NuSTAR*. These autumn observations were triggered upon an increase in the X-ray flux from the *Swift* monitoring (Mehdipour et al. 2015).

At the time of writing, nine articles based on the campaign have been published:

Paper 0: Kaastra et al. (2014), reporting the main results (summarized in Sec. 4.1.3).

Paper I: Mehdipour et al. (2015), focused on the broad-band spectrum and containing the full description of the campaign.

Paper II: Arav et al. (2015), giving a full physical description of the outflows.

Paper III: Ursini et al. (2015a), focused on the high-energy view (see Sec. 4.2).

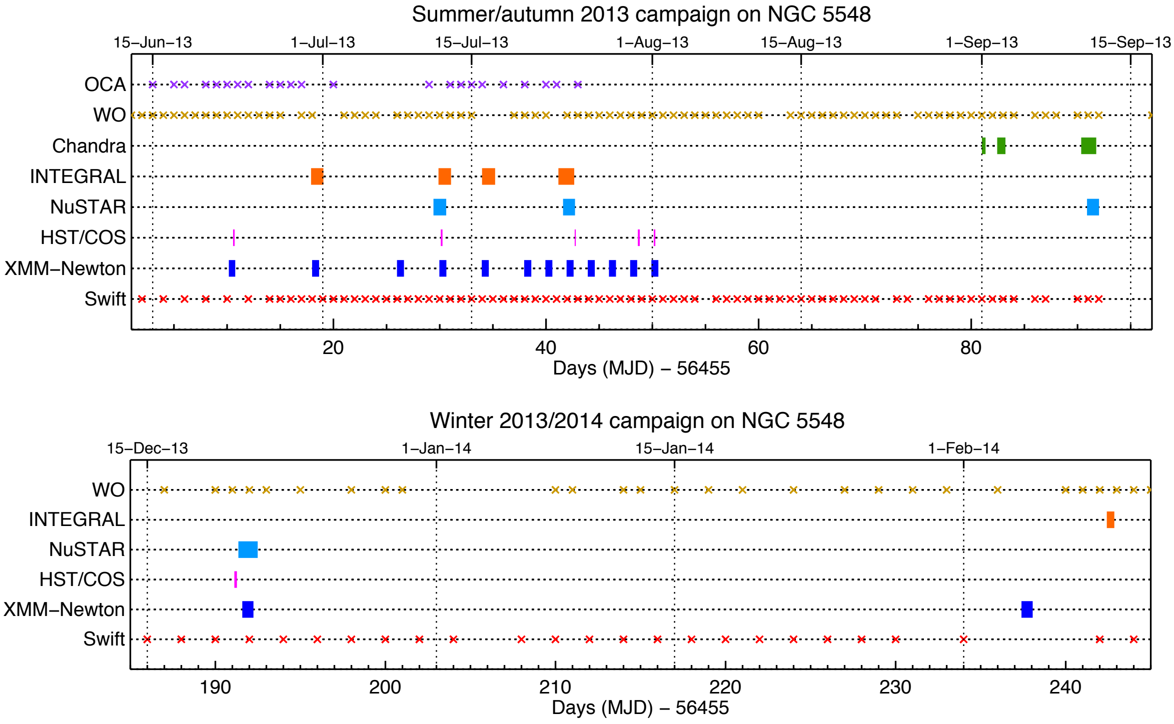

Figure 4.1 – Timeline of the campaign on NGC 5548 (Mehdipour et al. 2015).

Paper IV: Di Gesu et al. (2015), discussing the short-term variability of the outflows.

Paper V: Whewell et al. (2015), reporting on the narrow X-ray emission lines.

Paper VI: Ebrero et al. (2016), discussing the long-term variability of the warm absorber.

Paper VII: Mehdipour et al. (2016), reporting on the long *Swift* monitoring.

Paper VIII: Cappi et al. (2016), discussing in detail the *XMM-Newton* observations.

4.1.3 A fast and long-lived obscuring outflow

We will briefly summarize the main results from the campaign, as presented in Paper 0. The most important result was actually an unexpected event. Indeed, the appearance of the source was very different from past observations, due to a strong obscuration in the X-rays, simultaneously with a broad absorption line structure in the UV.

The average X-ray spectrum obtained during summer 2013 is shown in Fig. 4.2, together with a historical spectrum taken in 2002. The striking difference between the two spectra below 10 keV is due to heavy absorption, causing a strong decrease of the soft X-ray flux without greatly affecting the hard band. Moreover, broad and blue-shifted absorption troughs were visible in the UV spectra, on top of the "classical" and well-known warm absorber (Kaastra et al. 2000; Crenshaw et al. 2003a, 2009). Such troughs have blueshifts of about -1000 km s^{-1} and as high as -5000 km s^{-1}. In the following, I will always refer to the new absorbing medium as the "obscurer", to distinguish it from the known warm absorber.

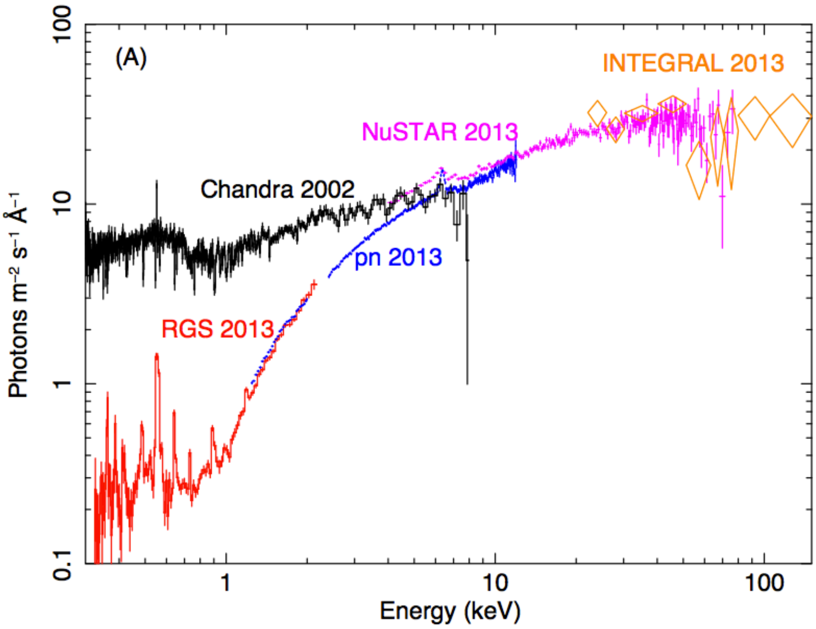

Figure 4.2 – The average X-ray spectrum of NGC 5548 during summer 2013 (*XMM-Newton*/RGS and pn, *NuSTAR* and *INTEGRAL*), to compare with the unobscured *Chandra*/LETGS spectrum taken in 2002 (figure from Kaastra et al. 2014).

In Paper 0, the parameters of the obscurer and of the warm absorber were derived using an iterative method. The initial spectral energy distribution is assumed to be the unobscured continuum observed in 2002, modified by the corresponding warm absorber observed at that epoch. The difference with respect to the observed average spectrum of 2013 is attributed to obscuration and fitted. Then, the obscured spectrum is used as the ionizing continuum in the photoionization modelling of the warm absorber. This process is iterated until convergence. The final outputs of this procedure are the obscurer parameters, the obscured spectrum illuminating the warm absorber, and the ionization parameters of the warm absorber.

The obscurer is actually composed of at least two partially covering obscuring components, which are found to explain both the X-ray and UV absorbed spectra. The first obscuring component covers $\sim 90\%$ of the X-ray source and has a column density of $\sim 1 \times 10^{22}$ cm^{-2} and ionization $\log \xi \simeq -1.2$, in units of ergs s^{-1} cm. This component reproduces all the broad absorption troughs seen in the UV. Moreover, it partially covers the UV broad emission lines from the BLR, with a covering fraction of $20 - 40\%$. The second obscuring component covers $\sim 30\%$ of the X-ray source with a column density of $\sim 1 \times 10^{23}$ cm^{-2}, and is almost neutral. Moreover, the strengths of the broad UV absorption troughs appear to correlate with the strength of the X-ray obscuration. These results indicate that UV and X-ray absorption arise in the same photoionized gas (for the details, see Paper 0).

The newly observed obscurer strongly affects the classical warm absorber, by reducing the level of ionization (Paper 0; Paper II; Paper VI). Indeed, the UV spectra show narrow absorption lines at the velocities of the classical warm absorber but originating from less-ionized gas. This means that the obscurer is located somewhere between the primary source and the warm absorber, namely within a few pc (e.g. Crenshaw et al. 2009). Furthermore, the obscurer covers the BLR, which lies a few light days away from the core (Pancoast et al. 2014). However, it does not cover the NLR, because the narrow emission lines are mostly unaffected by obscuration (Paper 0; Paper V). Since the X-ray source and the BLR are partially covered, the obscurer should be just outside of the BLR, as also

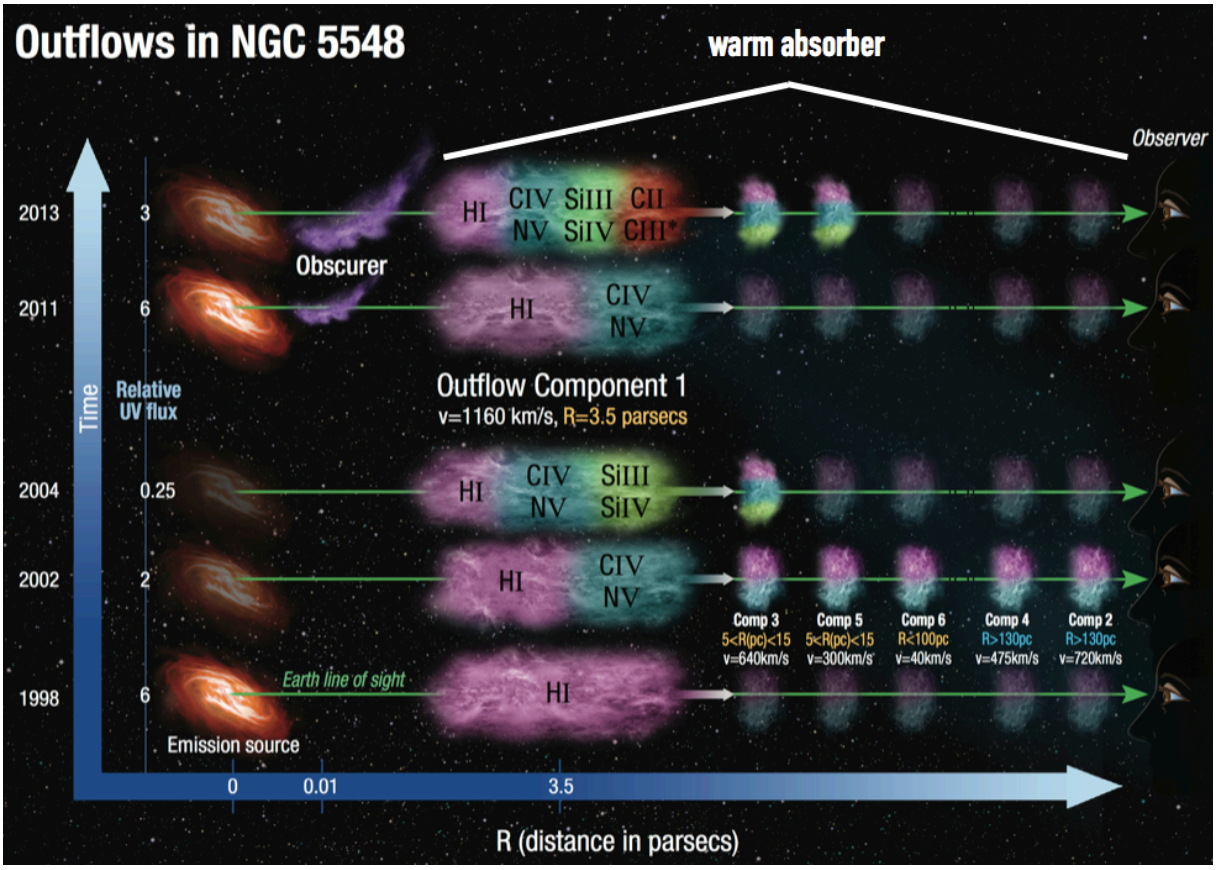

Figure 4.3 – Sketch of the physical, spatial and temporal properties of the outflows seen in NGC 5548 (adapted from Arav et al. 2015). Along the time axis, the UV behaviour of the primary source at 5 different epochs is shown (UV fluxes are measured at 1350 Å rest-frame and are in units of 10^{-14} ergs s^{-1} cm^{-2} $Å^{-1}$). The warm absorber has 6 distinct ionization phases (see also Kaastra et al. 2014; Ebrero et al. 2016). Different observed ionic species are represented as differently coloured zones within the absorbers. Dimmer clouds represent epochs in which components 2–6 did not show new absorption species with respect to 2002.

indicated by the high velocity (a few thousands km s^{-1}) of the gas and by the observed variability on time-scales of a few days (Paper 0; Paper IV; Paper VIII).

As shown in Paper VII, the source was unobscured until at least August 2007, from *Swift* data. No monitoring was later performed, until February 2012, when the source was obscured (again from *Swift* data, even if this was not realized before the campaign). After this date, the obscurer has been continuously present in our line of sight. Therefore, the transition to the obscured state occurred between August 2007 and February 2012, though it is not possible to determine the precise moment. In any case, the obscurer has been present for at least 4 years.

The geometrical, physical and variability properties of the obscuring outflow (fully discussed in Paper 0, Paper IV and Paper VIII) are consistent with a wind launched from the accretion disc (e.g. Proga 2000, 2003). Concerning the impact on the surrounding medium, the outflow itself cannot influence significantly the host galaxy. The kinetic luminosity is only a tiny fraction ($\sim 10^{-7}$) of the bolometric luminosity, and even the total kinetic luminosity of the ionized outflows is around 0.2% of the bolometric luminosity (Paper VI). This is below the minimum amount ($0.5 - 5\%$) required by current feedback models to regulate galaxy evolution (Paper VI). However, such obscuring winds might play a role in the launching of more powerful outflows, that could have an effective impact on the host galaxy (e.g. Arav 2010). Indeed, theoretical models of radiation driven winds require the presence of a "hitchhiking" gas that shields the accelerated gas from much of the UV/X-ray ionizing radiation, allowing line driving to be more effective (Murray et al. 1995; Proga 2000; Proga & Kallman 2004).

In conclusion, the main results can be summarized as follows: (i) strong, unexpected absorption was detected simultaneously in the X- rays and UV, in an otherwise archetypal Seyfert 1; (ii) the heavy, long-lasting and complex X-ray/UV obscuration indicates the presence of a long, inhomogeneous stream of matter, which may be identified with the onset of an accretion disc wind. The results on the outflows seen in NGC 5548 are summarized in Fig. 4.3.

The availability of high-quality data from this campaign made it possible to study the high-energy spectrum of NGC 5548 in detail, as I discuss in the following.

4.2 The high-energy view

In this section, I will present the spectral analysis of the high-energy data, that I led during this campaign. Results from this analysis were published in Ursini et al. (2015a), i.e Paper III, which is found in the appendix of the present chapter.

4.2.1 The data set

I report in Table 4.1 the log of the data sets, with their start date and net exposure time (see also Ursini et al. 2015a, Table 1). The seven observations from the 2013 campaign analysed in Ursini et al. (2015a) are those which included high-energy data, namely from *NuSTAR* and/or *INTEGRAL*, simultaneously with *XMM-Newton* or *Chandra*.

The latest *XMM-Newton* pointing is dated 2014 February 4, and the corresponding data were analysed jointly with average data obtained from three *INTEGRAL* exposures of 2014 January and February, because the corresponding spectra showed no significant variations. In the end, the full data set included three *XMM-Newton+INTEGRAL* observations (no. 1, 3 and 7), two *XMM-Newton* or *Chandra+NuSTAR* observations (no. 5 and 6) and two *XMM-Newton+NuSTAR+INTEGRAL* observations (no. 2 and 4). The exposure time was mostly around 40-50 ks (i.e. half-day), and up to 120 ks for *Chandra*. To compare the results of the 2013 campaign with the past behaviour of the source, I also re-analysed archival data from *BeppoSAX* (Nicastro et al. 2000) and *Suzaku* (Liu et al. 2010).

The source did not show significant spectral variations within each observation (see, e.g., the *XMM-Newton* light curves in Fig. 1 of Paper VIII). The lack of spectral variability justifies the use of time-averaged spectra over each observation. On the other hand, the source is spectrally variable on time-scales of a few days, therefore each observation was analysed independently (see the light curves reported in Ursini et al. 2015a, Fig. 1).

I briefly summarize the instruments used and the data reduction (for the details, see Ursini et al. 2015a, Sec. 2):

***XMM-Newton*:** In Ursini et al. (2015a), I only used EPIC-pn data, given the lower effective area of the MOS detectors. The detailed analysis reported in Paper VIII was

Table 4.1 – Obs. 1-7: The high-energy observations of NGC 5548 with *XMM-Newton* or *Chandra* simultaneous with *NuSTAR* and/or *INTEGRAL*, from the 2013 campaign (see Table 1 of Ursini et al. 2015a). Obs. A1-A2: Archival high-energy observations of NGC 5548 analysed in Ursini et al. (2015a).

Observation	Satellites	Start time (UTC) yyyy-mm-dd	Net exposure (ks)
1	*XMM-Newton*	2013-06-30	38
	INTEGRAL	2013-06-29	62
2	*XMM-Newton*	2013-07-11	37
	NuSTAR	2013-07-11	50
	INTEGRAL	2013-07-11	50
3	*XMM-Newton*	2013-07-15	37
	INTEGRAL	2013-07-15	50
4	*XMM-Newton*	2013-07-23	38
	NuSTAR	2013-07-23	50
	INTEGRAL	2013-07-23	52
5	*Chandra*	2013-09-10	120
	NuSTAR	2013-09-10	50
6	*XMM-Newton*	2013-12-20	38
	NuSTAR	2013-12-20	50
7	*XMM-Newton*	2014-02-04	38
	INTEGRAL	2014-01-17	94
		2014-01-22	40
		2014-02-09	30
A1	*BeppoSAX*	1997-08-14	314
A2	*Suzaku*†	2007-06-18	227

Notes. (†) I used the co-added spectrum of seven *Suzaku* observations, $\sim$ 30 ks each, separated by one week (Liu et al. 2010).

also based on pn data, while the MOS data were used for consistency checks. The data were processed using the standard *XMM-Newton* Science Analysis System (SAS), and the details of data reduction are reported in Paper VIII. The spectra were grouped to have at least 20 counts per spectral bin. I analysed the spectra in the full pn energy bandwidth, namely 0.3–10 keV. However, there was a technical issue affecting pn data. The Fe Kα line measurements presented a variable blueshift of 30-40 eV and a broadening of 40-50 eV, compared with the MOS and *NuSTAR* data. These effects are likely due to the long-term degradation of the charge transfer inefficiency (CTI), as discussed in Paper VIII. Therefore, to correct for these shifts, we needed to leave the redshift free to vary in our models. Moreover, this small offset yielded poor fits near the energy of the gold M-edge of the telescope mirror (around 2.3 keV), thus we cut out the spectra between 2.0 and 2.5 keV (the same was done in Paper 0, Paper IV and Paper VIII). Anyway, this problem has no effect upon the broad-band modelling. In particular, the measurement of the Fe Kα line strength is correct.

***NuSTAR*:** The *NuSTAR* data were reduced with the standard pipeline in the *NuSTAR* Data Analysis Software (NUSTARDAS)[1]. I analysed jointly the spectra from the two *NuSTAR* X-ray telescopes, i.e. focal plane modules A and B (FPMA and FPMB), without combining them. The FPMA and FPMB spectra were grouped to have at least 50 counts per bin.

***INTEGRAL*:** The *INTEGRAL* data were reduced with the Off-line Scientific Analysis software (OSA)[2]. IBIS/ISGRI spectra have been extracted using the standard spectral extraction tool IBIS_SCIENCE_ANALYSIS and combined together to generate the total ISGRI spectra. The data cover the range between 20 and 400 keV.

***Chandra*:** *Chandra* observed the source with HRC/LETG on Sep. 10, simultaneously with *NuSTAR*. I used the first order LETG spectrum, which was extracted with the package Chandra Interactive Analysis of Observations (CIAO).

Archival observations: I used a 1997 *BeppoSAX* observation with LECS, MECS and PDS (0.2–200 keV; Nicastro et al. 2000) and a 2007 *Suzaku* weekly monitoring consisting of seven observations, with XIS and HXD (0.2–600 keV; Liu et al. 2010). I re-extracted these data with the tool XSELECT, following standard procedures (Nicastro et al. 2000; Liu et al. 2010).

The average spectrum, obtained by co-adding respectively the *XMM-Newton*/pn, *NuSTAR* and *INTEGRAL* spectra, is shown in Fig. 4.4. In the following, I summarize the main steps of the analysis (the details are reported in Sect. 3 of Ursini et al. 2015a). Spectral analysis and model fitting was carried out using the package XSPEC (Arnaud 1996).

4.2.2 The hard X-ray spectrum: a constant reflection component

Let us begin with the hard X-ray view, which was useful for building the broad-band model. As a first step, I focused on the *NuSTAR* spectra above 10 keV, which show a curvature at high energies with respect to a simple power law (see Fig. 2 of Ursini et al. 2015a). This curvature suggests the addition of a high-energy cut-off in the power law, but also the presence of a reflection bump.

To constrain the reflection component, I fitted the data above 5 keV. This low-energy threshold was chosen to limit the effects of the strong absorption in the soft X-ray band. I focused on the four observations including *NuSTAR* data (obs. 2, 4, 5 and 6), as they have the best signal-to-noise ratio in the 20–40 keV range (i.e. where the reflection bump is expected).

I adopted a simple model consisting of a cut-off power law modified by absorption, and including a reflection component. I included a fully covering, neutral absorber with

---

[1] The *NuSTAR* data reduction was performed by D. Walton (Caltech).

[2] The *INTEGRAL* data reduction was performed by R. Boissay (ISDC).

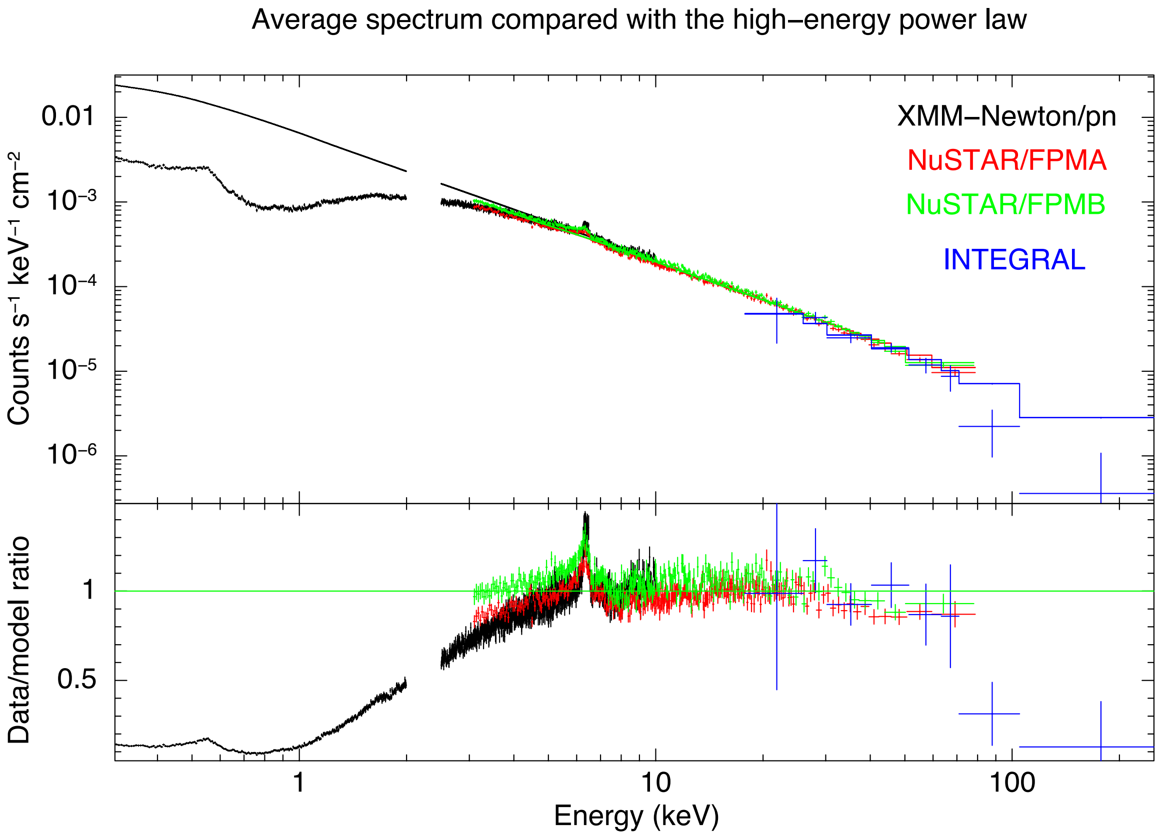

]

Figure 4.4 – The average spectrum of NGC 5548 obtained from the seven observations analysed in Ursini et al. (2015a) (see Table 4.1), plotted with the best-fitting power law above 5 keV. The data were co-added for each instrument, and rebinned for plotting purposes. The residuals show the strong absorption but also deviations from a simple power law at high energies.

variable column density. From Paper 0, we know that the obscurer has actually two components and is partially covering the source. However, fitting the data above 5 keV, it is possible to use a simpler model for the absorption, without affecting the results. Concerning the reflection component, I chose a model consistent with the observed properties of the Fe Kα line. After correcting for the effects of CTI, the Fe Kα line is found to be neutral (i.e. the energy is consistent with 6.4 keV), narrow (i.e. the intrinsic width is consistent with zero; the upper limit is 50 eV) and consistent with being constant during the campaign, as discussed in Paper VIII. These properties indicate that the line-emitting material is neutral and relatively distant from the primary source. I thus used the PEXMON model (Nandra et al. 2007) in XSPEC for the reflection component. This model combines a neutral Compton reflection, as described by the PEXRAV model (Magdziarz & Zdziarski 1995) in XSPEC, with Fe Kα, Fe Kβ, Ni Kα lines and the Fe Kα Compton shoulder, generated self-consistently by Monte-Carlo simulations (George & Fabian 1991b). In the end, the XSPEC model is simply (PHABS × CUTOFFPL + PEXMON), where PHABS is the neutral absorber. The reflection component is thus not modified by absorption. I fixed the inclination angle of PEXMON to 30 deg, appropriate for a type 1 source (e.g., Nandra et al. 1997). I left free to vary both the primary power law (photon index, cut-off energy and normalization) and the incident radiation in PEXMON, whose parameters were not tied to those of the primary power law. Indeed, the Fe Kα line suggests that the reflection component is constant and due to distant material, so that there could be no direct link between the primary power law seen by the observer at a given time and the incident radiation seen by the reflector.

The main result from these fits is that the PEXMON component is consistent with being constant (see Figs. 3 and 4 of Ursini et al. 2015a, showing the contour plots of the photon index, cut-off energy and normalization). Therefore, the distance of the reflecting material from the primary X-ray source is of at least a few light months, corresponding to the time separation between the different observations. Given the black hole mass of NGC 5548, this distance translates to a few $\times$ 10^4 gravitational radii. This is also a justification for the non-obscuration of the reflection component in our models, because the obscurer should be closer to the primary source. I used the results of this analysis to constrain the broad-band model, by fixing the parameters of the reflection component. In particular, the incident photon index in PEXMON was fixed to the average value of 1.9, which is consistent with the primary photon index during most of 2012, as reported in Paper VII based on *Swift* data.

4.2.3 Modelling the partial covering obscurer

Having obtained constraints on the reflection component, I fitted the broad-band spectra down to 0.3 keV. First of all, I needed to define a suitable model for the obscurer. As a first step, I tested the partially covering obscuring components found in Paper 0. However, the fits were never good, as I always found strong residuals below 1 keV. This is partly due to the fact that the results of Paper 0 are based on the average spectrum of the 2013 campaign, while in Ursini et al. (2015a) I focused on the single observations. I thus needed to take into account the absorption variability (which was further investigated in Paper IV and Paper VIII). However, I also found a discrepancy due to the different instruments used. Indeed, the *XMM-Newton* data analysed in Paper 0 were from both the reflection grating spectrometer (RGS) and EPIC-pn. RGS data were used in the range 0.32–2.2 keV, while EPIC-pn data were used only above 1.24 keV. However, in my analysis I focused on the broad-band X-ray spectrum and used only the pn data in the range 0.3–10 keV rather than RGS, which has a better spectral resolution but a smaller effective area. I then realized that the best-fitting model of Paper 0 gives a poor fit to the average pn spectrum, as I show in Fig. 4.5[3]. This discrepancy is likely due to cross-calibration between pn and RGS (Kirsch et al. 2004). This, together with the expected variability, prompted me to fit the pn data with a different model and leave the obscurer parameters free to vary, rather than fixing them to those of Paper 0.

As a first attempt, I tried to fit the broad-band spectra with a model including two ZXIPCF (Reeves et al. 2008) components in XSPEC. ZXIPCF is based on the XSTAR photoionization code (Kallman & Bautista 2001) and describes partial covering absorption by ionized material. Although the fits were statistically acceptable, the results were quite different from those of Paper 0. In particular, when fitting the average spectrum for a consistency check, the obscurer component 1 had $\log\xi \simeq -0.5$ instead of $\log\xi = -1.2$, and the obscurer component 2 had $\log\xi > 0.5$ instead of being almost neutral. I thus made a comparison between ZXIPCF and the obscurer of Paper 0. The spectral analysis

---

[3] Substantial help was provided by L. di Gesu (SRON).

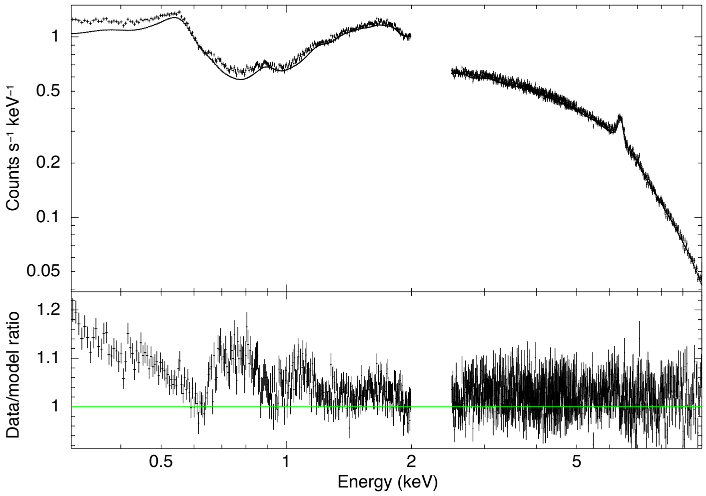

Figure 4.5 – The best-fitting model of Kaastra et al. (2014) plotted with the average 2013 *XMM-Newton*/pn spectrum. The residuals are due to the discrepancy between *XMM-Newton*/RGS (used by Kaastra et al. 2014 below 2 keV) and pn (see text).

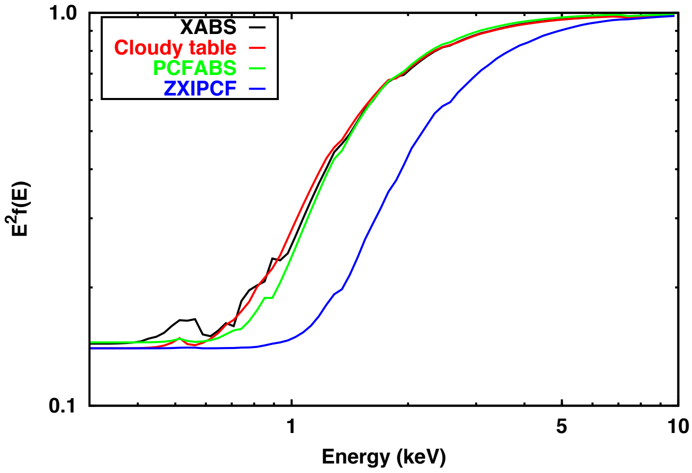

Figure 4.6 – Comparison between different ionized absorption models. The underlying continuum is a power law (Γ=2), modified by, respectively: the XABS model used in Paper 0 (black); a table model built with CLOUDY (red); the ZXIPCF model (blue); the neutral PCFABS model (green). The first three models have the same parameters: $\log \xi = -1.2$, $N_{\rm H} = 1.2 \times 10^{22}$ cm^{-2}, $C_F = 0.86$. PCFABS has $N_{\rm H} = 0.85 \times 10^{22}$ cm^{-2} and $C_F = 0.855$.

of Paper 0 was performed with the package SPEX (Kaastra et al. 1996), using the photoionized absorption model XABS for both the obscurer components. I thus needed to translate this model into a table that could be used in XSPEC[4]. I also tested two different absorption models, namely the neutral partially covering model PCFABS in XSPEC, and a table produced with the photoionization code CLOUDY (Ferland et al. 2013) using the spectral energy distribution of NGC 5548[5]. In Fig. 4.6, I show the effects of such absorption models on a power law, using the parameters of the obscurer component 1. There is a clear discrepancy between ZXIPCF and the table models (XABS and the CLOUDY table), which are instead in good agreement. The plot also shows that, albeit the PCFABS model is neutral, with slightly different values of column density and covering fraction it can reproduce the effects of the ionized table models.

I thus abandoned ZXIPCF in favour of the simpler, neutral model PCFABS. This choice is justified by the use of pn data. Both the obscurer components have a low degree of ionization, such that, at the pn energy resolution, they cannot be distinguished from neutral absorbers. I also produced fake pn spectra assuming the XABS model, finding that a model including PCFABS was able to fit them without problems. In particular, the obscurer component 1 ($N_{\rm H} = 1.2 \times 10^{22}$ cm^{-2}) is hardly distinguishable, using pn data,

---

[4] This table for XSPEC was produced by P.-O. Petrucci.

[5] This CLOUDY table model was provided by S. Bianchi.

from a PCFABS with a column density of 1.1×10^{22} cm^{-2}. To summarize, the column density and covering fraction are somewhat degenerate with the level of ionization at pn resolution, and PCFABS can reproduce the effects of XABS or the CLOUDY table with similar parameters. For my analysis, I thus decided to use the simpler and faster model PCFABS, which is sufficiently accurate for modelling the broad-band spectrum.

4.2.4 The broad-band spectral analysis

I briefly summarize the broad-band spectral analysis reported in Sec. 3.3 of Ursini et al. (2015a). The analysis was divided into two main steps: (i) analysis of each single observation with a phenomenological model; the energy range was 0.5–79 keV for obs. 5 (*Chandra*+*NuSTAR*), 0.3–79 keV for obs. 6 (*XMM-Newton*+*NuSTAR*) and from 0.3 up to 400 keV for the other observations, thanks to the *INTEGRAL* data; (ii) analysis of the average X-ray spectrum with a more physical Comptonization model, and comparison with archival data.

The phenomenological model consisted of the main following components:

- The primary continuum: modelled with a cut-off power law (CUTOFFPL in XSPEC), with variable photon index, cut-off energy and normalization.
- The obscurer: modelled with two PCFABS with variable column density and covering fraction.
- The warm absorber: for this component, I used the multiphase model of Paper 0, using a table with fixed parameters in XSPEC.
- The soft excess: NGC 5548 is known to exhibit a soft X-ray excess (e.g. Magdziarz et al. 1998). Its presence is not apparent in the 2013 spectra, due to the strong absorption. However, the analyses of soft X-ray data (both from *XMM-Newton* and *Swift*) reported in Paper I, Paper VII and Paper VIII show that a soft excess is still found. Moreover, Paper I and Paper VII report a correlation between UV and soft X-ray flux and an anti-correlation between the X-ray hardness ratio and the UV flux, supporting a warm Comptonization scenario. However, the obscuration makes it difficult to constrain realistic Comptonization models for the soft excess. I thus followed Paper I and included in my fits a thermal Comptonization component, modelled with COMPTT (Titarchuk 1994) in XSPEC. The parameters were frozen to the values reported in Paper VII.

I also included the narrow X-ray emission lines reported in Paper 0 and the constant reflection component discussed in Sec. 4.2.2. The narrow lines (NL) are covered by the warm absorber (WA) but not by the obscurer. Therefore, the model in XSPEC is:

$$\text{WA} \times [\text{NL} + \text{PEXMON} + \text{PCFABS} \times \text{PCFABS} \times (\text{COMPTT} + \text{CUTOFFPL})] \tag{4.1}$$

The most interesting result is the variability behaviour of the primary continuum. In Fig. 4.7, I show the contour plots of the high-energy cut-off versus the photon index. In most cases, we only have lower limits of about 100 keV on the cut-off energy, while for obs. 6 we have a measurement of 70^{+40}_{-10} keV (at 90% confidence level). Also the photon index undergoes significant variations, from ~ 1.7 in the first five observations (summer

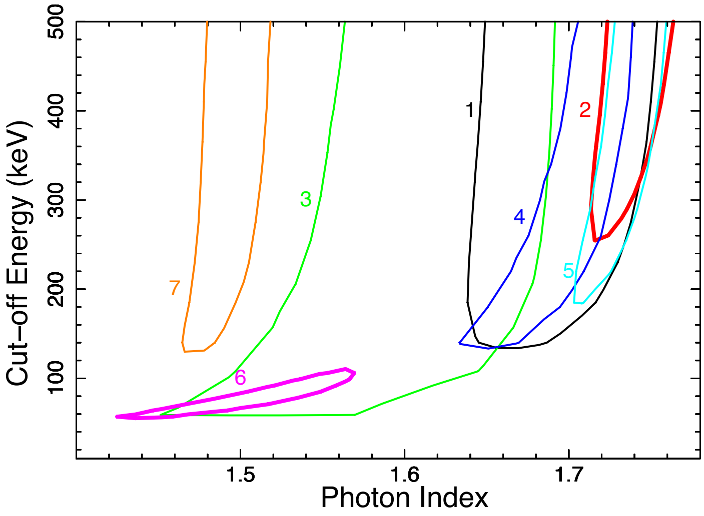

Figure 4.7 – Contour plots of the cut-off energy versus the primary photon index, at 90% confidence level, for the different observations. The thicker contours correspond to the most significant variation of both parameters (obs. 2 and 6). The figure is adapted from Fig. 6 of Ursini et al. (2015a).

2013) to ∼ 1.5 in the last two (winter 2013). Furthermore, I found good constraints on the obscuring components (see Figs. 8, 9 and 10 of Ursini et al. 2015a). The column densities and covering fractions are in rough agreement with Paper 0, however I found them to be variable for both components. I will further discuss the variability in Sec. 4.2.5.

The second step of the spectral analysis consisted in fitting the average high-energy spectrum with a a more physical Comptonization model. I thus replaced the cut-off power law in the model (4.1) with the thermal Comptonization model COMPPS (Poutanen & Svensson 1996). The code COMPPS is based on the two-phase model (Sec. 2.4.2) and takes into account the most important radiation processes (Comptonization, Bremsstrahlung, pair production/annihilation). The main parameters of COMPPS are the temperature and the Compton parameter $y = 4\tau(k_{\mathrm{B}}T/m_{\mathrm{e}}c^2)$ of the Comptonizing corona, for a given geometry and a given input soft spectrum. The optical depth can also be used in COMPPS, instead of the Compton parameter. However, using the Compton parameter minimizes the degeneracy, as the optical depth and temperature are generally correlated in the fitting procedure (e.g. Petrucci et al. 2001, 2013). I assumed a spherical geometry for the hot corona, obtaining a Compton parameter $y = 0.85^{+0.10}_{-0.05}$ and a temperature of 40^{+40}_{-10} keV. Then, the derived optical depth is $\tau = 2.7^{+0.7}_{-1.2}$. The $k_{\mathrm{B}}T - y$ contour plot is shown in Fig. 4.8. Finally, I compared the results on the average spectrum with the past observations of NGC 5548 (obs. A1, A2 of Table 4.1). I thus fitted the 1997 *Beppo*SAX spectrum and the 2007 *Suzaku* average spectrum using the COMPPS model with spherical geometry. I find that the temperature and the optical depth are significantly different from those of 2013 (see Fig. 4.8). I observe a decrease of the coronal temperature from about 300-400 keV in 1997 down to 40-50 keV in 2013, while the optical depth increased from 0.2-0.3 up to 2-3.

4.2.5 Principal components analysis

To further investigate variability patterns, I performed a principal component analysis (PCA; e.g., Kendall 1980; Francis & Wills 1999). PCA consists in the decomposition of a dataset into a set of orthogonal eigenvectors of the correlation matrix. If a small number

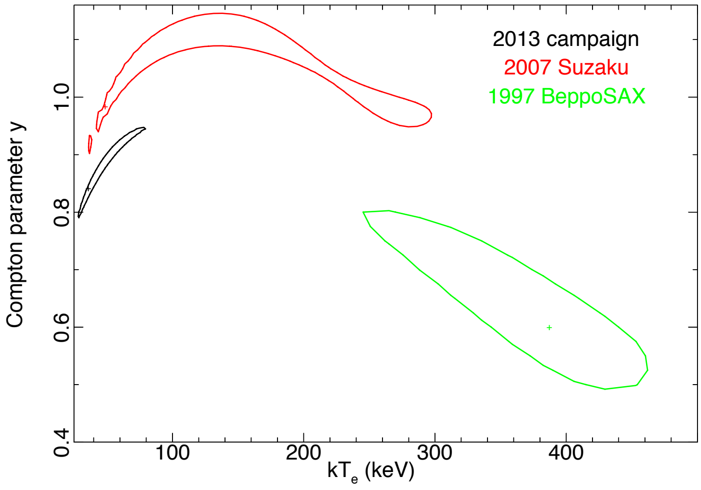

Figure 4.8 – $k_{\rm B}T-y$ 90% confidence level contour plots, for: the average spectrum of NGC 5548 from the campaign (black), the 2007 average *Suzaku* spectrum (red), and the 1997 *BeppoSAX* spectrum (green), all fitted with the COMPPS model.

of eigenvectors account for most of the variance, we will have a simpler description of the original dataset in terms of such variables, called principal components. PCA is often used in X-ray astronomy, e.g. to investigate the variability of X-ray binaries (e.g. Malzac et al. 2006) and AGNs (e.g. Blustin et al. 2006; Miller et al. 2007; Petrucci et al. 2013; Parker et al. 2015).

My procedure was as follows. Since the source is mostly variable in the soft X-ray band, due to the complex absorption, I focused on *XMM-Newton*/pn data. I thus performed a PCA on the twelve *XMM-Newton* observations of Summer 2013. The spectra were grouped in 87 energy bins, in the 0.3–10 keV range. We thus have $m = 12$ spectra taken at the times $t_1, t_2, ...t_m$ grouped into $n = 87$ energy bins $E_1, E_2, ...E_n$. The dataset can be described as an $m \times n$ matrix $\mathbf{F}$, where each element $\mathbf{F}(t_i, E_j)$ is the energy flux at the time t_i in the bin E_j. The covariance matrix $\mathbf{S}$ is the $n \times n$ symmetric matrix given by $1/(n-1)\mathbf{F}^T\mathbf{F}$. PCA consists in the diagonalization of this covariance matrix, obtaining its eigenvalues and eigenvectors $V_{k=1,...r}(E_i)$ where r is the rank of $\mathbf{S}$ (up to $m = 12$ in our case). Such eigenvectors, completed with additional $n - r$ orthogonal vectors, define an orthogonal basis that best describes the variance in the data. Indeed, the total variance in the data is equal to the trace of the covariance matrix or, equivalently, to the sum of all its eigenvalues. The eigenvector with the highest eigenvalue is the first principal component, corresponding to the largest variance. The second eigenvector with the second largest variance is the second principal component, and so forth, up to the r-th eigenvector (the other $n - r$ basis vectors have zero variance). In the end, the observed spectra $F(t_i, E_j)$ are decomposed using the basis containing the eigenvectors, with a set of coordinates $\alpha_k(t_i)$:

$$F(t_i, E_j) = \sum_{k=1}^{n} \alpha_k(t_i) V_k(E_j). \tag{4.2}$$

The eigenvectors define the different variability modes of each PCA component, while the variable coefficients α_k describe the sample variance. If there are recognizable variability patterns, the first few principal components should account for most of the variance, and reveal the shape of the spectral components having the stronger variability.

The results are illustrated in Fig. 4.9, where I plot the first three principal components, their ratio to the average spectrum, and their respective contribution to the total variance

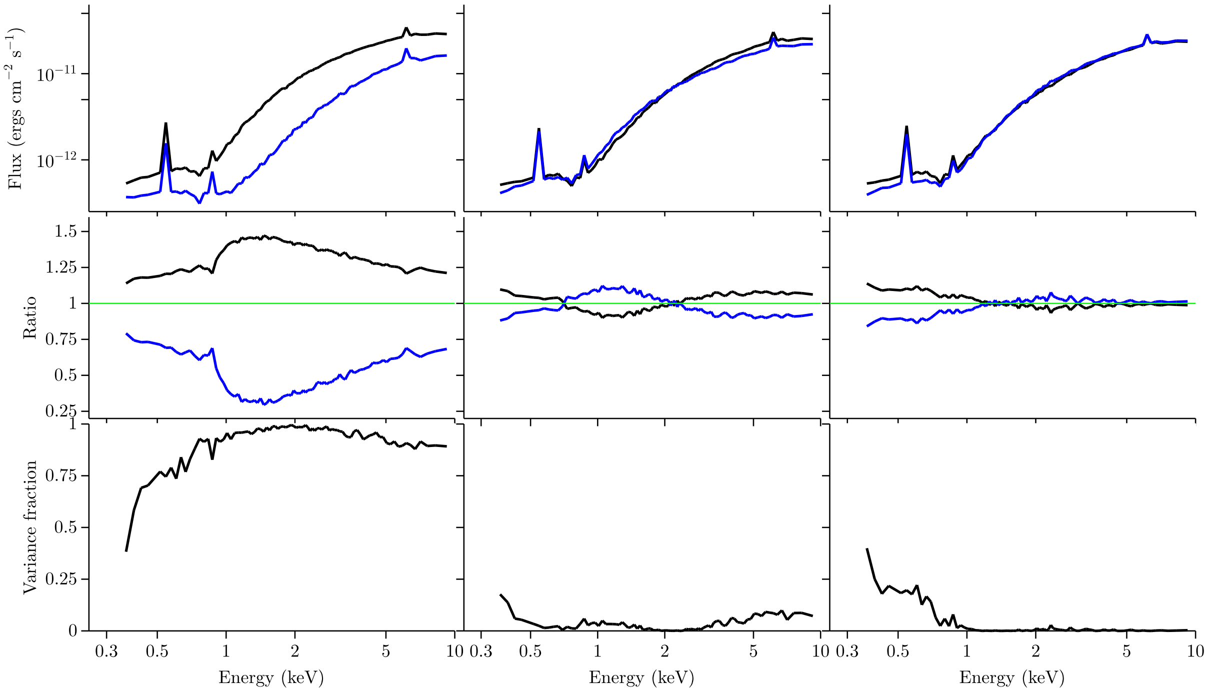

Figure 4.9 – The first (left panels), second (centre panels) and third (right panels) principal components of variability of the *XMM-Newton*/pn spectra taken during Summer 2013. Upper panels: spectra of the eigenvectors V_k with $k = 1$ (left), $k = 2$ (centre) and $k = 3$ (right) corresponding to the maximal (in black) and minimal (in blue) coordinate $\alpha_k(t_j)$ over the $j = 12$ observations. Middle panels: ratio of the maximum and minimum spectra to the average spectrum of the source. Bottom panels: contribution of each component to the total variance as a function of energy.

as a function of energy. The first principal component represents a variability mode dominated by variations in the flux, and it accounts for most of the variance above 1 keV. This component has a maximum around 1-2 keV, and is in agreement with the fractional variability $F_{\rm var}$ reported in Paper VIII. As discussed in Paper VIII, most of the observed variability at 1-2 keV can be explained by variations of the column density of the obscurer component 1 (i.e. that with the larger covering fraction), and of the power law normalization. Indeed, in Ursini et al. (2015a) I found that the obscurer component 1 is the most variable, with $N_{\rm H}$ varying from 0.5 to 1.5 $\times$ 10^{22} cm^{-2} (e.g., Fig. 8 of Ursini et al. 2015a). The second principal component is more difficult to interpret, as it seems to account for some variance below 0.5 keV, around 1 keV and above 2-3 keV. Part of this variability pattern might be explained by variations of the obscurer component 2. However, it may also indicate that PCA is not able to find really independent components in this case. The third principal component, on the other hand, only accounts for residual variance below 1 keV, which can be interpreted as being due to variations of the covering fraction of the obscurer component 1 (see also Paper VIII).

Finally, I note that PCA is a linear analysis, i.e. its output is linear with respect to changes in the signal. Strictly, the output has a physical meaning only if the signal (the spectrum, in our case) is a superposition of additive components. If there are non-linear relationships between components, PCA could give unphysical results. In our case, we want to test the results of PCA against a multiplicative model, where absorption variability plays a key role. I note that partial covering means that the model is equivalent to the sum of two components, one absorbed and one unabsorbed. Therefore, variations of the covering fraction mimic the effect of two additive components. On the other hand, the effects of column density variations can be more complex. I thus tested a slightly different procedure, called multiplicative PCA (MPCA). Essentially, this method consists in taking the logarithm of the data, performing PCA, and then taking the exponential of the results. The advantage of taking the logarithm is obvious, as multiplicative relationships are converted into additive ones. However, I observed that MPCA and PCA give similar results in our case. I also performed the same analyses on a series of simulated spectra, assuming a simple model consisting of a constant power law modified by variable absorption. I verified that the principal components found with MPCA are close to those found with PCA, provided that the variations of the absorbing column density are not dramatic (i.e. within a factor of 10).

Overall, the results of PCA are in agreement with the detailed timing analysis reported in Paper VIII. PCA and the analysis of F_{var} provide a model-independent characterization of variability. This analysis indicates that the strong variability in the soft band can be interpreted as being due to absorption, and in particular to the obscurer component 1, in agreement with the results of the spectral analysis.

4.2.6 Conclusions

The results of the high-energy view of the campaign on NGC 5548 are fully discussed in Ursini et al. (2015a). Here, I underline the most interesting conclusions in the context of the broader goal, namely constraining the high-energy sources in AGNs.

Thanks to the high-quality data from the multiwavelength campaign, I could study the broad-band (0.3–400 keV) X-ray spectrum of NGC 5548 in detail. A high-energy cut-off of about 70 keV, attributed to thermal Comptonization, is found in one observation out of seven, and a lower limit ranging from 50 to 250 keV is found in the other six observations. The reflection component is consistent with being constant, thus it is likely produced by material lying a few light months away from the primary source. The average spectrum is well described by thermal Comptonization component, with a temperature of about 40 keV and an optical depth of about 2-3. Furthermore, the comparison with past observations of the source indicates a significant long-term variability (up to a factor of 10 in 15 years) of the physical parameters of the corona.

The variability of the primary photon index and of the high-energy cut-off is a clear signature of short-term (i.e. over a few days/weeks) variability of the physical and/or geometrical parameters of the primary X-ray source. According to the two-phase model, the coronal optical depth and temperature should follow a univocal relationship for a given heating/cooling ratio (Sec. 2.4.2). Then, if the optical depth changes, the temperature will adjust to keep the heating/cooling ratio constant. But the heating/cooling ratio can also vary, responding e.g. to a variation in the disc/corona geometry, like a variation of the inner disc radius or of the velocity of an outflowing corona (Malzac et al. 2001). Then, the coronal optical depth and temperature will change in a non-trivial way to be consistent with the new heating/cooling ratio. Clearly, a phenomenological modelling, albeit needed for a basic understanding of the spectral properties of the source, does not allow for a unique interpretation. The strong absorption throughout the campaign makes it difficult to test detailed Comptonization models, such as in Petrucci et al. (2013). However, the approach based on multiple, broad-band observations brings crucial informations to build a self-consistent model, explaining both the physical parameters and their variability over different time-scales.

Appendix

Anatomy of the AGN in NGC 5548 III. The high-energy view with NuSTAR and INTEGRAL

F. Ursini[1,2,3], R. Boissay[4], P.-O. Petrucci[1,2], G. Matt[3], M. Cappi[5], S. Bianchi[3], J. Kaastra[6], F. Harrison[7], D. J. Walton[8,7], L. di Gesu[6], E. Costantini[6], B. De Marco[9], G. A. Kriss[10,11], M. Mehdipour[6,12], S. Paltani[4], B. M. Peterson[13,14], G. Ponti[9], and K. C. Steenbrugge[15,16]

[1] Univ. Grenoble Alpes, IPAG, F-38000 Grenoble, France.
[2] CNRS, IPAG, F-38000 Grenoble, France.
[3] Dipartimento di Matematica e Fisica, Università degli Studi Roma Tre, via della Vasca Navale 84, 00146 Roma, Italy.
[4] Department of Astronomy, University of Geneva, 16 Ch. d'Ecogia, 1290 Versoix, Switzerland.
[5] INAF-IASF Bologna, Via Gobetti 101, I-40129 Bologna, Italy.
[6] SRON Netherlands Institute for Space Research, Sorbonnelaan 2, 3584 CA Utrecht, the Netherlands.
[7] Cahill Center for Astronomy and Astrophysics, California Institute of Technology, Pasadena, CA 91125, USA.
[8] Jet Propulsion Laboratory, 4800 Oak Grove Dr., Pasadena, CA 91109, USA.
[9] Max-Planck-Institut für extraterrestrische Physik, Giessenbachstrasse, D-85748 Garching, Germany.
[10] Space Telescope Science Institute, 3700 San Martin Drive, Baltimore, MD 21218, USA.
[11] Department of Physics and Astronomy, The Johns Hopkins University, Baltimore, MD 21218, USA.
[12] Mullard Space Science Laboratory, University College London, Holmbury St. Mary, Dorking, Surrey, RH5 6NT, UK.
[13] Department of Astronomy, The Ohio State University, 140 W 18th Avenue, Columbus, OH 43210, USA.
[14] Center for Cosmology & AstroParticle Physics, The Ohio State University, 191 West Woodruff Avenue, Columbus, OH 43210, USA.
[15] Instituto de Astronomía, Universidad Católica del Norte, Avenida Angamos 0610, Casilla 1280, Antofagasta, Chile.
[16] Department of Physics, University of Oxford, Keble Road, Oxford, OX1 3RH, UK.

Published in *Astronomy & Astrophysics*, 577, A38 (2015)

A&A 577, A38 (2015)
DOI: 10.1051/0004-6361/201425401

Astronomy & Astrophysics

Anatomy of the AGN in NGC 5548

III. The high-energy view with NuSTAR and INTEGRAL

F. Ursini[1,2,3], R. Boissay[4], P.-O. Petrucci[1,2], G. Matt[3], M. Cappi[5], S. Bianchi[3], J. Kaastra[6], F. Harrison[7], D. J. Walton[8,7], L. di Gesu[6], E. Costantini[6], B. De Marco[9], G. A. Kriss[10,11], M. Mehdipour[6,12], S. Paltani[4], B. M. Peterson[13,14], G. Ponti[9], and K. C. Steenbrugge[15,16]

[1] Univ. Grenoble Alpes, IPAG, 38000 Grenoble, France
e-mail: `francesco.ursini@obs.ujf-grenoble.fr`
[2] CNRS, IPAG, 38000 Grenoble, France
[3] Dipartimento di Matematica e Fisica, Università degli Studi Roma Tre, via della Vasca Navale 84, 00146 Roma, Italy
[4] Department of Astronomy, University of Geneva, 16 Ch. d'Ecogia, 1290 Versoix, Switzerland
[5] INAF-IASF Bologna, via Gobetti 101, 40129 Bologna, Italy
[6] SRON Netherlands Institute for Space Research, Sorbonnelaan 2, 3584 CA Utrecht, The Netherlands
[7] Cahill Center for Astronomy and Astrophysics, California Institute of Technology, Pasadena, CA 91125, USA
[8] Jet Propulsion Laboratory, 4800 Oak Grove Dr., Pasadena, CA 91109, USA
[9] Max-Planck-Institut für extraterrestrische Physik, Giessenbachstrasse, 85748 Garching, Germany
[10] Space Telescope Science Institute, 3700 San Martin Drive, Baltimore, MD 21218, USA
[11] Department of Physics and Astronomy, The Johns Hopkins University, Baltimore, MD 21218, USA
[12] Mullard Space Science Laboratory, University College London, Holmbury St. Mary, Dorking, Surrey, RH5 6NT, UK
[13] Department of Astronomy, The Ohio State University, 140 W 18th Avenue, Columbus, OH 43210, USA
[14] Center for Cosmology & AstroParticle Physics, The Ohio State University, 191 West Woodruff Avenue, Columbus, OH 43210, USA
[15] Instituto de Astronomia, Universidad Católica del Norte, Avenida Angamos 0610, Casilla 1280, Antofagasta, Chile
[16] Department of Physics, University of Oxford, Keble Road, Oxford, OX1 3RH, UK

Received 25 November 2014 / Accepted 12 January 2015

ABSTRACT

We describe the analysis of the seven broad-band X-ray continuum observations of the archetypal Seyfert 1 galaxy NGC 5548 that were obtained with *XMM-Newton* or *Chandra*, simultaneously with high-energy (>10 keV) observations with NuSTAR and INTEGRAL. These data were obtained as part of a multiwavelength campaign undertaken from the summer of 2013 till early 2014. We find evidence of a high-energy cut-off in at least one observation, which we attribute to thermal Comptonization, and a constant reflected component that is likely due to neutral material at least a few light months away from the continuum source. We confirm the presence of strong, partial covering X-ray absorption as the explanation for the sharp decrease in flux through the soft X-ray band. The obscurers appear to be variable in column density and covering fraction on time scales as short as weeks. A fit of the average spectrum over the range 0.3–400 keV with a realistic Comptonization model indicates the presence of a hot corona with a temperature of 40^{+40}_{-10} keV and an optical depth of $2.7^{+0.7}_{-1.2}$ if a spherical geometry is assumed.

Key words. galaxies: active – galaxies: Seyfert – X-rays: galaxies

1. Introduction

The high-energy spectrum of active galactic nuclei (AGNs) is typically dominated by a primary power law component, which is generally believed to originate in a hot plasma, the so-called corona, localized in the inner part of the accretion flow (Reis & Miller 2013). The presence of a high-energy cut-off around ~100 keV has been observed in several sources (see, e.g., Perola et al. 2002; Malizia et al. 2014; Brenneman et al. 2014; Marinucci et al. 2014; Ballantyne et al. 2014) and is commonly interpreted as the signature of thermal Comptonization. Namely, the optical/UV photons from the accretion disk are upscattered by the hot electrons of the corona up to X-ray energies (see, e.g., Haardt & Maraschi 1991; Haardt et al. 1994, 1997). This primary emission can be modified by different processes, such as absorption from surrounding gas and Compton reflection from the disk itself or more distant material. Moreover, the spectra of many AGNs rise smoothly below 1–2 keV above the extrapolated high-energy power law (see, e.g., Bianchi et al. 2009). The nature of this so-called soft excess is still under debate (see, e.g., Done et al. 2012).

The geometrical and physical properties of the different structures leading to the different spectral components are still poorly known. First and foremost, a more complete understanding of the high-energy emission of AGNs requires disentangling the spectral properties of each component and constraining their characteristic parameters. For this goal, the availability of multiple broad-band observations with a high signal-to-noise ratio is essential. Using the data from a previous long multiwavelength campaign on Mrk 509 (Kaastra et al. 2011), Petrucci et al. (2013) made a detailed study of the high-energy spectrum of that AGN. In that case, the simultaneous data covering the range

Table 1. Logs of the simultaneous *XMM-Newton,* NuSTAR, and/or INTEGRAL observations of NGC 5548 during our campaign.

Obs.	Satellites	Obs. Id.	Start time (UTC) yyyy-mm-dd	Net exp. (ks)
1	*XMM-Newton*	0720110401	2013-06-30	38
	INTEGRAL	10700010001	2013-06-29	62
2	*XMM-Newton*	0720110601	2013-07-11	37
	NuSTAR	60002044002/3	2013-07-11	50
	INTEGRAL	10700010002	2013-07-11	50
3	*XMM-Newton*	0720110701	2013-07-15	37
	INTEGRAL	10700010003	2013-07-15	50
4	*XMM-Newton*	0720111101	2013-07-23	38
	NuSTAR	60002044005	2013-07-23	50
	INTEGRAL	10700010004	2013-07-23	52
5	*Chandra*	16314	2013-09-10	120
	NuSTAR	60002044006	2013-09-10	50
6	*XMM-Newton*	0720111501	2013-12-20	38
	NuSTAR	60002044008	2013-12-20	50
7	*XMM-Newton*	0720111601	2014-02-04	38
	INTEGRAL	11200110001	2014-01-17	94
		11200110002	2014-01-22	40
		11200110003	2014-02-09	30

from optical/UV to gamma-ray energies made it possible to test Comptonization models in full detail and provide a physically motivated picture of the inner regions of the source. The hard X-ray continuum was well fitted by a Comptonized spectrum produced by a hot, optically thin corona with $kT_e \sim 100$ keV and $\tau \sim 0.5$, probably localized in the very inner part of the accretion flow (Petrucci et al. 2013). Mehdipour et al. (2011), studying the optical to X-ray variability, found a correlation between the optical/UV and soft (<0.5 keV) X-ray flux, but no correlation between the optical/UV and hard (>3 keV) X-ray flux. This result was interpreted as indicating the presence of a second, "warm" corona with $kT_e \sim 1$ keV and $\tau \sim 15$, responsible for the soft excess as well as the optical/UV emission (Mehdipour et al. 2011; Petrucci et al. 2013).

In the present paper, we discuss results based on a multiwavelength monitoring program on the AGN NGC 5548, an X-ray bright Seyfert 1 galaxy, hosting a supermassive black hole of 3.9×10^7 solar masses (Pancoast et al. 2014) and lying at a redshift of $z = 0.017175$ (de Vaucouleurs et al. 1991, as given in the NASA/IPAC Extragalactic Database). The source historically presented a flux variability typical of an unobscured AGN of that black hole mass (Ponti et al. 2012). High spectral resolution X-ray and UV observations of this source have previously shown a typical ionized outflow, seen as the "warm absorber" through narrow lines absorbing the UV and soft X-ray emission from the core (Crenshaw et al. 2003; Steenbrugge et al. 2005).

The multiwavelength campaign was conducted from May 2013 to February 2014, involving observations with the *XMM-Newton*, HST, *Swift*, NuSTAR, INTEGRAL and *Chandra* satellites (Kaastra et al. 2014, hereafter K14). During the campaign, the nucleus was found to be obscured by a long-lasting and clumpy stream of ionized gas never seen before in this source. This heavy absorption manifests itself as a 90% decrease of the soft X-ray continuum emission, associated with deep and broad UV absorption troughs. The obscuring material has a distance of only a few light days from the nucleus, and it is outflowing with a velocity up to five times faster than those observed in the warm absorber (K14). Given its properties, this new obscuring stream likely arises in the accretion disk.

This work is part of a series of papers focusing on different aspects of the campaign. Here we concentrate on the broad band (0.3–400 keV) X-ray emission, focusing on the observations featuring high-energy (>10 keV) data provided by NuSTAR and INTEGRAL.

The paper is organized as follows. In Sect. 2, we describe the observations and data reduction. In Sect. 3 we present the analysis of the hard (>5 keV) X-ray and total (0.3–400 keV) X-ray spectrum, fitted with both a phenomenological and a realistic Comptonization model. In Sect. 4, we discuss the results and summarize our conclusions.

2. Observations and data reduction

The multi-satellite campaign was led by *XMM-Newton*, which observed NGC 5548 twelve times during 40 days in June and July 2013, plus once in December and once in February 2014. For the full description of the program, see K14 and Mehdipour et al. (2015). During the campaign, NuSTAR (Harrison et al. 2013) and INTEGRAL (Winkler et al. 2003) regularly observed the source simultaneously with *XMM-Newton*. A simultaneous *Chandra*/NuSTAR observation was also performed in September 2013. The log of the data sets analysed in this paper is reported in Table 1, with their observation ID, their start date, and net exposure time. The latest *XMM-Newton* observation is dated February 4, and the corresponding spectrum has been analysed jointly with an average spectrum obtained from three INTEGRAL exposures obtained in January and February, which show no significant variations.

In all the *XMM-Newton* observations, the EPIC instruments were operating in the Small-Window mode with the thin-filter applied. For our analysis, we used the EPIC-pn data only. The data were processed using the *XMM-Newton* Science Analysis System (SAS v13). The spectra were grouped such that each spectral bin contains at least 20 counts. Starting in 2013, a gain problem with the pn data appeared, causing a shift of about 50 eV near the Fe-K complex (see the detailed discussion in Cappi et al., in prep.). In the present paper this shift was corrected for by leaving the redshift free to vary in our models.

Moreover, this small offset yields poor fits near the energy of the gold M-edge of the telescope mirror, and for this reason the interval between 2.0 and 2.5 keV was omitted from the fit. However, this problem has no effect upon the broad-band modelling, in particular the Fe-K line strength is correct, thus allowing for the reflection component to be correctly modelled.

The NuSTAR data were reduced with the standard pipeline (NUPIPELINE) in the NuSTAR Data Analysis Software (NUSTARDAS, v1.3.1; part of the HEASOFT distribution as of version 6.14), using calibration files from NuSTAR CALDB v20130710. The raw event files were cleaned with the standard depth correction, which greatly reduces the internal background at high energies, and data from the passages of the satellite through the South Atlantic Anomaly were removed. Spectra and light curves were extracted from the cleaned event files using the standard tool NUPRODUCTS for each of the two hard X-ray telescopes aboard NuSTAR, focal plane modules A and B (FPMA and FPMB); the spectra from these telescopes are analysed jointly in this work, but are not combined. Finally, the spectra were grouped such that each spectral bin contains at least 50 counts.

INTEGRAL data were reduced with the Off-line Scientific Analysis software OSA 10.0 (Courvoisier et al. 2003). IBIS/ISGRI spectra have been extracted using the standard spectral extraction tool `ibis_science_analysis` and combined together using the OSA `spe_pick` tool to generate the total ISGRI spectrum, as well as the corresponding response and ancillary files.

The *Chandra* HRC/LETG spectra (first order) of the 120 ks observation of September 10 were reduced with the package CIAO v4.6 and reprocessed with the standard tool `chandra_repro`.

Finally, we made use of archival *Beppo*SAX and *Suzaku* data to compare the results of the campaign with past X-ray observations of the source. We focused on a 1997 *Beppo*SAX long (~300 ks) observation and on seven *Suzaku* observations (~30 ks each) performed in 2007. For a description of the observations and data reduction procedure we refer to Nicastro et al. (2000) for *Beppo*SAX, and Liu et al. (2010) for *Suzaku*.

In Fig. 1, we show the light curves of all the fourteen *XMM-Newton* observations, the four NuSTAR observations and the five INTEGRAL observations of the campaign. The variability shown by the light curves in the low-energy ranges is mainly due to obscuration, as shown in Sect. 3. We will also show that the primary emission exhibits intrinsic variations as well, which explain the variability observed at higher energies. We refer the reader to Mehdipour et al. (2015) for the full time-line of the campaign (see their Fig. 1).

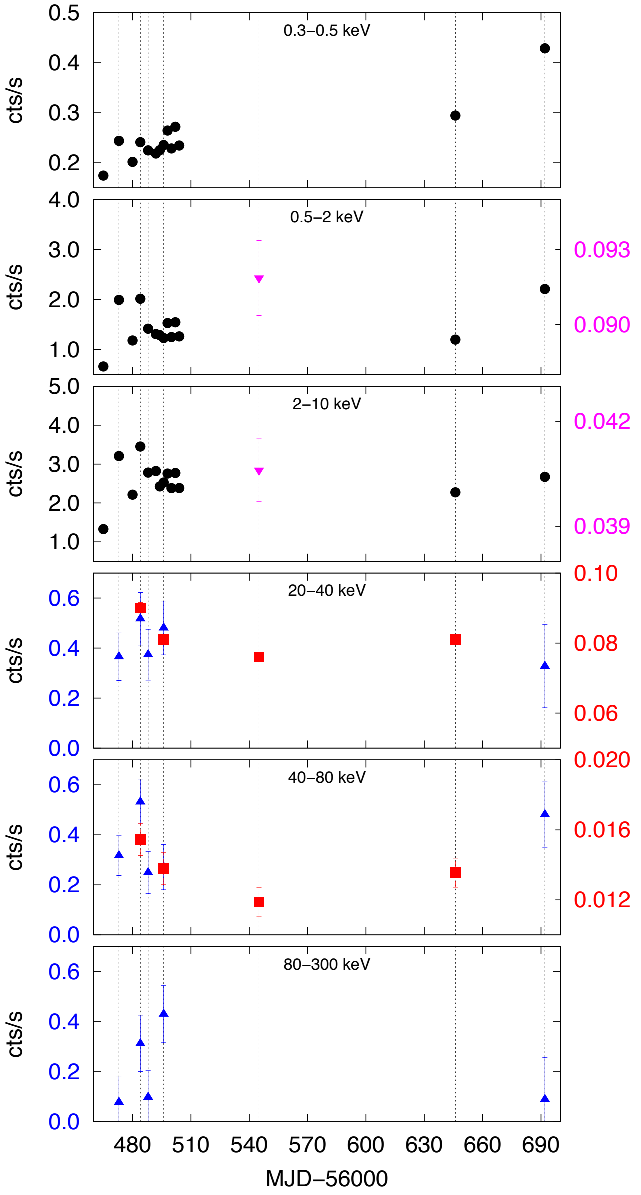

Fig. 1. Light curves in different energy ranges. On the x-axis, we report the last three digits of the Modified Julian Date. On the y-axis, on both left and right side, we report the count-rate. Black circles: *XMM-Newton* (0.3–0.5 keV, 0.5–2 keV, 2–10 keV); magenta nablas: *Chandra* (0.5–2 keV, 2–10 keV); red squares: NuSTAR (20–40 keV, 40–80 keV); blue triangles: INTEGRAL (20–40 keV, 40–80 keV, 80–300 keV). The vertical dotted lines highlight the seven observations we analysed in this paper (i.e., those including NuSTAR and/or INTEGRAL data).

3. Spectral analysis

Spectral analysis and model fitting was carried out with the XSPEC 12.8 package (Arnaud 1996), using the χ^2 minimisation technique throughout. In this paper, all errors are quoted at the 90% confidence level.

3.1. Spectral curvature above 10 keV

In Fig. 2 we plot for comparison the four NuSTAR/FPMA spectra above 10 keV, simultaneously fitted with a power law with tied parameters (χ^2/d.o.f. = 1549/1178). The photon index obtained is $\Gamma = 1.58 \pm 0.02$. The plot shows that the spectral variability in the hard X-rays during the campaign is not dramatic, while it is prominent in the soft X-rays (K14; Cappi et al., in prep.; di Gesu et al., in prep.) where obscuration plays a major role. After getting a general idea about the power law parameters, we tested the presence of spectral curvature by individually fitting each of the four NuSTAR spectra above 10 keV, first with a simple power law and as a second step including an exponential cut-off. The addition of the cut-off results in an improvement in all fits ($\Delta\chi^2 \lesssim -30$), with a probability of chance improvement less than 10^{-8} according to the F-test. This result motivates the

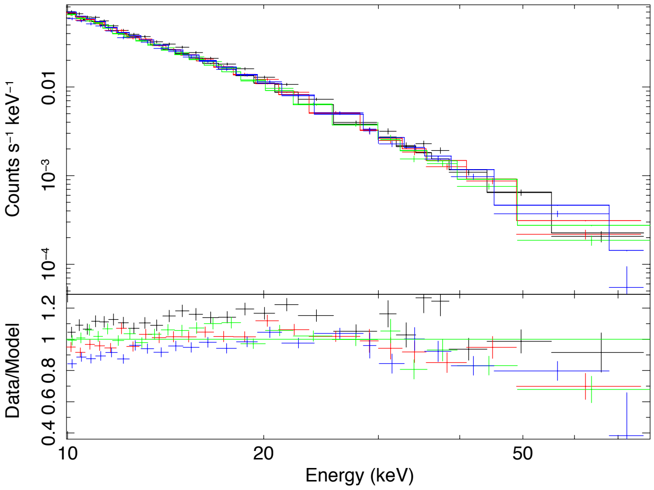

Fig. 2. *Upper panel*: 10–79 keV spectra of the four NuSTAR observations. *Lower panel*: residuals when simultaneously fitting with a power law. For clarity, we used only FPMA data, which are rebinned in the plot.

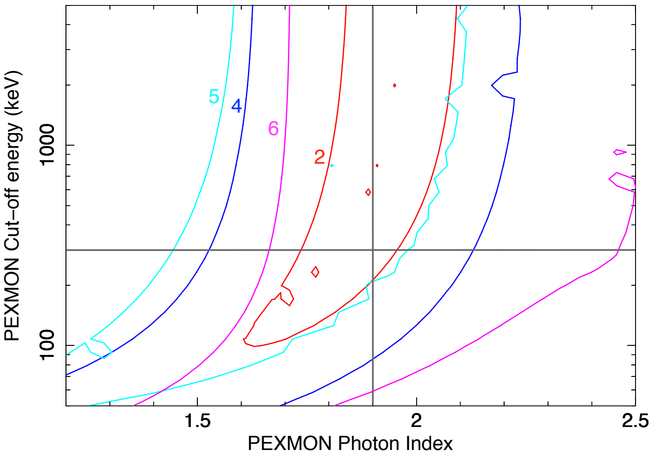

Fig. 3. PEXMON cut-off energy vs. photon index 90% confidence level contours for the 4 NuSTAR observations, fitted above 5 keV. The grey solid lines indicate the values we chose to fix in the later broad-band analysis (1.9 for the photon index, 300 keV for the cut-off energy).

use of a cut-off power law in the analysis of the data. However, as a next step we test whether the spectral curvature is partly due to a reflection component.

3.2. The reflection component

To test for the presence of a reflection component, we fitted the data above 5 keV. By choosing 5 keV as a lower energy limit, we avoid the effects due to the strong absorption in the soft band. Good statistics are needed, so we only consider the four observations including NuSTAR data (obs. 2, 4, 5 and 6 of Table 1).

We fitted the *XMM-Newton*/pn, NuSTAR and INTEGRAL data simultaneously, leaving the cross-calibration constants free to vary. The normalization factors with respect to pn were always between 1 and 1.1. In particular, the spectral agreement between *XMM-Newton* and NuSTAR is generally good in their common 3–10 keV bandpass (Walton et al. 2013, 2014). We used a simple model, consisting of a cut-off power law modified by absorption, plus reflection. We included a neutral absorber with covering fraction fixed to 1, while the column density was free to vary. This is clearly an arbitrary choice, but the way we model the absorption, with a lower energy limit of 5 keV, does not affect the results that follow.

Following the analysis done by Cappi et al. (in prep.) and motivated by their detection of a neutral, narrow and constant Fe Kα line, we used the PEXMON model (Nandra et al. 2007) in XSPEC for the reflection component. PEXMON combines a neutral Compton reflection, as described by the PEXRAV model (Magdziarz & Zdziarski 1995) in XSPEC, with Fe Kα, Fe Kβ, Ni Kα lines and the Fe Kα Compton shoulder, generated self-consistently by Monte-Carlo simulations (George & Fabian 1991). We fixed the inclination angle of the reflector to 30 deg, appropriate for a type 1 source (e.g., Nandra et al. 1997) and consistent with past analyses of the Fe K lines in NGC 5548 (Yaqoob et al. 2001; Liu et al. 2010), but also with the inclination estimated for the broad-line region (Pancoast et al. 2014) and for the disk-corona system (Petrucci et al. 2000). The photon index, cut-off energy and normalization of the incident radiation were free to vary and not tied to those of the primary power law. This choice is justified a priori by the observed constancy of the Fe Kα line, and a posteriori by our constraints on the reflection component, which is consistent with being constant during the campaign. In this case, the distance of the reflecting material from the X-ray emitting region should be at least a few light months, i.e. a few × 10^4 gravitational radii, as we will discuss in Sect. 4.

The 90% contour plots of cut-off energy and normalization vs. photon index of PEXMON are plotted in Figs. 3 and 4. The photon index and cut-off energy of the reflected continuum are not well constrained, however the contours are mutually consistent. The normalization vs. photon index contours are very similar for the four observations, with indication of a slightly larger normalization for obs. 6; nevertheless they are also marginally consistent with each other. These results are consistent with the reflected emission coming from remote material, and thus the parameters being constant during the campaign. For this reason, we chose to freeze hereafter the parameters of the reflection component to their weighted average derived from our analysis. We thus fixed the PEXMON photon index to 1.9, cut-off energy to 300 keV and normalization to 5.5×10^{-3} (XSPEC units). The photon index of 1.9 is relatively high compared to the average value for NGC 5548, which is ~1.7 (see, e.g., Sobolewska & Papadakis 2009) but has indeed been observed in the past (Nandra et al. 1991; Reynolds 1997; Chiang et al. 2000). More importantly, the *Swift* monitoring discussed in Mehdipour et al. (in prep.) shows that the photon index reached 1.8–1.9 during most of 2012. Finally, from the PEXMON parameters we estimate the average reflection fraction f as 0.3 ± 0.1, calculated as the ratio between the 20–40 keV flux illuminating the reflecting material and the 20–40 keV flux of the primary cut-off power law[1]. For a distant reflector, this ratio might not have a clear link with the covering factor as seen from the X-ray source (Malzac & Petrucci 2002), but this is discussed in more detail in Sect. 4.

3.3. Broad-band spectral analysis

Having obtained constraints on the parameters of the reflection component using the data above 5 keV, we now proceed to fit the

---

[1] This definition is slightly different from the traditional $R = \Omega/2\pi$, where Ω is the solid angle subtended by the reflector (Magdziarz & Zdziarski 1995).

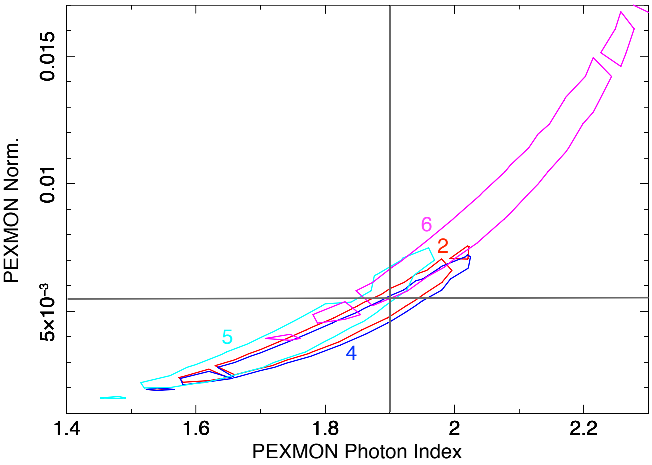

Fig. 4. PEXMON normalization vs. photon index 90% confidence level contours for the 4 NuSTAR observations, fitted above 5 keV. The grey solid lines indicate the values we chose to fix in the later broad-band analysis (1.9 for the photon index, 5.5×10^{-3} for the normalization).

total X-ray energy range available. We first use a phenomenological model, which is described below. Given the different satellites used in the seven observations, the energy range is limited to 0.5–79 keV for obs. 5 (*Chandra*/NuSTAR) and 0.3–79 keV for obs. 6 (*XMM-Newton*/NuSTAR). For all the other observations, the energy range is 0.3–400 keV, thanks to the addition of the INTEGRAL data.

3.3.1. The model components

Following Sects. 3.1 and 3.2, we modelled the continuum with a cut-off power law and the reflected component with PEXMON, whose parameters were fixed. We describe in the following the other spectral components.

Obscuration: the model presented by K14 includes two ionized, partially covering absorbers. Both were found to have a low degree of ionization, namely $\log \xi \leq -4$ and $\log \xi \simeq -1.2$, such that at the EPIC-pn energy resolution they are almost equivalent to neutral absorbers. In particular, the absorber with $\log \xi = -1.2$ was found to have a column density of 1.2×10^{22} cm^{-2} (K14) and such an absorber is indistinguishable, using pn data only, from a neutral one with a column density of 1.1×10^{22} cm^{-2}. Since a detailed modelling of the obscuration is out of the scope of the present paper, we modelled the two absorbing components with PCFABS in XSPEC, which describes partial covering absorption by a neutral medium. Both the column density and the covering fraction of the two components were free to vary between different observations.

The warm absorber: the model by K14 includes six warm absorber components, with different column densities ($N_{\rm H} \sim 10^{20}$–10^{21} cm^{-2}), ionization parameters ($\log \xi \sim 1$–3), and outflow velocities ($v \sim 250$–1000 km s^{-1}). We produced a table, with fixed parameters, from the best-fit model of the warm absorber derived by K14 and included it in XSPEC. For a comprehensive analysis of the UV properties of the warm absorber, see Arav et al. (2015).

The soft X-ray excess: the physical origin of this component is still under debate, and it can be modelled with several different spectral models. The most common interpretations rely on relativistically blurred reflection (see, e.g., Crummy et al. 2006; Cerruti et al. 2011; Walton et al. 2012) or Comptonization by a warm medium (see, e.g., Petrucci et al. 2013; Boissay et al. 2014; Matt et al. 2014). Detailed modelling of the soft X-ray excess is beyond the scope of this paper, we thus followed the analysis done by Mehdipour et al. (in prep.) and assumed a thermal Comptonization component modelled by COMPTT (Titarchuk 1994) in XSPEC. The parameters of COMPTT were frozen, for each individual observation, to the values reported by Mehdipour et al. (in prep.), to which we refer the reader for details. We note that Mehdipour et al. (in prep.) found a significant flux variability of the soft excess between different observations, which we take into account here, but no apparent spectral shape variability.

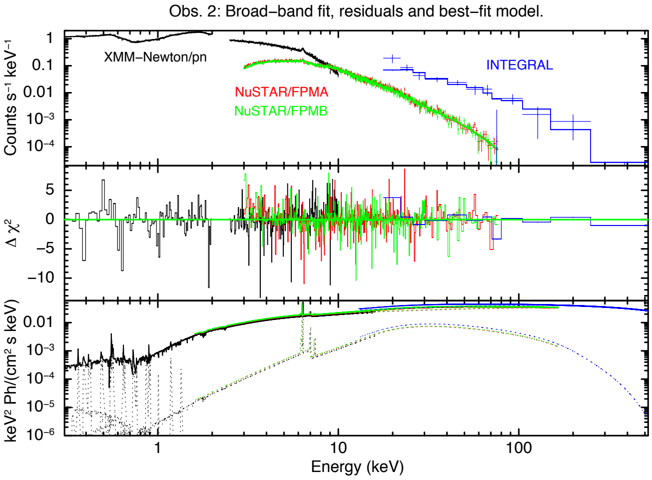

Fig. 5. Data and best-fit model for obs. 2 (*XMM-Newton*/NuSTAR/INTEGRAL, see Table 1). *Upper panel*: broad-band data and folded model. *Middle panel*: contribution to χ^2. *Lower panel*: best-fit model $E^2 f(E)$ with the plot of the various additive components, namely the cut-off power law, the reflection component, the soft excess and the narrow lines.

Narrow emission lines: a number of emission lines, such as [O VII] at 0.56 keV and [C V] at 0.3 keV, were detected in the *XMM-Newton* RGS spectra, as shown by K14. Again, we produced a table from the best-fit model and included it in XSPEC. These lines arguably originate from the Narrow-Line Region, therefore we do not expect line flux variations during the campaign (Peterson et al. 2013).

3.3.2. Best-fit results

The best-fit parameters are reported in Table 2, while in Fig. 5 we show the data, residuals and best-fit model for obs. 2 (*XMM-Newton*/NuSTAR/INTEGRAL). The broad-band fit allows us to constrain the spectral shape more reliably with respect to the fit above 5 keV. In Figs. 6 and 7, we show the contour plots of the high-energy cut-off and normalization versus photon index, both for the primary continuum. The contours show significant variability of the photon index from ∼1.5 (obs. 6, 7) to ∼1.7 (obs. 1, 2, 4, 5). It should be noted that the photon index given in Kaastra et al. (2014), i.e. $\Gamma = 1.566 \pm 0.009$, is a mean value which comes from the analysis of the co-added *XMM-Newton* and NuSTAR spectra of summer 2013.

Table 2. Best-fit parameters of the primary cut-off power law and the two absorbers (1) and (2), fitting the data down to 0.3 keV.

Obs.	Γ	E_c	$F_{1\,\mathrm{keV}}$	$N_H^{(1)}$	$C_F^{(1)}$	$N_H^{(2)}$	$C_F^{(2)}$	χ^2/d.o.f.
1	$1.70^{+0.04}_{-0.05}$	>120	0.96 ± 0.09	0.75 ± 0.03	$0.797^{+0.006}_{-0.007}$	9 ± 1	$0.29^{+0.05}_{-0.06}$	538/424
2	$1.74^{+0.01}_{-0.04}$	>250	$1.13^{+0.03}_{-0.07}$	0.85 ± 0.02	$0.829^{+0.004}_{-0.003}$	$9.2^{+0.8}_{-0.9}$	$0.32^{+0.02}_{-0.03}$	1587/1393
3	$1.6^{+0.1}_{-0.2}$	>50	$0.7^{+0.2}_{-0.1}$	$1.06^{+0.06}_{-0.10}$	$0.81^{+0.01}_{-0.02}$	9^{+3}_{-2}	$0.27^{+0.06}_{-0.10}$	508/420
4	1.68 ± 0.05	>120	$0.87^{+0.07}_{-0.06}$	1.27 ± 0.06	0.77 ± 0.01	$8.5^{+0.8}_{-0.7}$	0.46 ± 0.03	1346/1329
5	$1.74^{+0.01}_{-0.03}$	>180	1.00 ± 0.05	1.8 ± 0.02	0.62 ± 0.03	†	†	1113/1094
6	1.49 ± 0.05	70^{+40}_{-10}	0.56 ± 0.05	$1.5^{+0.2}_{-0.1}$	0.68 ± 0.04	8 ± 2	0.33 ± 0.06	1484/1308
7	1.49 ± 0.02	>120	0.50 ± 0.01	$0.44^{+0.05}_{-0.04}$	0.678 ± 0.007	†	†	452/420

Notes. In the case of obs. 7, the model included a Gaussian line and an absorption edge (see text). E_c is in keV, $F_{1\,\mathrm{keV}}$ is in units of 10^{-2} ph/keV cm^2 s and N_H is in units of 10^{22} cm^{-2}. $^{(\dagger)}$ The second absorber was not needed in obs. 5 (*Chandra* plus NuSTAR) and obs. 7. In these two cases, fixing $N_H^{(2)}$ to 8.5 resulted in $C_F^{(2)} = 0$.

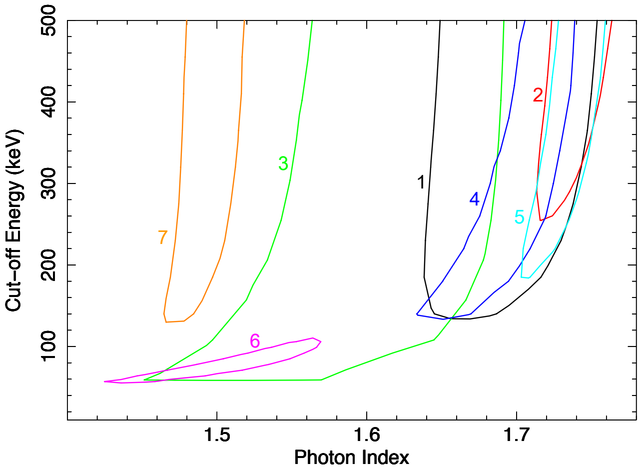

Fig. 6. Cut-off energy vs. primary photon index 90% confidence level contours for obs. 1 (black), obs. 2 (red), obs. 3 (green), obs. 4 (blue), obs. 5 (cyan), obs. 6 (magenta), obs. 7 (orange).

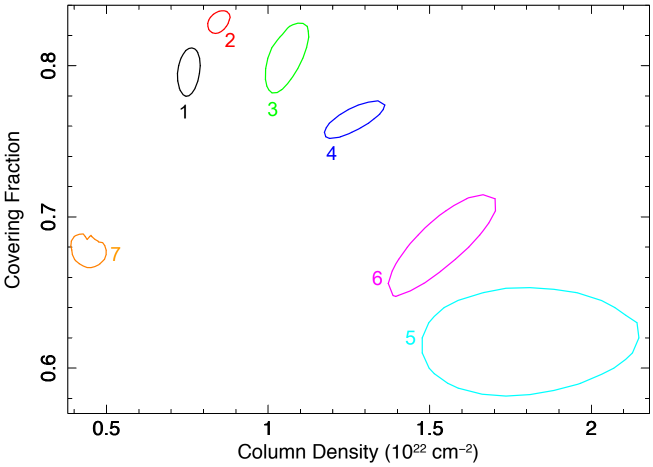

Fig. 8. Obscurer component 1: $N_H - C_F$ 90% confidence level contours for obs. 1 (black), obs. 2 (red), obs. 3 (green), obs. 4 (blue), obs. 5 (cyan), obs. 6 (magenta), obs. 7 (orange).

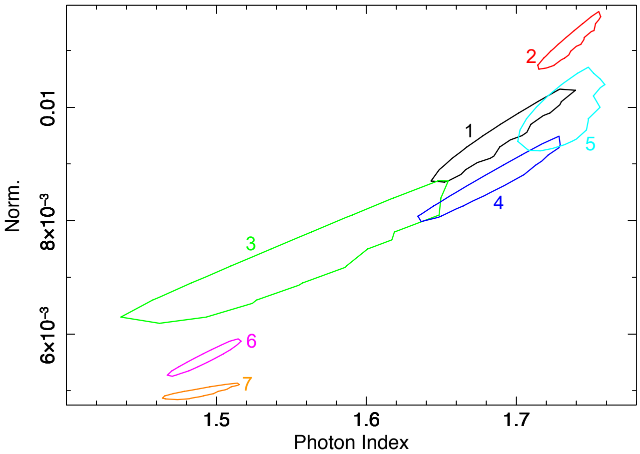

Fig. 7. Normalization vs. primary photon index 90% confidence level contours for obs. 1 (black), obs. 2 (red), obs. 3 (green), obs. 4 (blue), obs. 5 (cyan), obs. 6 (magenta), obs. 7 (orange).

By including the individual NuSTAR and INTEGRAL high-energy spectra, we could constrain the photon index for each observation. Furthermore, the cut-off energy shows significant variability as well. We derive a lower limit for the cut-off energy in all the observations, and a measure of 70^{+40}_{-10} keV for obs. 6. This measure is inconsistent, at 90% confidence level, with the lower limits determined from the other observations, with the exception of obs. 3. Finally, we note that the constraints we derived on the cut-off energy are mostly compatible with the average value estimated in Sect. 3.2 for the reflection component alone, i.e. 300 keV.

The broad-band fit helps constrain the obscurer components as well. In Figs. 8 and 9, we plot the contours of the covering fraction versus the column density of the two neutral absorbers, while in Fig. 10 we plot the contours of the two column densities versus each other. These contours show that absorption variability is statistically significant for both the low and high-N_H absorbers. This can be seen, for example, by comparing obs. 2 (red contours) with obs. 4 (blue contours). Since the time interval between obs. 2 and 4 is ~10 days, we can conclude that the variability is significant on this time scale. In two cases, namely obs. 5 and 7, only one, low-N_H absorber is needed, and adding the high-N_H component does not improve the fit. For obs. 5 this can be explained by the lower sensitivity of *Chandra* HRC/LETG with respect to *XMM-Newton* EPIC-pn, which results in a lower signal-to-noise ratio in the soft band. For

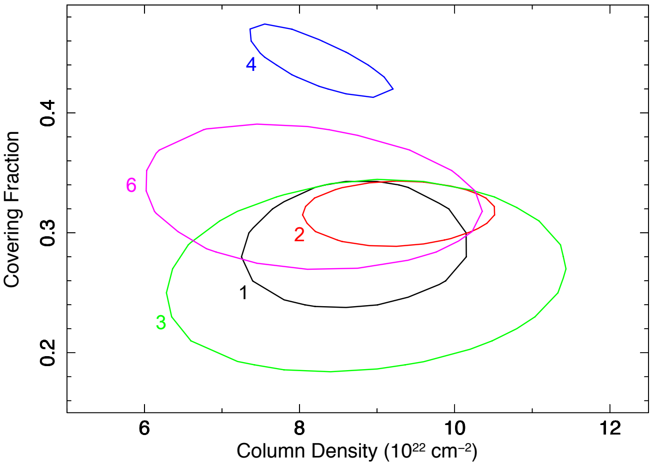

Fig. 9. Obscurer component 2: $N_{\rm H} - C_F$ 90% confidence level contours for obs. 1 (black), obs. 2 (red), obs. 3 (green), obs. 4 (blue), obs. 6 (magenta). This obscurer was not found in obs. 5 and 7.

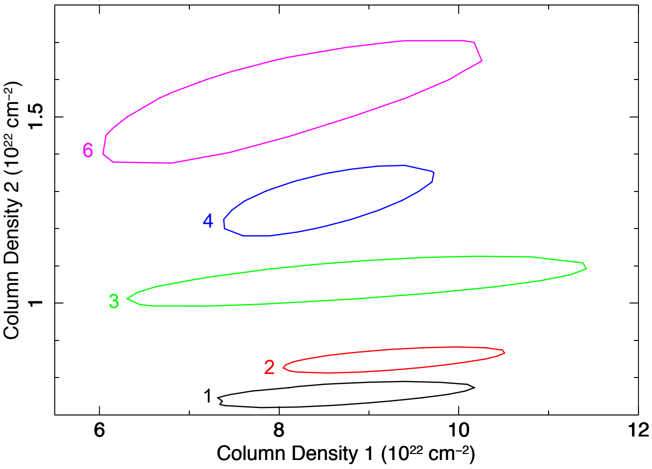

Fig. 10. $N_{\rm H}$–$N_{\rm H}$ 90% confidence level contours for obs. 1 (black), obs. 2 (red), obs. 3 (green), obs. 4 (blue), obs. 6 (magenta).

obs. 7, which is the last one and dated February 4, the absence of the high-$N_{\rm H}$ component could simply mean that the source started changing back to the more usual, unobscured condition. However, for the model described above, we only obtain a relatively poor fit (χ^2/d.o.f. = 651/424), with strong, positive residuals around 0.5 keV, and negative residuals around 0.8 keV. We stress that the models we used for the warm absorber and the narrow emission lines were obtained from the analysis of pn and RGS data (K14), while our analysis is based on pn data alone. We may thus attribute such residuals in obs. 7 to a combination of the previously mentioned gain problem of the pn data with cross-calibration issues between the pn and RGS instruments (Kirsch et al. 2004). We obtained a much better fit ($\Delta\chi^2 \simeq -200$) by adding a narrow Gaussian line with GAUSS in XSPEC, and an absorption edge with EDGE, without affecting the parameters of the primary cut-off power law. The emission line was found at $E = 0.54 \pm 0.01$ keV, with an upper limit on the equivalent width of 20 eV. The absorption edge was found at $E = 0.80 \pm 0.01$ keV with $\tau = 0.28 \pm 0.06$.

3.4. *Test of Comptonization model*

The last step of our analysis consists of fitting the average spectrum with a more realistic model, where the primary continuum is produced self-consistently via Comptonization of soft photons emitted by the disk. A more detailed analysis of the entire campaign with realistic Comptonization models is deferred to a future work.

First, we produced an average spectrum merging respectively the *XMM-Newton,* NuSTAR and INTEGRAL spectra used in this paper (Table 1) with the MATHPHA tool of HEASOFT. We then proceeded to fit this average spectrum over the range 0.3–400 keV, at first with the phenomenological model we have discussed above (Sect. 3.3.1). The resulting fit had χ^2/d.o.f. = 3314/2631, with strong, positive residuals around 0.5 keV, and negative residuals around 0.6 keV (analogously to the already discussed obs. 7). We thus included two narrow Gaussian lines, with $E = 0.53 \pm 0.06$ keV (in emission, equivalent width <50 eV) and $E = 0.60 \pm 0.02$ keV (in absorption, equivalent width <20 eV). Again, we note that such residuals are most likely unphysical and due to cross-calibration between pn and RGS (Kirsch et al. 2004). However, the addition of these lines, while improving the fit, does not affect the best-fit parameters of the cut-off power law, namely $\Gamma = 1.67 \pm 0.02$ and $E_c > 250$ keV, with χ^2/d.o.f. = 3080/2627 and no prominent residual features. The relatively large χ^2 is most likely an effect of averaging variable spectra (in particular in the soft band, due to absorption variability), and of the not perfect cross-calibration between *XMM-Newton* and NuSTAR, which especially appears in the co-added spectrum. We also note that *XMM-Newton* and NuSTAR do not cover strictly simultaneous times, since the exposure time of the two satellites is slightly different (see Table 1).

We then replaced the cut-off power law with the Comptonization model COMPPS (Poutanen & Svensson 1996) in XSPEC. COMPPS models the thermal Comptonization emission of a plasma cooled by soft photons with a disk black-body distribution. We chose a spherical geometry (parameter GEOM = −4 in COMPPS) for the hot plasma and a temperature at the inner disk radius of 10 eV, fitting for the electron temperature $kT_{\rm e}$ and Compton parameter $y = 4\tau(kT_{\rm e}/m_{\rm e}c^2)$. The best-fit parameters are reported in Table 3 and the $kT_{\rm e} - y$ contour plot is shown in Fig. 11 (black contour). From the best-fit temperature $kT_{\rm e} = 40$ keV and parameter $y = 0.85$, we derive an optical depth $\tau = 2.7^{+0.7}_{-1.2}$, where we estimate the errors from the $kT_{\rm e} - y$ contour.

4. Discussion and conclusions

The broad-band coverage of the *XMM-Newton*, NuSTAR and INTEGRAL data allowed us to study the different components of the high-energy spectrum of NGC 5548 in detail.

First, we have been able to constrain the reflected component, which is consistent with being constant on a few months time scale, while the primary emission exhibits significant variability on a few days time scale. For example, the flux in the 2–10 keV band exhibits variations up to a factor of two over about 5 days during the campaign, with an outburst of several days duration in August-September (Mehdipour et al. 2015, see their Fig. 2). The lack of variability of the reflection component indicates that reflection is produced by cold and distant matter, lying at least a few light months away from the central X-ray source. This is consistent with the analysis of the Fe Kα line by Cappi et al. (in prep.) and with the absence of a significant contribution from relativistic reflection in this source (see, e.g.,

Table 3. Best-fit parameters of the average data set, using the realistic Comptonization model COMPPS for the continuum.

kT_e (keV)	y	K ($\times 10^7$)	$N_H^{(1)}$	$C_F^{(1)}$	$N_H^{(2)}$	$C_F^{(2)}$	χ^2/d.o.f.
40^{+40}_{-10}	$0.85^{+0.10}_{-0.5}$	$6.0^{+0.4}_{-0.3}$	0.99 ± 0.02	0.766 ± 0.003	9.6 ± 0.5	0.36 ± 0.01	3079/2627

Notes. The physical units are the same as in Table 2. The normalization is defined as $K = R_{\rm km}/D_{10\,\rm kpc}$ where $R_{\rm km}$ is the source radius in km and $D_{10\,\rm kpc}$ the distance in units of 10 kpc.

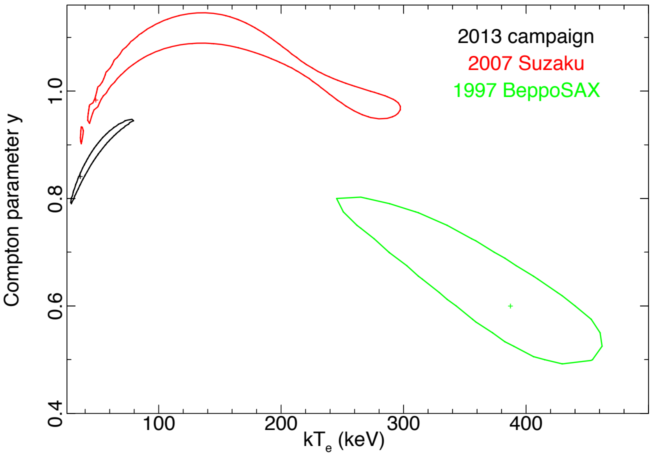

Fig. 11. $kT_e - y$ 90% confidence level contours for the spectra fitted with COMPPS, using spherical geometry. Black: average spectrum of the 2013 campaign; red: average spectrum of the seven *Suzaku* observations taken in 2007; green: *Beppo*SAX observation taken in 1997.

Brenneman et al. 2012). The lower limit of the reflector distance is consistent with this material being in the putative dusty torus, as the dust sublimation radius is estimated to be ~5 light months (Crenshaw et al. 2003). Furthermore, our results can be compared with past observations of the source. For this we focus on the 1997 *Beppo*SAX observation of NGC 5548 (Nicastro et al. 2000; Petrucci et al. 2000) and the average of seven *Suzaku* observations conducted in 2007 (Liu et al. 2010). In both cases, we re-fitted the archival data above 5 keV following the procedure described in Sect. 3.2. For the reflection component, we find that the spectral shape is always consistent with our best-fit parameters, i.e. a photon index of 1.9 and cut-off energy of 300 keV, while the reflected flux shows significant variations of about 50%. The primary flux (e.g., in the 2–10 keV band) shows similar variations, and we obtain a reflection fraction f consistent with that found during the 2013 campaign, i.e. $f \sim 0.3$, again calculated as the ratio between the illuminating and primary flux in the 20–40 keV range (see end of Sect. 3.2). Since f is consistent with being constant over a few years, the reflecting material should lie within a few light years from the primary X-ray source. In this case, the reflection fraction is indicative of the covering fraction of the reflector as seen from the X-ray source. From the definition of f, it follows that $f = \Omega/(4\pi - \Omega)$. According to our results, then, the solid angle covered by the reflecting material can be estimated as $\Omega \simeq \pi$, consistently with previous findings (e.g., Nandra & Pounds 1994; Pounds et al. 2003).

Then, we have been able to constrain the primary continuum and the effects of absorption. The primary continuum is well fitted by a power law with a photon index varying between ~1.5 and ~1.7, with at least a lower limit on the presence of a high-energy cut-off ($E_c > 50$ keV), which is usually considered a manifestation of Comptonization and is expected to be linked to the coronal temperature. The approximate relation between the temperature kT_e of an optically thick Comptonizing corona and the cut-off energy E_c is $kT_e = E_c/3$ (Petrucci et al. 2001). However, it should be noted that the cut-off of realistic Comptonization models is very different from an exponential cut-off. Moreover, the estimate of the temperature and of the optical depth also depends on the geometry assumed. In one case (obs. 6) we have obtained a measure of 70^{+40}_{-10} keV for the cut-off energy, which provides an estimate of 23^{+14}_{-3} keV for the coronal temperature, with the caveats we just mentioned. Moreover, our results suggest a statistically significant variation of both the photon index and the cut-off energy. For example, in the case of obs. 5 we find a lower limit of 180 keV for the cut-off energy. We can thus estimate the coronal temperature to be >60 keV for obs. 5 and <37 keV for obs. 6, both at 90% confidence level. Such a variation may be due to different reasons, like a variation of the disk-corona geometry. The coronal optical depth and temperature should follow a univocal relationship for a given heating/cooling ratio, i.e. the ratio of the power dissipated in the corona to the intercepted soft luminosity which cools the electrons via Comptonization (Haardt & Maraschi 1991; Haardt et al. 1994, 1997). If the coronal optical depth changes, due for instance to a change in the accretion rate, the temperature will change accordingly, to keep the heating/cooling ratio constant. But the heating/cooling ratio can also change, responding to a variation in the disk-corona geometry, like a variation of the inner disk radius or a velocity variation of a potentially outflowing corona (Malzac et al. 2001). Then, the coronal optical depth and temperature will change in a non-trivial way to be consistent with the new heating/cooling ratio. Owing to these complexities, fitting the data with a phenomenological cut-off power law does not allow for a unique interpretation. However, our findings motivate us to apply realistic Comptonization models to constrain the coronal parameters.

Concerning absorption, we needed to add two different partially covering components (only one in two cases out of seven). The obscurer component 1 has $N_H \sim 1 \times 10^{22}$ cm^{-2} and $C_F \sim 0.8$, while the obscurer component 2 has $N_H \sim 9 \times 10^{22}$ cm^{-2} and $C_F \sim 0.3$, consistently with the estimates of K14. Both show significant variability on a time-scale of a few days, indicating that the obscuring material varies along the line of sight. This relatively heavy obscuration was unexpected, since NGC 5548 is historically thought to be an archetypal unobscured Seyfert 1. The discussion reported in K14 ascribes this obscuration to a fast and massive outflow which may be interpreted as a disk wind.

Finally, we have made a first step towards a more physical description of the primary emission by replacing the simple cut-off power law with a thermal Comptonization model to fit the average spectrum. According to our analysis, the X-ray emitting corona has a mean temperature of 40^{+40}_{-10} keV and an optical depth of $2.7^{+0.7}_{-1.2}$, assuming a spherical geometry, during this campaign. We compared this result with past observations of NGC 5548 by re-fitting the 1997 *Beppo*SAX spectrum and the 2007 *Suzaku* average spectrum. We used the COMPPS model with spherical geometry (GEOM = −4) like we did in Sect. 3.4. The $kT_\mathrm{e} - y$ contours are shown in Fig. 11. We find that the temperature and the optical depth are not consistent, at 90% confidence level, between the different observations. According to this test, the average values of the coronal temperature and optical depth show a significant long-term variability, namely over 10–15 years, with a clear decrease of the coronal temperature from about 300–400 keV in 1997 down to 40–50 keV in 2013. The optical depth, on the other hand, increases from about 0.2–0.3 up to 2–3. Although the values quoted are specific to the assumed spherical geometry for the corona, the changes in temperature and optical depth are significant if one were to assume a different geometry for the corona. The corresponding variation of the Compton parameter y suggests a variation, of uncertain origin, of the coronal heating/cooling ratio between these different observations. The coronal parameters may be variable on shorter time scales as well, as suggested by the detected variations of the cut-off energy.

Comparing with the 1997 *Beppo*SAX observation and the 2007 *Suzaku* observations, the 2013 campaign provided us a broader energy range which, together with the high signal-to-noise ratio spectra, allows for much better constraints on the coronal parameters (as shown by the contours in Fig. 11). However, for the optimal study of Comptonization, UV spectra may give a significant contribution. For example, Petrucci et al. (2013) have been able to fit the UV and soft X-ray spectra of Mrk 509 with a Comptonization component interpreted as a "warm" corona above the disk. If this scenario is also valid for NGC 5548, we expect a correlation between the UV and soft X-ray emission. This correlation can only be detected after the variability of the obscurer is properly removed. The analysis of the UV and soft X-ray emission by Mehdipour et al. (in prep.) indeed suggests that such a correlation is present, and that it may be intrinsically similar to that of Mrk 509. This point, and a thorough test of realistic Comptonization models, will be the subject of a forthcoming paper.

Acknowledgements. We are grateful to the anonymous referee for his/her helpful comments, which have improved the manuscript. This work is based on observations obtained with: the NuSTAR mission, a project led by the California Institute of Technology, managed by the Jet Propulsion Laboratory and funded by NASA; INTEGRAL, an ESA project with instrument and science data center funded by ESA member states (especially the PI countries: Denmark, France, Germany, Italy, Switzerland, Spain), Czech Republic, and Poland and with the participation of Russia and the USA; *XMM-Newton*, an ESA science mission with instruments and contributions directly funded by ESA Member States and the USA (NASA). The data used in this research are stored in the public archives of the international space observatories involved. This research has made use of data, software and/or web tools obtained from NASA's High Energy Astrophysics Science Archive Research Center (HEASARC), a service of Goddard Space Flight Center and the Smithsonian Astrophysical Observatory. F.U., P.O.P., G.M., and S.B. acknowledge support from the French-Italian International Project of Scientific Collaboration: PICS-INAF project number 181542. F.U., P.O.P. acknowledge support from CNES. F.U. acknowledges support from Université Franco-Italienne (Vinci Ph.D. fellowship). F.U., G.M. acknowledges financial support from the Italian Space Agency under grant ASI/INAF I/037/12/0-011/13. G.A.K. was supported by NASA through grants for HST program number 13184 from the Space Telescope Science Institute, which is operated by the Association of Universities for Research in Astronomy, Incorporated, under NASA contract NAS5-26555. B.M.P. acknowledges support from the US NSF through grant AST-1008882. G.P. acknowledges support via an E.U. Marie Curie Intra-European fellowship under contract no. FP-PEOPLE-2012-IEF- 331095. K.C.S. acknowledges financial support from the Fondo Fortalecimiento de la Productividad Científica VRIDT 2013. We acknowledge support by ISSI in Bern; The Netherlands Organization for Scientific Research; the UK STFC; the French CNES, CNRS/PICS and CNRS/PNHE; the Swiss SNSF; the Italian INAF/PICS; the German Bundesministerium für Wirtschaft und Technologie/Deutsches Zentrum für Luft- und Raumfahrt (BMWI/DLR, FKZ 50 OR 1408); we acknowledge support from the Italian Space Agency under grants ASI-INAF I/037/12/P1 and ASI/INAF NuSTAR I/037/12/0.

References

Arav, N., Chamberlain, C., Kriss, G. A., et al. 2015, A&A, 577, A37 (Paper II)
Arnaud, K. A. 1996, in Astronomical Data Analysis Software and Systems V, eds. G. H. Jacoby, & J. Barnes, ASP Conf Ser., 101, 17
Ballantyne, D. R., Bollenbacher, J. M., Brenneman, L. W., et al. 2014, ApJ, 794, 62
Bianchi, S., Guainazzi, M., Matt, G., Fonseca Bonilla, N., & Ponti, G. 2009, A&A, 495, 421
Boissay, R., Paltani, S., Ponti, G., et al. 2014, A&A, 567, A44
Brenneman, L. W., Elvis, M., Krongold, Y., Liu, Y., & Mathur, S. 2012, ApJ, 744, 13
Brenneman, L. W., Madejski, G., Fuerst, F., et al. 2014, ApJ, 788, 61
Cerruti, M., Ponti, G., Boisson, C., et al. 2011, A&A, 535, A113
Chiang, J., Reynolds, C. S., Blaes, O. M., et al. 2000, ApJ, 528, 292
Courvoisier, T. J.-L., Walter, R., Beckmann, V., et al. 2003, A&A, 411, L53
Crenshaw, D. M., Kraemer, S. B., Gabel, J. R., et al. 2003, ApJ, 594, 116
Crummy, J., Fabian, A. C., Gallo, L., & Ross, R. R. 2006, MNRAS, 365, 1067
de Vaucouleurs, G., de Vaucouleurs, A., Corwin, Jr., H. G., et al. 1991, Third Reference Catalogue of Bright Galaxies, Vol. I: Explanations and references, Vol. II: Data for galaxies between 0h and 12h, Vol. III: Data for galaxies between 12h and 24h
Done, C., Davis, S. W., Jin, C., Blaes, O., & Ward, M. 2012, MNRAS, 420, 1848
George, I. M., & Fabian, A. C. 1991, MNRAS, 249, 352
Haardt, F., & Maraschi, L. 1991, ApJ, 380, L51
Haardt, F., Maraschi, L., & Ghisellini, G. 1994, ApJ, 432, L95
Haardt, F., Maraschi, L., & Ghisellini, G. 1997, ApJ, 476, 620
Harrison, F. A., Craig, W. W., Christensen, F. E., et al. 2013, ApJ, 770, 103
Kaastra, J. S., Petrucci, P.-O., Cappi, M., et al. 2011, A&A, 534, A36
Kaastra, J. S., Kriss, G. A., Cappi, M., et al. 2014, Science, 345, 64
Kirsch, M. G. F., Altieri, B., Chen, B., et al. 2004, in UV and Gamma-Ray Space Telescope Systems, eds. G. Hasinger, & M. J. L. Turner, SPIE Conf. Ser., 5488, 103
Liu, Y., Elvis, M., McHardy, I. M., et al. 2010, ApJ, 710, 1228
Magdziarz, P. & Zdziarski, A. A. 1995, MNRAS, 273, 837
Malizia, A., Molina, M., Bassani, L., et al. 2014, ApJ, 782, L25
Malzac, J., & Petrucci, P.-O. 2002, MNRAS, 336, 1209
Malzac, J., Beloborodov, A. M., & Poutanen, J. 2001, MNRAS, 326, 417
Marinucci, A., Matt, G., Kara, E., et al. 2014, MNRAS, 440, 2347
Matt, G., Marinucci, A., Guainazzi, M., et al. 2014, MNRAS, 439, 3016
Mehdipour, M., Branduardi-Raymont, G., Kaastra, J. S., et al. 2011, A&A, 534, A39
Mehdipour, M., Kaastra, J. S., Kriss, G. A., et al. 2015, A&A, 575, A22 (Paper I)
Nandra, K. & Pounds, K. A. 1994, MNRAS, 268, 405
Nandra, K., Pounds, K. A., Stewart, G. C., et al. 1991, MNRAS, 248, 760
Nandra, K., George, I. M., Mushotzky, R. F., Turner, T. J., & Yaqoob, T. 1997, ApJ, 477, 602
Nandra, K., O'Neill, P. M., George, I. M., & Reeves, J. N. 2007, MNRAS, 382, 194
Nicastro, F., Piro, L., De Rosa, A., et al. 2000, ApJ, 536, 718
Pancoast, A., Brewer, B. J., Treu, T., et al. 2014, MNRAS, 445, 3073
Perola, G. C., Matt, G., Cappi, M., et al. 2002, A&A, 389, 802
Peterson, B. M., Denney, K. D., De Rosa, G., et al. 2013, ApJ, 779, 109
Petrucci, P. O., Haardt, F., Maraschi, L., et al. 2000, ApJ, 540, 131
Petrucci, P. O., Haardt, F., Maraschi, L., et al. 2001, ApJ, 556, 716
Petrucci, P.-O., Paltani, S., Malzac, J., et al. 2013, A&A, 549, A73
Ponti, G., Papadakis, I., Bianchi, S., et al. 2012, A&A, 542, A83
Pounds, K. A., Reeves, J. N., Page, K. L., et al. 2003, MNRAS, 341, 953
Poutanen, J., & Svensson, R. 1996, ApJ, 470, 249
Reis, R. C., & Miller, J. M. 2013, ApJ, 769, L7
Reynolds, C. S. 1997, MNRAS, 286, 513
Sobolewska, M. A. & Papadakis, I. E. 2009, MNRAS, 399, 1597
Steenbrugge, K. C., Kaastra, J. S., Crenshaw, D. M., et al. 2005, A&A, 434, 569
Titarchuk, L. 1994, ApJ, 434, 570
Walton, D. J., Nardini, E., Fabian, A. C., Gallo, L. C., & Reis, R. C. 2012, MNRAS, 428, 2901
Walton, D. J., Fuerst, F., Harrison, F., et al. 2013, ApJ, 779, 148
Walton, D. J., Harrison, F. A., Grefenstette, B. W., et al. 2014, ApJ, 793, 21
Winkler, C., Courvoisier, T. J.-L., Di Cocco, G., et al. 2003, A&A, 411, L1
Yaqoob, T., George, I. M., Nandra, K., et al. 2001, ApJ, 546, 759

Chapter 5

The low-luminosity AGN in NGC 7213

Contents

The Seyfert galaxy NGC 7213 belongs to the class of low-luminosity AGNs (LLAGNs). *NuSTAR* observed this source in 2014, as part of the program on bright, nearby AGNs (PI: F. Harrison, at Caltech). I was in charge of this data analysis as a member of the *NuSTAR* Science Team. I note that *NuSTAR*, launched in June 2012, is the first telescope with focusing optics operating in hard X-rays, from 3 up to 79 keV (Harrison et al. 2013). Being 100 times more sensitive in the 10–79 keV band than older observatories, it yields high signal-to-noise ratio spectra that allow us to study the high-energy emission of AGNs in great detail.

5.1 NGC 7213: a low-luminosity, weakly variable, reflection-free AGN

LLAGNs are essentially faint AGNs, i.e. their bolometric luminosity is less than 10^{44} ergs s^{-1}. These objects thus show a weak nuclear activity compared with more luminous AGNs. However, their central engine is thought to be powered by the same process, namely accretion onto a supermassive black hole (for a review, see Ho 2008). Interestingly, the mass accretion rate of LLAGNs is generally found to be smaller than luminous AGNs. In terms of the Eddington ratio, LLAGNs usually have $L/L_{\rm Edd} < 10^{-2}$, while luminous AGNs have $L/L_{\rm Edd} \sim 0.1 - 1$ (e.g. Panessa et al. 2006; Kollmeier et al. 2006). Another characteristic of LLAGNs is their lack of a strong UV bump, which might be explained by the presence of a RIAF (see Sect. 1.2.3) instead of a standard Shakura-Sunyaev disc (e.g. Ho 2009; Yu et al. 2011).

NGC 7213 is a nearby ($z = 0.006$, Pereira-Santaella et al. 2010) LLAGN with a bolometric luminosity of 1.7×10^{43} ergs s^{-1} (Emmanoulopoulos et al. 2012), hosting a supermassive black hole with a mass of $\sim 10^8 M_\odot$ (Woo & Urry 2002). Its Eddington ratio is thus 1.4×10^{-3}. The optical spectrum shows broad emission lines similar to that of normal Seyfert 1s, i.e. with a full width at half maximum (FWHM) of a few thousand km/s (Phillips 1979), but the UV bump is weak or absent (Wu et al. 1983; Starling et al. 2005).

The X-ray spectrum of NGC 7213 is peculiar, as past observations with *XMM-Newton*, *BeppoSAX* and *Suzaku* show that it lacks a Compton hump (Bianchi et al. 2003; Lobban et al. 2010) although an iron K complex is clearly detected between 6.4 and 7 keV. In particular Bianchi et al. (2008), from the analysis of *Chandra* data, found three narrow Kα emission lines at 6.4, 6.7 and 6.966 keV, from neutral Fe, Fe XXV and Fe XXVI respectively. If there is no Compton hump, the Fe K lines cannot originate from Compton-thick material, such as the accretion disc or the torus. Indeed, Bianchi et al. (2008) argued in favour of an origin in the BLR, because the FWHM of the neutral Fe Kα line is consistent with that of the Hα line ($\sim$ 2600 km/s). Concerning the high-energy spectrum, past studies gave ambiguous results, as Bianchi et al. (2003) reported a high-energy cut-off at 95^{+75}_{-45} keV from *XMM-Newton* and *BeppoSAX* data, while Lobban et al. (2010) found only a lower limit of 350 keV from *Suzaku* and *Swift* data.

The X-ray variability time-scale of NGC 7213 is of several days or weeks, from *RXTE* data (Emmanoulopoulos et al. 2012). Moreover, Emmanoulopoulos et al. (2012) reported an anticorrelation between the X-ray photon index and the X-ray luminosity, namely a harder-when-brighter behaviour which is just the opposite of what is commonly found in luminous Seyferts (see Sect. 2.3).

5.2 X-ray spectroscopy of NGC 7213 with *NuSTAR*

NuSTAR observed NGC 7213 on 2014 October 5, with a net exposure of 109 ks. The spectral analysis of *NuSTAR* data is fully discussed in Ursini et al. (2015b), reported in the appendix of this chapter. Before summarizing the main results, I discuss technical issues of the *NuSTAR* data that I needed to resolve, and that are not fully explained in the paper[1].

5.2.1 Data reduction

We reduced the data following a standard procedure[2]. We used the standard pipeline in the NUSTARDAS software, using the latest calibration files available at that time. We extracted the spectra from the cleaned event files of the two detectors FPMA and FPMB using the standard tool NUPRODUCTS. The source data were extracted from circular regions (radius 75 arcsec; see Fig. 5.1), and background was extracted from a blank area on the same chip (initially, with a radius of 1 arcmin; see Fig. 5.1, green circles). Then,

---

[1] Substantial help was provided by A. Marinucci (Roma Tre), and by F. Fuerst and D. Walton (Caltech), from the *NuSTAR* Science Team.

[2] I worked on the data reduction with A. Marinucci.

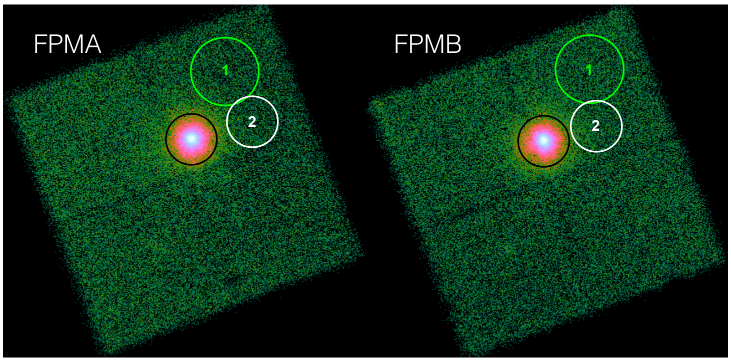

Figure 5.1 – *NuSTAR* event images from the observation of NGC 7213. The black circles enclose the source region. The green (no. 1) and white (no. 2) circles represent two different background regions used for the data reduction, the white circles being the final choice.

we tested the consistency between the two spectra from FPMA and FPMB. We thus fitted both the 3–80 keV spectra with a simple cut-off power law, without tying the model parameters. The results were only marginally consistent with each other: the photon indexes measured for FPMA and FPMB were $1.86^{+0.02}_{-0.04}$ and 1.78 ± 0.05 respectively, while the cut-off energies were > 140 keV and 100^{+90}_{-30} keV. Apparently, then, the FPMB spectrum showed a well constrained high-energy cut-off, whereas from the FPMA spectrum we only obtained a lower limit. We also analysed jointly the two spectra, namely using a model with tied parameters and only allowing for a free cross-calibration constant. In this case, we obtained a photon index of 1.83 ± 0.03 and a cut-off energy of 170^{+170}_{-60} keV. Given the not complete (even if statistically acceptable) agreement between FPMA and FPMB, the results of our preliminary spectral analysis could hardly be considered satisfactory. In particular, the measurement of the high-energy cut-off could be flawed.

Then, we extracted the spectra again, aiming at minimizing the discrepancy between FPMA and FPMB. We found that a different choice of the background region affected the spectral parameters of FPMB. Using a background somewhat smaller and closer to the source (radius 75 arcsec; see Fig. 5.1, white circles), we found that the two spectra were in better agreement. Indeed, the photon index of FPMB was 1.85 ± 0.05, with a lower limit on the cut-off energy of 150 keV. We thus decided to use this FPMB spectrum, which was more compatible with FPMA (i.e. the spectral parameters are in better agreement). There are two main reasons that led us to consider the FPMA results to be more reliable. First, the source in FPMB partially falls on a chip gap (see also Fig. 5.2, top panels), implying a slight loss in the signal-to-noise ratio. Second, the source in FPMA is closer to the optical axis, where the effective area is highest (Fig. 5.2, bottom panels).

5.2.2 Spectral analysis

The *NuSTAR* light curves of NGC 7213 (see Fig. 1 of Ursini et al. 2015b) show that there is not significant variability during the observation, since the total variation in the light curve is below 2 percent (as shown by a fit with a straight line). Therefore, I analysed the time-averaged spectrum.

I note that *Swift* generally performs a snapshot of 1-2 ks simultaneous with *NuSTAR* observations. In the case of NGC 7213, there was a 2 ks exposure with *Swift*/XRT (0.3–10 keV) but not with the UVOT monitor in the optical/UV band. The spectra are shown in Fig. 5.3. My final choice was to avoid using the XRT spectrum, because it was inconsistent with *NuSTAR*. I found that, allowing for a free cross-calibration between the detectors, the normalization factor for XRT with respect to *NuSTAR*/FPMA and FPMB was around 0.6. Moreover, the XRT data add no useful information at low energies, since

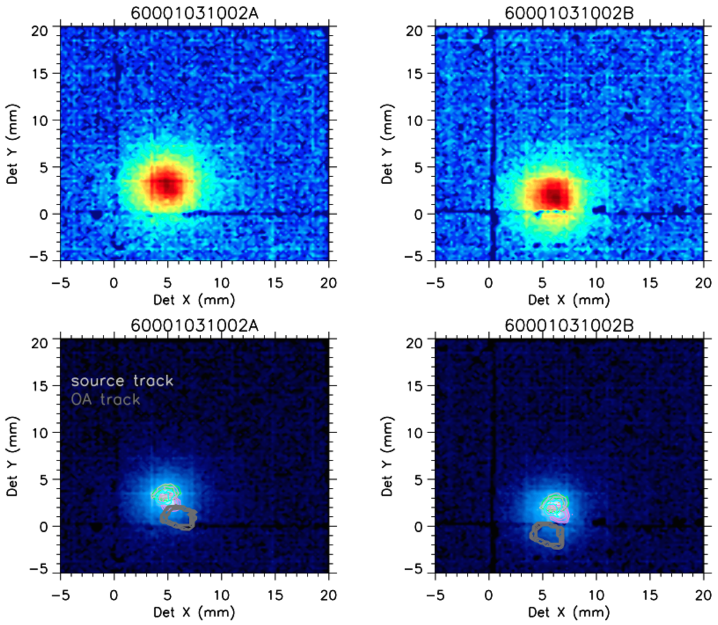

Figure 5.2 – *NuSTAR* sky images for FPMA (left panels) and FPMB (right panels). The top panels show the position of the source on the detectors. The bottom panels also show the position of the optical axis.

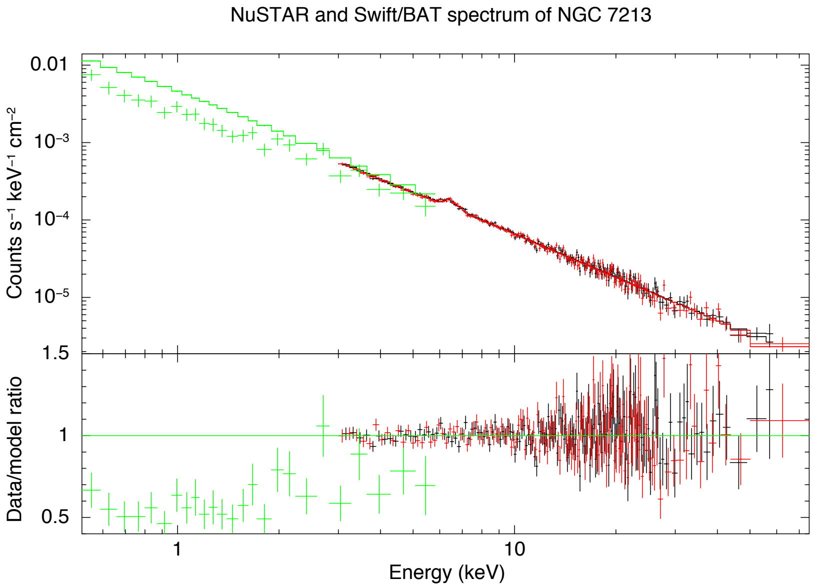

Figure 5.3 – The *NuSTAR*/FPMA (black) and FPMB (red) spectra of NGC 7213, fitted with a power law plus three narrow Gaussian lines, and plotted together with the spectrum from the *Swift*/XRT snapshot (green).

they show no signatures either of a soft excess or of absorption.

A simple model including a cut-off power law and three narrow Gaussian lines for the Fe K complex provides a good fit to the data (see Table 1 of Ursini et al. 2015b). My main findings, discussed in the following, are: (i) a lower limit on the high-energy cut-off of 140 keV, (ii) the lack of a strong reflection component, and (iii) the indication of a very high coronal temperature.

To check for the presence of a reflection component, I used two different models. First, I included neutral Compton reflection with the PEXRAV model in XSPEC. However, the reflection fraction is consistent with zero, with an upper limit of 0.13 (see Fig. 4 of Ursini et al. 2015b). Then, I used MYTORUS (Murphy & Yaqoob 2009) in XSPEC. This model includes Compton reflection and iron fluorescent lines from a gas torus with an opening angle of 60 deg, where the column density is a free parameter (whereas it is

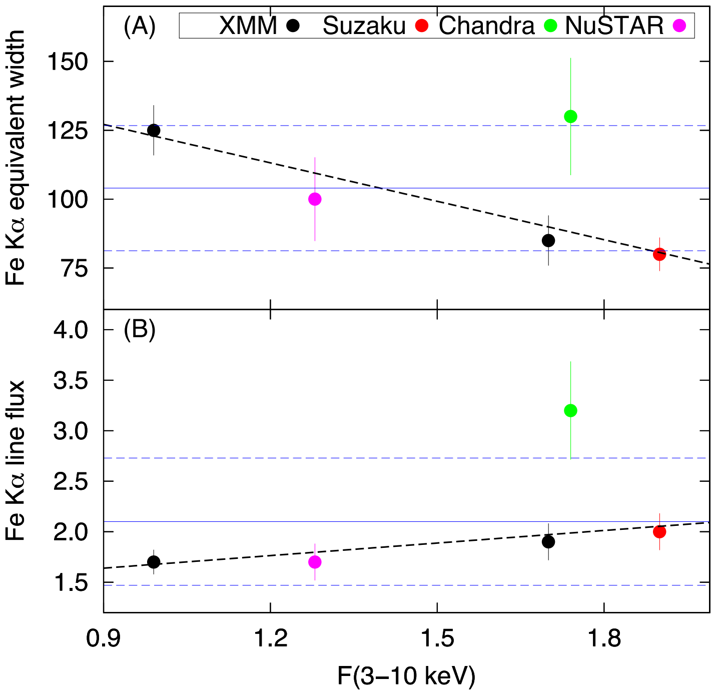

Figure 5.4 – The neutral Fe Kα line parameters versus the 3–10 keV primary flux, for *NuSTAR* and four archival observations. Panel (A): Fe Kα equivalent width in eV. Panel (B): Fe Kα line flux in units of 10^{-5} photons cm^{-2} s^{-1}. Error bars denote the 1-σ uncertainty. The blue solid lines represent the mean value for each parameter, while the blue dashed lines correspond to the standard deviation. The black dashed lines represent linear fits to the data. The anticorrelation between equivalent width and primary flux is not significant: the Spearman's rank correlation coefficient is -0.4 with a p value of 0.42. See also Fig. 6 of Ursini et al. (2015b).

infinite in models like PEXRAV). I used the standard MYTORUS configuration ("coupled" reprocessor; see, e.g., Yaqoob 2012), i.e. the normalizations of the scattered and line components were tied to the normalization of the primary power law. This corresponds to a covering fraction of 0.5. The column densities of the scattered and line components were linked and free to vary. This common column density $N_{\rm H}$ is the main parameter determining the spectral shape of MYTORUS: a large column density means a significant Compton hump, while a column density below 10^{24} cm^{-2} can give significant emission lines but a weak hump. Indeed, I found $N_{\rm H} = 5.0^{+2.0}_{-1.6} \times 10^{23}$ cm^{-2}.

Then, I tested a Comptonization model for the continuum. I replaced the phenomenological power law with the COMPPS model in XSPEC. Setting a spherical geometry, I found a temperature of 295^{+70}_{-250} keV and a Compton parameter $y = 0.52^{+0.24}_{-0.10}$ (the contour plots are shown in Fig. 5 of Ursini et al. 2015b), with an optical depth $\tau = 0.2^{+0.7}_{-0.1}$. Analogous results are found setting a slab geometry, although the Compton parameter and the optical depth are a factor of 2 smaller (due to the different definition of τ, which is the vertical optical depth for a slab and the radial one for a sphere).

Finally, to try to further constrain the origin of the Fe Kα lines, I analysed their time evolution using archival data from *XMM-Newton* (two observations in 2001 and 2009), *Suzaku* (one observation in 2006) and *Chandra* (one observation in 2007)[3]. No clear behaviour is observed: the flux of the neutral Fe Kα line shows a significant variation only during the *Chandra*/HEG observation of 2007, while the equivalent width shows a hint of an anticorrelation with the primary continuum (see Fig. 5.4, and Fig. 6 of Ursini et al. 2015b).

---

[3] The fits of the archival spectra in the 3–10 keV band were performed by A. Tortosa, using the baseline model of Ursini et al. (2015b).

5.3 Conclusions

The analysis of the high-quality *NuSTAR* spectrum of the LLAGN NGC 7213 yields interesting results.

First, I confirm the presence of a Fe K complex not related to a Compton hump. This makes NGC 7213 one of the few AGNs not showing Compton reflection from circumnuclear material, despite the strong Fe K emission (together with NGC 2110, see Marinucci et al. 2015). According to the spectral analysis, the line-emitting material has a column density of a few $\times 10^{23}$ cm^{-2}, which is consistent with an origin in the BLR (Bianchi et al. 2008). However, it is still possible that the lines originate from more distant, dust-rich material, because the presence of dust can reduce the backscattering opacity and hence the reflected continuum (Gohil & Ballantyne 2015).

I find only a lower limit on the presence of a high-energy exponential cut-off. Consistent with this, by fitting the data with a physical Comptonization model, I find indications that the coronal temperature is high ($>$ 40 keV, with a best-fitting value around 300 keV). This is not unexpected, given the low luminosity and the lack of a strong UV bump in this source. Indeed, if the X-ray emission is due to thermal Comptonization, a high coronal temperature is expected when the soft photon input radiation is weak, because inverse Compton scattering is inefficient in cooling the corona. Moreover, in Ursini et al. (2015b) I estimate the accretion rate to be $\sim$ 0.1 per cent of the Eddington limit, i.e. close to the value of 0.14 per cent reported by Emmanoulopoulos et al. (2012). This accretion rate is lower than the typical value for luminous AGNs, and is in agreement with the theoretical predictions of the RIAF models (Narayan et al. 1998; Ho 2009). Therefore, we may suggest that the source accretes via a RIAF, at least in the inner region (e.g. below 100 R_G). The lack of a strong Compton hump nicely agrees with this scenario, because RIAFs are optically thin (see Sect. 1.2.3).

Alternatively, the corona could be outflowing rather than being static (Beloborodov 1999; Malzac et al. 2001; Merloni & Fabian 2002). The lack of a UV bump would then be explained if the corona is energetically dominant over the standard accretion disc, and the lack of reflection would be due to the beaming effect. For example, the corona could form the base of a radio jet. Indeed, although NGC 7213 is not a radio-loud object, its radio and X-ray emissions are weakly correlated with each other (Bell et al. 2011).

In the Comptonization framework, we may expect that high coronal temperatures generally correspond to low accretion rates in AGNs. So far, two other weakly accreting AGNs have been observed by *NuSTAR*, namely NGC 5506 (Matt et al. 2015) and NGC 2110 (Marinucci et al. 2015), both having an estimated Eddington ratio of a few percent. Interestingly, Matt et al. (2015) and Marinucci et al. (2015) found lower limits on the high-energy cut-off of $\sim$ 500 keV for NGC 5506 and 210 keV for NGC 2110, respectively. These results are promising and motivate further studies on a greater number of sources.

Appendix

The *NuSTAR* spectrum of the low-luminosity active galactic nucleus in NGC 7213

F. Ursini[1,2,3], A. Marinucci[3], G. Matt[3], S. Bianchi[3], A. Tortosa[3], D. Stern[4], P. Arévalo[5], D. R. Ballantyne[6], F. E. Bauer[7,8,9], A. C. Fabian[10], F. A. Harrison[11], A. M. Lohfink[10], C. S. Reynolds[12,13], and D. J. Walton[14,4]

[1] Univ. Grenoble Alpes, IPAG, F-38000 Grenoble, France.
[2] CNRS, IPAG, F-38000 Grenoble, France.
[3] Dipartimento di Matematica e Fisica, Università degli Studi Roma Tre, via della Vasca Navale 84, 00146 Roma, Italy.
[4] Jet Propulsion Laboratory, California Institute of Technology, 4800 Oak Grove Drive, Mail Stop 169-221, Pasadena, CA 91109, USA.
[5] Instituto de Física y Astronomía, Facultad de Ciencias, Universidad de Valparaíso, Gran Bretana N. 1111, Playa Ancha, Valparaíso, Chile.
[6] Center for Relativistic Astrophysics, School of Physics, Georgia Institute of Technology, Atlanta, GA 30332, USA.
[7] Instituto de Astrofísica, Facultad de Física, Pontificia Universidad Católica de Chile, Casilla 306, Santiago 22, Chile.
[8] Millennium Institute of Astrophysics, Vicuña Mackenna 4860, 7820436 Macul, Santiago, Chile.
[9] Space Science Institute, 4750 Walnut Street, Suite 205, Boulder, CO 80301, USA.
[10] Institute of Astronomy, University of Cambridge, Madingley Road, Cambridge CB3 0HA, UK.
[11] Cahill Center for Astronomy and Astrophysics, California Institute of Technology, Pasadena, CA 91125, USA.
[12] Department of Astronomy, University of Maryland, College Park, MD 20742-2421, USA.
[13] Joint Space-Science Institute (JSI), College Park, MD 20742- 2421, USA.
[14] Cahill Center for Astronomy and Astrophysics, California Institute of Technology, Pasadena, CA 91125, USA.

Published in *Monthly Notices of the Royal Astronomical Society*, 452, 3266 (2015)

Monthly Notices
of the
ROYAL ASTRONOMICAL SOCIETY

MNRAS **452,** 3266–3272 (2015) doi:10.1093/mnras/stv1527

The *NuSTAR* X-ray spectrum of the low-luminosity active galactic nucleus in NGC 7213

F. Ursini,[1,2,3]⋆ A. Marinucci,[3] G. Matt,[3] S. Bianchi,[3] A. Tortosa,[3] D. Stern,[4]
P. Arévalo,[5] D. R. Ballantyne,[6] F. E. Bauer,[7,8,9] A. C. Fabian,[10] F. A. Harrison,[11]
A. M. Lohfink,[10] C. S. Reynolds[12,13] and D. J. Walton[4,14]

[1] *Univ. Grenoble Alpes, IPAG, F-38000 Grenoble, France*
[2] *CNRS, IPAG, F-38000 Grenoble, France*
[3] *Dipartimento di Matematica e Fisica, Università degli Studi Roma Tre, via della Vasca Navale 84, I-00146 Roma, Italy*
[4] *Jet Propulsion Laboratory, California Institute of Technology, 4800 Oak Grove Drive, Mail Stop 169-221, Pasadena, CA 91109, USA*
[5] *Instituto de Física y Astronomía, Facultad de Ciencias, Universidad de Valparaíso, Gran Bretaña 1111, Playa Ancha, 2360102 Valparaíso, Chile.*
[6] *Center for Relativistic Astrophysics, School of Physics, Georgia Institute of Technology, Atlanta, GA 30332, USA*
[7] *Instituto de Astrofísica, Facultad de Física, Pontificia Universidad Católica de Chile, Casilla 306, Santiago 22, Chile.*
[8] *Millennium Institute of Astrophysics, Vicuña Mackenna 4860, 7820436 Macul, Santiago, Chile*
[9] *Space Science Institute, 4750 Walnut Street, Suite 205, Boulder, CO 80301, USA.*
[10] *Institute of Astronomy, University of Cambridge, Madingley Road, Cambridge CB3 0HA, UK*
[11] *Cahill Center for Astronomy and Astrophysics, California Institute of Technology, Pasadena, CA 91125, USA.*
[12] *Department of Astronomy, University of Maryland, College Park, MD 20742-2421, USA*
[13] *Joint Space-Science Institute (JSI), College Park, MD 20742-2421, USA*
[14] *Cahill Center for Astronomy and Astrophysics, California Institute of Technology, Pasadena, CA 91125, USA*

Accepted 2015 July 7. Received 2015 May 27; in original form 2015 April 17

ABSTRACT

We present an analysis of the 3–79 keV *NuSTAR* spectrum of the low-luminosity active galactic nucleus NGC 7213. In agreement with past observations, we find a lower limit to the high-energy cut-off of $E_c > 140$ keV, no evidence for a Compton-reflected continuum and the presence of an iron K α complex, possibly produced in the broad-line region. From the application of the MYTORUS model, we find that the line-emitting material is consistent with the absence of a significant Compton reflection if arising from a Compton-thin torus of gas with a column density of $5.0^{+2.0}_{-1.6} \times 10^{23}$ cm^{-2}. We report variability of the equivalent width of the iron lines on the time-scale of years using archival observations from *XMM–Newton*, *Chandra* and *Suzaku*. This analysis suggests a possible contribution from dusty gas. A fit with a Comptonization model indicates the presence of a hot corona with a temperature $kT_e > 40$ keV and an optical depth $\tau \lesssim 1$, assuming a spherical geometry.

Key words: galaxies: active – galaxies: individual: NGC 7213 – galaxies: Seyfert – X-rays: galaxies.

1 INTRODUCTION

The central engine of low-luminosity active galactic nuclei (LLAGNs) is thought to be powered by accretion of surrounding matter on to a supermassive black hole, similar to more powerful AGNs, like Seyfert galaxies and quasars (see Ho 2008, for a review). The X-ray spectrum of AGNs is generally dominated by a primary power-law component, which is thought to be produced by Comptonization of optical/UV photons emitted by the underlying accretion disc in a hot plasma, the so-called corona (see e.g. Haardt & Maraschi 1991; Haardt, Maraschi & Ghisellini 1994, 1997). A signature of this process is the presence of a high-energy cut-off in the X-ray emission, which has been observed in a number of sources (see e.g. Perola et al. 2002; Malizia et al. 2014; Brenneman et al. 2014; Ballantyne et al. 2014; Marinucci et al. 2014; Baloković et al. 2015; Ursini et al. 2015).

The distinctive characteristic of LLAGNs is their intrinsic faintness ($L_{\mathrm{bol}} < 10^{44}$ erg s^{-1}). Moreover, the mass accretion rate of LLAGNs is generally small; in terms of the Eddington ratio, most of them have $L/L_{\mathrm{Edd}} < 10^{-2}$ while luminous AGNs have $L/L_{\mathrm{Edd}} \sim 0.01$–1 (see e.g. Panessa et al. 2006; Kollmeier et al. 2006). Whether LLAGNs are simply a scaled-down version of classical AGNs is a matter of debate. A standard geometrically thin, optically thick accretion disc (Shakura & Sunyaev 1973) may power LLAGNs (Maoz 2007), as is commonly assumed for

---

⋆ E-mail: francesco.ursini@obs.ujf-grenoble.fr

Published by Oxford University Press on behalf of the Royal Astronomical Society

luminous AGNs. However, radiative-inefficient accretion flows (RIAFs; see e.g. Narayan & Yi 1994) have been proposed to explain some observational properties, in particular their lack of a UV bump (see e.g. Ho 2009; Yu, Yuan & Ho 2011). Furthermore, in luminous AGNs the hard X-ray photon index and the Eddington ratio are positively correlated (see e.g. Sobolewska & Papadakis 2009), while an anticorrelation is found in LLAGNs (Gu & Cao 2009). This result is consistent with the X-ray emission of LLAGNs originating from Comptonization in RIAFs, and it suggests a similarity between LLAGNs and black hole X-ray binaries (BHXRBs) in the low/hard state, where the accretion rate is low (Wu & Gu 2008). The low accretion rate might not only affect the structure of the inner accretion flow, but also that of the putative obscuring torus. The torus is predicted to disappear in low-luminosity sources by models depicting it as a clumpy wind, arising from the outer accretion disc (see e.g. Elitzur & Shlosman 2006, and references therein), or as a collection of many self-gravitating, dusty molecular clouds (see e.g. Hönig & Beckert 2007).

NGC 7213 is a nearby ($z = 0.005\,839$, as given in the NASA/IPAC Extragalactic Database; distance 25.80 Mpc; Pereira-Santaella et al. 2010) LLAGN with $L_{\rm bol} = 1.7 \times 10^{43}$ erg s^{-1} (Emmanoulopoulos et al. 2012) that hosts a supermassive black hole of $\sim 10^8$ solar masses (estimated from the stellar velocity dispersion, see Woo & Urry 2002), yielding an Eddington ratio of 1.4×10^{-3}. It has been historically classified as a Seyfert 1 because its optical spectrum shows broad emission lines, i.e. with a full width at half-maximum (FWHM) of a few thousand km s^{-1} (Phillips 1979). However, it has also been classified as a low-ionization nuclear emission region galaxy (LINER) because of the low excitation observed in the narrow-line spectrum (Filippenko & Halpern 1984). Low-ionization lines were also detected in the soft X-ray band (Starling et al. 2005). Wu, Boggess & Gull (1983) measured a UV flux higher than the extrapolated optical flux, thus indicating a possible UV bump, but it is still weaker than in most Seyfert galaxies. More recently, Starling et al. (2005) found no evidence for an optical/UV bump using *XMM–Newton*/OM data.

The X-ray spectrum of NGC 7213 shows peculiarities as well. The Compton reflection component is found to be weak or absent with *XMM–Newton*, *BeppoSAX* and *Suzaku* observations (see e.g. Bianchi et al. 2003; Lobban et al. 2010), in contrast to what is commonly observed in Seyfert 1 galaxies. This may suggest that the accretion disc is truncated in the inner region, perhaps replaced by a Compton-thin RIAF (Lobban et al. 2010). An iron line complex is clearly detected between 6.4 and 7 keV, consisting of three narrow K α emission lines respectively from neutral Fe, Fe XXV and Fe XXVI (see e.g. the analysis of *Chandra* data by Bianchi et al. 2008). Given the lack of an observed Compton reflection hump, such lines cannot originate from Compton-thick material, like the accretion disc or a parsec-scale torus. Bianchi et al. (2008) found the FWHM of the neutral Fe K α line to be consistent with that of the H α line ($\sim$2600 km s^{-1}), thus suggesting a common origin in the broad-line region (BLR). Another possibility is reprocessed emission from dusty gas, which can produce strong, neutral Fe K α emission with a weak associated continuum (Gohil & Ballantyne 2015). Emmanoulopoulos et al. (2012) found an anticorrelation between the X-ray photon index and the X-ray luminosity that, together with the low accretion rate of the source, indicates a spectral behaviour similar to that of BHXRBs in the hard state. Finally, Bianchi et al. (2003) reported a high-energy cut-off of 95^{+75}_{-45} keV using *XMM–Newton*+*BeppoSAX* data, while Lobban et al. (2010) found a lower limit of 350 keV using *Suzaku*/XIS+PIN and *Swift*/BAT data.

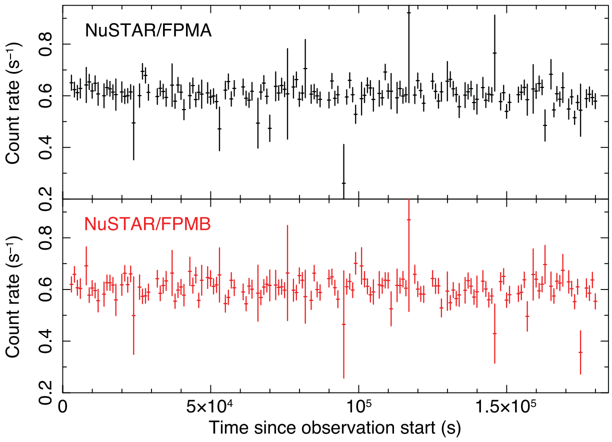

Figure 1. The *NuSTAR*/FPMA and FPMB 3–79 keV light curve. Bins of 1000 s are used.

In this paper, we report on a *NuSTAR* observation of NGC 7213 performed in 2014 October. The primary focus of this work is modelling the broad-band X-ray spectrum of the source and constraining the origin of the X-ray emission. In Section 2, we describe the observations and data reduction. In Section 3, we present the analysis of the 3–79 keV spectrum, fitted with both a phenomenological and a realistic Comptonization model, and we study the time evolution of the iron line complex by analysing archival *XMM–Newton*, *Chandra* and *Suzaku* data. In Section 4, we discuss the results and summarize our conclusions.

2 OBSERVATIONS AND DATA REDUCTION

NuSTAR (Harrison et al. 2013) observed NGC 7213 starting on 2014 October 5, with a net exposure of 109 ks (Obs. Id. 60001031002). The *NuSTAR* data were reduced with the standard pipeline (NUPIPELINE) in the *NuSTAR* Data Analysis Software (NUSTARDAS, v1.3.1; part of the HEASOFT distribution as of version 6.14), using calibration files from *NuSTAR* CALDB v20141107. Spectra and light curves were extracted from the cleaned event files using the standard tool NUPRODUCTS for each of the two hard X-ray telescopes aboard *NuSTAR*, which have corresponding focal plane modules A and B (FPMA and FPMB). The spectra from FPMA and FPMB are analysed jointly, but are not combined, allowing for a free cross-calibration constant. The source data were extracted from circular regions (radius 75 arcsec), and background was extracted from a blank area close to the source. Finally, the spectra were binned to have a signal-to-noise ratio greater than 3 in each spectral channel, and not to oversample the instrumental resolution by a factor greater than 2.5.

In Fig. 1, we show the *NuSTAR*/FPMA and FPMB light curves obtained in the 3–79 keV energy range. The total variation in the light curve is of the order of a few per cent. Therefore, in the following we analyse the time-averaged spectrum of the source.

3 SPECTRAL ANALYSIS

Spectral analysis and model fitting was carried out with the XSPEC 12.8 package (Arnaud 1996), using the χ^2 minimization technique throughout. In this work, the errors are quoted at the 90 per cent confidence level, if not stated otherwise.

Table 1. Best-fitting parameters of the baseline model including a primary cut-off power law and three Gaussian lines (line 1 at 6.4 keV, line 2 at 6.7 keV, line 3 at 6.966 keV).

Γ	1.84 ± 0.03
E_c (keV)	>140
$F_{3\text{–}10\,\mathrm{keV}}$ (10^{-11} erg cm^{-2} s^{-1})	1.3 ± 0.1
EW$_1$ (eV)	98^{+30}_{-20}
F_1 (10^{-5} ph cm^{-2} s^{-1})	$1.7^{+0.3}_{-0.4}$
EW$_2$ (eV)	29^{+24}_{-18}
F_2 (10^{-5} ph cm^{-2} s^{-1})	$0.5^{+0.5}_{-0.3}$
EW$_3$ (eV)	42 ± 20
F_3 (10^{-5} ph cm^{-2} s^{-1})	0.6 ± 0.3
χ^2/d.o.f.	375/366

3.1 The *NuSTAR* spectrum

As a first step, we define a phenomenological model, which we describe below. We fit the *NuSTAR* data in the 3–79 keV range, allowing for a free cross-calibration constant between the modules FPMA and FPMB. The two modules are in good agreement, with a cross-calibration factor $K_{A-B} = 0.99 \pm 0.01$ fixing the constant for the FPMA data to unity.

We modelled the continuum with a cut-off power law, modified by neutral absorption (PHABS model in XSPEC) from Galactic hydrogen with column density $N_{\mathrm{H}} = 2.04 \times 10^{20}$ cm^{-2} (Dickey & Lockman 1990). This simple model yields a poor fit (reduced $\chi^2 = 556/369$), with positive residuals between 6 and 7 keV, which can be attributed to the known Fe complex between 6.4 and 7 keV (Bianchi et al. 2003, 2008). Bianchi et al. (2008) found three emission lines in the *Chandra*/HEG spectrum, at 6.4, 6.7 and 6.966 keV. These lines are interpreted as emission from neutral Fe, Fe XXV and Fe XXVI, respectively. *Chandra*/HEG data provide much higher energy resolution near the Fe complex compared with *NuSTAR*. We thus followed the analysis of Bianchi et al. (2008) and tested for the presence of three narrow Gaussian lines fixing their energies at 6.4, 6.7 and 6.966 keV, leaving the normalizations free to vary. The inclusion of a narrow Gaussian line at 6.4 keV yields a significantly improved fit (reduced $\chi^2 = 417/368$). Adding a second line at 6.7 keV further improves the fit (reduced $\chi^2 = 388/367$), with a probability of chance improvement less than 4×10^{-7} according to the *F*-test. The inclusion of a third line at 6.966 keV yields a good fit (reduced $\chi^2 = 375/367$), without prominent residuals and a probability of chance improvement less than 5×10^{-4} according to the *F*-test.

We report the results of this fit in Table 1, and in Fig. 2 we show the contour plots of the cut-off energy versus photon index. In Fig. 3, we show the data, residuals and best-fitting model. To further test the presence of a high-energy cut-off, we included the 70-month average *Swift*/BAT spectrum (Baumgartner et al. 2013); however, the results are essentially unchanged.

We tested for the presence of a reflection continuum by including the PEXRAV model in XSPEC, which describes neutral Compton reflection of infinite column density in a slab geometry (Magdziarz & Zdziarski 1995). This model is adequate for reflection off a standard accretion disc, given the high column densities expected for these structures (see e.g. Svensson & Zdziarski 1994). We fixed the inclination angle of the reflector to 30 deg, appropriate for a type 1 source (e.g. Nandra et al. 1997). The photon index and cut-off energy of the incident spectrum were tied to those of the primary power law. However, no improvement is found, with only an upper limit to the reflection fraction $\mathcal{R}$ of 0.13, at 90 per cent confidence level. In Fig. 4, we show the contour plots of $\mathcal{R}$ versus photon index. This is consistent with the iron lines originating from Compton-thin material ($N_{\mathrm{H}} = 10\text{–}10^{23}$ cm^{-2}), which does not produce a prominent Compton reflection hump (Bianchi et al. 2003). To test this result further, we replaced the PEXRAV component and the neutral Fe K α line with the MYTORUS model, which includes Compton reflection and iron fluorescent lines from a gas torus with an opening angle of 60 deg (Murphy & Yaqoob 2009). The inclination angle of the torus was fixed at 30 deg. The column densities of the scattered and line components were linked and free to vary. The normalizations of the scattered and line components were tied to the normalization of the primary power law, i.e. the standard MYTORUS configuration ('coupled' reprocessor; see e.g. Yaqoob 2012). The assumed geometry corresponds to a covering fraction

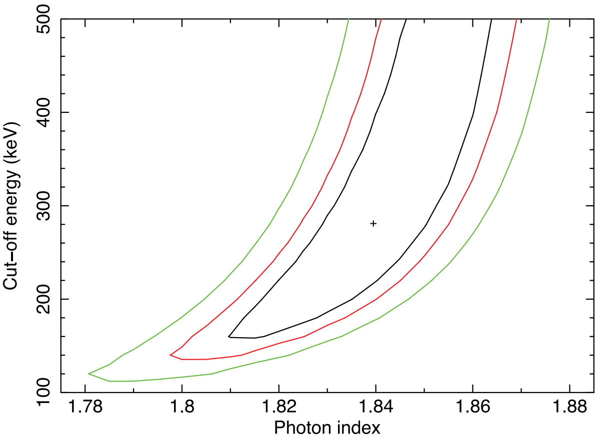

Figure 2. Primary continuum cut-off energy versus photon index contours. Solid green, red and black lines correspond to 99, 90 and 68 per cent confidence levels, respectively.

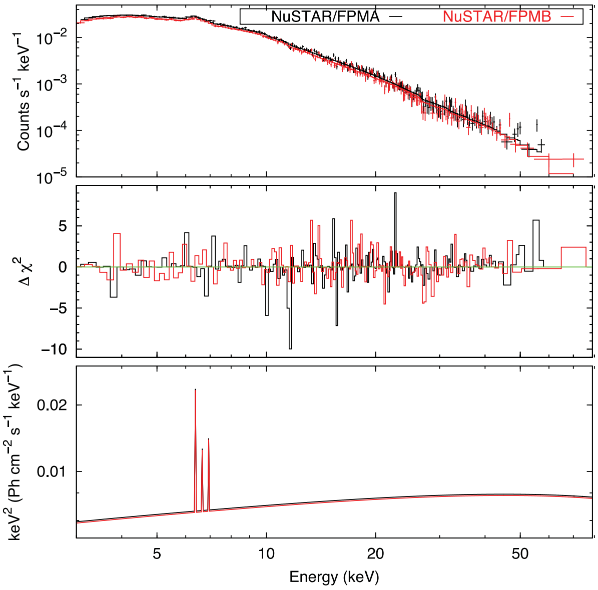

Figure 3. The *NuSTAR* spectrum and baseline model (see Table 1). Upper panel: *NuSTAR* data and folded model. Middle panel: contribution to χ^2. Lower panel: best-fitting model $E^2 f(E)$ with the plot of the additive components, namely the cut-off power law and the three Fe K α lines.

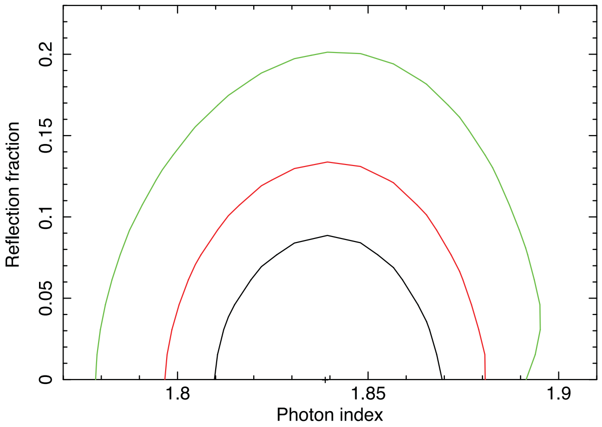

Figure 4. pexrav reflection fraction versus photon index contours. Solid green, red and black lines correspond to 99, 90 and 68 per cent confidence levels, respectively.

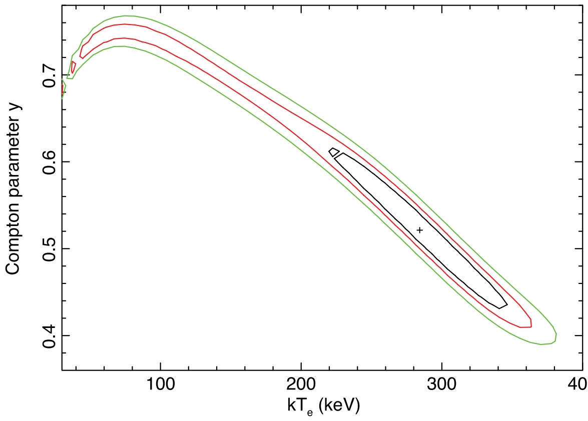

Figure 5. compps Compton parameter versus temperature contours. Solid green, red and black lines correspond to 99, 90 and 68 per cent confidence levels, respectively.

of 0.5. We obtain a good fit (reduced $\chi^2 = 373/363$) and we find a column density of $5.0^{+2.0}_{-1.6} \times 10^{23}$ cm^{-2}. This result is consistent with the estimate of $\sim 3 \times 10^{23}$ cm^{-2} for the Fe K α line-emitting material reported in Bianchi et al. (2008).

We next replaced the cut-off power law with the Comptonization model compps (Poutanen & Svensson 1996) in xspec. compps models the thermal Comptonization emission of a hot plasma cooled by soft photons with a disc blackbody distribution. We set a spherical geometry (parameter geom $= -4$ in compps) for the hot plasma and a temperature at the inner disc radius of 10 eV, fitting for the electron temperature kT_e and Compton parameter $y = 4\tau(kT_\mathrm{e}/m_\mathrm{e}c^2)$. The model yields a good fit (reduced $\chi^2 = 375/366$) with best-fitting parameters $kT_\mathrm{e} = 295^{+70}_{-250}$ keV and $y = 0.52^{+0.34}_{-0.10}$, which imply an optical depth $\tau = 0.2^{+0.7}_{-0.1}$. In Fig. 5, we show the kT_e–y contour plots.

3.2 Time evolution of the Fe K α line

To try to understand the origin of the Fe K α lines, we compared our results with past observations of NGC 7213 by re-analysing the archival *XMM–Newton* (2001, 2009), *Chandra* (2007) and *Suzaku* (2006) data. We fitted the 3–10 keV data sets with the baseline model described in Section 3.1, i.e. including a cut-off power law and three narrow Gaussian lines. The best-fitting parameters are consistent with those reported in Bianchi et al. (2003, 2008) and Lobban et al. (2010).

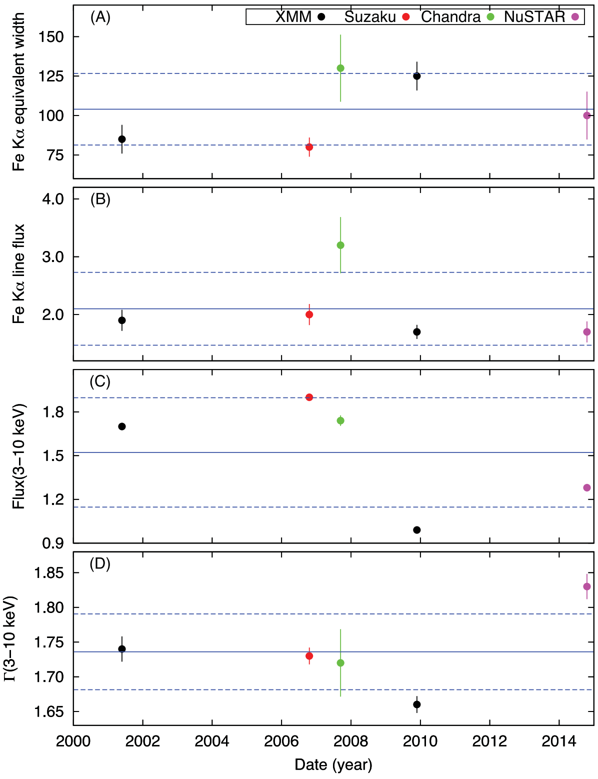

Figure 6. Time evolution of Fe K α line parameters and 3–10 keV primary flux and photon index. Panel (A): Fe K α equivalent width in eV units. Panel (B): Fe K α line flux in units of 10^{-5} photons cm^{-2} s^{-1}. Panel (C): continuum 3–10 keV flux in units of 10^{-11} erg cm^{-2} s^{-1}. Panel (D): 3–10 keV photon index. Error bars denote the 1σ uncertainty. The blue solid lines represent the mean value for each parameter, while the blue dashed lines correspond to the standard deviation.

In Fig. 6, we show the time evolution of the neutral Fe K α line EW and flux, and of the 3–10 keV continuum flux and photon index. The continuum flux variations reach up to a factor of 2, while the line flux varies at the 1σ confidence level only during the *Chandra*/HEG observation of 2007. The line EW, on the other hand, exhibits significant variations up to a factor of 1.7. The data show a hint of an anticorrelation between the continuum flux and the line EW, though we cannot formally establish a significant relation. The Spearman rank correlation coefficient is -0.4, but the test returns a *P* value of 0.42, implying that the null hypothesis is not rejected. Similar results hold for the Fe XXV and Fe XXVI lines, albeit with larger uncertainties on their parameters.

4 DISCUSSION AND CONCLUSIONS

We reported results based on a *NuSTAR* observation of the LLAGN/LINER NGC 7213. We derived constraints on the parameters describing the high-energy (3–79 keV) spectrum, and studied variability over a few year time-scale comparing our results with archival observations of the source.

We have been able to constrain the reflection component, finding no evidence for a significant Compton reflection continuum.

This is consistent with previous results (e.g. Bianchi et al. 2003; Lobban et al. 2010; Emmanoulopoulos et al. 2013). We note that the constraints on the reflection component are derived assuming a static X-ray source (Magdziarz & Zdziarski 1995; Murphy & Yaqoob 2009), but it may actually be outflowing (Beloborodov 1999; Malzac, Beloborodov & Poutanen 2001). An outflowing, energetically dominant corona can be generated by a geometrically thin, optically thick accretion disc at low accretion rates (Merloni & Fabian 2002). This scenario is consistent with the lack of a significant optical/UV bump from the disc, if the power output is dominated by the corona. Furthermore, an outflowing X-ray corona could account for the absence of a disc reflection component, since the primary emission would be beamed away from the disc. This has been suggested especially for radio-loud sources having relativistic jets, where the X-ray corona might be the base of the jet itself (see e.g. Lohfink et al. 2013; Walton et al. 2013; Ballantyne et al. 2014; Fabian et al. 2014). Although NGC 7213 is a radio-intermediate source with no clear evidence for a strong jet (Blank, Harnett & Jones 2005; Bell et al. 2011), its radio emission is found to be weakly correlated with the X-ray emission (Bell et al. 2011). Therefore, the outflowing corona scenario cannot be ruled out in this source.

We confirm the presence of an iron complex between 6.4 and 7 keV (Bianchi et al. 2003), consisting of three narrow K α emission lines from neutral Fe, Fe XXV and Fe XXVI. The lack of a Compton reflection hump above 10 keV indicates that these lines cannot originate from Compton-thick material. Using the MYTORUS self-consistent model, we find that the neutral Fe K α line may be produced by material with a covering fraction of 0.5 and a column density of $5.0^{+2.0}_{-1.6} \times 10^{23}$ cm^{-2}. This result is consistent with the iron line complex being produced in the BLR (Bianchi et al. 2008). Assuming that the line widths represent a Keplerian velocity, it is possible to estimate the distance of the BLR using the virial theorem, i.e. $R_{\rm pc} \simeq 4.5 \times 10^5 f^{-1} M_8 (\Delta V_{\rm km\,s^{-1}})^{-2}$, where $R_{\rm pc}$ is the distance in units of parsecs, f is a coefficient that accounts for the unknown geometry and orientation (Peterson et al. 2004), M_8 is the black hole mass in units of 10^8 solar masses and $\Delta V_{\rm km\,s^{-1}}$ is the line width in units of km s^{-1}. Bianchi et al. (2008) report an FWHM of 2400^{+1100}_{-600} km s^{-1} for the neutral Fe K α line using the *Chandra*/HEG data, and 2640^{+110}_{-90} km s^{-1} for the H α line using ESO-NTT optical data. Setting $f = 4.3$ (Grier et al. 2013), the virial theorem yields a BLR distance of ~0.02 pc. Alternatively, reprocessing may occur in dusty gas, since the presence of dust may enhance the neutral Fe K α EW (Gohil & Ballantyne 2015). This effect is due to a suppression of the reflected continuum, caused by the reduction of backscattering opacity in dusty gas (Draine 2003). This hypothesis is supported by the presence of strong silicate emission features in the mid-IR spectrum of NGC 7213 (Hönig et al. 2010; Ruschel-Dutra et al. 2014). The dust sublimation radius is estimated to be ~0.03 pc from the optical luminosity (Hönig et al. 2010). Therefore, if the line originates from dusty gas, the line-emitting region should be more distant than the BLR, as suggested by the constancy of the line flux on a few year time-scale (see below). We also note that the lack of any cold reflection from Compton-thick material is consistent with the models of clumpy tori, which are predicted to disappear in low-luminosity sources (Elitzur & Shlosman 2006; Hönig & Beckert 2007).

We analysed the neutral Fe K α line time evolution over ~15 years by re-fitting archival *XMM–Newton*, *Suzaku* and *Chandra* data of the source. According to our estimate, the BLR distance is ~0.02 pc, or ~20 light days (see also Kaspi et al. 2005; Balmaverde & Capetti 2014). The observed X-ray variability time-scale of NGC 7213 is of several days or weeks (Emmanoulopoulos et al. 2012), in agreement with the lack of variability during the ~100 ks *NuSTAR* observation. We would thus expect the Fe K α line flux to vary in response to the continuum variations, albeit with a time delay due to the light-travel time. However, we only detect a marginal variability of the line flux during the *Chandra* observation of 2007. Therefore, a contribution from more distant material cannot be ruled out. The *Astro-H* satellite, providing an unprecedented combination of high spectral resolution and effective area at 6–7 keV, will likely enable us to solve the ambiguous origin of the Fe K α line. For example, the line might be the superposition of two components, namely a broad component from the BLR and a narrow one produced further away, which *Astro-H* should be able to disentangle (Reynolds et al. 2014).

The primary continuum is well fitted by a power law with a photon index $\Gamma = 1.84 \pm 0.03$, and an extrapolated 2–10 keV flux $F_{2\text{–}10} = (1.6 \pm 0.1) \times 10^{-11}$ erg cm^{-2} s^{-1}. The 3–10 keV continuum flux and photon index that we found for the archival observations do not show a clear trend (see Fig. 6). The extrapolated 2–10 keV luminosity is $L_{2\text{–}10} = (1.2 \pm 0.1) \times 10^{42}$ erg s^{-1}. Using the 2–10 keV bolometric correction of Marconi et al. (2004), we estimate the bolometric luminosity to be $L_{\rm bol} = (1.3 \pm 0.1) \times 10^{43}$ erg s^{-1}. For a black hole mass of 10^8 M$_\odot$, the Eddington luminosity is 1.2×10^{46} erg s^{-1}. These estimates yield an accretion rate of ~0.1 per cent of the Eddington limit, in rough agreement with the value of 0.14 per cent by Emmanoulopoulos et al. (2012) based on the broad-band spectral energy distribution. An Eddington ratio $\sim 10^{-3}$ is lower than what is typically found for luminous AGNs, namely $\sim 0.01 - 1$, and it lies within the theoretically predicted RIAF regime (Narayan, Mahadevan & Quataert 1998; Ho 2009).

We can only place a lower limit on the presence of a high-energy cut-off, $E_{\rm c} > 140$ keV, consistent with the lower limit of 350 keV found by Lobban et al. (2010) using *Suzaku*+*Swift*/BAT data, and marginally consistent with the value of 95^{+75}_{-45} keV found by Bianchi et al. (2003) using *XMM–Newton*+*BeppoSAX* data. Replacing the cut-off power law with a Comptonization model and assuming a spherical geometry, we estimate the coronal temperature to be >40 keV ($kT_{\rm e} = 295^{+70}_{-250}$ keV) and we measure an optical depth $\tau = 0.2^{+0.7}_{-0.1}$. The lack of an upper limit on the high-energy cut-off does not conflict with the upper limit on the coronal temperature, because a cut-off power law is known to be a rough approximation of Comptonization models (see e.g. Stern et al. 1995). First, the high-energy turnover of a Comptonization spectrum is much sharper than an exponential cut-off (see e.g. Zdziarski et al. 2003). Moreover, a Comptonization spectrum is actually a superposition of several orders of Compton scattering spectra. When the optical depth is small, the different scattering orders are separated in energy, thus resulting in a bumpy spectral shape (see e.g. Poutanen & Svensson 1996). But the optical depth and temperature are inversely related for a given heating/cooling ratio, i.e. the ratio of the power dissipated in the corona to the intercepted soft luminosity (Stern et al. 1995; Haardt et al. 1997). This can produce an upper limit on the coronal temperature even if no exponential cut-off is required (see e.g. Petrucci et al. 2013).

The combination of a weak or absent reflected continuum, a weak UV bump and a low accretion rate suggest that the standard optically thick, geometrically thin accretion disc is truncated in the inner region of the source (Starling et al. 2005; Lobban et al. 2010). A possible explanation is that the nucleus accretes via a RIAF, with the inner edge of any standard disc restricted to large distances, $\sim 10^2$ gravitational radii (see e.g. Quataert et al. 1999). This is a natural suggestion for an LLAGN, since RIAFs are only expected in sub-Eddington systems and the low radiative efficiency would explain the observed low luminosity. The X-ray emission from an RIAF is likely dominated by thermal Comptonization, in agreement with observations of X-ray binaries in the hard state (see e.g. Narayan 2005, and references therein). The soft seed photons can be synchrotron photons produced in the hot accretion flow itself (synchrotron self-Compton), or thermal photons from the outer thin disc (see e.g. Yuan & Zdziarski 2004; Nemmen, Storchi-Bergmann & Eracleous 2014). As we noted above, the X-ray variability timescale of NGC 7213 is of the order of days/weeks (Emmanoulopoulos et al. 2012). Therefore, the Comptonization process is consistent with taking place in an extended region with $kT_e > 40$ keV and $\tau \lesssim 1$, possibly illuminated by the outer thin disc. The relatively small optical depth is a further indication that the corona should be extended and subtend a large solid angle as seen from the disc, in order to scatter a sufficient number of soft photons to produce a substantial X-ray continuum.

Finally, our results can be compared with those on other weakly accreting AGNs observed so far by *NuSTAR*, namely NGC 5506 (estimated Eddington ratio as low as 0.7×10^{-2}; see Matt et al. 2015)[1] and NGC 2110 (estimated Eddington ratio of 0.25–3.7×10^{-2}; see Marinucci et al. 2015). Matt et al. (2015) found a lower limit on the high-energy cut-off of ∼500 keV for NGC 5506, while Marinucci et al. (2015) inferred $E_c > 210$ keV for NGC 2110. In these objects, then, a weak disc emission may be accompanied by a relatively high coronal temperature, in agreement with our present work on NGC 7213. The number of observed sources with good measurements of the high-energy cut-off is too small to establish any statistical correlation with other parameters. However, if the X-ray emission is due to a Comptonizing corona, a high coronal temperature is expected when the disc radiation is weak, because inverse Compton scattering is inefficient in cooling the corona. Further studies on a greater number of sources will be required to confirm this scenario by constraining the physical parameters of the disc/corona system.

ACKNOWLEDGEMENTS

We thank the anonymous referee for his/her helpful comments, which improved the manuscript. FU thanks Pierre-Olivier Petrucci for useful discussions and comments. This work is based on observations obtained with the *NuSTAR* mission, a project led by the California Institute of Technology, managed by the Jet Propulsion Laboratory and funded by NASA. This research has made use of data, software and/or web tools obtained from NASA's High Energy Astrophysics Science Archive Research Center (HEASARC), a service of Goddard Space Flight Center and the Smithsonian Astrophysical Observatory. FU, GM and SB acknowledge support from the French-Italian International Project of Scientific Collaboration: PICS-INAF project number 181542. FU acknowledges support from CNES and Université Franco-Italienne (Vinci PhD fellowship). FU, AM and GM acknowledge financial support from the Italian Space Agency under grant ASI/INAF I/037/12/0-011/13. SB acknowledges financial support from the Italian Space Agency under grant ASI-INAF I/037/12/P1. PA acknowledges support from FONDECYT 1140304. FEB acknowledges support from CONICYT-Chile (Basal-CATA PFB-06/2007, FONDECYT 1141218, 'EMBIGGEN' Anillo ACT1101) and the Ministry of Economy, Development, and Tourism's Millennium Science Initiative through grant IC120009, awarded to The Millennium Institute of Astrophysics, MAS.

REFERENCES

Arnaud K. A., 1996, in Jacoby G. H., Barnes J., eds, ASP Conf. Ser. Vol. 101, Astronomical Data Analysis Software and Systems V. Astron. Soc. Pac., San Francisco, p. 17
Ballantyne D. R. et al., 2014, ApJ, 794, 62
Balmaverde B., Capetti A., 2014, A&A, 563, A119
Baloković M. et al., 2015, ApJ, 800, 62
Baumgartner W. H., Tueller J., Markwardt C. B., Skinner G. K., Barthelmy S., Mushotzky R. F., Evans P. A., Gehrels N., 2013, ApJS, 207, 19
Bell M. E. et al., 2011, MNRAS, 411, 402
Beloborodov A. M., 1999, ApJ, 510, L123
Bianchi S., Matt G., Balestra I., Perola G. C., 2003, A&A, 407, L21
Bianchi S., La Franca F., Matt G., Guainazzi M., Jimenez Bailón E., Longinotti A. L., Nicastro F., Pentericci L., 2008, MNRAS, 389, L52
Blank D. L., Harnett J. I., Jones P. A., 2005, MNRAS, 356, 734
Brenneman L. W. et al., 2014, ApJ, 788, 61
Dickey J. M., Lockman F. J., 1990, ARA&A, 28, 215
Draine B. T., 2003, ApJ, 598, 1026
Elitzur M., Shlosman I., 2006, ApJ, 648, L101
Emmanoulopoulos D., Papadakis I. E., McHardy I. M., Arévalo P., Calvelo D. E., Uttley P., 2012, MNRAS, 424, 1327
Emmanoulopoulos D., Papadakis I. E., Nicastro F., McHardy I. M., 2013, MNRAS, 429, 3439
Fabian A. C., Parker M. L., Wilkins D. R., Miller J. M., Kara E., Reynolds C. S., Dauser T., 2014, MNRAS, 439, 2307
Filippenko A. V., Halpern J. P., 1984, ApJ, 285, 458
Gohil R., Ballantyne D. R., 2015, MNRAS, 449, 1449
Grier C. J. et al., 2013, ApJ, 773, 90
Gu M., Cao X., 2009, MNRAS, 399, 349
Guainazzi M., Bianchi S., Matt G., Dadina M., Kaastra J., Malzac J., Risaliti G., 2010, MNRAS, 406, 2013
Haardt F., Maraschi L., 1991, ApJ, 380, L51
Haardt F., Maraschi L., Ghisellini G., 1994, ApJ, 432, L95
Haardt F., Maraschi L., Ghisellini G., 1997, ApJ, 476, 620
Harrison F. A. et al., 2013, ApJ, 770, 103
Ho L. C., 2008, ARA&A, 46, 475
Ho L. C., 2009, ApJ, 699, 626
Hönig S. F., Beckert T., 2007, MNRAS, 380, 1172
Hönig S. F., Kishimoto M., Gandhi P., Smette A., Asmus D., Duschl W., Polletta M., Weigelt G., 2010, A&A, 515, A23
Kaspi S., Maoz D., Netzer H., Peterson B. M., Vestergaard M., Jannuzi B. T., 2005, ApJ, 629, 61
Kollmeier J. A. et al., 2006, ApJ, 648, 128
Lobban A. P., Reeves J. N., Porquet D., Braito V., Markowitz A., Miller L., Turner T. J., 2010, MNRAS, 408, 551
Lohfink A. M. et al., 2013, ApJ, 772, 83
Magdziarz P., Zdziarski A. A., 1995, MNRAS, 273, 837
Malizia A., Molina M., Bassani L., Stephen J. B., Bazzano A., Ubertini P., Bird A. J., 2014, ApJ, 782, L25
Malzac J., Beloborodov A. M., Poutanen J., 2001, MNRAS, 326, 417
Maoz D., 2007, MNRAS, 377, 1696
Marconi A., Risaliti G., Gilli R., Hunt L. K., Maiolino R., Salvati M., 2004, MNRAS, 351, 169
Marinucci A. et al., 2014, MNRAS, 440, 2347
Marinucci A. et al., 2015, MNRAS, 447, 160
Matt G. et al., 2015, MNRAS, 447, 3029
Merloni A., Fabian A. C., 2002, MNRAS, 332, 165
Murphy K. D., Yaqoob T., 2009, MNRAS, 397, 1549
Nandra K., George I. M., Mushotzky R. F., Turner T. J., Yaqoob T., 1997, ApJ, 477, 602

---

[1] This value of the Eddington ratio is obtained by assuming the highest estimate of the black hole mass in NGC 5506, namely $\sim 10^8$ M$_\odot$. The mass is poorly known, with a lower limit of a few $\times 10^6$ M$_\odot$ (see Guainazzi et al. 2010), which would yield an Eddington ratio above 0.1.

Narayan R., 2005, Ap&SS, 300, 177
Narayan R., Mahadevan R., Quataert E., 1998, in Abramowicz M. A., Björnsson G., Pringle J. E., eds, Theory of Black Hole Accretion Disks. Cambridge Univ. Press, p. 148
Narayan R., Yi I., 1994, ApJ, 428, L13
Nemmen R. S., Storchi-Bergmann T., Eracleous M., 2014, MNRAS, 438, 2804
Panessa F., Bassani L., Cappi M., Dadina M., Barcons X., Carrera F. J., Ho L. C., Iwasawa K., 2006, A&A, 455, 173
Pereira-Santaella M., Diamond-Stanic A. M., Alonso-Herrero A., Rieke G. H., 2010, ApJ, 725, 2270
Perola G. C., Matt G., Cappi M., Fiore F., Guainazzi M., Maraschi L., Petrucci P. O., Piro L., 2002, A&A, 389, 802
Peterson B. M. et al., 2004, ApJ, 613, 682
Petrucci P.-O. et al., 2013, A&A, 549, A73
Phillips M. M., 1979, ApJ, 227, L121
Poutanen J., Svensson R., 1996, ApJ, 470, 249
Quataert E., Di Matteo T., Narayan R., Ho L. C., 1999, ApJ, 525, L89
Reynolds C. et al., 2014, preprint (arXiv:1412.1177)
Ruschel-Dutra D., Pastoriza M., Riffel R., Sales D. A., Winge C., 2014, MNRAS, 438, 3434
Shakura N. I., Sunyaev R. A., 1973, A&A, 24, 337
Sobolewska M. A., Papadakis I. E., 2009, MNRAS, 399, 1597
Starling R. L. C., Page M. J., Branduardi-Raymont G., Breeveld A. A., Soria R., Wu K., 2005, MNRAS, 356, 727
Stern B. E., Poutanen J., Svensson R., Sikora M., Begelman M. C., 1995, ApJ, 449, L13
Svensson R., Zdziarski A. A., 1994, ApJ, 436, 599
Ursini F. et al., 2015, A&A, 577, A38
Walton D. J., Nardini E., Fabian A. C., Gallo L. C., Reis R. C., 2013, MNRAS, 428, 2901
Woo J.-H., Urry C. M., 2002, ApJ, 579, 530
Wu Q., Gu M., 2008, ApJ, 682, 212
Wu C.-C., Boggess A., Gull T. R., 1983, ApJ, 266, 28
Yaqoob T., 2012, MNRAS, 423, 3360
Yu Z., Yuan F., Ho L. C., 2011, ApJ, 726, 87
Yuan F., Zdziarski A. A., 2004, MNRAS, 354, 953
Zdziarski A. A., Lubiński P., Gilfanov M., Revnivtsev M., 2003, MNRAS, 342, 355

This paper has been typeset from a TEX/LATEX file prepared by the author.

Chapter 6

The high-energy monitoring of NGC 4593

Contents

In this chapter, I will discuss a joint *XMM-Newton*+*NuSTAR* monitoring program, performed in early 2015, on the Seyfert 1 NGC 4593. Our group presented an *XMM-Newton* proposal (PI: P.-O. Petrucci[1]), approved in *XMM-Newton* AO13, designed to study the broad-band spectrum of this source (from the UV up to hard X-rays) and in particular the variability on a few days time-scale. After a brief introduction on the monitoring program, I will present the timing properties and the main results of the X-ray spectral analysis. This campaign shows that studying the variability of Seyfert 1s on different time-scales gives us important insights into the high-energy emission of AGNs.

6.1 A joint monitoring with *XMM-Newton* and *NuSTAR*

NGC 4593 ($z = 0.009$, Strauss et al. 1992) is an X-ray bright Seyfert 1, hosting a supermassive black hole of $(9.8 \pm 2.1) \times 10^6$ solar masses (Denney et al. 2006). Previous observations of this source with *BeppoSAX* (Guainazzi et al. 1999), *XMM-Newton* (Reynolds et al. 2004; Brenneman et al. 2007) and *Suzaku* (Markowitz & Reeves 2009) have shown a strong reflection hump above 10 keV and an iron line complex at 6-7 keV, a significant soft X-ray excess below 2 keV and a lower limit on the high-energy cut-off of 150 keV. These

---

[1] co-Is: F. Ursini, S. Bianchi, M. Cappi, G. Ponti, A. De Rosa, B. De Marco, J. Malzac.

Table 6.1 – The logs of the joint *XMM-Newton* and *NuSTAR* observations of NGC 4593.

Obs.	Satellites	Start time (UTC) yyyy-mm-dd	Net exp. (ks)
1	*XMM-Newton*	2014-12-29	16
	NuSTAR		22
2	*XMM-Newton*	2014-12-31	17
	NuSTAR		22
3	*XMM-Newton*	2015-01-02	17
	NuSTAR		21
4	*XMM-Newton*	2015-01-04	15
	NuSTAR		23
5	*XMM-Newton*	2015-01-06	21
	NuSTAR		21

properties make NGC 4593 an interesting source to perform broad-band spectroscopy and variability analysis. Our monitoring consisted of five simultaneous observations with *XMM-Newton* and *NuSTAR* (from 2014, Dec. 29 to 2015, Jan. 6), each exposure being separated by 2 days and lasting about 20 ks. The log of the data sets is reported in Table 6.1. The spacing between the different observations was chosen according to the UV two-folding time-scale of 2-3 days observed with *IUE* (Santos-Lleo et al. 1995). This has been the first joint *XMM-Newton*+*NuSTAR* program explicitly aimed at studying the high-energy emission of an AGN through its variability on time-scales of days down to a few ks. The primary goals of the monitoring were constraining the physical and variability properties of the hot corona, and investigating the nature of the soft X-ray excess and of the reflection component.

The analysis of the data was divided into two main steps. First, I performed a simple timing analysis, to have a general idea of the behaviour of the source during the monitoring. As I show in the following, the source was found to be remarkably variable, both in flux and spectral shape, on the time-scales of the campaign (Ursini et al. 2016a). A more detailed timing analysis is in progress (De Marco et al., in prep.). Then, I performed a detailed X-ray spectral analysis (Ursini et al. 2016b), which is also discussed in the following. A follow-up spectral analysis, focused on testing physical Comptonization models, will be the subject of a future work (Ursini et al., in prep.).

6.2 Timing properties

The preliminary timing analysis was presented in Ursini et al. (2016a, proceedings of the 2015 *XMM-Newton* Science Workshop). I will now summarize the main variability properties of NGC 4593 as observed during the campaign. I show in Fig. 6.1 the *XMM-Newton* and *NuSTAR* light curves of NGC 4593 (see also Fig. 1 of Ursini et al. 2016a and Fig. 1 of Ursini et al. 2016b). The source exhibits a strong flux variability, up to a factor of 2 in count rate, on time-scales as short as a few ks. The hardness ratio light curves also show a significant spectral variability, particularly in the soft band below 10

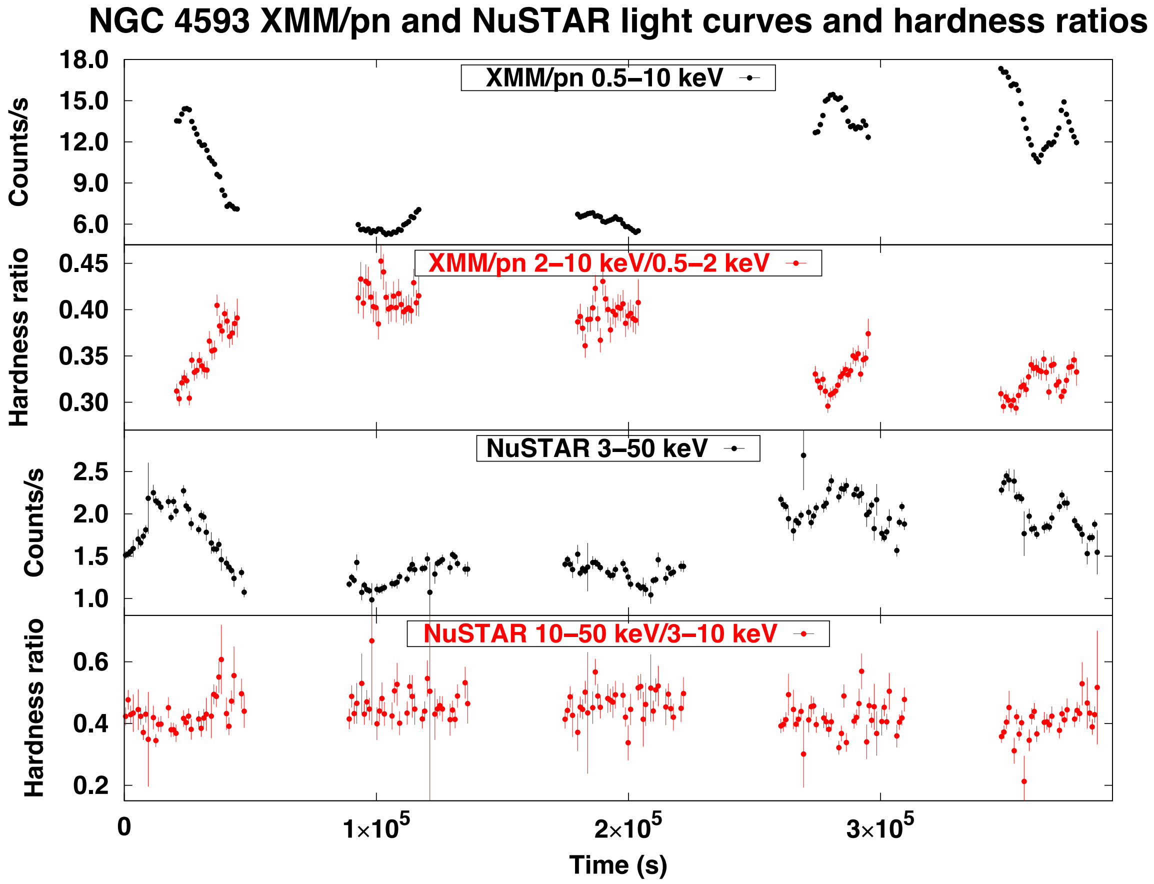

Figure 6.1 – Count rate light curves of NGC 4593. Top panel: *XMM-Newton*/pn count rate in the 0.3–10 keV range. Second panel: *XMM-Newton*/pn hardness ratio 2–10 keV/0.5–2 keV. Third panel: *NuSTAR* count rate in the 3–50 keV range (co-added FPMA and FPMB data). Bottom panel: *NuSTAR* hardness ratio 10–50 keV/3–10 keV. Time bins of 1 ks are used.

keV. We observe a clear softer-when-brighter behaviour, as a higher flux corresponds to a lower hardness ratio (see also Fig. 6.2). Above 10 keV, on the other hand, the spectral variability is less pronounced. The most prominent flux and spectral variations occur during the first observation. For this reason, I decided to split obs. 1 into two $\sim$ 10 ks long bits to perform the spectral analysis (Ursini et al. 2016b). I show the different *XMM-Newton*/pn and *NuSTAR* spectra in Fig. 6.3, fitted with a simple power law for comparison. Besides the strong variability in the soft band, the spectra show the presence of a significant and variable soft excess below 1 keV, as well as an iron emission complex at 6-7 keV. The soft excess seems to be correlated to the primary emission, being stronger during the high-flux states (see also Fig. 6.4).

NGC 4593 was observed also by the optical monitor (OM) onboard *XMM-Newton*, using the optical filter U and the UV filters UVW1 and UVW2. The latter filter operates at the shortest wavelengths (2120 ± 500 Å), and had also slightly longer exposures (7–10 ks per observation) compared with U and UVW1 (5 ks each). I show in Fig. 6.5 the UVW2 count rate during the five exposures, plotted against the 0.3–0.5 keV count rate (time-averaged during the corresponding time intervals). Interestingly, there is a linear relationship between the UV and soft X-ray flux. The Pearson's correlation coefficient is $\rho = 0.95$, with a p-value of 0.01.

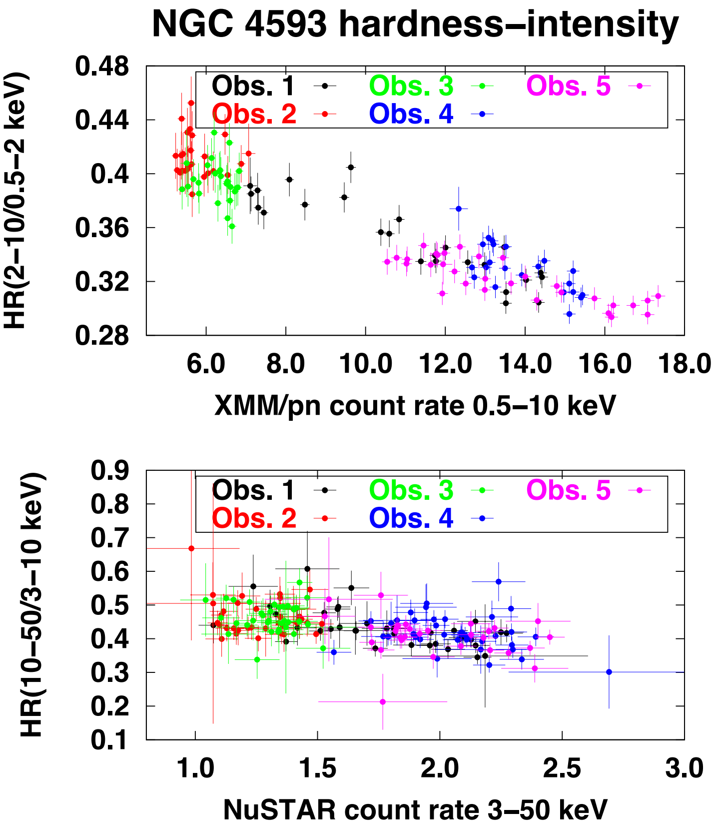

Figure 6.2 – "Hardness- intensity diagram" of the five observations of NGC 4593 (adapted from Fig. 2 of Ursini et al. 2016a). Each point corresponds to a time bin of 1 ks. Top panel: *XMM-Newton*/pn hardness ratio (2–10 keV)/(0.5–2 keV) plotted against the 0.5–10 keV count rate. Bottom panel: *NuSTAR* hardness ratio (10–50 keV)/(3–10 keV) plotted against the 3–50 keV count rate.

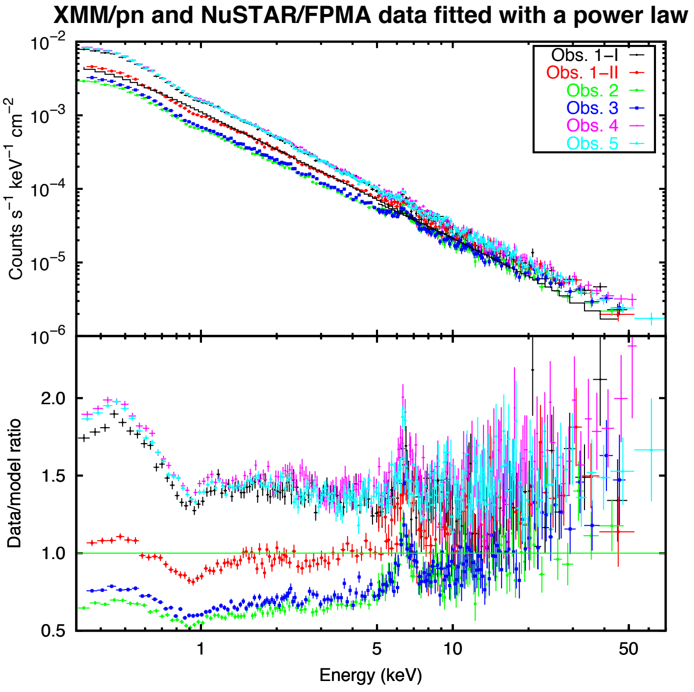

Figure 6.3 – Upper panel: the *XMM-Newton*/pn and *NuSTAR* spectra of NGC 4593. Lower panel: the ratio of the spectra to a power law. Only *NuSTAR*/FPMA data are shown for clarity. (Fig. 2 of Ursini et al. 2016b)

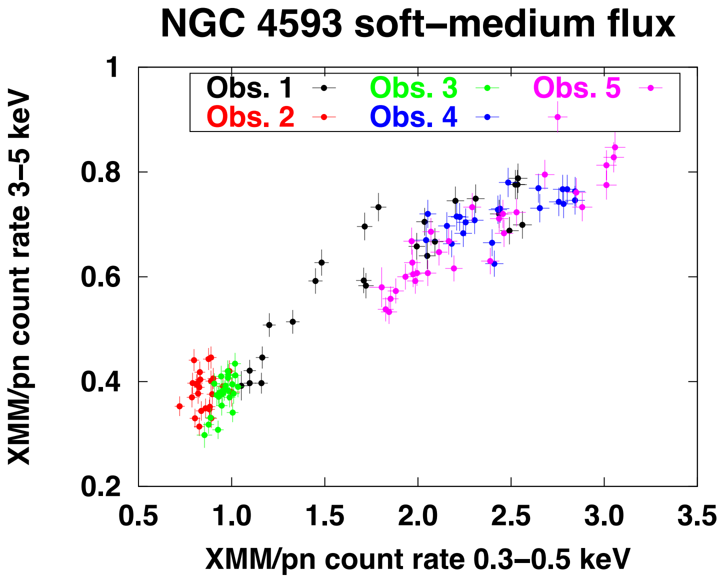

Figure 6.4 – *XMM-Newton*/pn count rate in the 3–5 keV range plotted against the pn count rate in the 0.3–0.5 keV range, where the soft excess is expected to dominate (adapted from Fig. 4 of Ursini et al. 2016a). Each point corresponds to a time bin of 1 ks.

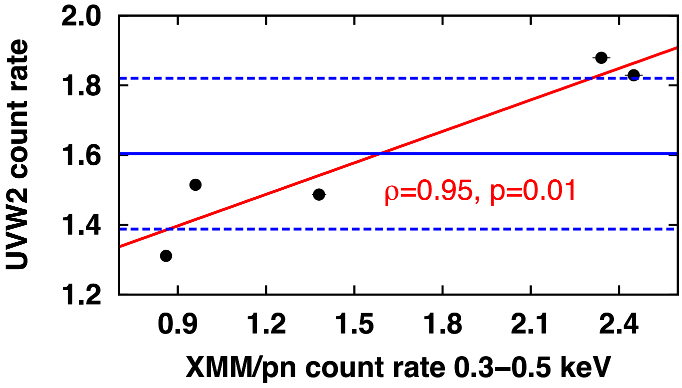

Figure 6.5 – *XMM-Newton*/OM UVW2 fliter count rate plotted against the pn count rate in the 0.3–0.5 keV range. The blue solid line represents the average UVW2 count rate, while the blue dashed lines correspond to the standard deviation. The red solid line represents a linear fit to the data.

6.3 X-ray spectral analysis

The detailed X-ray spectral analysis was presented in Ursini et al. (2016b), reported in the appendix to this chapter. This work was aimed at obtaining a good phenomenological description of the spectral and variability properties of the source. This is a necessary prelude before testing physical Comptonization models. The main steps of this analysis were: (i) the analysis of *XMM-Newton*/RGS data, to study the soft X-ray features (narrow emission lines and ionized absorption); (ii) a study of the properties of the iron K complex between 6 and 7 keV; (iii) broad-band fits to the pn and *NuSTAR* data in the available energy range (0.3–80 keV). I will now summarize these main steps, referring to Ursini et al. (2016b) for a detailed discussion.

6.3.1 The *XMM-Newton*/RGS data

I exploited the high spectral resolution of the RGS with the main goal of constraining the warm absorber (e.g. Ebrero et al. 2013). I fitted the spectra from the two detectors, RGS1 and RGS2, co-adding the data from different time intervals, to obtain a better signal-to-noise ratio. Indeed, past studies showed that the warm absorber is located at least a few pc away from the primary source, so we did not expect strong variability on

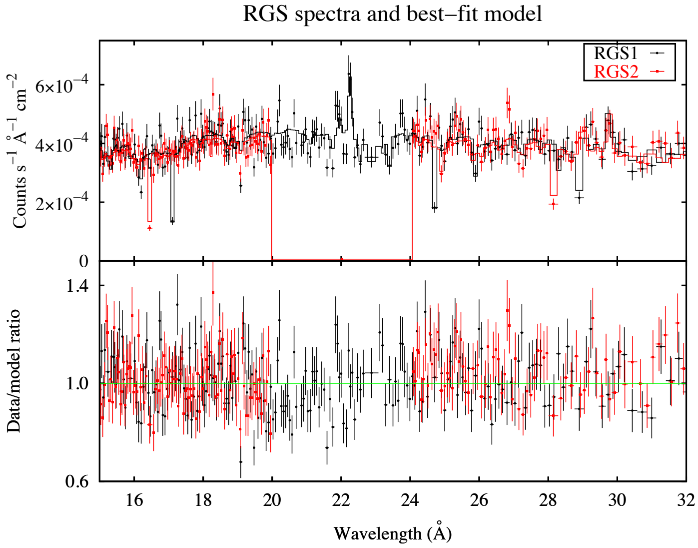

Figure 6.6 – Upper panel: the RGS spectra in the 15–32 Å range, with the best-fitting model. Lower panel: the ratio of the spectra to the model. (Fig. 3 of Ursini et al. 2016b)

a few days time-scale (Ebrero et al. 2013). As a first step, I fitted the data in the 0.3–2 keV range with a simple model including a power law and the warm absorber, modelled with a CLOUDY table as for NGC 5548 (see Chapter 4). I actually found the presence of two different absorption components, with different ionization parameters ($\log \xi \simeq 2.2$ and 0.4) and column densities ($N_{\rm H} \simeq 7 \times 10^{21}$ and 8×10^{20} cm^{-2}, respectively). Moreover, significant residuals indicated the presence of at least four emission lines in the spectra. I identified such features as two Kα lines from O VII (intercombination and forbidden) and two Kα lines from N VI (resonance and forbidden). I thus included four narrow Gaussian lines at those energies, finding a good fit with no strong residuals left. The properties of the emission lines are summarized in Table 2 of Ursini et al. (2016b). Then, I replaced the Gaussian lines with a more physical model, namely the emission spectrum from a photoionized plasma. This component was modelled with a CLOUDY table[2], yielding a statistically equivalent fit. The properties of the warm absorber and of the photoionized plasma are reported in Table 3 of Ursini et al. (2016b).

6.3.2 The iron K complex: narrow and broad Fe Kα lines

To investigate the properties of the Fe K complex at 6-7 keV, I fitted the *XMM-Newton*/pn spectra in the 3–10 keV band, with a model consisting of a power law plus a number of Gaussian lines. To find a good fit, I needed to include three Gaussian lines, i.e. a narrow line and a broad line at 6.4 keV, and a further narrow line at ∼ 7 keV (see Table 4 of Ursini et al. 2016b). The two neutral Fe Kα lines at 6.4 keV have an intrinsic width of 0 and ∼ 300 eV, respectively. The narrow component is consistent with having a constant flux, despite the strong variations of the primary X-ray flux (see Fig. 4 of Ursini et al. 2016b). The flux of the broad component is instead found to be variable (see Fig. 5 of Ursini et al. 2016b). The different intrinsic width and variability behaviour indicate a different origin of these two lines. The narrow Fe Kα line-emitting material is likely located at least a few light days away from the primary X-ray source, given the lack of variability. The broad Fe Kα component should instead originate from within a few tens of gravitational radii, from the intrinsic width. Concerning the third line at around 7

---

[2] This table, like the warm absorber table, was produced by S. Bianchi.

keV, it may be identified as either a Kα line from Fe XXVI at 6.966 keV, or a neutral Fe Kβ line at 7.056 keV. The latter interpretation is supported by the ratio of the flux of this line to that of the neutral, narrow Fe Kα line, which is roughly consistent with the predicted ratio of fluorescence yields for Kβ/Kα (~ 0.13, e.g. Kaastra & Mewe 1993).

6.3.3 The broad-band fits

After studying the properties of the warm absorber and of the iron K complex, I proceeded to fit the broad-band *XMM-Newton*/pn and *NuSTAR* spectra in the available energy range (0.3–79 keV). I used a phenomenological model, consisting of the following components:

- The primary continuum: modelled with a cut-off power law (CUTOFFPL in XSPEC); the photon index, cut-off energy and normalization were all free to vary between the different observations.
- The reflection component: since I found evidence for both a narrow and a broad Fe Kα line at 6.4 keV, I included two distinct reflection components, modelled with XILLVER (García & Kallman 2010; García et al. 2013) and RELXILL (García et al. 2014), respectively. Both models self-consistently incorporate fluorescence lines and the Compton reflection hump, and in RELXILL such components are relativistically blurred. Therefore, RELXILL is suited for describing the reflection component associated with the broad Fe Kα line. The XILLVER component was consistent with being constant, like the narrow component of the Fe Kα line. Concerning the RELXILL component, I assumed it to originate relatively close to the primary source, thus I tied the photon index of the illuminating continuum to the primary power law, leaving free to vary the normalization between the different observations. Concerning the ionization parameter, I found $\log \xi = 0$ for XILLVER and $\log \xi = 3$ for RELXILL. The inner radius of RELXILL was found to be 40 ± 15 R_G, consistent with the intrinsic width of the broad Fe Kα line.
- The warm absorber: modelled with the CLOUDY tables (see Sect. 6.3.1). The parameters were free, to account for cross-calibration uncertainties between pn and RGS (Kirsch et al. 2004, see also Chapter 4), but tied between the different observations.
- The soft emission lines: modelled with a CLOUDY table fixed to the RGS best-fitting values (see Sect. 6.3.1), as it was poorly constrained by pn data. This component also adds a minor contribution to the hard X-ray band, because it produces self-consistently a weak iron line and reflection hump.
- The soft X-ray excess: including only the components described above, I found strong, positive residuals below 1 keV. Ionized reflection, then, does not explain the soft excess in NGC 4593, and Comptonization in a warm corona is a more likely scenario. However, in Ursini et al. (2016b) I tested a simple phenomenological model. I first included a soft cut-off power law, expecting a relatively steep photon index (around 2.5–3; see also Chapter 7) and a cut-off energy below 1 keV, roughly corresponding to the temperature of the putative warm Comptonizing medium. This model, albeit yielding statistically acceptable fits, gave best-fitting parameters

difficult to justify on physical grounds. First, I found only a lower limit, of the order of a few keV, on the cut-off energy of the soft power law (while its photon index was 2.8–3.2), with a best-fitting value pegged at hard limit (10^6 keV). This would indicate a relatively high temperature of the warm corona, and a "soft" excess extending to energies much above 1 keV. Moreover, the primary power law was very flat, having a photon index as low as 1.3. These are likely artefacts of an imperfect modelling of the soft excess. Then, I replaced the soft power law with the model DISKBB (Mitsuda et al. 1984; Makishima et al. 1986), which describes the emission from a multicolour disc-blackbody. This model, even if phenomenological, yielded statistically good fits and more plausible best-fitting parameters than the soft power law (see also Fig. 6.7 and Fig. 6.8, where I show the best-fitting model including respectively DISKBB and the soft power law). In particular, the primary photon index was found to be between 1.6 and 1.85 (see Fig. 6.9). Such a difference coming from the modelling of the soft excess was unexpected. However, this could be understood if the soft excess represented the tail of a Comptonized spectrum, as its turnover is sharper than an exponential cut-off (e.g. Zdziarski et al. 2003). Then, it might be better reproduced (phenomenologically) by the turnover of a disc blackbody spectrum (see Fig. 6.10). This effect is likely less important for the hard power law, because of the lower statistics.

The final model in XSPEC is:

$$\mathrm{WA}_1 \times \mathrm{WA}_2 \times (\mathrm{SOFT\ LINES} + \mathrm{CUTOFFPL} + \mathrm{DISKBB} + \mathrm{RELXILL} + \mathrm{XILLVER}) \qquad (6.1)$$

The primary photon index Γ undergoes significant variations during the campaign, up to $\Delta\Gamma \simeq 0.2$. Moreover, the high-energy cut-off is also found to be variable, from 90^{+40}_{-20} to > 700 keV. I show the contour plots of these parameters in Fig. 6.9 (see also Table 5 of Ursini et al. 2016b). Interestingly, both the photon index and cut-off energy vary on time-scales of a few days (e.g. comparing obs. 3 and 4) but also on shorter time-scales, of a few ks (comparing the two time intervals of obs. 1).

Another interesting result is the linear relationship between the soft excess and the primary continuum, as shown in Fig. 6.11. In particular, the flux of the soft excess (i.e. that of the DISKBB component alone) in the 0.3–2 keV band is correlated with the flux of the primary power law in the 3–10 keV band, with a Pearson's coefficient $\rho = 0.98$ and a p-value of 8×10^{-4}.

6.4 Conclusions

The results obtained on NGC 4593 show that such observational campaigns, based on probing the source variability on different time-scales, are very useful to investigate the high-energy emission of AGNs in detail.

First, the combined capabilities of *XMM-Newton* and *NuSTAR* enabled a detailed study of the reflection component, which was disentangled from the primary continuum. Moreover, the primary photon index and cut-off energy were well constrained and found to be variable on the time-scales of the campaign, i.e. from a few days down to a few ks. Such variations are most probably indicative of physical variations of the hot corona, as discussed in Ursini et al. (2016b). For example, from the variability of the cut-off energy we expect huge variations of the coronal temperature (from a few tens up to a few

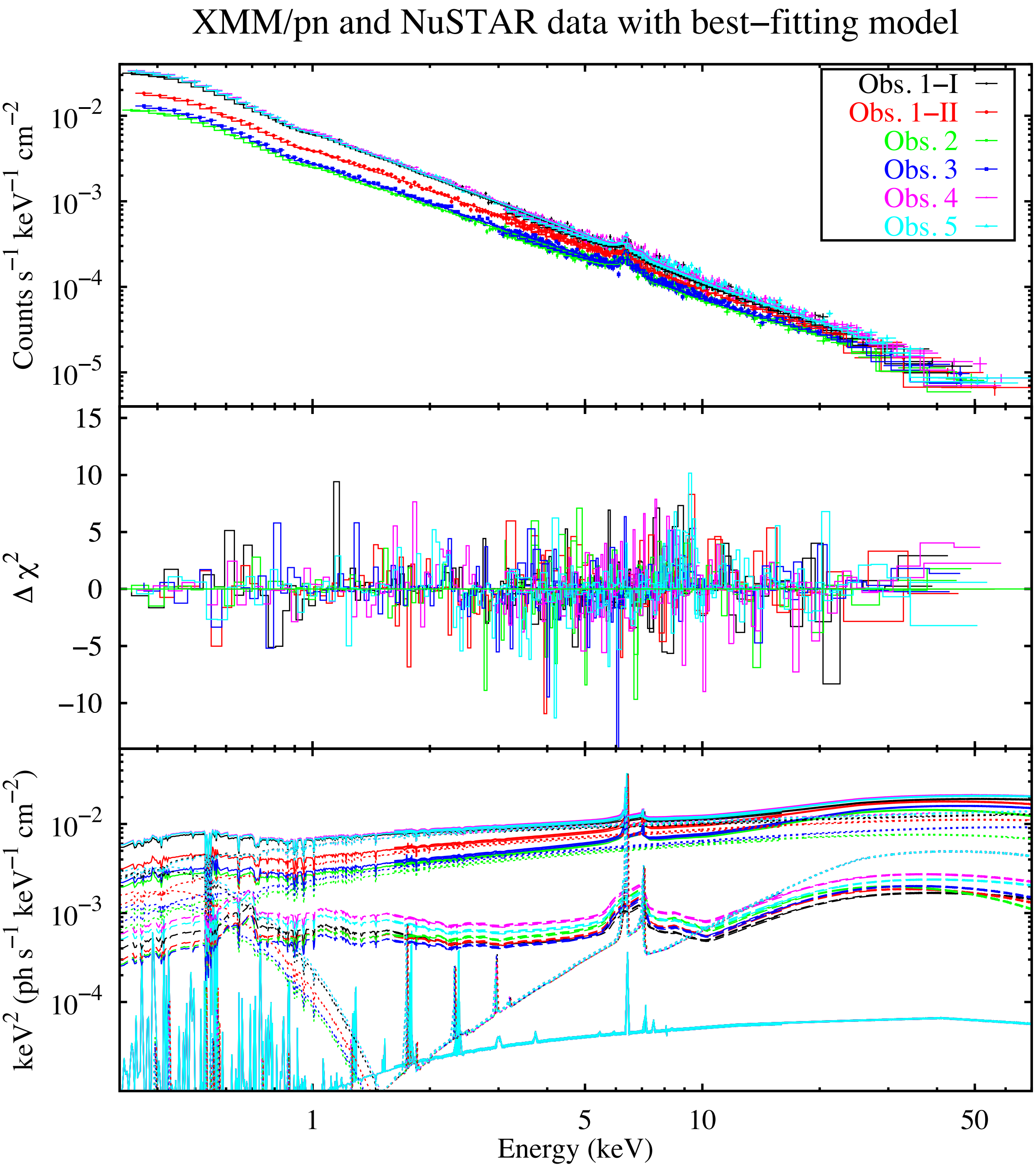

Figure 6.7 – Broad-band X-ray data and best-fitting model of NGC 4593. Upper panel: *XMM-Newton*/pn and *NuSTAR* data and folded model. Middle panel: contribution to χ^2. Lower panel: best-fitting model $E^2 f(E)$, with the plot of the reflection components XILLVER (dotted line) and RELXILL (dashed lines), the CLOUDY model for the soft X-ray emission lines with associated reflected continuum (solid line), and the DISKBB component for the soft excess below 1 keV (dotted lines). (Fig. 7 of Ursini et al. 2016b)

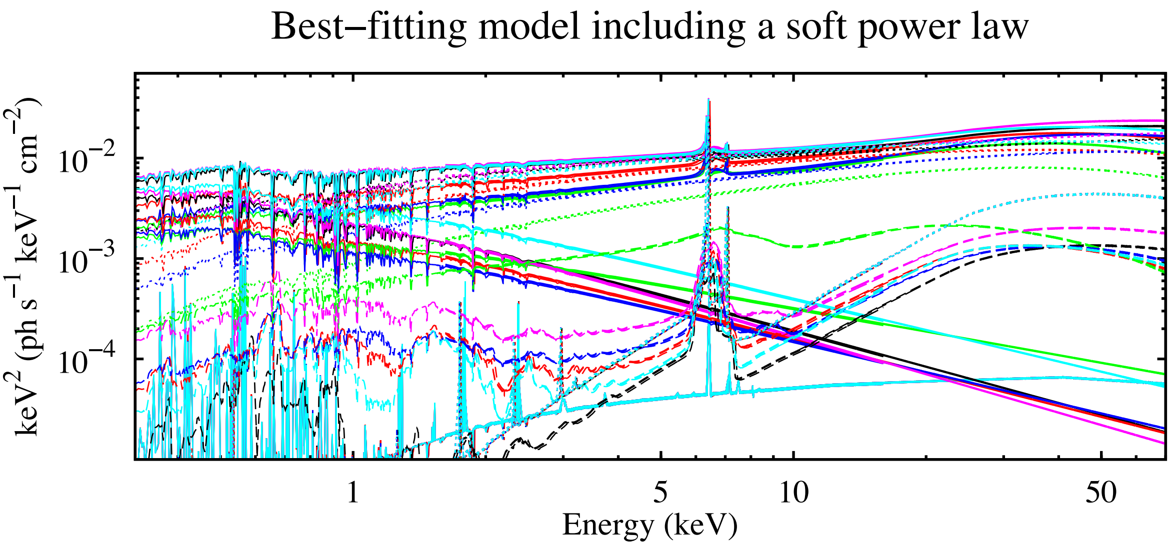

Figure 6.8 – Best-fitting model of NGC 4593, when including a cut-off power law to model the soft excess. See Fig. 6.7 for comparison (the scales of the x and y-axes are the same). The "soft" power law (solid lines) extends to much higher energies than the DISKBB component, thus failing to correctly reproduce the soft excess and yielding implausible parameters for the primary continuum (dotted lines, as in Fig. 6.7), and in particular photon indexes as low as 1.3. Also the RELXILL component (dashed lines, as in Fig. 6.7) exhibits an oddly variable behaviour.

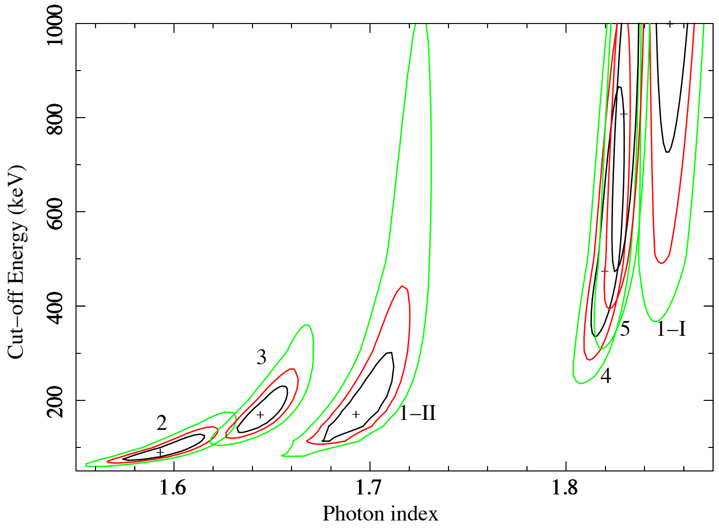

Figure 6.9 – Contour plots of the primary continuum cut-off energy versus photon index for each observation. Green, red and black lines correspond to 99, 90 and 68% confidence levels, respectively. (Fig. 8 of Ursini et al. 2016b)

hundreds of keV) during a few days. This behaviour needs to be confirmed by an analysis with physical Comptonization models (Ursini et al., in prep.).

Concerning the soft X-ray excess, this component is not explained by ionized reflection in NGC 4593. The existence of a correlation between the UV and soft X-ray fluxes supports a warm Comptonization scenario. Moreover, the correlation between the soft excess and the primary continuum indicates a link between the regions producing such components. It should be noted that, even if the soft excess is due to a warm Comptonizing corona, the relation with the hot corona is not obvious. For example, the two coronae might be illuminated by the same source of seed photons (i.e. the disc), but in this case they should be located relatively close to each other. Another possibility is that the warm corona itself acts as a seed photon source for the hot corona. In any case, the

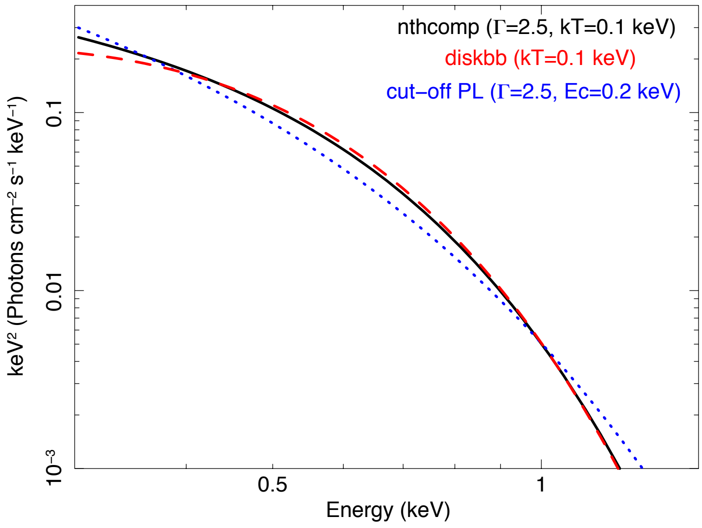

Figure 6.10 – Comparison between three different models in XSPEC that could reproduce the soft X-ray excess: the thermal Comptonization model NTHCOMP (black solid line), the DISKBB model (red dashed line), and a cut-off power law (blue dotted line). Overall, the cut-off power law offers a poorer approximation of the turnover of the Comptonized spectrum.

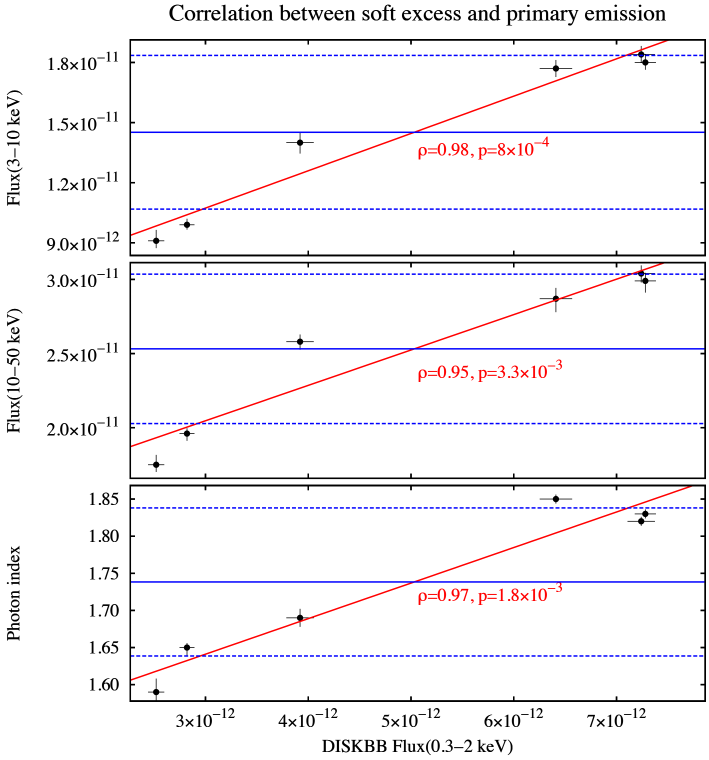

Figure 6.11 – Three parameters of the primary power law plotted against the flux of the soft excess (i.e. the 0.3–2 keV flux of the DISKBB component alone). Upper panel: primary flux in the 3–10 keV range. Middle panel: primary flux in the 10–50 keV range. Lower panel: primary photon index. All fluxes are in units of ergs s^{-1} cm^{-2}. The blue solid lines represent the mean value for each parameter, while the blue dashed lines represent the standard deviation. The red lines represent linear fits to the data. (Fig. 9 of Ursini et al. 2016b)

promising results of the campaign on NGC 4593 prompt us to carry out further analyses to characterize the spectral (Ursini et al., in prep.) and timing (De Marco et al., in prep.) properties of the source.

Appendix

High-energy monitoring of NGC 4593 with *XMM-Newton* and *NuSTAR*. X-ray spectral analysis

F. Ursini[1,2,3], P.-O. Petrucci[1,2], G. Matt[3], S. Bianchi[3], M. Cappi[4], B. De Marco[5], A. De Rosa[6], J. Malzac[7,8], A. Marinucci[3], G. Ponti[5], and A. Tortosa[3]

[1] Univ. Grenoble Alpes, IPAG, F-38000 Grenoble, France.
[2] CNRS, IPAG, F-38000 Grenoble, France.
[3] Dipartimento di Matematica e Fisica, Università degli Studi Roma Tre, via della Vasca Navale 84, 00146 Roma, Italy.
[4] INAF-IASF Bologna, Via Gobetti 101, I-40129 Bologna, Italy.
[5] Max-Planck-Institut für extraterrestrische Physik, Giessenbachstrasse, D-85748 Garching, Germany.
[6] INAF/Istituto di Astrofisica e Planetologia Spaziali, via Fosso del Cavaliere, 00133 Roma, Italy.
[7] Université de Toulouse, UPS-OMP, IRAP, Toulouse, France.
[8] CNRS, IRAP, 9 Av. colonel Roche, BP44346, F-31028 Toulouse cedex 4, France.

Accepted for publication in *Monthly Notices of the Royal Astronomical Society.* First published online on August 12, 2016; doi: 10.1093/mnras/stw2022.

MNRAS Advance Access published August 12, 2016

High-energy monitoring of NGC 4593 with *XMM-Newton* and *NuSTAR*. X-ray spectral analysis

F. Ursini,[1,2,3⋆] P.-O. Petrucci,[1,2] G. Matt,[3] S. Bianchi,[3] M. Cappi,[4]
B. De Marco,[5] A. De Rosa,[6] J. Malzac,[7,8] A. Marinucci,[3] G. Ponti[5] and A. Tortosa[3]
[1] *Univ. Grenoble Alpes, IPAG, F-38000 Grenoble, France.*
[2] *CNRS, IPAG, F-38000 Grenoble, France.*
[3] *Dipartimento di Matematica e Fisica, Università degli Studi Roma Tre, via della Vasca Navale 84, 00146 Roma, Italy.*
[4] *INAF-IASF Bologna, Via Gobetti 101, I-40129 Bologna, Italy.*
[5] *Max-Planck-Institut für extraterrestrische Physik, Giessenbachstrasse, D-85748 Garching, Germany.*
[6] *INAF/Istituto di Astrofisica e Planetologia Spaziali, via Fosso del Cavaliere, 00133 Roma, Italy.*
[7] *Université de Toulouse, UPS-OMP, IRAP, Toulouse, France.*
[8] *CNRS, IRAP, 9 Av. colonel Roche, BP44346, F-31028 Toulouse cedex 4, France.*

Released Xxxx Xxxxx XX

ABSTRACT
We present results from a joint *XMM-Newton*/*NuSTAR* monitoring of the Seyfert 1 NGC 4593, consisting of 5×20 ks simultaneous observations spaced by two days, performed in January 2015. The source is variable, both in flux and spectral shape, on time-scales down to a few ks and with a clear softer-when-brighter behaviour. In agreement with past observations, we find the presence of a warm absorber well described by a two-phase ionized outflow. The source exhibits a cold, narrow and constant Fe K α line at 6.4 keV, and a broad component is also detected. The broad-band (0.3–79 keV) spectrum is well described by a primary power law with $\Gamma \simeq 1.6 - 1.8$ and an exponential cut-off varying from 90^{+40}_{-20} keV to > 700 keV, two distinct reflection components, and a variable soft excess correlated with the primary power law. This campaign shows that probing the variability of Seyfert 1 galaxies on different time-scales is of prime importance to investigate the high-energy emission of AGNs.

Key words: galaxies: active — galaxies: Seyfert — X-rays: galaxies — X-rays: individuals (NGC 4593)

1 INTRODUCTION

Active galactic nuclei (AGNs) are thought to be powered by an accretion disc around a supermassive black hole, mostly emitting in the optical/UV band. According to the standard paradigm, the X-ray emission is due to thermal Comptonization of the soft disc photons in a hot region, the so-called corona (Haardt & Maraschi 1991; Haardt et al. 1994, 1997). This process explains the power-law shape of the observed X-ray spectrum of AGNs. A feature of thermal Comptonization is a high-energy cut-off, which has been observed around ∼ 100 keV in several sources thanks to past observations with *CGRO*/OSSE (Zdziarski et al. 2000), *BeppoSAX* Perola et al. (2002), and more recently *Swift*/BAT (Baumgartner et al. 2013) and *INTEGRAL* (Malizia et al. 2014; Lubiński et al. 2016). From the application of Comptonization models, such high-energy data allow to constrain the plasma temperature, which is commonly found to range from 50 to 100 keV (e.g., Zdziarski et al. 2000; Lubiński et al. 2016). Furthermore, the cut-off energy is now well constrained in an increasing number of sources thanks to the unprecedented sensitivity of *NuSTAR* up to ∼ 80 keV (e.g., Brenneman et al. 2014; Marinucci et al. 2014; Baloković et al. 2015; Ursini et al. 2015; Ballantyne et al. 2014; Matt et al. 2015). The primary X-ray emission can be modified by different processes, such as absorption from neutral or ionized gas (the so-called warm absorber), and Compton reflection from the disc (e.g., George & Fabian 1991; Matt et al. 1991) or from more distant material, like the molecular torus at pc scales (e.g., Matt et al. 2003). A smooth rise below 1-2 keV above the extrapolated high-energy power law is commonly observed in the spectra of AGNs (see, e.g., Bianchi et al. 2009). The origin of this so-called soft excess is uncertain (see, e.g., Done et al. 2012). Ionized reflection is able to explain the soft excess in some sources (e.g., Crummy et al. 2006; Ponti et al. 2006; Walton et al. 2013), while Comptonization in a "warm" region is favoured in other cases (e.g., Mehdipour et al. 2011; Boissay et al. 2014).

The current knowledge of the geometrical and physi-

⋆ e-mail: `francesco.ursini@univ-grenoble-alpes.fr`

cal properties of the X-ray corona is far from being complete, as in most sources we still lack good constraints on the coronal temperature, optical depth and geometry. The approach based on multiple, broad-band observations with a high signal-to-noise ratio is a powerful tool to study the high-energy emission in Seyfert galaxies. Strong and fast X-ray variability, both in flux and spectral shape, is a hallmark of AGNs, and of historical importance to rule out alternatives to supermassive black holes as their central engine (e.g., Elliot & Shapiro 1974). The analysis of X-ray variability allows disentangling the different spectral components and constraining their characteristic parameters, as shown by recent campaigns on Mrk 509 (Kaastra et al. 2011; Petrucci et al. 2013) and NGC 5548 (Kaastra et al. 2014; Ursini et al. 2015).

In this paper, we discuss results based on a joint *XMM-Newton* and *NuSTAR* monitoring program on NGC 4593 ($z = 0.009$, Strauss et al. 1992), an X-ray bright Seyfert 1 galaxy hosting a supermassive black hole of $(9.8 \pm 2.1) \times 10^6$ solar masses (from reverberation mapping; see Denney et al. 2006). This is the first monitoring carried out by *XMM-Newton* and *NuSTAR* specifically designed to study the high-energy emission of an AGN through the analysis of its variability on time-scales of days. We reported preliminary results from a phenomenological timing analysis in Ursini et al. (2016). Here we focus on the broad-band (0.3–80 keV) X-ray spectral analysis. Past observations of NGC 4593 with *BeppoSAX* (Guainazzi et al. 1999), *XMM-Newton* (Reynolds et al. 2004; Brenneman et al. 2007) and *Suzaku* (Markowitz & Reeves 2009) have shown a strong reflection bump above 10 keV and the presence of two narrow Fe K α emission lines at 6.4 and around 7 keV. A soft excess below 2 keV has been reported, both in the 2002 *XMM-Newton* data (Brenneman et al. 2007) and in the 2007 *Suzaku* data, with a drop in the 0.4–2 keV flux by a factor > 20 in the latter (Markowitz & Reeves 2009). Guainazzi et al. (1999) found a lower limit on the high-energy cut-off of 150 keV from *BeppoSAX* data.

This paper is organized as follows. In Sect. 2, we describe the observations and data reduction. In Sect. 3 we present the analysis of the *XMM-Newton* and *NuSTAR* spectra. In Sect. 4, we discuss the results and summarize our conclusions.

2 OBSERVATIONS AND DATA REDUCTION

XMM-Newton (Jansen et al. 2001) and *NuSTAR* (Harrison et al. 2013) simultaneously observed NGC 4593 five times, spaced by two days, between 29 December 2014 and 6 January 2015. Each pointing had an exposure of ~ 20 ks. We report in Table 1 the log of the data sets.

Table 1. The logs of the joint *XMM-Newton* and *NuSTAR* observations of NGC 4593.

Obs.	Satellites	Obs. Id.	Start time (UTC) yyyy-mm-dd	Net exp. (ks)
1	*XMM-Newton* *NuSTAR*	0740920201 60001149002	2014-12-29	16 22
2	*XMM-Newton* *NuSTAR*	0740920301 60001149004	2014-12-31	17 22
3	*XMM-Newton* *NuSTAR*	0740920401 60001149006	2015-01-02	17 21
4	*XMM-Newton* *NuSTAR*	0740920501 60001149008	2015-01-04	15 23
5	*XMM-Newton* *NuSTAR*	0740920601 60001149010	2015-01-06	21 21

XMM-Newton observed the source using the EPIC cameras (Strüder et al. 2001; Turner et al. 2001) and the Reflection Grating Spectrometer (RGS; den Herder et al. 2001). The EPIC instruments were operating in the Small Window mode, with the medium filter applied. Because of the significantly lower effective area of the MOS detectors, we only report the results obtained from pn data. The data were processed using the *XMM-Newton* Science Analysis System (SAS v14). Source extraction radii and screening for high-background intervals were determined through an iterative process that maximizes the signal-to-noise ratio (Piconcelli et al. 2004). The background was extracted from circular regions with a radius of 50 arcsec, while the source extraction radii were in the range 20–40 arcsec. The EPIC-pn spectra were grouped such that each spectral bin contains at least 30 counts, and not to oversample the spectral resolution by a factor greater than 3. The RGS data were extracted using the standard SAS task `rgsproc`.

The *NuSTAR* data were reduced using the standard pipeline (NUPIPELINE) in the *NuSTAR* Data Analysis Software (NUSTARDAS, v1.3.1; part of the HEASOFT distribution as of version 6.14), using calibration files from *NuSTAR* CALDB v20150316. Spectra and light curves were extracted using the standard tool NUPRODUCTS for each of the two hard X-ray detectors aboard *NuSTAR*, which sit inside the corresponding focal plane modules A and B (FPMA and FPMB). The source data were extracted from circular regions with a radius of 75 arcsec, and background was extracted from a blank area with the same radius, close to the source. The spectra were binned to have a signal-to-noise ratio greater than 5 in each spectral channel, and not to oversample the instrumental resolution by a factor greater than 2.5. The spectra from FPMA and FPMB were analysed jointly but not combined.

In Fig. 1 we show the light curves in different energy ranges of the five *XMM-Newton* and *NuSTAR* observations. The light curves exhibit a strong flux variability, up to a factor of ~ 2, on time-scales as short as a few ks. In Fig. 1 we also show the *XMM-Newton*/pn (2–10 keV)/(0.5–2 keV) hardness ratio light curve and the *NuSTAR* (10–50 keV)/(3–10 keV) hardness ratio light curve. These light curves show a significant spectral variability, particularly in the softer band, with a less prominent variability in the harder band. From these plots, it can be seen that a higher flux is associated with a lower hardness ratio, i.e. we observe a “softer when brighter” behaviour (see also Ursini et al. 2016). During the first observation, both flux and spectral variability are particularly strong. To investigate the nature of these variations, we analysed the spectra of each observation separately, splitting only the first observation into two ~ 10 ks long bits (see Fig. 1). We did not split the time intervals for

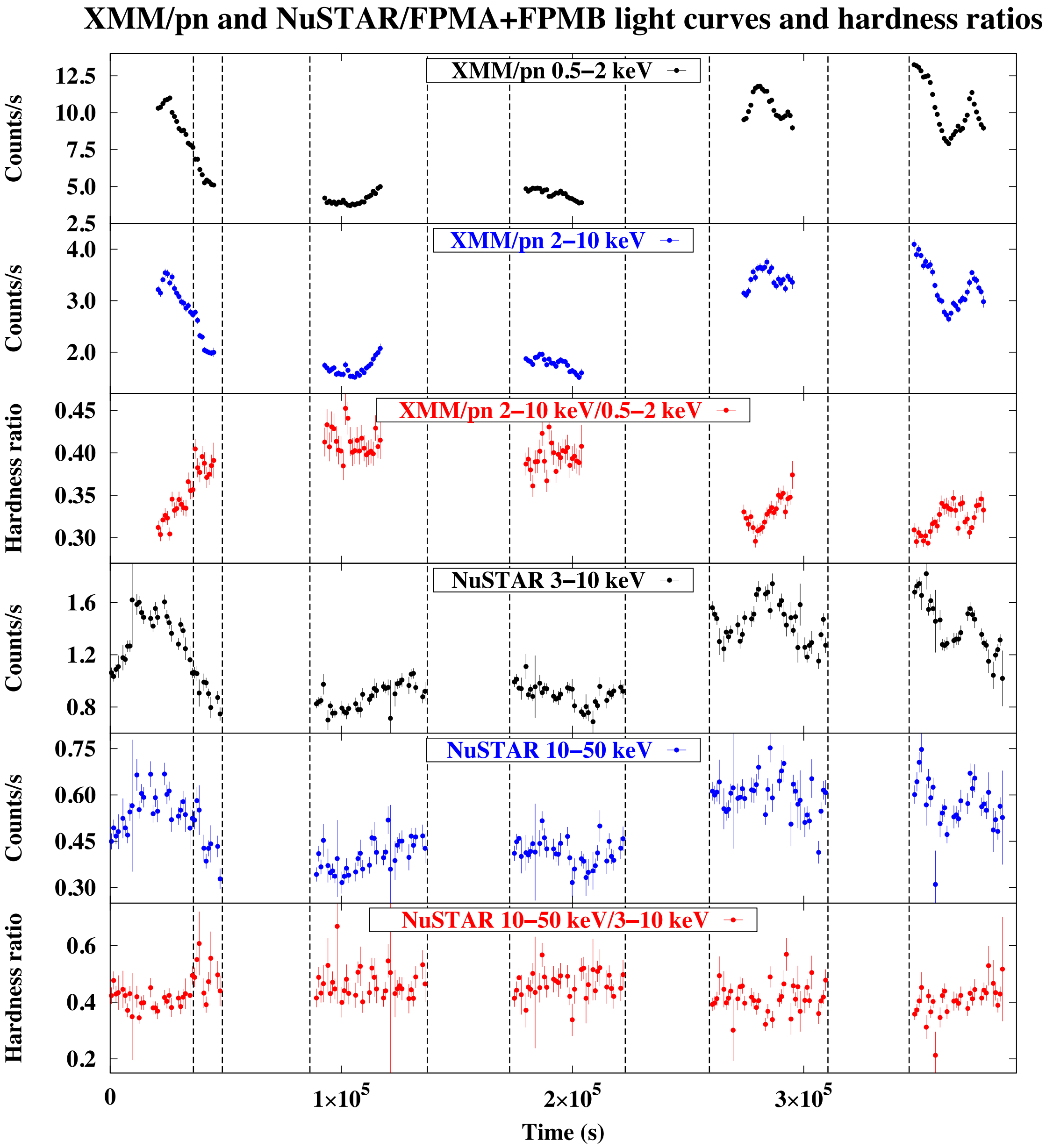

Figure 1. The light curves of the five joint *XMM-Newton* and *NuSTAR* observations of NGC 4593. Time bins of 1 ks are used. Top panel: the *XMM-Newton*/pn count-rate light curve in the 0.5–2 keV band. Second panel: the *XMM-Newton*/pn count-rate light curve in the 2–10 keV band. Third panel: the *XMM-Newton*/pn hardness ratio (2–10/0.5–2 keV) light curve. Fourth panel: the *NuSTAR* count-rate light curve in the 3–10 keV band (FPMA and FPMB data are co-added). Fifth panel: the *NuSTAR* count-rate light curve in the 10–50 keV band. Bottom panel: the *NuSTAR* hardness ratio (10–50/3–10 keV) light curve. The vertical dashed lines separate the time intervals used for the spectral analysis.

the extraction of the spectra further, because in the other observations the spectral variability is less pronounced. This choice leaves us with a total of six spectra from our campaign, which we analyse in the following.

3 SPECTRAL ANALYSIS

Spectral analysis and model fitting was carried out with the XSPEC 12.8 package (Arnaud 1996). RGS spectra were not binned and were analysed using the C-statistic (Cash 1979), to take advantage of the high spectral resolution of the gratings. Broad-band (0.3–80 keV) fits were instead performed on the binned EPIC-pn and *NuSTAR* spectra, using the χ^2

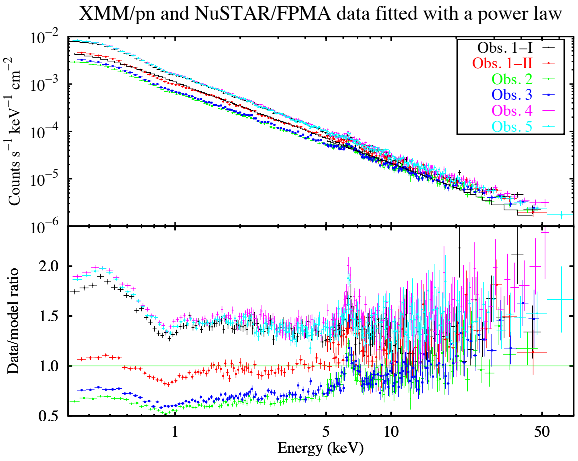

Figure 2. Upper panel: the six *XMM-Newton*/pn and *NuSTAR* spectra of NGC 4593. Lower panel: the ratio of the six spectra to a single power law. Only *NuSTAR*/FPMA data are shown for clarity.

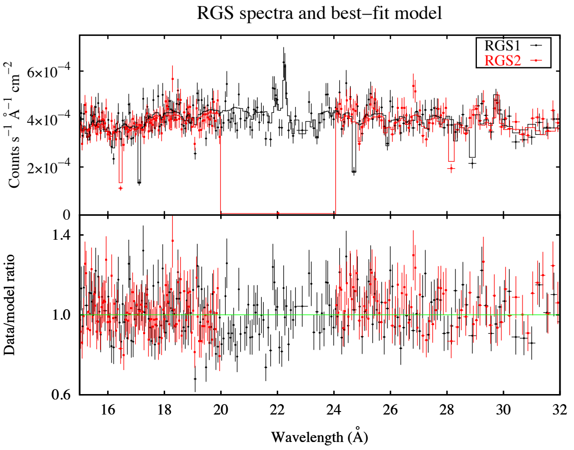

Figure 3. Upper panel: the *XMM-Newton*/RGS spectra (15–32 Å) with the best-fitting model. Data are rebinned for displaying purposes only. Lower panel: the ratio of the spectra to the model.

minimisation technique. All errors are quoted at the 90% confidence level ($\Delta C = 2.71$ or $\Delta\chi^2 = 2.71$) for one interesting parameter.

In Fig. 2 we plot the six *XMM-Newton*/pn and *NuSTAR*/FPMA spectra, simultaneously fitted with a power law with tied parameters for comparison. The plot in Fig. 2 shows that the spectral variability is especially strong in the soft band, i.e. below 10 keV. Furthermore, the ratio of the spectra to the power law below 1 keV suggests the presence of a soft excess which is stronger in the high flux states. The prominent feature at 6-7 keV can be attributed to the Fe K α emission line at 6.4 keV (Reynolds et al. 2004; Brenneman et al. 2007; Markowitz & Reeves 2009), as we will discuss in the following.

To fully exploit the data set, we always fitted all the *XMM-Newton*/pn and *NuSTAR*/FPMA and FPMB data simultaneously, allowing for free cross-calibration constants. The FPMA and FPMB modules are in good agreement with pn, with cross-calibration factors of 1.02 ± 0.01 and 1.05 ± 0.01 respectively, fixing the constant for the pn data to unity. All spectral fits include neutral absorption (PHABS model in XSPEC) from Galactic hydrogen with column density $N_{\rm H} = 1.89 \times 10^{22}$ cm^{-2} (Kalberla et al. 2005). We assumed the element abundances of Lodders (2003).

3.1 The RGS spectra

NGC 4593 is known to host a warm absorber from previous observations with *Chandra* and *XMM-Newton* (McKernan et al. 2003; Steenbrugge et al. 2003; Brenneman et al. 2007; Ebrero et al. 2013). The location of this ionized absorber is at least a few pc from the central source (Ebrero et al. 2013), therefore we do not expect it to significantly vary on a few days time-scale. We thus co-added the RGS data from the different epochs, for each detector, to obtain a better signal-to-noise ratio. We fitted the RGS1 and RGS2 co-added spectra in the 0.3–2 keV band. We used a simple model including a power law and the warm absorber. To find a good fit, we needed to include two ionized absorbers, both modelled using the spectral synthesis code CLOUDY (Ferland et al. 2013). We built a CLOUDY table model with an allowed range for the ionization parameter $\log\xi$ of 0.1–4.9 (in units of ergs s^{-1} cm), while the allowed range for the column density is 10^{19}–10^{24} cm^{-2}. These ranges are suitable for both absorption components. Starting with a fit including only one absorption component, we find C/dof = 6131/5388. Adding a second component, we find C/dof = 5941/5384 (ΔC/Δdof = $-190/-4$) and positive residuals around 22 and 29 Å, that may be attributed to the K α triplets of the He-like ions O VII and N VI. To constrain the parameters of such emission lines, we performed two local fits at the corresponding wavelengths, on intervals $\sim$ 100 channels wide. Due to the small bandwidth, the underlying continuum is not sensitive to variations of the photon index. We thus fixed it at 2, leaving free the normalization of the power law. With such fits, we detect four significant (at 90% confidence level) emission lines. We identify the lines as the intercombination ($1s^2\,{}^1S_0 - 1s2p\,{}^3P_{2,1}$) and forbidden ($1s^2\,{}^1S_0 - 1s2s\,{}^3S_1$) components of the O VII K α triplet, and the resonance ($1s^2\,{}^1S_0 - 1s2p\,{}^1P_1$) and forbidden components of the N VI K α triplet (see Table 2). We first modelled these lines using four Gaussian components. After including the lines in the fit over the whole energy range, we find C/dof = 5869/5376 (i.e. ΔC/Δdof = $-72/-8$). Then, we replaced the Gaussian lines with the emission spectrum from a photoionized plasma, modelled with a CLOUDY table having the ionization parameter, the column density and the normalization as free parameters. We find a nearly equivalent fit, C/dof = 5866/5379 (ΔC/Δdof = $-3/+3$) and no prominent residuals that can be attributed to strong atomic transitions (see Fig. 3). The best-fitting parameters of the warm absorbers and of the emitter are reported in Table 3.

Table 2. The emission lines detected in RGS spectra. λ_T and E_T are the theoretical wavelength and energy of the lines (rest-frame), as reported in the ATOMDB database (Foster et al. 2012). σ is the intrinsic line width and v is the velocity shift with respect to the systemic velocity of NGC 4593; these two parameters were fixed between lines of the same multiplet. The flux is in units of 10^{-5} photons cm^{-2} s^{-1}.

line id.	λ_T (Å)	E_T (keV)	σ (eV)	v (km s^{-1})	flux
O VII (f)	21.091	0.561	$0.7^{+0.4}_{-0.6}$	-450 ± 110	$6.2^{+2.0}_{-1.9}$
O VII (i)	21.795	0.569	-	-	$2.3^{+1.8}_{-1.6}$
N VI (r)	28.738	0.431	< 1	-360^{+270}_{-180}	$4.0^{+1.4}_{-3.2}$
N VI (f)	29.528	0.420	-	-	$4.6^{+2.7}_{-2.1}$

Table 3. Best-fitting parameters of the warm absorbers (WA1, WA2) and photoionized emission (EM), for the RGS spectra. For all these models, ξ is the ionization parameter, σ_v is the turbulent velocity, $N_{\rm H}$ is the column density and v is the velocity shift with respect to the systemic velocity of NGC 4593; $N_{\rm EM}$ is the normalization of the photoionized emission table.

$\log \xi_{\rm WA1}$ (ergs s^{-1} cm)	2.22 ± 0.01
$\log \sigma_{v,\rm WA1}$ (km s^{-1})	1.72 ± 0.07
$\log N_{\rm H,WA1}$ (cm^{-2})	$21.83^{+0.07}_{-0.02}$
$v_{\rm WA1}$ (km s^{-1})	-870 ± 60
$\log \xi_{\rm WA2}$ (ergs s^{-1} cm)	0.43 ± 0.08
$\log \sigma_{v,\rm WA2}$ (km s^{-1})	unconstr.
$\log N_{\rm H,WA2}$ (cm^{-2})	20.90 ± 0.02
$v_{\rm WA2}$ (km s^{-1})	-300 ± 200
$\log \xi_{\rm EM}$ (ergs s^{-1} cm)	0.56 ± 0.03
$\log \sigma_{v,\rm EM}$ (km s^{-1})	unconstr.
$\log N_{\rm H,EM}$ (cm^{-2})	> 21.4
$v_{\rm EM}$ (km s^{-1})	-720 ± 60
$N_{\rm EM}$ ($\times 10^{-18}$)	6 ± 1

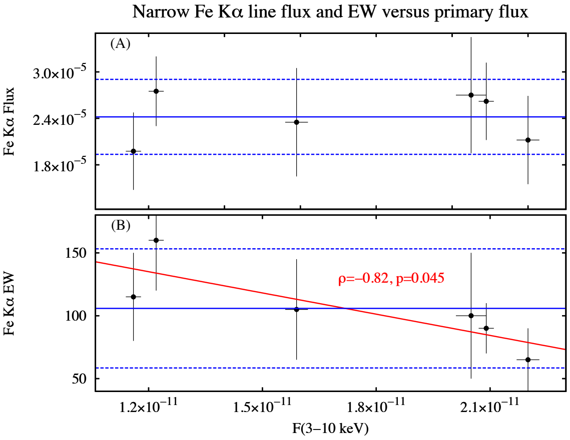

Figure 4. Parameters of the narrow Fe K α line at 6.4 keV, plotted against the primary flux in the 3–10 keV band. Panel (A): the line flux in units of photons cm^{-2} s^{-1}. Panel (B): the line equivalent width (EW) in units of eV. Error bars denote the 1-σ uncertainty. The blue solid lines represent the mean value for each parameter, while the blue dashed lines represent the standard deviation (i.e. the root mean square of the deviations from the mean). The red line represents a linear fit to the data.

3.2 The Fe K α line

We next investigated the properties of the Fe K α line at 6.4 keV. We focused on *XMM-Newton*/pn data, given their better energy resolution compared with *NuSTAR* in that energy band. We fitted the six pn spectra between 3 and 10 keV, to avoid the spectral complexities in the soft X-ray band. The model included a power law plus a Gaussian line at 6.4 keV. Due to a known calibration problem in pn data, the energy of the Gaussian line is blueshifted by ~ 50 eV with respect to the theoretical value of 6.4 keV (for a detailed discussion, see Cappi et al. 2016). The shifts vary between different observations and are present using either single plus double or single-only events, despite the use of the latest correction files for charge transfer inefficiency (CTI) and procedure as described in Smith et al. (2014, XMM-CCF-REL-323[1]). This is likely an effect of the long-term degradation of the EPIC/pn CTI. To correct for such uncertainty, we fixed the Gaussian line energy at 6.4 keV, implying production by "cold" iron, i.e. less ionized than Fe XII, while leaving the redshift free to vary in pn data. We find an acceptable fit (χ^2/dof $= 648/571$) assuming an intrinsically narrow line, i.e. its intrinsic width σ is fixed at zero. If σ is left free, we find a slightly better fit (χ^2/dof $= 643/570$, i.e. $\Delta\chi^2/\Delta$dof $= -5/-1$), with $\sigma = 50 \pm 30$ eV and a probability of chance improvement (calculated with the F-test) around 0.04.

We then looked for the presence of a broad line component at 6.4 keV. We added a second Gaussian line at 6.4 keV, leaving free the intrinsic width of both lines. The fit improves significantly (χ^2/dof $= 608/563$, i.e. $\Delta\chi^2/\Delta$dof $= -35/-7$). The narrow line component has now an intrinsic width consistent with zero, therefore we fixed it at $\sigma = 0$. The broad component has $\sigma = 450^{+110}_{-70}$ eV. We report in Fig. 4 and 5 the flux and equivalent width of both the narrow and broad components, plotted against the primary flux in the 3–10 keV band. The strong variability of the primary flux is not accompanied by a corresponding variability of the narrow line flux, which is consistent with being constant. As a consequence, the equivalent width is anticorrelated with the primary flux. The Pearson's coefficient is -0.82, with a p value of 4.5×10^{-2}. The broad line flux, instead, shows hints of variability (a fit with a constant gives a reduced chi-square of 1.44), while the equivalent width is consistent with being constant (a fit with a constant gives a reduced chi-square of 0.67; the Pearson's coefficient is -0.55, with a p value of 0.25). However, by including only two Gaussian lines at 6.4 keV, we find positive residuals around 7 keV which could be a potential signature of line emission from ionized iron, such as the K α line of Fe XXVI at 6.966 keV (rest-frame), or of the K β line of neutral iron at 7.056 keV. Brenneman et al. (2007) found evidence for a narrow, hydrogen-like Fe K α

---

[1] http://xmm2.esac.esa.int
/docs/documents/CAL-SRN-0323-1-1.ps.gz

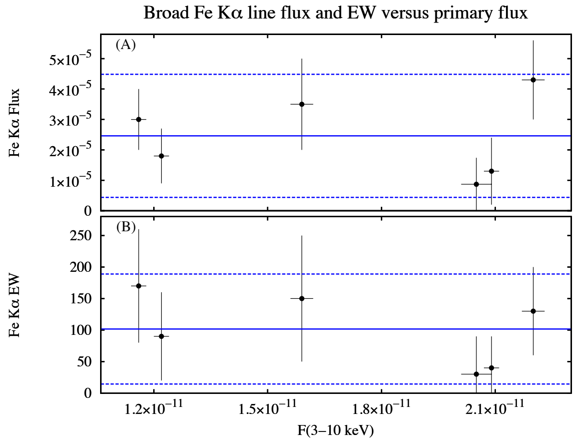

Figure 5. Parameters of the broad Fe K α line at 6.4 keV, plotted against the primary flux in the 3–10 keV band. Panel (A): the line flux in units of photons cm^{-2} s^{-1}. Panel (B): the line equivalent width (EW) in units of eV. Error bars denote the 1-σ uncertainty. The blue solid lines represent the mean value for each parameter, while the blue dashed lines represent the standard deviation.

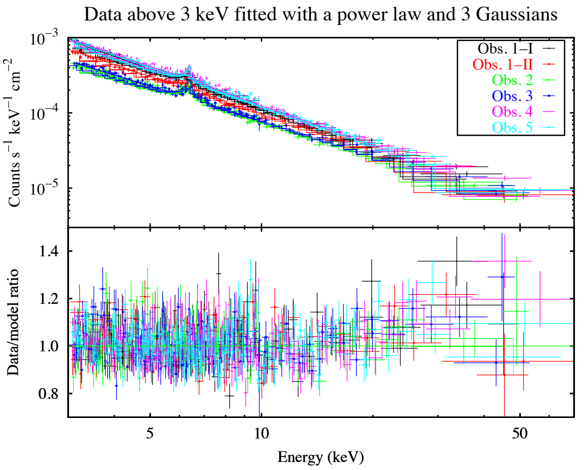

Figure 6. Upper panel: the pn and *NuSTAR* spectra above 3 keV fitted with a model including a simple power law and three Gaussian lines. Lower panel: the ratio of the spectra to the model, showing an excess around 30 keV. The data were binned for plotting purposes.

emission line in this source by using *XMM-Newton*/pn data. Markowitz & Reeves (2009) found only an upper limit on the presence of this line by using *Suzaku* data, but instead found a significant neutral Fe K β line. To test for the presence of such components, we included a third, narrow Gaussian line. We kept the line flux tied between different observations. Fixing the line energy at 6.966 keV, we find $\chi^2/\mathrm{dof} = 596/573$ ($\Delta\chi^2/\Delta\mathrm{dof} = -20/-1$), and no improvement by adding another Gaussian line at 7.056 keV. The fit is only slightly worse if we fix the energy of the third line at 7.056 keV instead of 6.966 keV ($\Delta\chi^2 = +2$). We measure a flux of $(6 \pm 2) \times 10^{-6}$ photons cm^{-2} s^{-1} for this line, and an equivalent width ranging from 25 ± 10 eV to 40 ± 20 eV. The ratio of the flux to that of the narrow Fe K α line is 0.25 ± 0.14, roughly consistent with the predicted ratio of fluorescence yields for K β/K α (~ 0.13, see Kaastra & Mewe 1993; Molendi et al. 2003). Finally, we note that the intrinsic width of the broad component at 6.4 keV is now found to be $\sigma = 300^{+130}_{-70}$ eV, while all the other parameters of the narrow and broad components are not significantly altered by the addition of the third line. We also tried to thaw the energy of the broad component, to test if it could be due to ionized material. However, the fit is not significantly improved, and the line energy is found to be $E = 6.44 \pm 0.11$ keV.

Overall, these results are consistent with the cold, narrow Fe K α line being produced by reflection off relatively distant material, lying at least a few light days away from the nucleus. A statistically significant broad component is detected, showing hints of variability, albeit with no clear trend with respect to the primary flux. The results on the iron lines are summarized in Table 4. Finally, we had a first look at the presence of reflection components associated with the iron lines, using the energy range from 3 keV up to 79 keV. We fitted the *XMM-Newton*/pn and *NuSTAR* data with a simple power law plus three Gaussian emission lines, i.e. the narrow lines at 6.4 keV and 6.966 keV and the broad component at 6.4 keV, finding $\chi^2/\mathrm{dof} = 2084/1923$. The residuals indicate the presence of a moderate Compton hump peaking at around 30 keV (see Fig. 6).

3.3 The broad-band fit

After getting a clue to the origin of the iron line and to the presence of a reflection component, we fitted the pn and *NuSTAR* data in the whole X-ray energy range (0.3–79 keV). We modelled the primary continuum with a cut-off power law. The other components are described below. In XSPEC notation, the model reads: PHABS*WA1*WA2*(SOFT LINES + CUTOFFPL + DISKBB + RELXILL + XILLVER), where WA1, WA2 and SOFT LINES denote the CLOUDY tables described in Sec. 3.1.

The reflection component: In Sect. 3.2, we found the presence of both a narrow and a broad Fe K α line components together with a Compton hump. We thus modelled the reflection component with XILLVER (García & Kallman 2010; García et al. 2013) and RELXILL (García et al. 2014) in XSPEC. Both models self-consistently incorporate fluorescence lines and the Compton reflection hump, and in RELXILL such components are relativistically blurred. We used the XILLVER-A-EC4 version, which takes into account the angular dependence of the emitted radiation and includes a primary power law with an exponential cut-off up to 1 MeV[2], and the RELXILL version 0.4c[3]. Since the inclination angle of both reflectors was poorly constrained, we fixed it to 50 deg, consistently with past studies on this source (Nandra et al. 1997; Guainazzi et al. 1999). We assumed for XILLVER and RELXILL the same iron abundance A_{Fe}, which was a free

---

[2] `http://hea-www.cfa.harvard.edu/~javier/xillver/`

[3] http://www.sternwarte.uni-erlangen.de / dauser/research/relxill/index.html

Table 4. The properties of the iron K emission lines (see text and Figs. 4, 5 for the details). E is the energy of the lines (rest-frame), σ is the intrinsic line width and EW is the equivalent width. The flux is in units of 10^{-5} photons cm^{-2} s^{-1}. Parameters in italics were frozen.

E (keV)	σ (eV)	average flux	average EW (eV)
6.4 (narrow)	*0*	2.42	106
6.4 (broad)	300^{+130}_{-70}	2.36	102
7.056	*0*	0.6	30

parameter of the fit, but tied between the different observations.

In RELXILL, the normalization was left free to vary between the different observations. The input photon index and cut-off energy were tied to that of the primary power law, as this reflection component was assumed to originate relatively close to the primary source. *A priori*, also the ionization could change among the observations, responding to the different ionizing flux from the primary source. However, the ionization parameter was always found to be consistent with a common value of $\log\xi \simeq 3$, therefore we tied this parameter between the different observations. Similarly, the inner radius of the disc was a free parameter of the fit, but tied between the different observations since it was consistent with being constant. Since the emissivity index was poorly constrained, we fixed it at 3 (the classical case, see e.g. Wilkins & Fabian 2012). We found no improvement by assuming a broken power law for the emissivity profile. Moreover, since the black hole spin parameter a was poorly constrained, we assumed $a = 0.998$.

The XILLVER component was consistent with being constant, being associated with the narrow, constant component of the Fe K α line. The normalization was a free parameter of the fit, but tied between the different observations. Since the input photon index and cut-off energy of XILLVER were poorly constrained, we fixed them to the average values of the photon indexes and of the cut-off energies of the primary power law found in each observation. We fixed the ionization parameter at the minimum value in XILLVER, $\log\xi = 0$, with no improvement by leaving it free.

We also tested the possibility that the iron line and the reflection hump are not directly correlated. We thus included an additional narrow Gaussian line at 6.4 keV, not related to the reflection components. Such a line could originate from Compton-thin gas, which does not produce a significant Compton hump (e.g., Bianchi et al. 2008). However, the fit is only marginally improved, and the parameters of the reflection components are not significantly altered. Therefore, for the sake of simplicity, we included only XILLVER and RELXILL in our model.

The warm absorber and soft lines: Following Sect. 3.1, we included two ionized absorbers and the soft X-ray emission lines found with RGS, modelled with CLOUDY. To account for cross-calibration uncertainties between pn and RGS, especially below 0.5 keV, the parameters of the absorbers were left free, but kept constant between the different observations. We found no significant improvement by leaving the warm absorber free to vary between the different observations. The CLOUDY table for the emission lines was fixed to the RGS best-fitting values, as it was poorly constrained by pn data. This reflected spectrum also adds a weak contribution in the hard X-ray band, because it produces self-consistently an iron line and a reflection hump (see Fig. 7).

We also tested a partial covering scenario for the warm absorbers. However, we find that if the covering fraction of both components is allowed to vary, it is consistent with 1.

The soft excess: Ionized reflection alone does not explain all the observed soft excess in this source, because including only the reflection components leaves strong, positive residuals below 1 keV. We modelled the soft excess phenomenologically with a multicolour disc blackbody component, through the DISKBB model in XSPEC (Mitsuda et al. 1984; Makishima et al. 1986). The normalization was left free to vary between different observations, while the inner disc temperature was found to be consistent with a common value of around 110 eV, thus it was tied between the different observations.

In Fig. 7 we show the data, residuals and best-fitting model, while all the best-fitting parameters are reported in Table 5. According to our results, the unblurred reflection component (XILLVER) is consistent with being constant and due to neutral matter. The reflection strength $\mathcal{R}_{s,\textsc{xillver}}$, calculated as the ratio between the 20–40 keV flux of the XILLVER component and the 20–40 keV primary flux, ranges between ~ 0.35 and ~ 0.6. This ratio is slightly different from the traditional reflection fraction $\mathcal{R}_f = \Omega/2\pi$, where Ω is the solid angle subtended by the reflector (Magdziarz & Zdziarski 1995). We discuss this further in Sect. 4. The blurred component (RELXILL) is due to an ionized disc with $\xi \sim 1000$ ergs s^{-1} cm, and with an inner radius $R_{\rm in} \simeq 40\ R_{\rm G}$. The reflection strength $\mathcal{R}_{s,\textsc{relxill}}$, i.e. the ratio between the 20–40 keV flux of RELXILL and that of the 20–40 keV primary flux, ranges between ~ 0.15 and ~ 0.25. Analogous results are found calculating the ratio between fluxes in a broader energy range, such as 0.1–100 keV (e.g., Wilkins et al. 2015). With this choice, we find similar values for $\mathcal{R}_{s,\textsc{relxill}}$, while for $\mathcal{R}_{s,\textsc{xillver}}$ we find 0.15–0.35. However, using the 20–40 keV range is likely more appropriate, as the reflection spectrum in that band is dominated by Compton scattering, only weakly depending on the iron abundance or the ionization state (Dauser et al. 2016). We also estimated the equivalent width of the broad iron line associated with RELXILL, finding values consistent with those measured in Sec. 3.2, namely 100–150 eV.

Concerning the primary continuum, we find significant variations of the photon index (up to $\Delta\Gamma \simeq 0.2$) and of the high-energy cut-off. The contour plots of the cut-off energy versus photon index are shown in Fig. 8. To check the significance of the cut-off energy variability, we repeated the fit keeping the cut-off energy $E_{\rm c}$ tied between the different observations. We find $E_{\rm c} = 420^{+400}_{-130}$ keV, however the fit is significantly worse ($\Delta\chi^2/\Delta{\rm dof} = +48/+5$ with a p value of 3×10^{-8} from an F-test). We also performed a fit to the co-added pn and *NuSTAR* spectra (see Table 5), finding a photon index of 1.84 ± 0.01 and a cut-off energy > 640 keV. More importantly, the parameters are consistent with those that were kept constant in the simultaneous fit of the single observations.

A multicolour disc black-body with an inner temperature of ∼ 110 eV is found to describe well the soft excess seen on top of the primary power law and of the ionized reflection component. We note that, if the primary power law is due to Comptonization, it should have a low-energy roll-over dependent on the temperature of the seed photons, which could enhance the soft excess. However, if the seed photons are in the optical/UV band, the effect is negligible when fitting the data above 0.3 keV (see also the discussion in Sect. 4). We also found a significant correlation between the soft excess flux and the primary emission. We show in Fig. 9 the 3–10 keV flux of the primary power law, the 10–50 keV flux and the photon index, plotted against the DISKBB flux in the 0.3–2 keV band. The correlation between the DISKBB flux and the soft primary flux has a Pearson's coefficient of 0.98 and a p value of 8×10^{-4}. For the hard band, the Pearson's coefficient is 0.95, with a p value of 3.3×10^{-3}. For the photon index, the Pearson's coefficient is 0.97, with a p value of 1.8×10^{-3}. A detailed modelling of the soft excess is beyond the scope of this paper, and it is deferred to a following paper.

4 DISCUSSION AND CONCLUSIONS

We reported results based on a joint *XMM-Newton* and *NuSTAR* monitoring of NGC 4593, aimed at studying the broadband variability of this AGN in detail.

The source shows a remarkable variability, both in flux and in spectral shape, on time-scales of a few days and down to a few ks. While flux variability is significant at all energies, the spectral variability is mostly observed below 10 keV. Moreover, the spectrum is softer when the source is brighter, as generally found in luminous Seyfert galaxies (e.g., Markowitz et al. 2003; Sobolewska & Papadakis 2009; Soldi et al. 2014). If the X-ray emission is produced by Comptonization, the relation between observed flux and photon index can be understood as an effect of that process. The spectral shape primarily depends on the optical depth and temperature of the Comptonizing corona, albeit in a non-trivial way (e.g., Sunyaev & Titarchuk 1980). The photon index can be also related to the Compton amplification ratio, i.e. the ratio between the total corona luminosity and the soft luminosity that enters and cools the corona. A higher amplification ratio corresponds to a harder spectrum (e.g., Haardt & Maraschi 1993). In the limiting case of a "passive" disc, which is not intrinsically radiative but rather reprocesses the coronal emission, the amplification ratio is fixed by geometry alone (e.g., Haardt & Maraschi 1991; Stern et al. 1995). Then, in steady states (i.e. the system is in radiative equilibrium), the coronal optical depth and temperature adjust to keep the amplification ratio constant. But the amplification ratio can change following geometry variations of the accretion flow. For example, the inner radius of the disc may be different from the innermost stable circular orbit (as suggested by the fit with the relativistic reflection) and change in time[4], causing a decrease of the soft luminosity supplied by the disc. This, in turn, may increase the amplification ratio, leading to a harder spectrum. This kind of behaviour is especially apparent during obs. 1, where a significant flux drop (a factor of ∼ 2 in the 0.5–2 keV count rate) is accompanied by a significant hardening of the spectrum ($\Delta\Gamma \simeq 0.15$).

However, we also find a significantly variable high-energy cut-off (see Fig. 8). In particular, the lowest cut-off is seen during obs. 2, where $E_{\rm c} = 90^{+40}_{-20}$ keV. This corresponds to the hardest spectrum, with $\Gamma \simeq 1.6$. For the softest spectra, like obs. 1-I and obs. 5, we only find a lower limit on $E_{\rm c}$ of several hundreds of keV. Since the cut-off energy is generally related to the coronal temperature ($E_{\rm c} \simeq$ 2-3 kT, e.g. Petrucci et al. 2001), our results might suggest that this temperature undergoes huge variations (from a few tens up to a few hundreds of keV) during a few days. However, it should be noted that the turnover of a Comptonized spectrum is much sharper than a simple exponential cut-off (e.g., Zdziarski et al. 2003). Then, fitting the data with a cut-off power law provides only a phenomenological description that does not allow for an unambiguous physical interpretation (e.g., Petrucci et al. 2001).

We confirm the presence of a warm absorber affecting the soft X-ray spectrum. Ebrero et al. (2013), using a 160 ks *Chandra* data set, found evidence for a multi-phase ionized outflow with four distinct degrees of ionization, namely $\log\xi = 1.0, 1.7, 2.4$ and 3.0. The low-ionization components were found to have lower velocities (300-400 km s^{-1}) than the high-ionization components (up to ∼ 1000 km s^{-1}). According to our results, a two-phase ionized outflow provides an adequate characterization of this gas, both for RGS and pn spectra. These two components have different degrees of ionization, namely $\log\xi \simeq$ 2.2-2.5 and 0.1-0.4, and different column densities, $N_{\rm H} \simeq (2\text{-}7) \times 10^{21}$ and $(0.8\text{-}1.2) \times 10^{21}$ cm^{-2}, with uncertainties due to the different estimates based on pn and RGS data. The two components are also kinematically distinct, with the high-ionization component outflowing faster ($v \simeq -900$ km s^{-1}) than the low-ionization one ($v \simeq -300$ km s^{-1}). We can derive a rough upper limit on the distance of such components in the following way (see also Ebrero et al. 2013). By definition, $\xi = L_{\rm ion}/nR^2$, where $L_{\rm ion}$ is the ionizing luminosity in the 1–1000 Ryd range, n is the hydrogen gas density and R the distance. If we assume that the gas is concentrated within a layer with thickness $\Delta r \leqslant R$, we can write $R \leqslant L_{\rm ion}/N_{\rm H}\xi$, where $N_{\rm H} = n\Delta r$. The average ionizing luminosity that we obtain from our best-fitting model is $\sim 1 \times 10^{43}$ ergs s^{-1}. Then, from the measurements of $N_{\rm H}$ and ξ we get an upper limit on R. For the high-ionization component we estimate $R \lesssim 3$ pc, while for the low-ionization component $R \lesssim 1.5$ kpc. The outflows are thus consistent with originating at different distances from the nucleus, as found by Ebrero et al. (2013), with the high-ionization and high-velocity component possibly being launched closer to the central source.

We find evidence for a cold, narrow Fe K α line which is consistent with being constant during the monitoring. A broad component is also detected, and is consistent with originating at a few tens of gravitational radii from the black

---

[4] We do not detect significant variations of the inner radius of the RELXILL reflection component. However, given the uncertainty, we cannot exclude variations by up to a factor of 2 (from ∼ 25 to ∼ 50 $R_{\rm G}$).

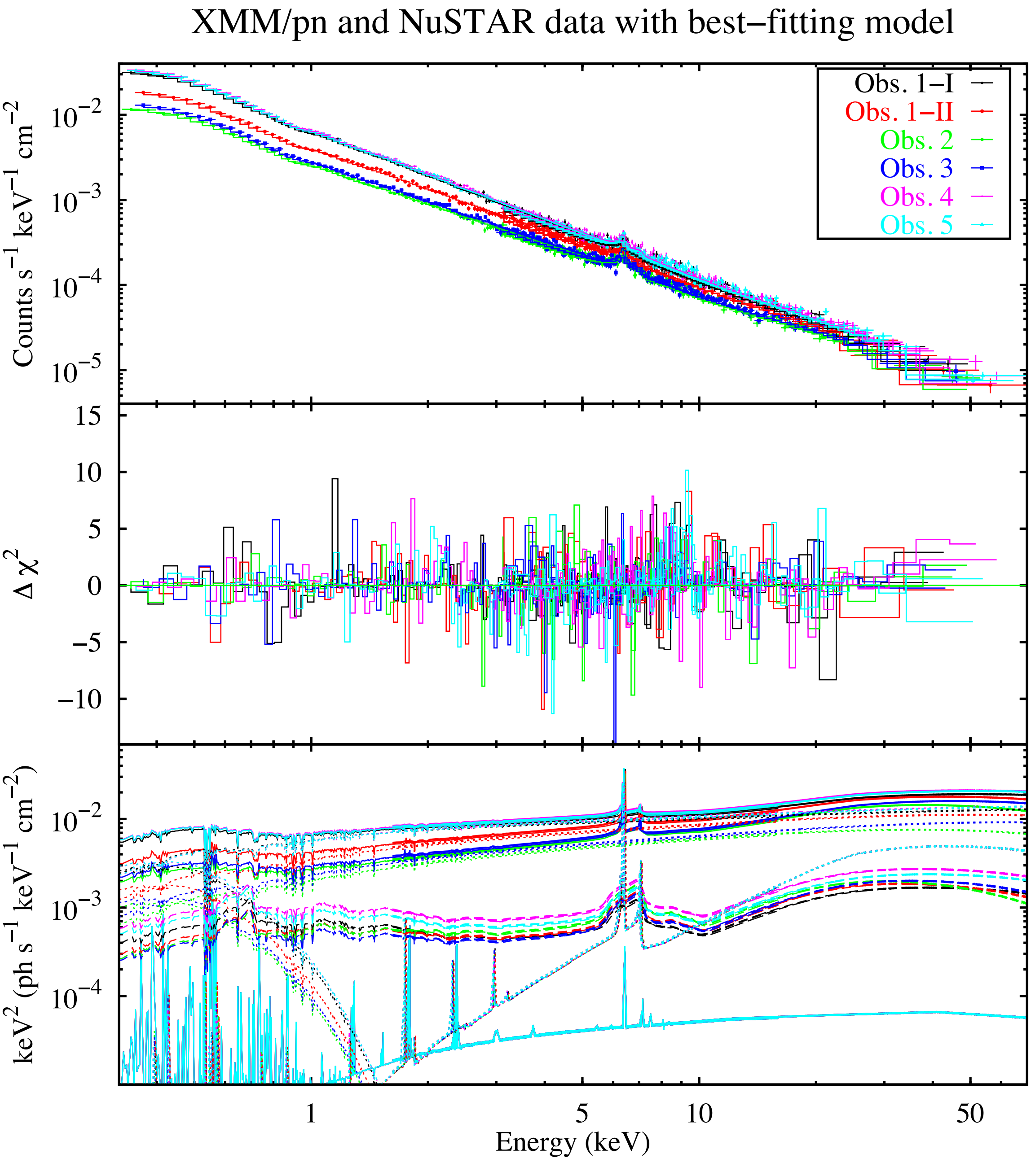

Figure 7. Broad-band X-ray data and best-fitting model (see Table 5). Upper panel: *XMM-Newton*/pn and *NuSTAR* data and folded model. Middle panel: contribution to χ^2. Lower panel: best-fitting model $E^2 f(E)$, with the plot of the reflection components XILLVER (dotted line) and RELXILL (dashed lines), the CLOUDY model for the soft emission lines with associated reflected continuum (solid line), and the DISKBB component for the soft excess (dotted lines). The data were rebinned for plotting purposes.

hole. The Fe K α line is accompanied by a moderate Compton hump (the total reflection strength is approximately 0.5–0.8). All these features are well modelled by including two different reflection components, both requiring an iron overabundance of 2-3. One component (XILLVER) is responsible for the narrow core of the Fe K α line, and is consistent with arising from a slab of neutral, Compton-thick material. This component is also consistent with being constant, despite the observed strong variability of the primary continuum. The variability of the primary emission can be diluted in a distant reflector, if the light-crossing time across the reflecting region is more than the variability time-scale of the primary continuum. In this case, the reflector responds to a time-averaged illumination from the primary source. Therefore,

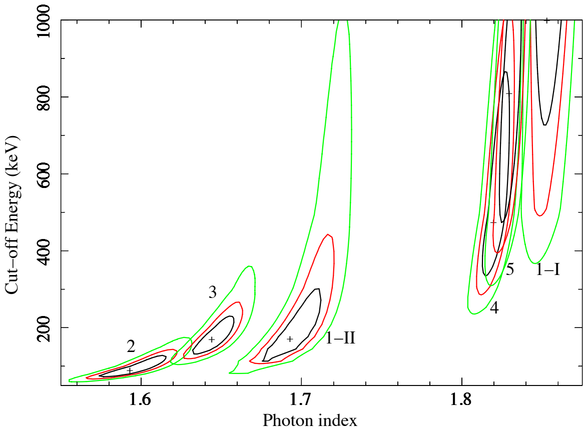

Figure 8. Contour plots of the primary continuum cut-off energy versus photon index for each observation (see also table 5). Green, red and black lines correspond to 99%, 90% and 68% confidence levels, respectively.

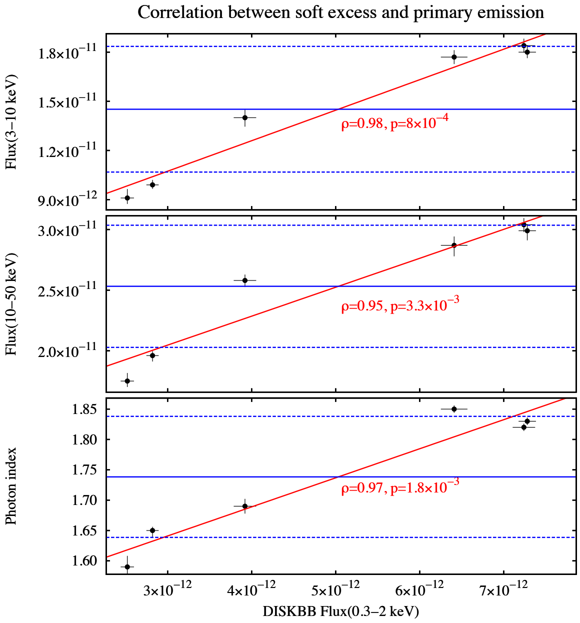

Figure 9. Three parameters of the primary power law plotted against the flux of the soft excess (calculated as the 0.3–2 keV flux of the DISKBB component, see Sect. 3.3). Upper panel: primary flux in the 3–10 keV range. Middle panel: primary flux in the 10–50 keV range. Lower panel: primary photon index. All fluxes are in units of ergs s^{-1} cm^{-2}. The blue solid lines represent the mean value for each parameter, while the blue dashed lines represent the standard deviation. The red lines represent linear fits to the data.

the reflecting material should lie at least a few light days away from the primary source, and it can be interpreted as the outer part of the accretion disc. The reflection strength $\mathcal{R}_{s,\textsc{xillver}}$, namely the ratio between the reflected and the primary flux in the 20–40 keV band, is in the range 0.35–0.6. According to Dauser et al. (2016), the reflection strength is likely an underestimate of the reflection fraction $\mathcal{R}_f$, defined as the ratio between the primary intensity illuminating the disc and the intensity reaching the observer. The difference is that $\mathcal{R}_s$ depends on the inclination of the reflector, while $\mathcal{R}_f$ does not. For an isotropic source, $\mathcal{R}_f = \Omega/2\pi$, where Ω is the solid angle covered by the reflector as seen from the primary source. Dauser et al. (2016) report $\mathcal{R}_s \simeq 0.7$ when $\mathcal{R}_f$ is set to 1 in XILLVER, for an inclination angle of 50 deg. Therefore, in our case, we estimate $\mathcal{R}_{f,\textsc{xillver}}$ to be in the range 0.5–0.85. This would correspond to a solid angle between π and 1.7π. However, there are a few caveats. First, if the reflecting material is more distant (e.g. a torus at pc scales), the reflection fraction might not be closely related to the viewing angle (e.g., Malzac & Petrucci 2002). Furthermore, the X-ray emitting corona could be outflowing or inflowing rather than being static (Beloborodov 1999; Malzac et al. 2001). In this case, the reflection fraction would depend also on the velocity of the corona, because the relativistic beaming would result in an anisotropic illumination (Malzac et al. 2001).

The second reflection component (RELXILL) is responsible for the broad Fe K α line, and is consistent with originating from the inner part of the accretion disc, down to ~ 40 $R_{\rm G}$. Given the black hole mass of $\sim 1 \times 10^7$ solar masses, a distance of 40 $R_{\rm G}$ corresponds to a light-travel time of ~ 2 ks. Indeed, this reflection component appears to respond to the variability of the primary continuum (see Table 5 and Fig. 5 from the phenomenological fit of the broad Fe K α line with a Gaussian component). A more detailed discussion is deferred to a forthcoming paper, where a timing analysis will be performed (De Marco et al., in prep.). The reflection strength $\mathcal{R}_{s,\textsc{relxill}}$ is ~ 0.2, and the effects of light bending in RELXILL may complicate the geometrical interpretation (Dauser et al. 2016). However, given the relatively large inner disc radius, we do not expect a strong modification of the reflection fraction (e.g., Dauser et al. 2014). Using the same relations as for XILLVER, we find a covering angle $\Omega \simeq \pi$. Finally, our results suggest that a slightly larger $\mathcal{R}_{s,\textsc{relxill}}$ corresponds to the low-flux states, i.e. to a flatter Γ, whereas a correlation between the photon index and the reflection fraction is usually found in AGNs (e.g. Zdziarski et al. 1999; Malzac & Petrucci 2002). According to Zdziarski et al. (1999), a correlation can be explained if the reflecting medium is also the source of seed soft photons that get Comptonized in the hot corona. In our case, the lack of such a correlation and the presence of a strong soft excess suggest that the source of soft photons and the reflecting medium are not one and the same.

The soft X-ray excess is phenomenologically well described by a variable multicolour disc black-body. Physically, the soft excess could be produced by a warm corona upscattering the optical/UV photons from the accretion disc (see, e.g., Magdziarz et al. 1998; Petrucci et al. 2013). This warm corona could be the upper layer of the disc (e.g., Różańska et al. 2015). The observed correlation between the flux of the soft excess and that of the primary power law (Fig. 9) could indicate that these two components arise from the Comptonization of the same seed photons. Then, the observed correlation between the soft excess and the primary photon index can be seen as a simple consequence of the flux correlation and of the softer-when-brighter behaviour of the primary continuum. However, the actual scenario could be more complex. Assuming that the soft excess is produced by a warm corona, part of this emission (depending on geometry) could be in turn upscattered in the hot corona and contribute to its Compton cooling. In this case, a larger flux from the warm corona would imply a more efficient cooling of the hot corona, thus a softer X-ray emission. These results motivate a further, detailed investigation using realistic Comptonization models, which will be the subject of a forthcoming paper.

ACKNOWLEDGEMENTS

We thank the anonymous referee for helpful comments and suggestions that improved the paper.
This work is based on observations obtained with: the *NuSTAR* mission, a project led by the California Institute of Technology, managed by the Jet Propulsion Laboratory and funded by NASA; *XMM-Newton*, an ESA science mission with instruments and contributions directly funded by ESA Member States and the USA (NASA). This research has made use of data, software and/or web tools obtained from NASA's High Energy Astrophysics Science Archive Research Center (HEASARC), a service of Goddard Space Flight Center and the Smithsonian Astrophysical Observatory. FU, POP, GM, SB, MC, ADR and JM acknowledge support from the french-italian International Project of Scientific Collaboration: PICS-INAF project number 181542. FU, POP acknowledge support from CNES. FU acknowledges support from Université Franco-Italienne (Vinci PhD fellowship). FU, GM acknowledges financial support from the Italian Space Agency under grant ASI/INAF I/037/12/0-011/13. POP acknowledges financial support from the Programme National Hautes Energies. SB, MC and ADR acknowledge financial support from the Italian Space Agency under grant ASI-INAF I/037/12/P1. GP ackowledges support by the Bundesministerium für Wirtschaft und Technologie/Deutsches Zentrum für Luft und Raumfahrt (BMWI/DLR, FKZ 50 OR 1408) and the Max Planck Society.

REFERENCES

Arnaud K. A., 1996, in Jacoby G. H., Barnes J., eds, Astronomical Society of the Pacific Conference Series Vol. 101, Astronomical Data Analysis Software and Systems V. p. 17
Ballantyne D. R., et al., 2014, ApJ, 794, 62
Baloković M., et al., 2015, ApJ, 800, 62
Baumgartner W. H., Tueller J., Markwardt C. B., Skinner G. K., Barthelmy S., Mushotzky R. F., Evans P. A., Gehrels N., 2013, ApJS, 207, 19
Beloborodov A. M., 1999, ApJ, 510, L123
Bianchi S., La Franca F., Matt G., Guainazzi M., Jimenez Bailón E., Longinotti A. L., Nicastro F., Pentericci L., 2008, MNRAS, 389, L52
Bianchi S., Guainazzi M., Matt G., Fonseca Bonilla N., Ponti G., 2009, A&A, 495, 421
Boissay R., et al., 2014, A&A, 567, A44
Brenneman L. W., Reynolds C. S., Wilms J., Kaiser M. E., 2007, ApJ, 666, 817
Brenneman L. W., et al., 2014, ApJ, 788, 61
Cappi M., et al., 2016, preprint, (`arXiv:1604.01777`)
Cash W., 1979, ApJ, 228, 939
Crummy J., Fabian A. C., Gallo L., Ross R. R., 2006, MNRAS, 365, 1067
Dauser T., García J., Parker M. L., Fabian A. C., Wilms J., 2014, MNRAS, 444, L100
Dauser T., García J., Walton D. J., Eikmann W., Kallman T., McClintock J., Wilms J., 2016, A&A, 590, A76
Denney K. D., et al., 2006, ApJ, 653, 152
Done C., Davis S. W., Jin C., Blaes O., Ward M., 2012, MNRAS, 420, 1848
Ebrero J., Kaastra J. S., Kriss G. A., de Vries C. P., Costantini E., 2013, MNRAS, 435, 3028
Elliot J. L., Shapiro S. L., 1974, ApJ, 192, L3
Ferland G. J., et al., 2013, Rev. Mex. Astron. Astrofis., 49, 137
Foster A. R., Ji L., Smith R. K., Brickhouse N. S., 2012, ApJ, 756, 128
García J., Kallman T. R., 2010, ApJ, 718, 695
García J., Dauser T., Reynolds C. S., Kallman T. R., McClintock J. E., Wilms J., Eikmann W., 2013, ApJ, 768, 146
García J., et al., 2014, ApJ, 782, 76
George I. M., Fabian A. C., 1991, MNRAS, 249, 352
Guainazzi M., Perola G. C., Matt G., Nicastro F., Bassani L., Fiore F., dal Fiume D., Piro L., 1999, A&A, 346, 407
Haardt F., Maraschi L., 1991, ApJ, 380, L51
Haardt F., Maraschi L., 1993, ApJ, 413, 507
Haardt F., Maraschi L., Ghisellini G., 1994, ApJ, 432, L95
Haardt F., Maraschi L., Ghisellini G., 1997, ApJ, 476, 620
Harrison F. A., et al., 2013, ApJ, 770, 103
Jansen F., et al., 2001, A&A, 365, L1
Kaastra J. S., Mewe R., 1993, A&AS, 97, 443
Kaastra J. S., et al., 2011, A&A, 534, A36
Kaastra J. S., et al., 2014, Science, 345, 64
Kalberla P. M. W., Burton W. B., Hartmann D., Arnal E. M., Bajaja E., Morras R., Pöppel W. G. L., 2005, A&A, 440, 775
Lodders K., 2003, ApJ, 591, 1220
Lubiński P., et al., 2016, MNRAS, 458, 2454
Magdziarz P., Zdziarski A. A., 1995, MNRAS, 273, 837
Magdziarz P., Blaes O. M., Zdziarski A. A., Johnson W. N., Smith D. A., 1998, MNRAS, 301, 179
Makishima K., Maejima Y., Mitsuda K., Bradt H. V., Remillard R. A., Tuohy I. R., Hoshi R., Nakagawa M., 1986, ApJ, 308, 635
Malizia A., Molina M., Bassani L., Stephen J. B., Bazzano A., Ubertini P., Bird A. J., 2014, ApJ, 782, L25
Malzac J., Petrucci P.-O., 2002, MNRAS, 336, 1209
Malzac J., Beloborodov A. M., Poutanen J., 2001, MNRAS, 326, 417
Marinucci A., et al., 2014, MNRAS, 440, 2347
Markowitz A. G., Reeves J. N., 2009, ApJ, 705, 496
Markowitz A., Edelson R., Vaughan S., 2003, ApJ, 598, 935
Matt G., Perola G. C., Piro L., 1991, A&A, 247, 25
Matt G., Guainazzi M., Maiolino R., 2003, MNRAS, 342, 422
Matt G., et al., 2015, MNRAS, 447, 3029
McKernan B., Yaqoob T., George I. M., Turner T. J., 2003, ApJ, 593, 142
Mehdipour M., et al., 2011, A&A, 534, A39
Mitsuda K., et al., 1984, PASJ, 36, 741
Molendi S., Bianchi S., Matt G., 2003, MNRAS, 343, L1
Nandra K., George I. M., Mushotzky R. F., Turner T. J., Yaqoob T., 1997, ApJ, 477, 602
Perola G. C., Matt G., Cappi M., Fiore F., Guainazzi M., Maraschi L., Petrucci P. O., Piro L., 2002, A&A, 389, 802
Petrucci P. O., et al., 2001, ApJ, 556, 716
Petrucci P.-O., et al., 2013, A&A, 549, A73
Piconcelli E., Jimenez-Bailón E., Guainazzi M., Schartel N., Rodríguez-Pascual P. M., Santos-Lleó M., 2004, MNRAS, 351, 161
Ponti G., Miniutti G., Cappi M., Maraschi L., Fabian A. C., Iwasawa K., 2006, MNRAS, 368, 903

Table 5. Best-fitting parameters of the broad-band (0.3–80 keV) phenomenological model described in Sect. 3.3: WA1*WA2*(SOFT LINES + CUTOFFPL + DISKBB + RELXILL + XILLVER). In the second column we report the fit parameters that were kept constant, i.e. they were constrained by all observations. In the third to eighth column, we report the fit parameters that were free to vary for each observation. In the last column, we report the best-fitting parameters for the summed spectra. Parameters in italics were frozen due to poor constraints.

	all obs.	obs. 1-I	obs. 1-II	obs. 2	obs. 3	obs. 4	obs. 5	summed
$\log \xi_{\rm WA1}$	2.71 ± 0.05							$2.70^{+0.09}_{-0.05}$
$\log \sigma_{v,\rm WA1}$	> 2.2							*2.5*
$\log N_{\rm H,WA1}$	21.4 ± 0.1							21.4 ± 0.1
$\log \xi_{\rm WA2}$	*0.1*							*0.1*
$\log \sigma_{v,\rm WA2}$	$2.01^{+0.01}_{-0.05}$							$2.2^{+0.2}_{-0.4}$
$\log N_{\rm H,WA2}$	$21.09^{+0.01}_{-0.07}$							$21.13^{+0.02}_{-0.03}$
Γ		1.85 ± 0.01	1.69 ± 0.02	$1.59^{+0.03}_{-0.02}$	$1.65^{+0.01}_{-0.02}$	1.82 ± 0.01	1.83 ± 0.01	1.84 ± 0.01
$E_{\rm c}$ (keV)		> 700	170^{+160}_{-60}	90^{+40}_{-20}	170^{+70}_{-40}	470^{+430}_{-150}	> 450	> 640
$N_{\rm POW}(\times 10^{-3})$		$7.1^{+0.2}_{-0.1}$	4.4 ± 0.2	$2.5^{+0.2}_{-0.1}$	2.9 ± 0.1	7.1 ± 0.2	$7.0^{+0.2}_{-0.1}$	5.4 ± 0.1
$kT_{\rm DISKBB}$ (eV)	110 ± 3							105^{+4}_{-3}
$N_{\rm DISKBB}(\times 10^{3})$		$6.8^{+0.2}_{-0.3}$	$4.1^{+0.3}_{-0.2}$	$2.7^{+0.1}_{-0.2}$	$2.9^{+0.2}_{-0.1}$	$7.6^{+0.3}_{-0.2}$	7.7 ± 0.2	$7.5 \pm 1.61.$
$\log \xi_{\rm RELXILL}$	$3.00^{+0.01}_{-0.13}$							$2.93^{+0.08}_{-0.11}$
$R_{\rm in}$ ($R_{\rm G}$)	40 ± 15							40^{+15}_{-30}
$N_{\rm RELXILL}(\times 10^{-5})$		3.1 ± 0.7	2.5 ± 0.5	2.4 ± 0.3	2.6 ± 0.3	$4.6^{+0.6}_{-0.5}$	$4.2^{+0.4}_{-0.5}$	$3.3^{+0.7}_{-0.5}$
$N_{\rm XILLVER}(\times 10^{-5})$	2.5 ± 0.3							$3.1^{+0.3}_{-0.4}$
$A_{\rm Fe}$	$2.6^{+0.2}_{-0.4}$							2.0 ± 0.3
χ^2/dof	2506/2299							2401/2264
individual χ^2/dof		383/362	389/340	380/376	404/387	491/426	459/421	

Reynolds C. S., Brenneman L. W., Wilms J., Kaiser M. E., 2004, MNRAS, 352, 205

Różańska A., Malzac J., Belmont R., Czerny B., Petrucci P.-O., 2015, A&A, 580, A77

Sobolewska M. A., Papadakis I. E., 2009, MNRAS, 399, 1597

Soldi S., et al., 2014, A&A, 563, A57

Steenbrugge K. C., et al., 2003, A&A, 408, 921

Stern B. E., Poutanen J., Svensson R., Sikora M., Begelman M. C., 1995, ApJ, 449, L13

Strauss M. A., Huchra J. P., Davis M., Yahil A., Fisher K. B., Tonry J., 1992, ApJS, 83, 29

Strüder L., et al., 2001, A&A, 365, L18

Sunyaev R. A., Titarchuk L. G., 1980, A&A, 86, 121

Turner M. J. L., et al., 2001, A&A, 365, L27

Ursini F., et al., 2015, A&A, 577, A38

Ursini F., et al., 2016, Astronomische Nachrichten, 337, 552

Walton D. J., Nardini E., Fabian A. C., Gallo L. C., Reis R. C., 2013, MNRAS, 428, 2901

Wilkins D. R., Fabian A. C., 2012, MNRAS, 424, 1284

Wilkins D. R., Gallo L. C., Grupe D., Bonson K., Komossa S., Fabian A. C., 2015, MNRAS, 454, 4440

Zdziarski A. A., Lubiński P., Smith D. A., 1999, MNRAS, 303, L11

Zdziarski A. A., Poutanen J., Johnson W. N., 2000, ApJ, 542, 703

Zdziarski A. A., Lubiński P., Gilfanov M., Revnivtsev M., 2003, MNRAS, 342, 355

den Herder J. W., et al., 2001, A&A, 365, L7

Chapter 7

The CHEESES project

Contents

The ongoing project CHEESES (Constraining the High-Energy Emission Sources in the Environment of Supermassive Black Holes) is aimed at performing a systematic and detailed spectral analysis of the good quality data of a large sample of AGNs with physical Comptonization models. In this chapter I will describe this project, which is a French/Italian collaboration funded by a PICS (*Projet International de Coopération Scientifique*) CNRS/INAF (co-PIs: P.-O. Petrucci, A. De Rosa) from 2013 to 2016[1], focusing on the specific contribution of this thesis.

7.1 Goals and sample selection

The scientific goal of the project is deriving informations on the geometrical, dynamical and energetic properties of the accretion flow that powers AGNs, and on the radiative processes responsible for their high-energy emission.

As I have discussed in the previous chapters, constraining the high-energy emission of AGNs requires disentangling the different components that contribute to the spectrum. For this goal, the availability of multiple observations on adequate timescales is of great importance. For example, the relation between optical/UV and X-ray emission carries information on the physical link existing between the accretion disc and the corona. More generally, the different spectral parameters (such as the X-ray spectral index, the luminosities in different energy bands and so forth) and their correlations bring useful informations on the physical properties of the sources. In the previous chapters, I have presented observational campaigns on single objects, which allow us to perform detailed

---

[1] The consortium includes A. De Rosa (INAF/IAPS), M. Cappi (INAF/IASF), G. Matt, S. Bianchi (Roma Tre), P.-O. Petrucci, G. Henri (IPAG) and J. Malzac (IRAP).

spectral analyses thanks to the high-quality data. The CHEESES project is based on a complementary approach, as it focuses on a large sample of sources with archival data.

In recent years, a number of multiwavelength analyses have been performed on large samples of AGNs, especially to study their broad-band spectral energy distribution (e.g. Vasudevan & Fabian 2009, Jin et al. 2012c, and references therein), their X-ray to optical/UV properties (e.g. Lusso et al. 2010, Jin et al. 2012a, and references therein), and the correlations between different spectral and physical parameters (e.g. Jin et al. 2012b). However, these past analyses were not aimed at testing physically motivated Comptonization models. On the other hand, the CHEESES project is mainly focused on testing realistic physical models and studying the variability properties of the sources.

To study the link between the cold phase (UV-emitting) and the hot phase (X-ray-emitting) of the accretion flow, the CHEESES sample must include bright sources with simultaneous data in the optical/UV and X-ray bands. The capabilities of *XMM-Newton* are optimal for this task, as it provides both high-quality X-ray spectra with the EPIC-pn camera, and optical/UV data with the optical monitor (OM). The sample was thus built starting from the sources observed by *XMM-Newton*, with public data as of April 16, 2014, cross-correlated with the AGNs and quasars catalogue of Véron-Cetty & Véron (2010). The sources were further selected using the criteria of the CAIXA catalogue (Bianchi et al. 2009a), i.e. the sources are radio-quiet and unobscured ($N_{\rm H} < 2 \times 10^{22}$ cm^{-2}). In addition to this, they have more than one exposure with pn. Finally, the observations for each source were selected to have at least one OM filter out of six, cross-correlating the initial sample with the *XMM-Newton*/OM serendipitous UV source survey catalogue (OMSUSS v2.1, Page et al. 2012)[2]. We report the sample in Table 7.1. The sample includes 70 sources with a total number of 251 observations.

7.2 Data analysis: physical modelling of the SED

One of the primary goals of the project is to perform a spectral analysis with a physical Comptonization model. Given the large number of observations, a careful source-by-source analysis would require an extremely long time. We thus considered the possibility of fitting the spectra through an automatic process using XSPEC, which has been my main contribution to the project. I fitted the pn data in the 0.3–10 keV range[3], simultaneously with the available OM filters. In the following, I describe the strategy and the preliminary results.

7.2.1 Model and strategy: an automatic fitting procedure

We aimed at fitting each spectrum with a realistic thermal Comptonization model for the continuum emission. In particular, I tested a model including two Comptonized components, in a similar fashion as Petrucci et al. (2013): one component accounts for the UV bump and the soft X-ray excess, and models emission from a warm ($k_{\rm B}T \sim$ a few hundreds of eV) and optically thick ($\tau \sim 10$) corona, while the second component accounts for the hard X-ray emission. I also included a reflection component (with XILLVER, García & Kallman 2010) and absorption, as explained below. Moreover, since we

---

[2] The selection of the sample was carried out by A. De Rosa.

[3] The data reduction was performed by S. Bianchi, see Bianchi et al. (2009a) for the details.

Table 7.1 – The CHEESES sample. For each source, I report the number of *XMM-Newton*/pn exposures (2nd column) and the number of exposures with the six OM filters (3rd to 8th column).

Source	pn	V	B	U	UVW1	UVM2	UVW2
1AXGJ044749-0629	2	1	2	1	2	1	1
1H0419-577	8	5	7	5	8	2	7
1H0707-495	14	5	6	9	12	4	8
2MASXJ09195126-0735413	1	0	0	0	1	0	0
AKN564	11	0	0	0	2	2	10
ESO113-G010	1	0	0	1	1	1	1
ESO141-G055	4	0	0	0	2	2	4
ESO198-G24	3	0	1	2	2	1	2
FAIRALL1146	1	0	1	1	1	0	0
FAIRALL51	2	2	2	2	2	2	2
FAIRALL9	2	1	0	0	2	1	1
H0557-385	5	4	3	5	5	4	1
HB890405-123	2	0	0	2	2	0	2
HE1029-1401	2	1	0	1	1	1	2
IRAS13349+2438	4	0	0	0	3	0	1
IRAS17020+4544	2	0	0	2	1	1	0
IRAS20051-1117	2	0	2	0	2	0	1
IRASF12397+3333	2	1	2	2	2	2	1
IRASF21325-6237	2	0	0	0	0	2	0
KUV18217+6419	7	0	0	0	6	0	1
LBQS1228+1116	2	2	2	2	1	2	2
MCG-01-13-025	2	0	0	0	0	0	2
MCG-02-14-009	1	0	0	0	1	0	0
MCG-6-30-15	5	0	0	3	0	0	2
MRK1018	2	0	0	2	2	2	1
MRK1502	2	0	0	1	1	1	2
MRK205	3	3	2	2	0	0	0
MRK279	3	0	0	3	3	3	3
MRK290	4	0	0	0	4	0	0
MRK335	3	2	3	3	3	3	3
MRK507	2	0	0	0	2	2	0
MRK509	16	10	10	11	14	14	15
MRK590	2	1	2	2	2	2	2
MRK609	2	0	0	0	0	1	1
MRK766	7	1	5	6	7	7	7
MRK841	1	0	0	1	0	0	0
MRK876	2	0	0	0	1	1	1
MRK883	4	0	4	4	4	3	3
NEP1640	2	0	0	2	2	2	0
NGC2622	2	0	0	0	1	2	1
NGC3516	6	0	0	4	0	0	2
NGC3783	1	0	0	0	0	0	1
NGC4051	16	0	1	1	16	1	1
NGC4593	2	0	0	0	2	1	2
NGC5033	2	0	0	0	1	1	1
NGC526A	2	1	1	1	2	2	1
NGC5548	3	0	0	3	1	0	1
NGC7213	1	0	1	1	1	1	1
NGC7469	4	2	0	2	2	2	4
PDS456	3	0	0	0	2	2	1
PG0804+761	2	2	0	2	2	2	0
PG0844+349	2	1	1	2	1	1	1
PG1114+445	12	1	1	1	12	12	12
PG1115+080	1	0	0	1	0	0	0
PG1116+215	5	1	1	4	4	5	3
PG1211+143	4	3	3	4	4	4	4
PG1351+640	3	1	1	1	3	3	1
PG1402+261	2	0	0	2	2	2	2
PG1407+265	1	0	0	0	0	0	1
PG1440+356	4	1	0	1	4	1	4
PG1543+489	4	0	0	3	0	2	0
PGC033842	2	0	0	0	1	2	0
Q0056-363	3	0	0	1	2	2	3
Q2251-178	5	4	3	4	4	4	4
RE1034+396	8	1	1	2	8	1	2
RXJ0057.2-2223	2	0	0	0	0	0	2
SDSSJ135724.51+652505.9	2	0	0	0	1	2	0
UGC3973	5	0	1	0	4	1	5

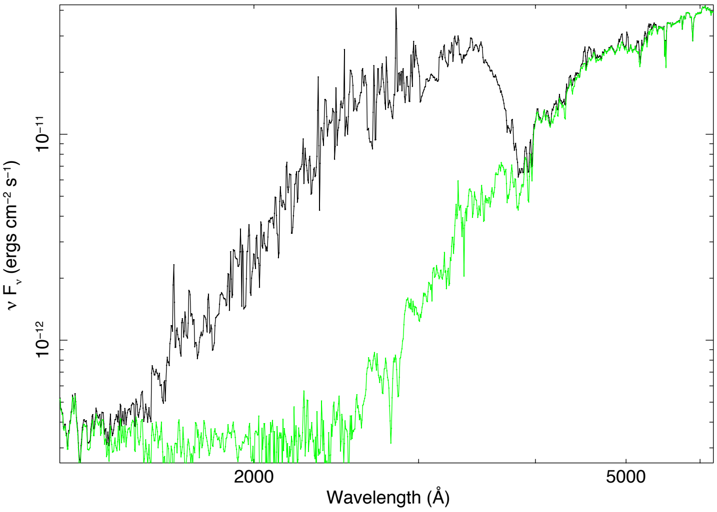

Figure 7.1 – The table model for the small blue bump imported in XSPEC, plus the galaxy template (in green). See also Fig. 1.2.

use optical/UV data, we must take into account two main components that can give a significant contribution in the optical/UV. One is the host galaxy, especially in the optical band (while its UV emission is normally negligible). The second main component is the BLR, which is responsible for the so-called small blue bump around 3000 Å. I refer the reader to Fig. 1.2 (from Mehdipour et al. 2015) for a clear view of these contributions in the case of NGC 5548. For the galaxy contribution, I assumed the same template spectrum as the one used by Mehdipour et al. (2015) for NGC 5548, because the precise spectral shape does not matter when using only six broad-band filters.

I developed a script to automatically fit all the spectra, using XSPEC, with the model sketched above. This model takes into account the main spectral components that are generally seen in AGNs, yet it is relatively simple and suited for a large sample. I describe the components in more detail below.

The small blue bump: For this component, I needed to build a model suitable for XSPEC. I neglected the contribution from narrow emission lines, given the low resolution of the OM filters. I did not use the OM grisms because I was mainly interested in fitting the continuum. The small blue bump is due to the superposition of two components: blended Fe II emission lines and Balmer continuum. The Fe II in the BLR produces thousands of emission lines, resulting in a complex spectrum between 2000 and 4000 Å (Netzer & Wills 1983; Wills et al. 1985). The Balmer continuum is due to H recombination, and its flux can be expressed as $F_\nu^{\rm BC} = F_\nu^{\rm BE} \exp[-h(\nu - \nu_{\rm BE})/k_{\rm B}T]$, where $F_\nu^{\rm BE}$ is the flux at the Balmer edge ($\lambda_{\rm BE} = 3646$ Å) and T is the electron temperature (Grandi 1982). I used the model calculated by Wills et al. (1985) for the Fe II emission[4] and the formula of Grandi (1982) for the Balmer continuum to produce a spectral model for XSPEC. A similar procedure was implemented by Mehdipour et al. (2015) for the NGC 5548 campaign, using the SPEX package (instead of XSPEC) and optimizing the model to exploit the resolution of the grisms. In our case, including this component is important mainly for the UVW1 filter, whose bandpass (2080–3740 Å) covers the wavelength range where the small blue bump can be significant. I show the small blue bump model and the galaxy template in Fig. 7.1.

---

[4] The model for Fe II was kindly provided by G. A. Kriss (STScI).

The X-ray continuum: In the model, the X-ray continuum is the sum of two thermal Comptonization components, one warm and one hot, both modelled with NTHCOMP (Zdziarski et al. 1996; Życki et al. 1999). The main parameters of NTHCOMP are the electron temperature, the seed photon temperature, and the photon index of the asymptotic power law. The distribution of the seed photons can be a blackbody or a multicolour disc blackbody (Mitsuda et al. 1984; Makishima et al. 1986). I chose the latter distribution, leaving the inner disc temperature free to vary and assuming it to be the same for the two NTHCOMP components (but see the discussion in Sect. 7.3). I also left the asymptotic photon index of both NTHCOMP components free to vary, expecting $\Gamma_{\rm w} \simeq 2.5 - 3$ for the warm component (e.g. Petrucci et al. 2013) and $\Gamma_{\rm h} \simeq 1.5 - 2$ for the hot component. The electron temperature of the warm NTHCOMP was also free to vary, while I fixed the electron temperature of the hot component to 100 keV, because of the lack of high-energy data that would have been able to constrain the high-energy cut-off.

The reflection component: I used XILLVER for the reflection component, leaving only the normalization as a free parameter. Indeed, the main feature of XILLVER in the 0.3–10 keV band is the Fe Kα line, plus some contribution to the continuum above 8 keV. Therefore, the spectral shape of the illuminating radiation of XILLVER is not crucial. I thus fixed the photon index of XILLVER to the arbitrary value of 1.9 and assumed an iron abundance of 1 and an ionization parameter $\log \xi = 0$. However, linking the photon index of XILLVER to that of the primary continuum does not alter much the results. For each source, the redshift is taken from the NASA/IPAC Extragalactic Database (NED) or from the SIMBAD database operated at CDS, Strasbourg.

Absorption: I included the Galactic neutral hydrogen column density, appropriate for the sky coordinates of the source, from Kalberla et al. (2005). I also included the reddening, calculated from the Galactic extinction following Güver & Özel (2009). For several sources, I found a bad fit below 1-2 keV, with strong residuals likely due to ionized absorption. Therefore, I included a warm absorber modelled with a CLOUDY table (see Chapters 4 and 6), leaving free the column density and the ionization parameter.

For each source, I included the optical/UV corrections (i.e. the galaxy and/or the small blue bump) depending on the OM filters available and on the redshift. For example, I included the galaxy template only in the presence of optical (especially V and B) filters. I note that the number of observations per source is variable between 1 and 16, and the time intervals between the different observations of the same source are very disparate among the sample. Then, for simplicity, I allowed all the free parameters of the model to vary between different observations of the same source.

7.2.2 Results

The preliminary results of the spectral analysis of the CHEESES sample are various and encouraging. A number of sources are well fitted by the model, with reasonable parameters. I show four examples of statistically good fits in Fig. 7.3, for Fairall 9 and Mrk 279, and in Fig. 7.4, for Mrk 1018 and PG 1114+445.

In some cases, I find statistically bad fits, likely due to complex spectra that require a more detailed analysis. In particular, some sources show strong residuals below 1-2 keV, most likely due to an imperfect modelling of the warm absorber (e.g., more than one ionized absorber is probably needed to obtain a good fit). For example, the analysis yields bad fits for sources like MCG –6-30-15, Mrk 335 and NGC 4051, all known to host complex, multiphase warm absorbers (e.g. Turner et al. 2003; Grupe et al. 2008; Krongold et al. 2007), or Mrk 766, which is also affected by partially covering, neutral obscuration (Risaliti et al. 2011). Also complex NLS1s, such as 1H 0707-495 (e.g. Fabian et al. 2012, see also Chapter 8), are poorly fitted. I show in Fig. 7.5 two examples of unacceptable fits, for Mrk 335 and Mrk 766. However, in these two cases, the fits yield reasonable parameters of the continuum. For other sources, instead, the statistically bad fits also yield unphysical parameters, such as a flat photon index for the warm corona (Γ_{w} is sometimes pegged at 2, which is the lower limit I set in the model) and/or a very low temperature of the warm corona (close to the lower limit of 50 eV).

In any case, from the best-fitting parameters we can estimate several key parameters of the warm and hot coronae. From the photon index and electron temperature, we can estimate the optical depth, e.g. using eq. 2.75: $\Gamma \simeq (9/4)y^{-2/9}$ where $y = 4\max(\tau, \tau^2)(k_{\mathrm{B}}T/m_{\mathrm{e}}c^2)$ is the Compton parameter. From the fit, we also obtain the model luminosity of both NTHCOMP components, corresponding to the luminosity of the warm and hot coronae. Then, we can calculate the amplification factor (see Sect. 2.4.2), namely the ratio between the coronal luminosity L_{tot} and the input soft luminosity L_{s}, which is related to the geometry.

In particular, it is interesting to estimate the amplification factor $A_{\mathrm{w}} = L_{\mathrm{tot,w}}/L_{\mathrm{s,w}}$ for the warm corona. Indeed, we can test the hypothesis of a plane-parallel corona in thermal equilibrium above a passive disc, in which case we expect an amplification factor A_{w} close to 2, since the corona is optically thick (Petrucci et al. 2013, see also Sect. 2.4.2). Indeed, from eq. 2.70 we have

$$A_{\mathrm{w}} = \frac{L_{\mathrm{tot,w}}}{L_{\mathrm{s,w}}} = 2\left(1 - \frac{L_{\mathrm{s,intr}}}{L_{\mathrm{s,w}}}\right). \tag{7.1}$$

I also recall that, for an optically thick corona, the total luminosity is immediately derived from the observed one: $L_{\mathrm{tot,w}} = 2L_{\mathrm{obs,w}}$ (see eq. 2.67).

From the spectral fits, finding $L_{\mathrm{obs,w}}$ and thus $L_{\mathrm{tot,w}}$ is straightforward. However, estimating $L_{\mathrm{s,w}}$ is not immediate and requires further analysis. For this goal, I use the model DISKBB of XSPEC, consistently with the input photon distribution that I set in NTHCOMP. First, I calculate the observed photon flux n_{obs} of the best-fitting warm NTHCOMP component. Then, I assume that the intrinsic soft photon flux is $n_{\mathrm{s}} = 2n_{\mathrm{obs}}$, appropriate for an optically thick corona which fully covers the disc (see eq. 2.61). Then, I set in DISKBB a photon rate n_{s} and a temperature equal to that of the inner disc temperature in NTHCOMP. I then calculate the DISKBB model luminosity and, in so doing, I estimate $L_{\mathrm{s,w}}$.

If $L_{\mathrm{tot,w}} = 2L_{\mathrm{s,w}}$ (i.e. $A_{\mathrm{w}} = 2$), the model is self-consistent: all the optical/UV emission and the soft X-ray excess can be produced by a warm corona covering the (passive) accretion disc. If $L_{\mathrm{tot,w}} < 2L_{\mathrm{s,w}}$, we have an indication that the accretion disc has some intrinsic emission contributing to $L_{\mathrm{s,w}}$ rather than being passive (see eq. 7.1). Finally, if $L_{\mathrm{tot,w}} > 2L_{\mathrm{s,w}}$, we have an indication that the observed optical/UV luminosity is not totally due to the warm corona, for example because the corona does not entirely cover the disc. In this case, we should see part of the disc emission that does not cross the corona, and include this emission in the spectral model. I also point out that the estimate of $L_{\mathrm{s,w}}$ is not self-consistent in this case.

To summarize: the case $A_{\mathrm{w}} = 2$ is consistent with a plane-parallel geometry, where the warm, optically thick corona fully covers a passive disc. The case $A_{\mathrm{w}} < 2$ is also con-

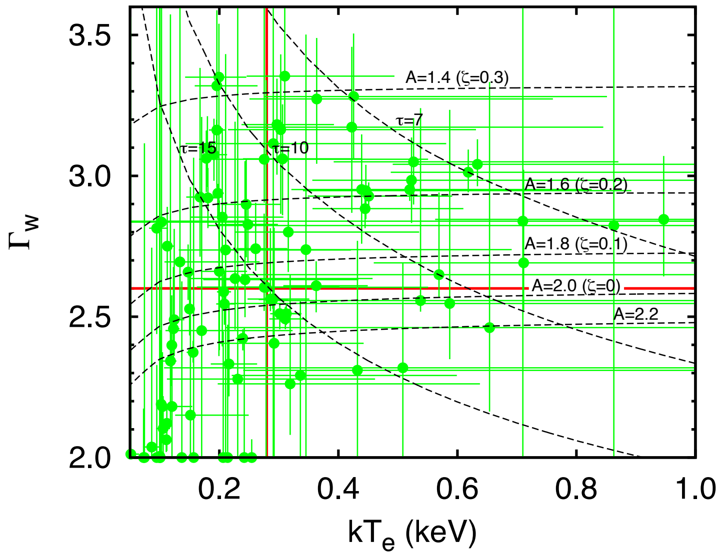

Figure 7.2 – Photon index and temperature of the warm NTHCOMP component. The dashed lines indicate contours of constant amplification factor A (or equivalently, of intrinsic luminosity ratio $\zeta = L_{\rm s,intr}/L_{\rm s}$) and optical depth τ. The red solid lines represent the average photon index ($\simeq 2.6$) and temperature ($\simeq 0.28$ keV).

sistent with the plane-parallel geometry, but the seed luminosity is larger than expected (i.e. the disc is not passive). When $A_{\rm w}$ is substantially above 2, the corona might be patchy instead of fully covering, and a further optical/UV emission component should be included. Finally, I note that eq. 7.1 can be rewritten as

$$\zeta \equiv \frac{L_{\rm s,intr}}{L_{\rm s,w}} = 1 - \frac{A_{\rm w}}{2} \tag{7.2}$$

where ζ is the intrinsic luminosity ratio (provided that $A_{\rm w} \leq 2$).

In general, most of the fits for the different sources show that (i) the optical depth is large for the warm corona, i.e. $\tau \sim 10 - 50$; (ii) for the hot corona, the optical depth is between 1 and 2; (iii) the temperature of the warm corona is mostly between 100 and 500 eV, with some indications of variability between the different observations of the same source; (iv) $A_{\rm w}$ is generally close to 2, and down to 1.4 in some cases; (v) a number of fits are not statistically good in terms of chi-square, mostly because of residuals in the soft X-ray band that can be attributed to complex ionized absorption, however the best-fitting parameters and variability behaviour are generally reasonable.

I plot in Fig. 7.2 the values of the photon index and of the electron temperature found for the warm corona, together with contours of constant amplification factor and optical depth[5]. I exclude the statistically worse fits, i.e. those with $\chi^2/\text{dof} > 1.5$. Interestingly, the results on the warm corona seem to agree well with a little or no intrinsic emission from the accretion disc, as I mostly find $\zeta < 0.3$, i.e. less than 30% of the soft emission is intrinsic.

7.3 Discussion and perspectives

The CHEESES project is aimed at studying the spectral and variability properties of a large sample of AGNs in the optical/UV and X-rays. As a first step, I performed

---

[5] I computed these contours using the NTHCOMP model in XSPEC. I defined a grid of 100 × 100 pairs of photon indexes and temperatures, and calculated for each of them $A_{\rm w}$ (with the procedure described in the text) and τ (inverting eq. 2.75). I fixed the inner disc temperature of NTHCOMP to 3 eV, however this parameter does not affect much the results.

a spectral analysis on a sample of AGNs with good quality data from *XMM-Newton*, simultaneously fitting the spectra in the optical/UV band and in the 0.3–10 keV range. I tested a two-corona Comptonization model (Petrucci et al. 2013), where the UV and part of the soft X-ray emission (the soft excess) is due to a warm, optically thick corona and the hard X-ray emission is due to a hot, optically thin corona. The results show that this approach is viable and can give us new insights on the physical processes at play in AGNs. In particular, the results of the spectral analysis yield informations on the physical and geometrical parameters of the disc/corona system, such as the coronal optical depth, temperature, and amplification factor.

A number of improvements and extensions are suggested by my preliminary analysis. As I noted above, complex absorption affects several sources, so that the inclusion of only one warm absorber is not always sufficient. In these cases, to obtain statistically good fits, we likely need to add several ionized absorption components. Another possibility is to exclude the objects showing evidences of a warm absorber (this was the choice of, e.g., Jin et al. 2012c). However, this would exclude many sources and it is probably not necessary.

In some cases, the results of the analysis imply that the model must be corrected, in particular when the amplification factor of the warm corona is significantly greater than 2. In this case, warm Comptonization in a plane-parallel corona does not explain the observed data, and an additional UV emission component should be included. Interestingly, when the amplification factor is about 2, the results are consistent with all the heating taking place in the warm corona lying above a passive disc. A passive disc, i.e. that just reprocesses coronal emission, would question the validity of the standard, Shakura-Sunyaev model. Comparing the results of the spectral fits with theoretical calculations is another interesting facet of this analysis. In particular, from the calculations of Różańska et al. (2015), the values of the coronal optical depth and temperature that are commonly found in the CHEESES sample seem to be consistent with an energetically dominant, magnetic pressure-supported warm corona. My preliminary results indeed suggest that most sources are consistent with having a warm corona on top of a nearly passive disc, encouraging us to conduct further investigations (Petrucci et al., in prep.).

The flux and spectral variability of the sources can also give important informations. For example, the existence (or lack) of a correlation between the UV and X-ray flux in different energy bands is useful to constrain the relation between the UV and X-ray-emitting regions. In particular, a model-independent correlation between the UV and soft X-ray emission would support the warm corona scenario (e.g. Mehdipour et al. 2011; Petrucci et al. 2013). I also note that I left all the parameters free to vary between different observations of the same source. However, it is possible to tie the parameters which are consistent with being constant to find better constraints. If, on the other hand, the physical parameters of the coronae are found to be significantly variable, we can infer constraints on their size and location from the variability time-scale.

With only *XMM-Newton* data, we cannot investigate the properties of the hot corona in full detail, because of the lack of high-energy data. However, a sample including data from *Suzaku*, *Swift*, *INTEGRAL* and *NuSTAR* will make it possible to constrain the temperature and optical depth of the hot corona. The high-energy data will also allow us to study the reflection component constraining the Compton hump. For example, some sources are characterized by strong reflection, giving rise to relativistic features (see Sect. 2.2.2) and relativistically blurred, ionized reflection could explain the soft excess

(Sect. 2.2.3). A positive correlation between the reflection strength and the soft excess is expected in the ionized reflection scenario (Vasudevan et al. 2014). However, Boissay et al. (2016) found no correlation between reflection and soft excess, from the analysis of *XMM-Newton* and *Swift*/BAT data of about 100 sources. Rather, Boissay et al. (2016) suggested that the strength of the soft excess correlates with both the primary photon index of the hot corona and the Eddington ratio of the source. Such correlations can be explained by warm Comptonization: a stronger soft excess might imply a more efficient cooling of the hot corona and hence a steeper spectrum, while the relation with the Eddington ratio may suggest a direct link between the accretion disc and the warm corona.

The relation between the warm and hot corona is another interesting point that is worth examining. For example, I assumed a common temperature of the input soft photons for the warm and hot coronae (generally found to be of a few eV from the fits). However, this could not be the case if the two coronae are located at different radial distances from the black hole (Petrucci et al. 2013, see also Chapter 3). In the case of Mrk 509, Petrucci et al. (2013) found a soft photon temperature of $\sim$ 100 eV for the hot corona, and of $\sim$ 3 eV for the warm corona. These different temperatures indicate a spatial separation of the two coronae, the hot corona being closer to the black hole (within 10-20 R_G, Petrucci et al. 2013). In any case, UV data are pivotal to constrain the low-energy cut-off corresponding to the soft photon temperature, thus constraining the location of the coronae. The inclusion of *HST* or *FUSE* data could thus prove useful to perform more detailed spectral analyses.

In conclusion, the preliminary results of the spectral analysis of the CHEESES sample are promising. In a number of cases, the warm/hot Comptonization model that I tested provides a good description of the data, and allows us to derive constraints on the physics and geometry of the accretion flow. Perhaps the most intriguing result is that the UV/soft X-ray emission of a large fraction of sources is well described by a disc/warm corona system, where most of the power is released in the warm corona rather than in the disc. From these results, I am also able to indicate corrections to the model and suggest extensions of the sample and of the spectral and variability analysis. Part of this work will be included in a forthcoming paper (Petrucci et al., in prep.).

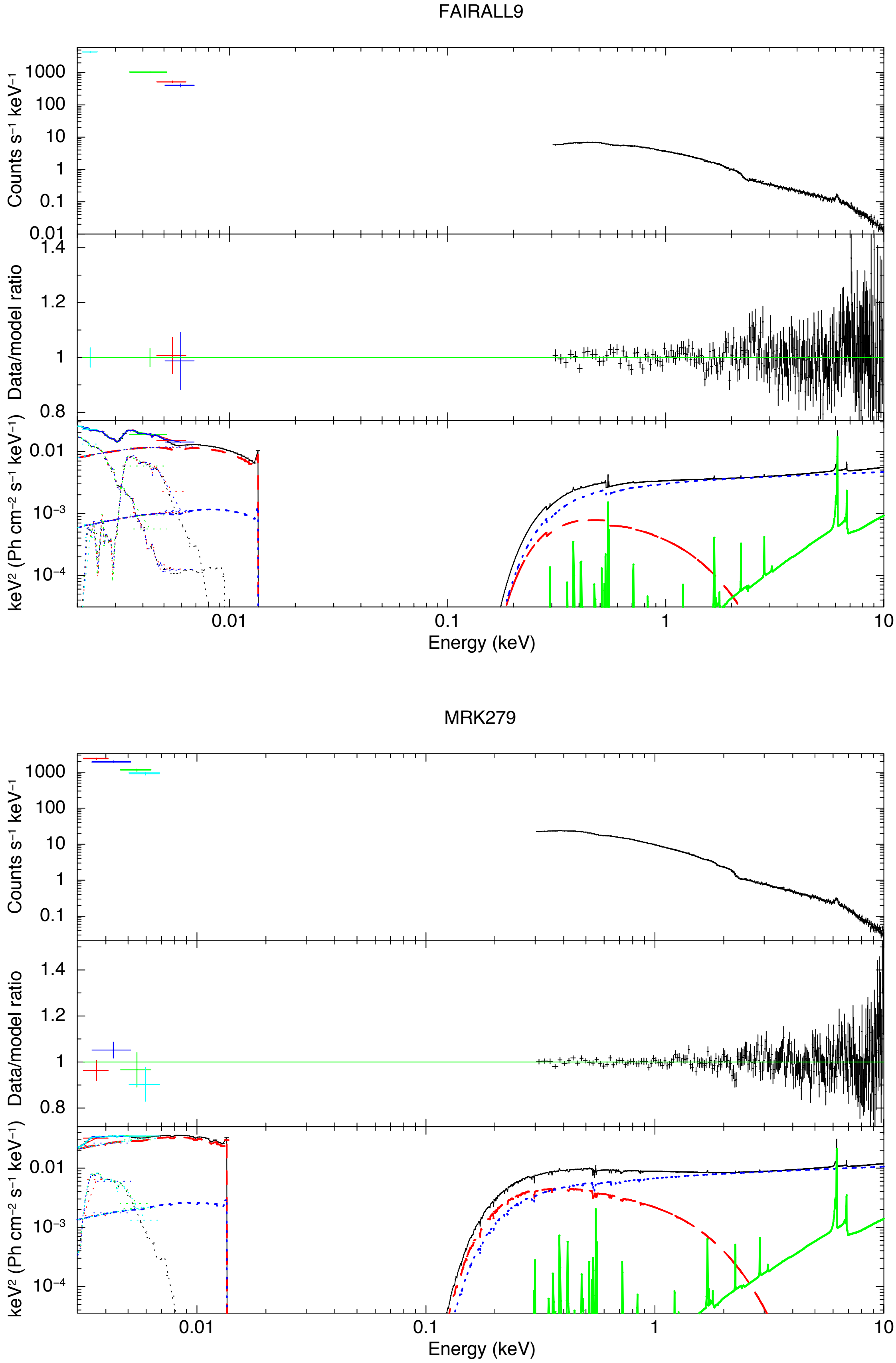

Figure 7.3 – Two results of the spectral fitting, for Fairall 9 ($\chi^2/\text{dof} = 249/238$) and Mrk 279 ($\chi^2/\text{dof} = 250/244$). Upper panel: The *XMM-Newton*/OM and pn data with folded model (see Sec. 7.2.1). Middle panel: Data-to-model ratio. Lower panel: Best-fitting model $E^2 f(E)$, with the hot NTHCOMP (blue dotted line), the warm NTHCOMP (red dashed line) and XILLVER (green solid line).

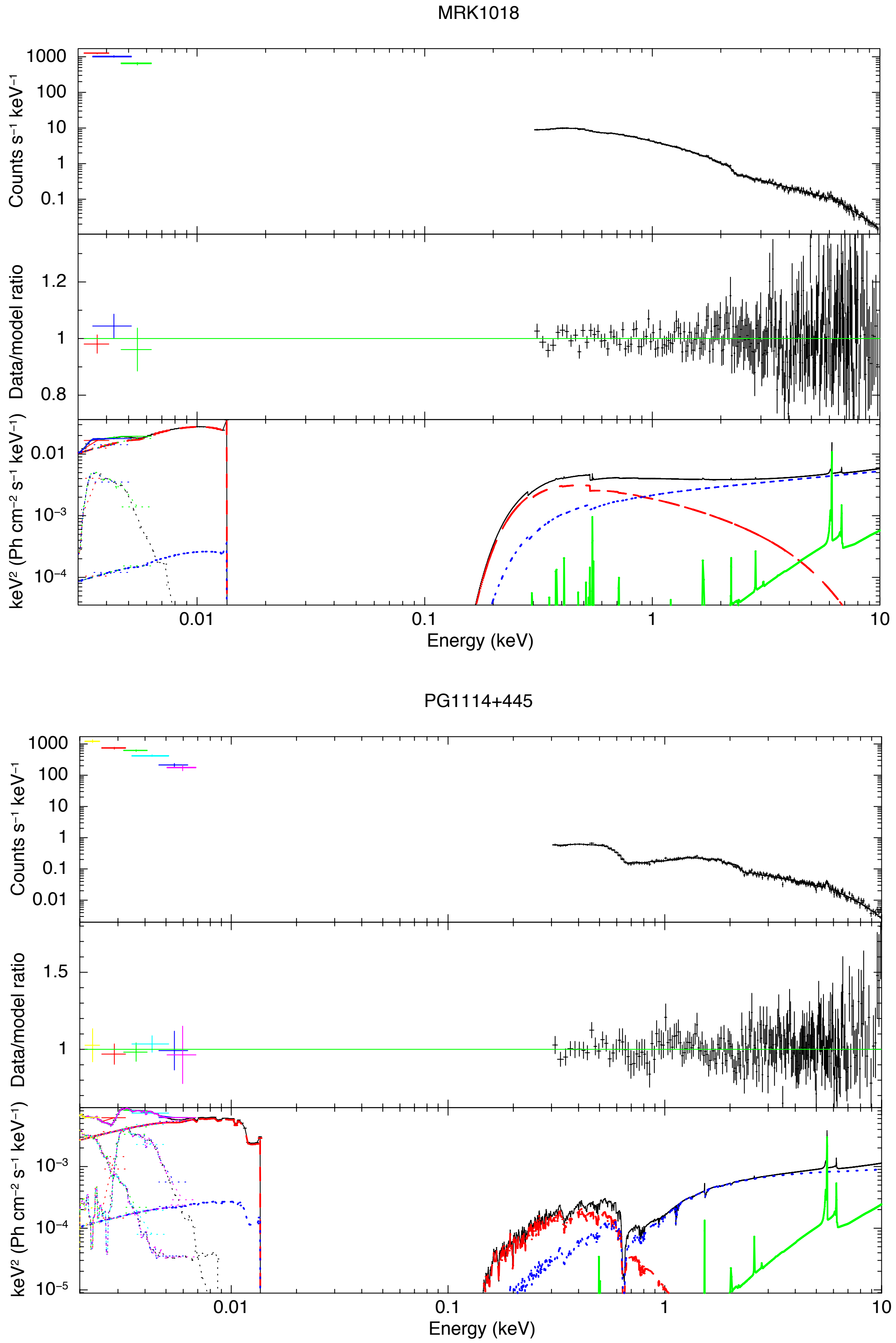

Figure 7.4 – Two results of the spectral fitting, for Mrk 1018 (χ^2/dof = 216/222) and PG 1114+445 (χ^2/dof = 193/209). Upper panel: The *XMM-Newton*/OM and pn data with folded model (see Sec. 7.2.1). Middle panel: Data-to-model ratio. Lower panel: Best-fitting model $E^2 f(E)$, with the hot NTHCOMP (blue dotted line), the warm NTHCOMP (red dashed line) and XILLVER (green solid line).

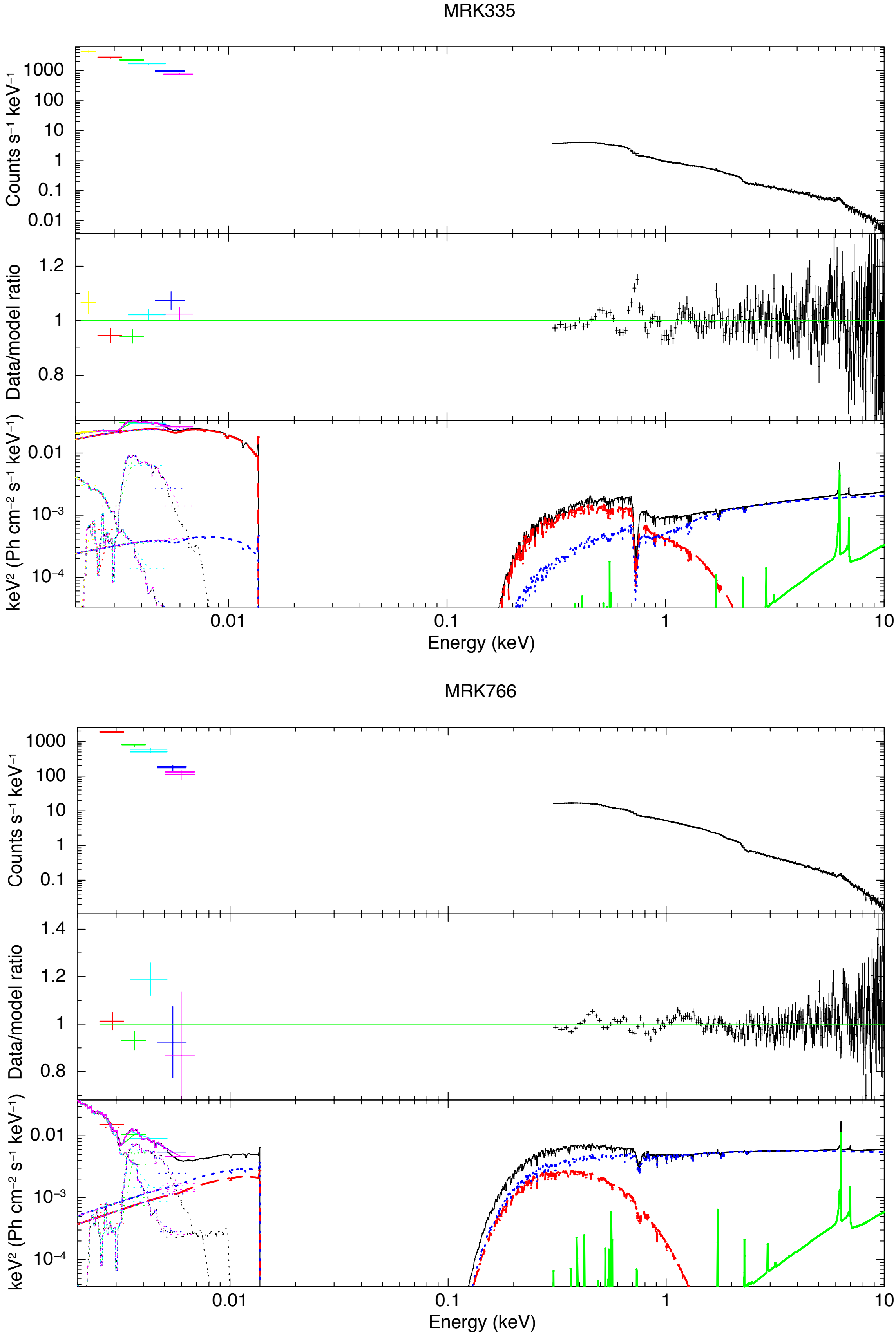

Figure 7.5 – Two statistically unacceptable fits, for Mrk 335 (χ^2/dof = 645/245) and Mrk 766 (χ^2/dof = 736/244). Upper panel: The *XMM-Newton*/OM and pn data with folded model. Lower panel: Data-to-model ratio. Lower panel: Best-fitting model $E^2 f(E)$, with the hot NTHCOMP (blue dotted line), the warm NTHCOMP (red dashed line) and XILLVER (green solid line).

Chapter 8

Numerical simulations

Contents

In this final chapter, I will present numerical simulations using a relativistic ray-tracing code, developed by M. Dovčiak (Astronomical Institute, Academy of Sciences of the Czech Republic) and C. Done (Durham University). The code calculates the minimum size that a hot corona should have in order to Comptonize enough UV photons to explain the observed X-ray flux. My work has been aimed at testing this code on a large sample of sources, as I will explain in the following.

8.1 The D&D code: constraining the coronal geometry with ray-tracing

The code discussed in this chapter is presented in detail in Dovčiak & Done (2015, hereafter DD15) and Dovčiak & Done (2016). The main issue addressed by the code of Dovčiak & Done (hereafter D&D code) is the consistency between the lamp-post geometry, which assumes a point-like corona (see Sect. 2.4.3), and the constraints on the coronal geometry derived from Comptonization. As we have seen in Sect. 2.4.3, the X-ray spectral and variability properties of some sources seem to be well described by a lamp-post scenario, namely by a compact hot corona lying very close (within a few gravitational radii) to the accretion disc. This configuration seems to be particularly appropriate for sources showing extreme, reflection-dominated X-ray spectra. However, the hot corona cannot be arbitrarily compact: it must intercept a number of seed photons sufficient to explain the observed X-ray flux, as Comptonization conserves the number of photons. Many lamp-post models assume a point-like corona, which is clearly an approximation. In a few cases, extended geometries were considered, mainly to determine the impact on

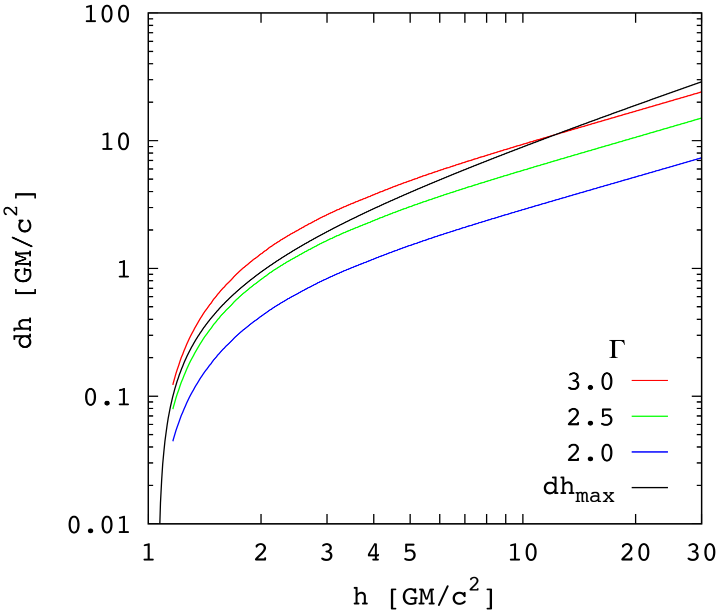

Figure 8.1 – The coronal radius dh, calculated with a full general relativistic treatment, required to produce $L_X/L_{disc} = 0.03$ with $L_{disc} = L_{Edd}$ and mass $10^7\ M_\odot$, for different values of Γ (from Dovčiak & Done 2015). The spin parameter is $a = 0.998$. The radius dh and height h are in Boyer-Lindquist coordinates. The black line indicates the maximum radius for the source fitting above the event horizon r_H, i.e. $h - r_H$. When $\Gamma = 3$ (red line), the corona intercepts enough disc photons to produce the observed Comptonized emission only for $h > 12$.

the reflection spectrum (e.g. Fukumura & Kazanas 2007; Wilkins & Fabian 2012; Dauser et al. 2013b; Wilkins et al. 2014). The D&D code is aimed at setting a lower limit on the radius of a spherical hot corona, located on the symmetry axis of the disc, and assuming that its X-ray emission is due to Comptonization of seed photons from the disc itself. This imposes a constraint on the location of the corona as well, because the height of the corona above the event horizon must be larger than the minimum coronal radius. The D&D code takes into account all general relativistic effects, such as the energy shifts of the disc radiation as seen by the corona, light bending and aberration.

DD15 tested the geometry of the NLS1 1H 0707-495, whose most extreme spectrum seems to be consistent with a lamp-post corona located within 1 gravitational radius of the event horizon (Fabian et al. 2012, see Sect. 2.4.3). Moreover, Wilkins et al. (2014) suggested that the flux and spectral variability of the source is consistent with an expansion of the corona in high-flux states and a contraction to a more confined region in low-flux states. As noted by DD15, the crucial parameter determining the minimum source size is the ratio between the photons required for Comptonization and the available seed disc photons, which in terms of luminosities translates to L_X/L_{disc}. Concerning the X-ray spectral shape, the D&D code assumes a fixed electron temperature of 100 keV, so the main parameter is the photon index Γ. For example, DD15 found that for $L_X/L_{disc} = 0.03$ (typically observed in NLS1s, Jin et al. 2012c), the coronal radius (thus its height) must be more than 10 R_G for the steepest spectra ($\Gamma = 3$; see Fig. 8.1). In general, steeper spectra require more seed photons to produce a given X-ray luminosity, and also intercept a smaller fraction of photons because of the lower optical depth. Moreover, the intrinsic X-ray luminosity L_X can be much larger than the observed X-ray luminosity $L_{X,obs}$ because of the relativistic effects. If we assume the corona to be within 1 R_G of the event horizon, most of the X-ray photons are actually swallowed by the black hole because of light bending. To reproduce the observed spectrum of 1H 0707-495 with such an extreme geometry, the intrinsic X-ray luminosity should be very high, i.e. at least $1.9 L_{Edd}$. According to DD15, this is not impossible, especially because 1H 0707-495 might have a very high accretion rate (up to 200 in Eddington units: Done & Jin 2016, see also Chapter 7). However, in this case, the corona should have a radius much

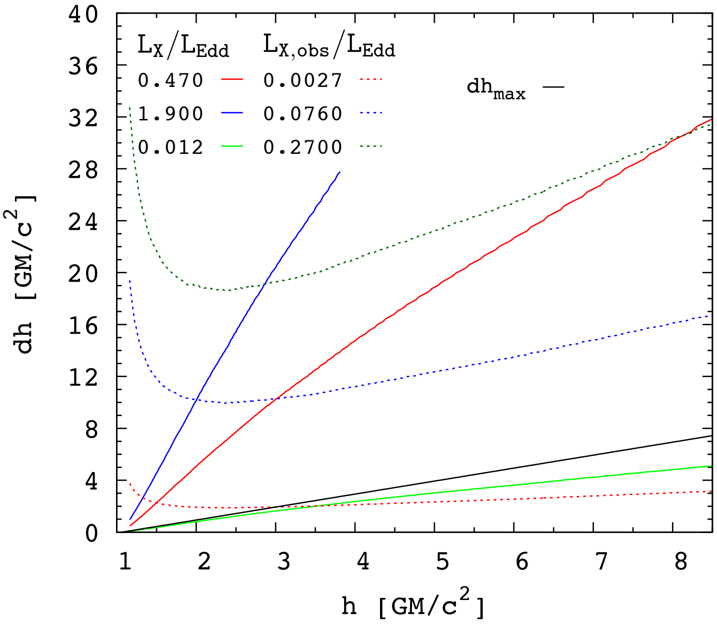

Figure 8.2 – Required radius dh of the corona for 1H 0707-495 (from Dovčiak & Done 2015), for a given intrinsic (solid curves) or observed (dotted curves) X-ray luminosity. The radius normally increases with the height, except for very small heights, where a larger size is needed to get the same observed luminosity (because of flux suppression from light bending). Like in Fig. 8.1, only the curves below d$h_{\rm max}$ (black solid line) are consistent with the lamp-post geometry.

larger than 1 R_G to intercept enough seed photons and produce the required luminosity, making it impossible to fit within 1 R_G (see Fig. 8.2). Moreover, if the accretion rate of 1H 0707 495 is indeed very high, the hypothesis of a standard thin disc assumed by the lamp-post models is likely to break down (Done & Jin 2016, see also the discussion in Sect. 8.3).

The D&D code was used by DD15 to test the lamp-post geometry in the case of 1H 0707-495, but it can be applied to any source with a known $L_{\rm X}/L_{\rm disc}$ and spectral shape. I thus undertook a program based on the use of the D&D code to constrain the geometry of the hot corona, in the lamp-post scenario, on a large sample of sources. This ongoing program consists in testing the D&D code on the CHEESES sample (see Chapter 7). The *XMM-Newton* data allow us to constrain the X-ray luminosity and spectral shape, as well as the the seed photon luminosity from the optical/UV data. The D&D code was adapted by M. Dovčiak for the application to several sources.

8.2 The D&D code and CHEESES

I now summarize the main input parameters of the D&D code, which I set using the results from the CHEESES sample analysis, as presented in Chapter 7. The black hole mass (taken from the literature[1]) is used in the code to calculate the Eddington luminosity. The hard X-ray photon index Γ is the best-fitting photon index of the hot NTHCOMP component (see Sect. 7.2.1). Albeit the results of the CHEESES project are preliminary, we consider the measurements of the hard X-ray photon index accurate enough for testing the D&D code. An important parameter is the X-ray luminosity, which I computed in the 2–10 keV range, again from the CHEESES best-fitting model. The total X-ray luminosity is calculated by the code, to match the observed 2–10 keV luminosity and photon index. The code assumes the NTHCOMP model for the Comptonized emission from the hot corona, setting an arbitrary temperature of 100 keV (i.e. the same as the

---

[1] The compilation of black hole masses was done by S. Bianchi (see Bianchi et al. 2009a).

hot NTHCOMP component in the CHEESES model). Then, we need to compute the UV luminosity. The D&D code assumes that the corona is illuminated by an accretion disc with a Novikov-Thorne temperature profile (the relativistic extension of the Shakura-Sunyaev model, Novikov & Thorne 1973) through the model KYNBB (Dovčiak et al. 2004). The disc blackbody-like emission is thus determined by the (known) black hole mass and the accretion rate or the luminosity. From the best-fitting CHEESES model, I computed the UV luminosity in the 5–7 eV range (roughly covering the bandpass of the UVM2 and UVW2 filters of the *XMM-Newton*/OM). Incidentally, we may note that the model assumed by the D&D code is different from the CHEESES model: in the latter, the optical/UV emission is produced by a warm Comptonizing corona, whereas in the D&D code it is due to a Novikov-Thorne disc. However, we only make use of the luminosity estimated from the CHEESES model in a small energy range, which is not strongly model-dependent. I will return to this point in Sect. 8.4. We also need to assume a black hole spin, which determines the inner disc radius (by hypothesis equal to the innermost stable circular orbit), and a disc inclination (which does not strongly affect the results: see DD15). The code then computes the accretion rate needed to reproduce the observed 5–7 eV luminosity using the KYNBB model. The disc emission is now completely determined, and from its integration the code calculates the bolometric luminosity.

To summarize, the main input parameters of the D&D code are the X-ray and UV luminosities and the X-ray spectral shape. Then, in the hypothesis of a lamp-post corona Comptonizing the blackbody-like disc emission, the code finds the minimum needed coronal size, taking into account all relativistic effects. The D&D code, in the version I used, calculates the minimum coronal radius for different coronal heights (2.5, 5, 10 and 30 R_G), spin parameters of the black hole ($a = 0$ and 0.998), and disc inclinations ($i = 5$, 30 and 60 deg), assuming the inner disc radius equal to the innermost stable circular orbit.

8.3 Preliminary results

From the results of the D&D code, we can compare the coronal radius and the height of the corona above the event horizon. The coronal radius must be less than the height, for the lamp-post geometry to be consistent with Comptonization. However, we must check that the physical parameters calculated by the code are consistent with the assumed model. In particular, the Eddington ratio $\epsilon_{\rm Edd} = L_{\rm bol}/L_{\rm Edd}$ of the source should not exceed 1. Indeed, sources showing super-Eddington luminosities are thought to be powered by advection-dominated slim discs, rather than by standard thin discs (e.g. Mineshige et al. 2000; Abramowicz & Fragile 2013; Du et al. 2014; Castelló-Mor et al. 2016, see also Sect. 1.2.3). Then, super-Eddington sources are probably not well described by a Novikov-Thorne disc, as assumed in the D&D code. On the other hand, Eddington ratios much lower than 1 might suggest the presence of ADAF/RIAFs (see Sect. 1.2.3 and Chapter 5). Therefore, the calculations are self-consistent only when $\epsilon_{\rm Edd} \lesssim 1$.

8.3.1 The Eddington ratio

I plot in Fig. 8.3 $\epsilon_{\rm Edd}$ versus the black hole mass, in the case $a = 0.998$ and $i = 30$ deg. For 20 sources out of 70, I find unexpectedly high Eddington ratios, up to 100-200. 1H 0707-495 (red points in Fig. 8.3) is the most peculiar source, as in all the 14 observations of the CHEESES sample I find $\epsilon_{\rm Edd}$ spanning from 90 up to 400. These

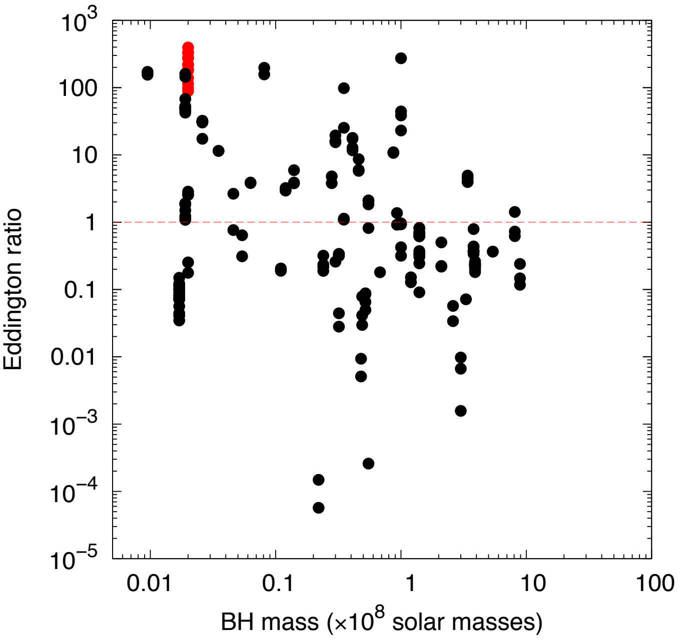

Figure 8.3 – The Eddington ratio $L_{\rm bol}/L_{\rm Edd}$ as calculated by the D&D code for the CHEESES sample, assuming spin $a = 0.998$ and inclination $i = 30$ deg, plotted against the black hole mass in units of $10^8 M_\odot$. The red points correspond to 1H 0707-495.

values, albeit very large, are in rough agreement with the results of a more detailed analysis on 1H 0707-495 by Done & Jin (2016): they estimated an Eddington ratio up to ~ 200, fitting the observed optical/UV spectrum with the disc model of Done et al. (2013). However, Done & Jin (2016) also found that this model greatly over-predicts the soft X-ray emission and the observed bolometric luminosity, so there must be some further form of energy loss besides radiation. For example, some of the power can be advected rather than radiated away, or it could be channelled into a disc wind, or both. Only assuming a low spin ($a = 0$) and high mass ($10^7 M_\odot$), Done & Jin (2016) were able to find a sub-Eddington accretion rate for 1H 0707-495. However, these assumptions are at odds with the high spin ($a = 0.998$) and low mass ($2 \times 10^6 M_\odot$) required by the spectral-timing models based on relativistic reflection in the lamp-post geometry (Fabian et al. 2012). These constraints on mass and spin might be inconsistent, if the disc is not thin. However, Done & Jin (2016) pointed out that the black hole mass should indeed be low, from simple X-ray variability arguments. Then, the source requires super-Eddington accretion rates. Some kind of ADAF should replace the standard disc in the inner region, and clumpy turbulent winds can be present, strongly altering the view of the central region (also depending on the inclination). Done & Jin (2016) suggested that these could be features of the most complex NLS1s. Interestingly, the CHEESES sources showing the largest Eddington ratios are NLS1s (such as Ark 564, $\epsilon_{\rm Edd} = 50 - 150$) or narrow-line quasars (such as PG 1543+489, $\epsilon_{\rm Edd} = 40 - 270$). These results are preliminary, and no errors on the Eddington ratio have been estimated. However, we may expect relatively small errors on the 5–7 eV luminosity. The Eddington luminosity, on the other hand, depends on the black hole mass, which is not always measured with good precision. In particular, if the mass is underestimated, $\epsilon_{\rm Edd}$ is overestimated by the same factor. Even more importantly, a higher mass would also imply a different shape of the disc emission, and a lower bolometric luminosity. As shown by Done & Jin (2016), for a given black hole spin and disc inclination, a black hole mass of 10^7 $M_\odot$ would imply a mass accretion rate around 20 times smaller than a mass of 2×10^6 $M_\odot$. Indeed, a number of studies suggest that the black hole mass of some NLS1s could be larger than previously estimated (e.g.

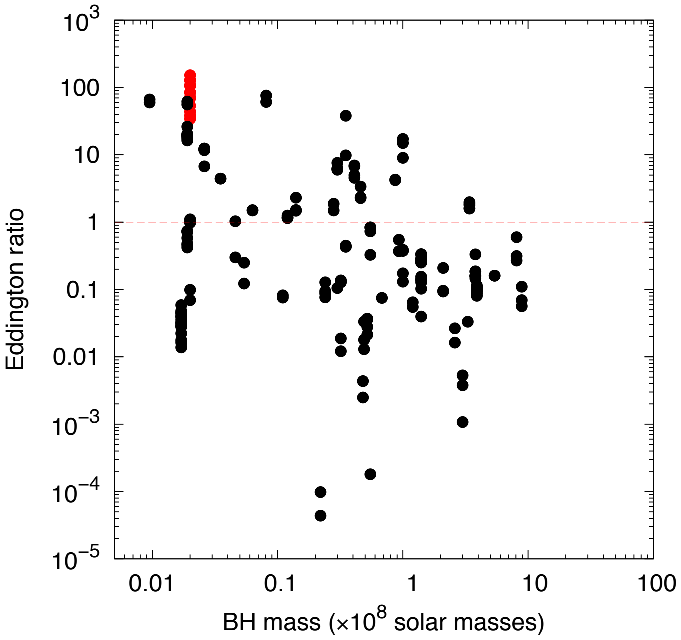

Figure 8.4 – Same as Fig. 8.3, assuming spin $a = 0$.

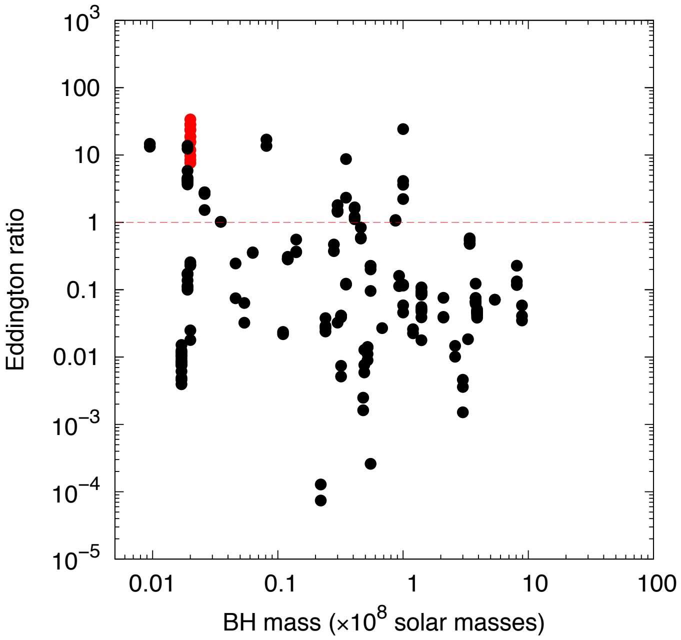

Figure 8.5 – Same as Fig. 8.3, assuming an inner disc radius of 100 R_G.

Calderone et al. 2013; Baldi et al. 2016).

The inner disc radius also plays an important role in the calculation of the bolometric luminosity. In my first run of the D&D code, this radius was fixed at the innermost stable circular orbit, i.e. $R_{\text{in}} = 1.24\ R_G$ for $a = 0.998$ and $R_{\text{in}} = 6\ R_G$ for $a = 0$. The outer radius was fixed at 1000 R_G. In general, if the inner disc radius is larger, the bolometric luminosity is smaller (for a given mass). Indeed, the Eddington ratio for spin $a = 0$ is smaller of a factor of 2-3 than for the maximal spin $a = 0.998$ (see Fig. 8.4). Then, I performed further calculations with the D&D code, setting an inner disc radius $R_{\text{in}} = 100\ R_G$. In this case, the Eddington ratio is reduced roughly by a factor of 10 with respect to $R_{\text{in}} = 1.24\ R_G$, as shown in Fig. 8.5.

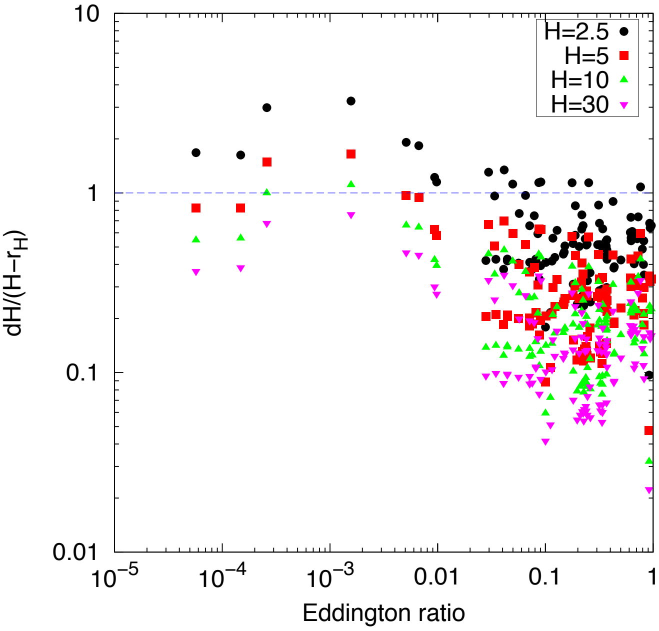

Figure 8.6 – Ratio between the coronal radius dH and height above the horizon, $H - r_H$, plotted against the Eddington ratio of the source, in the case $a = 0.998$, $i = 30$ deg. Different heights are used: $H = 2.5\ R_G$ (black circles), 5 R_G (red squares), 10 R_G (green triangles) and 30 R_G (magenta nablas). Only the sources with $\epsilon_{\mathrm{Edd}} < 1$ are shown, as the D&D code might give inconsistent results for super-Eddington sources.

8.3.2 The coronal radius/height ratio

I show in Fig. 8.6 the ratio of the coronal radius, as calculated by the D&D code, to the height above the horizon, assuming maximal black hole spin, a disc inclination of 30 deg and an inner disc radius equal to the innermost stable circular orbit. When the code gives an Eddington ratio above 1, the results might be inconsistent, as I discussed above. Another caveat is that very small Eddington ratios, e.g. below 0.01, might indicate the presence of a RIAF. The radius/height ratio is mostly below 1, indicating that the corona can intercept enough seed photons to produce the observed Comptonized luminosity. In a number of cases, the corona cannot fit within the smallest height of 2.5 R_G. On the other hand, the corona can always fit within the largest height, i.e. 30 R_G. I show in Fig. 8.7 a similar plot of the radius/height ratio, assuming $a = 0$. In this case, the inner disc radius is 6 R_G and (as I noted above) the Eddington ratio is 2-3 times smaller than in the case $a = 0.998$, while the required coronal size is $\sim$ 10 times larger. Indeed, in the case $a = 0$ the corona cannot fit within 2.5 R_G above the horizon, and even within 5 R_G in most sources; the only height which is always permitted is 30 R_G. Finally, I show in Fig. 8.8 the radius/height ratio assuming an inner disc radius of 100 R_G. In this case, it is almost impossible for the corona to fit within 30 R_G, therefore a larger height is required.

8.4 Discussion

The lamp-post geometry is often used to describe the hard X-ray emission of AGNs, especially for sources showing reflection-dominated spectra with a strong spectral variability. DD15 focused on the extreme case of 1H 0707-495, which requires a hot corona located less than 1 gravitational radius above the event horizon (e.g. Fabian et al. 2012). However, DD15 found that there is no viable lamp-post geometry for a Comptonizing corona in 1H 0707-495, meaning that the source must be somewhat extended. Moreover, the black hole mass and spin required by the lamp-post models indicate that the accretion

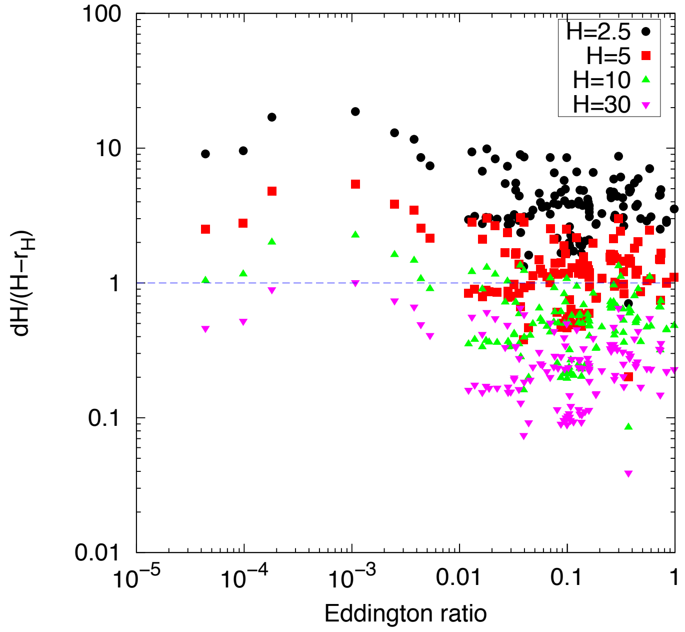

Figure 8.7 – Same as Fig. 8.6, but assuming a spin $a = 0$.

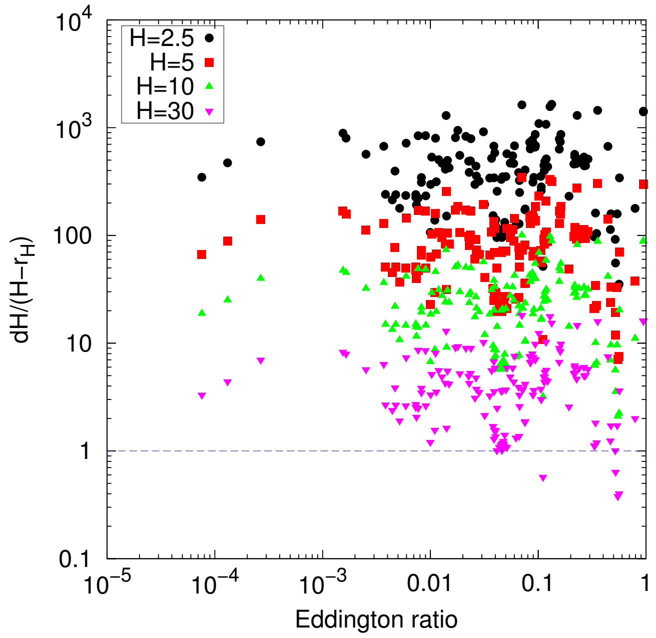

Figure 8.8 – Same as Fig. 8.6, now assuming an inner disc radius of 100 R_G.

rate of 1H 0707-495 is highly super-Eddington (Done & Jin 2016, see also Fig. 8.3). Then, it is unlikely that the reflecting disc remains flat, so the reflector geometry as well as the coronal size and shape should be carefully considered to use self-consistently a lamp-post model.

I applied the D&D code to the CHEESES sample, with the goal of constraining the geometry of a "lamp-post Comptonizing corona" in a large number of sources. The preliminary results indicate that, at least for the sub-Eddington sources, the lamp-post Comptonizing corona is generally a viable scenario. However, such a corona can only exist beyond a certain height above the event horizon, depending on the black hole spin and on the inner disc radius. If the disc is extended down to the innermost stable circular orbit of a maximally spinning black hole ($a = 0.998$, $R_{\rm in} = 1.24\ R_G$, event horizon $r_H = 1.06\ R_G$), the corona can be located close to the black hole (down to $H = 2.5\ R_G$), having a tiny radius (i.e. less than $H - r_H = 1.44\ R_G$) - albeit not for all sources, see Fig. 8.6. Anyway, in most cases the corona can be at a height as small as $H = 5\ R_G$, having a radius less than $H - r_H = 3.94\ R_G$. If the disc is extended down to the innermost stable circular orbit of a non-spinning black hole ($a = 0$, $r_H = 2\ R_G$), it becomes difficult for the corona to fit within a height of 5 R_G (see Fig. 8.7). However, generally the corona can be at a height as small as $H = 10\ R_G$, having a radius less than $H - r_H = 8\ R_G$.

On the other hand, assuming a relatively small inner disc radius yields a very large Eddington ratio (up to ~ 400) in a number of sources, especially narrow-line Seyferts and quasars (Fig. 8.3). This is not implausible, and in particular the results on 1H 0707-495 are in rough agreement with those of Done & Jin (2016). However, if the accretion rate is really super-Eddington, the D&D code might give inconsistent results, as it assumes a flat Novikov-Thorne disc. One way to recover a smaller Eddington ratio would be to assume a larger inner disc radius, e.g. of 100 R_G (Fig. 8.5). In this case, the corona would need to be located at $H > 30\ R_G$ (Fig. 8.8) and it could hardly be considered compact. Constraining the inner disc radius is not straightforward, but it could be done with the spectral fits. For example, if a Fe Kα line is present, and it is produced by reflection off the disc, the intrinsic width can be linked to the inner disc radius (see, e.g., the analysis on NGC 4593 in Chapter 6). Then, fitting the CHEESES sample with a model including a relativistically broadened reflection component, we could derive useful constraints on the inner disc radius.

Another source of uncertainty is the temperature of the hot corona, which is assumed to be of 100 keV. Constraining this temperature from the CHEESES spectral fits is not feasible, because of the lack of high-energy data. A different temperature would slightly change the results. For example, a smaller temperature would imply a somewhat lower X-ray luminosity, so that the minimum needed coronal radius would likely be reduced. The inclusion of high-energy data, in particular from *NuSTAR*, would thus be useful to further refine the estimates of the coronal size.

In any case, the preliminary results from the D&D code nicely complement the spectral fits of the CHEESES sample that I discussed in Chapter 7. Generally, the optical/UV to soft X-ray emission seem to be well described by a warm corona lying above a passive disc, while the hard X-ray emission can be due to a lamp-post Comptonizing corona. To further explore this scenario, the D&D code would need to be extended to include the emission from the warm corona, besides the standard Novikov-Thorne disc. Moreover, taking into account the effects of Comptonization would most probably reduce the effective temperature of the disc and the estimated Eddington ratio (e.g. Czerny & Elvis 1987). However, taking the current results of the D&D code as a first approximation, the two-corona model seems to adequately describe most of the sources in our sample. While the warm corona can be thought of as the upper layer of the accretion disc, the hot corona is consistent with being compact and located relatively close to the black hole (e.g. within 10 gravitational radii). This is an intriguing possibility to build a self-consistent model for the high-energy emission of AGNs.

Chapter 9

Conclusions and perspectives

Contents

Several questions on the physics of AGNs still lack conclusive answers: what is the nature and origin of the high-energy emission, and what are the geometrical and physical properties of the accretion flow? In this thesis, I have studied the high-energy emission processes in AGNs from an observational point of view. I have carried out detailed spectral analyses of high-quality UV/X-ray data of single sources, which is needed for testing and validating physically motivated models. I have also worked on a larger sample of sources, performing both a spectral analysis and numerical simulations. I will now summarize the main results obtained in this thesis and discuss the future perspectives.

9.1 Main results from this thesis work

9.1.1 A scanner darkly into NGC 5548

The most striking result of the long, multiwavelength campaign on NGC 5548 is clearly the unexpected obscuration simultaneously observed in the UV and X-rays, and likely due to a wind launched from the accretion disc. However, the high-energy view gave some interesting results as well. First, it was possible to disentangle the reflection component from the primary continuum. The fact that the reflection component is consistent with being constant indicates that the reflecting material is located a few light months away from the primary X-ray source. The primary X-ray emission shows instead a significant variability over a few days/weeks, indicating short-term variations of the coronal optical depth and temperature. According to the two-phase model, there is a univocal relationship between the optical depth and the temperature, for a given amplification factor (or, equivalently, for a given heating/cooling ratio), the latter being essentially fixed by geometry. Then, for a given geometry of the disc/corona system, the physical parameters of the corona can vary following a given relationship. However, the geometry can also change (e.g. the inner radius of the disc might vary), leading to a variation of the amplification factor and thus to non-trivial variations of the coronal optical depth and temperature. In any case, the mean temperature derived from the X-ray spectral analysis is $k_{\mathrm{B}}T = 40^{+40}_{-10}$ keV, while the mean optical depth is $\tau = 2.7^{+0.7}_{-1.2}$ (assuming a spherical corona). Comparing with past observations of NGC 5548, both the optical depth and temperature are found to vary significantly over ~ 10 years (reaching $\tau \simeq 0.2 - 0.3$ and $k_{\mathrm{B}}T \simeq 300 - 400$ keV). The corresponding variability of the Compton parameter y seems to suggest a long-term variability of the amplification factor, thus of the geometry of the system.

Unfortunately, the strong obscuration complicates the analysis, in particular concerning the UV and soft X-ray spectrum, making it difficult to test a warm Comptonization scenario for the soft excess. However, the high-energy view allows us to constrain the properties of the obscurer, independently supporting the main findings of the campaign. In particular, the obscurer is well described by two components with different column density and covering fraction. Moreover, both the spectral and timing analysis indicate that most of the strong variability seen in the soft band is specifically due to one of the two obscuring components.

9.1.2 The hot corona of NGC 7213

This source is a low-luminosity, weakly accreting ($\sim 0.1\%$ of the Eddington limit) source with a peculiar X-ray spectrum, lacking a significant Compton reflection component. The 3–79 keV *NuSTAR* spectrum is well explained by Comptonization taking place in a relatively hot ($k_{\mathrm{B}}T > 40$ keV) and optically thin ($\tau < 1$) corona. The apparent lack of a significant optical/UV bump, from past observations, indicates that the power output is dominated by the hot corona. Two main scenarios can explain the properties of this source. First, the corona could be outflowing, rather than being static. The absence of a disc reflection component would then be due to the beaming of the primary X-ray emission, strongly reducing the flux received by the disc. Second, the accretion disc could be truncated, and possibly replaced by an ADAF/RIAF, in agreement with the low estimated accretion rate. The low radiative efficiency would then explain the low luminosity. Of course, these two possibilities are not mutually exclusive. Moreover, the X-ray variability of NGC 7213 is relatively slow, being of the order of days/weeks (according to past observations). The hot corona, then, is expected to be relatively extended. The small estimated optical depth is a further indication that the corona should subtend a large solid angle as seen from the disc, to intercept a sufficient number of seed soft photons.

These might be general properties of low-luminosity AGNs. If the X-ray emission is due to a Comptonizing corona, a weak emission from the disc would imply an inefficient cooling of the corona from inverse Compton scattering. Therefore, weakly accreting sources might indeed be characterized by a relatively high temperature of the hot corona.

9.1.3 The variability of NGC 4593

NGC 4593 shows a strong and fast variability, both in flux and spectral shape, over time-scales as short as a few ks. From the spectral analysis, we can clearly separate the reflection component and the soft excess from the primary continuum. Interestingly, the reflection component is found to be the superposition of a distant component and a component originating from the inner region of the accretion flow. The spectral variability of the primary continuum is remarkable (in particular, the high-energy cut-off varies between ~ 100 keV and more than 700 keV), indicating significant short-term variability of the physical parameters of the hot corona. The soft excess is likely another key piece of the puzzle. On the one hand, this component is not explained by blurred, ionized reflection. A warm Comptonization scenario is thus favoured, also given the observed correlation between the UV and soft X-ray emission. On the other hand, the soft excess is significantly correlated with the primary continuum. Then, there should be a physical link between the warm corona producing the UV/soft X-rays and the hot corona producing the hard X-rays. For example, these two regions could simply be illuminated by the same seed photons. However, there is another intriguing possibility. If the warm corona is coupled to a passive disc, most of the seed photons entering the hot corona would be emitted by the warm corona itself. The hard X-ray emission, in this scenario, would be due to a "double Comptonization" taking place first in the warm corona and then in the hot one. Moreover, if the warm corona covers a large part of the disc, the reflection component would partly be due to the warm corona. Since the warm plasma at temperatures of $0.1 - 1$ keV should be highly ionized, reflection off the warm corona could resemble that off a highly photoionized disc (see also Boissay et al. 2016).

9.1.4 The CHEESES sample: a warm corona above a passive disc?

The optical/UV to soft X-ray emission of the sources in the CHEESES sample is consistent with a Comptonized spectrum from a warm, optically thick corona covering a nearly passive disc. The luminosity of the soft phase (i.e. the disc) is thus consistent with being due to reprocessing of the emission from the warm corona, with an intrinsic contribution from the disc of less than 30%. In some cases, the results suggest a geometry where the warm corona does not fully cover the disc.

The structure and heating mechanism of such a warm corona, as well as their dependence on fundamental parameters like the accretion rate and black hole mass, are still unclear and a matter of active research (e.g. Różańska et al. 2015). However, the results from the CHEESES spectral analysis will provide important constraints and help building up detailed theoretical models.

9.1.5 The D&D code: size and location of the hot lamp-post corona

From the fully relativistic calculations of the D&D code, the hot corona producing the hard X-ray emission is mostly consistent with being compact and located within a few gravitational radii of the black hole event horizon. However, there are limitations on the minimal size of such a lamp-post Comptonizing corona, depending (i) on the observed optical/UV and X-ray luminosities, and (ii) on the assumed size of the UV-emitting region (in particular on the inner disc radius). The results are promising, even though the D&D code assumes illumination from a standard accretion disc, instead of a warm corona as suggested by the spectral analysis. In the future, we will likely need to include the illumination from the warm corona, to obtain a coherent description. Moreover, in this case, the hot corona will intercept the soft X-ray photons emitted by the warm corona, besides the optical/UV ones. This might reduce the minimum size required for the hot corona to explain the observed hard X-ray luminosity.

9.2 What do we learn?

First of all, I underline that an approach based on multiple, broad-band observations on adequate time-scales is extremely useful to investigate the high-energy processes in AGNs, allowing us to disentangle the different spectral components notably through their variability, and to test physically motivated models. Broad-band monitoring campaigns, such as those on NGC 5548 and NGC 4593, give the opportunity to take a step forward in the understanding of the central engine of AGNs. The monitoring of NGC 4593 offers perhaps the clearest indications, as we are able (i) to disentangle the reflection component and the soft excess from the primary continuum, (ii) to rule out the ionized reflection scenario for the soft excess thanks to the high-energy data, and (iii) to study the correlations between the different spectral components. As I argued above, an accurate analysis of single sources is needed to devise a detailed and self-consistent physical scenario. On the other hand, to study the average properties of the high-energy emission of AGNs, we should focus on large samples.

Overall, the results of this thesis support the idea that, at least in high-luminosity, broad-line Seyfert galaxies, the high-energy emission is explained by a two-corona model. The warm ($k_{\mathrm{B}}T \sim 0.1-1$ keV), optically thick ($\tau \sim 10$) Comptonizing corona is consistent with a slab covering (fully or partially) a nearly passive accretion disc. The hot Comptonizing corona is mostly consistent with being compact, and also strongly and rapidly variable, over time-scales ranging from years down to a few ks (like in NGC 5548 and NGC 4593). In low-luminosity objects (such as NGC 7213), we have a tentative evidence that the hot corona tends to have a higher temperature and to be more extended. The differences between high-luminosity and low-luminosity objects may suggest that the accretion rate, and ultimately the nature of the inner accretion flow, plays a major role in determining the physical and geometrical characteristics of the hot corona.

9.3 Future perspectives

Clearly, further work will be needed to increase and deepen our knowledge on AGNs, the most luminous and long-lived objects in the Universe. The two-corona scenario is a promising model, deserving further detailed analyses, both from the observational and theoretical point of view. In particular, the formation process, heating mechanism and structure of the warm and hot coronae are not yet fully understood, nor is their interplay with the accretion disc and among themselves. Also the dependence on fundamental parameters of the system, like the accretion rate and the black hole mass, is still mostly a matter of speculation. In the near future, broad-band observational campaigns on different classes of AGNs (high and low-luminosity, high and low-black hole mass, broad-line and narrow-line Seyferts) will improve our understanding of the nature of their central engine.

Besides such wide-ranging perspectives, there are a number of direct extensions of this thesis work that follow this path. First, the results on NGC 4593 strongly support a follow-up analysis focused on realistic Comptonization models. We will have the opportunity to test the two-corona model with an unprecedented, high-quality data set. Further work is also needed on the spectral analysis and numerical simulations of the CHEESES sample, first of all to obtain good fits to the data. We will also be able to study the variability properties of the sources in the sample, and to test the possible correlations between the different physical parameters.

Finally, I discuss below a new observing campaign, somehow analogous to that on NGC 4593, but on a source belonging to a different class: that of radio-loud AGNs.

9.3.1 The *NuSTAR/XMM-Newton/VLBA* monitoring of the broad-line radio galaxy 3C 382

Our understanding of the central engine of AGNs mostly derives from radio-quiet sources, like all the objects discussed in this thesis. This is partly due to the lower number density of radio-loud AGNs, which are roughly 10-20% of the total, meaning that there are fewer bright objects (see Sect. 1.3.3). Moreover, the emission of radio-loud sources is often quite complex, because of the broad-band jet component producing radio through gamma-ray radiation. As a result, the dichotomy between radio-quiet and radio-loud AGNs is still debated. A physical connection is likely to exist between the accretion flow and the jet activity in AGNs, as indicated by the existence of the so-called fundamental plane of black hole activity (Merloni et al. 2003), namely a correlation between the radio luminosity, the X-ray luminosity and the black hole mass. However, the underlying mechanism is a matter of speculation. For example, it is possible that the X-ray corona is actually the base of the radio jet (e.g. Markoff et al. 2005, and see also the conclusions on NGC 7213 in Chapter 5).

Broad-line radio galaxies (BLRGs, Sect. 1.3.3) are considered to be the radio-loud counterparts of Seyfert 1s. They are thus ideal targets to perform detailed spectral studies of their high-energy emission, for two main reasons. First, the jet of BLRGs does not dominate the spectral emission by pointing directly towards the observer (like, e.g., in blazars). Second, they are generally not obscured in X-rays, just like Seyfert 1 galaxies. Past studies on BLRGs, such as 3C 120 (Chatterjee et al. 2009; Lohfink et al. 2013) and 3C 111 (Chatterjee et al. 2011), have revealed a relationship between events in the radio jet and the X-ray emission. In particular, the ejection of bright, superluminal knots in the radio jet are preceded by significant dips in the X-ray light curve, indicating a physical connection between the accretion disc and the jet, similar to black hole X-ray binaries (Marscher et al. 2002).

During the *NuSTAR* AO2 (2015), I have been PI of an accepted proposal on the BLRG 3C 382. Our group[1] was awarded a joint *NuSTAR/XMM-Newton* monitoring, consisting of 5×20 ks simultaneous observations spaced by 12 days. The observations are currently planned to be carried out from 2016, Aug. 29 to 2016, Oct. 16. The simultaneous coverage from the UV to hard X-rays will allow us to study the high-energy spectrum

---

[1] Co-Is: D. Ballantyne, S. Bianchi, M. Cappi, M. Dadina, B. De Marco, A. De Rosa, M. Giroletti, P. Grandi, J. Malzac, A. Marinucci, G. Matt, P.-O. Petrucci, G. Ponti, E. Torresi, A. Tortosa.

and variability of a BLRG with unprecedented accuracy and test physically motivated Comptonization models, not differently from NGC 4593. Then, I have been PI of an accompanying *VLBA* proposal, to obtain simultaneous radio coverage. We were awarded five *VLBA* observations, coordinated with the X-ray campaign, to follow in detail flux and morphological variations of the radio jet at sub-parsec scales. This will allow us to explore the relation between the radio emission from the jet and the UV/X-ray emission from the disc/corona system with high sensitivity. This campaign will be the first monitoring of a BLRG with both *VLBA* and the combination of *NuSTAR* and *XMM-Newton*. The high-quality radio and X-ray data will give us a unique opportunity to probe the connection between the accretion flow and the jet of a radio-loud AGN.

Bibliography

Abramowicz, M. A., Czerny, B., Lasota, J. P., & Szuszkiewicz, E. 1988, ApJ, 332, 646

Abramowicz, M. A. & Fragile, P. C. 2013, Living Reviews in Relativity, 16

Antonucci, R. 1993, ARA&A, 31, 473

Antonucci, R. R. J. & Miller, J. S. 1985, ApJ, 297, 621

Arav, N. 2010, in IAU Symposium, Vol. 267, Co-Evolution of Central Black Holes and Galaxies, ed. B. M. Peterson, R. S. Somerville, & T. Storchi-Bergmann, 350–353

Arav, N., Chamberlain, C., Kriss, G. A., et al. 2015, A&A, 577, A37

Arav, N., Moe, M., Costantini, E., et al. 2008, ApJ, 681, 954

Arévalo, P. & Uttley, P. 2006, MNRAS, 367, 801

Arnaud, K. A. 1996, in Astronomical Society of the Pacific Conference Series, Vol. 101, Astronomical Data Analysis Software and Systems V, ed. G. H. Jacoby & J. Barnes, 17

Arnaud, K. A., Branduardi-Raymont, G., Culhane, J. L., et al. 1985, MNRAS, 217, 105

Baldi, R. D., Capetti, A., Robinson, A., Laor, A., & Behar, E. 2016, MNRAS, 458, L69

Bassani, L., Cappi, M., & Malaguti, G. 1999, Astrophysical Letters and Communications, 39, 41

Beckmann, V. & Shrader, C. R. 2012, Active Galactic Nuclei

Bell, M. E., Tzioumis, T., Uttley, P., et al. 2011, MNRAS, 411, 402

Beloborodov, A. M. 1999, ApJL, 510, L123

Bennert, N., Jungwiert, B., Komossa, S., Haas, M., & Chini, R. 2006, A&A, 459, 55

Bianchi, S., Guainazzi, M., Matt, G., Fonseca Bonilla, N., & Ponti, G. 2009a, A&A, 495, 421

Bianchi, S., La Franca, F., Matt, G., et al. 2008, MNRAS, 389, L52

Bianchi, S., Maiolino, R., & Risaliti, G. 2012a, Advances in Astronomy, 2012, 782030

Bianchi, S., Matt, G., Balestra, I., & Perola, G. C. 2003, A&A, 407, L21

Bianchi, S., Panessa, F., Barcons, X., et al. 2012b, MNRAS, 426, 3225

Bianchi, S., Piconcelli, E., Chiaberge, M., et al. 2009b, ApJ, 695, 781

Blandford, R. & Eichler, D. 1987, Physics Reports, 154, 1

Blustin, A. J., Fuerst, S. V., Branduardi-Raymont, G., et al. 2006, in ESA Special Publication, Vol. 604, The X-ray Universe 2005, ed. A. Wilson, 597

Boissay, R., Paltani, S., Ponti, G., et al. 2014, A&A, 567, A44

Boissay, R., Ricci, C., & Paltani, S. 2016, A&A, 588, A70

Brandt, W. N. & Alexander, D. M. 2015, A&ARv, 23, 1

Brenneman, L. W., Reynolds, C. S., Wilms, J., & Kaiser, M. E. 2007, ApJ, 666, 817

Bühler, R. & Blandford, R. 2014, Reports on Progress in Physics, 77, 066901

Calderone, G., Ghisellini, G., Colpi, M., & Dotti, M. 2013, MNRAS, 431, 210

Cappi, M., De Marco, B., Ponti, G., et al. 2016, A&A, 592, A27

Carilli, C. L. & Barthel, P. D. 1996, A&ARv, 7, 1

Castelló-Mor, N., Netzer, H., & Kaspi, S. 2016, MNRAS, 458, 1839

Cerruti, M., Ponti, G., Boisson, C., et al. 2011, A&A, 535, A113

Chartas, G., Kochanek, C. S., Dai, X., Poindexter, S., & Garmire, G. 2009, ApJ, 693, 174

Chatterjee, R., Marscher, A. P., Jorstad, S. G., et al. 2011, ApJ, 734, 43

Chatterjee, R., Marscher, A. P., Jorstad, S. G., et al. 2009, ApJ, 704, 1689

Chiang, C.-Y., Walton, D. J., Fabian, A. C., Wilkins, D. R., & Gallo, L. C. 2015, MNRAS, 446, 759

Coffey, D., Longinotti, A. L., Rodríguez-Ardila, A., et al. 2014, MNRAS, 443, 1788

Coppi, P. S. 1992, MNRAS, 258, 657

Costantini, E. 2010, Space Science Reviews, 157, 265

Crenshaw, D. M. & Kraemer, S. B. 2012, ApJ, 753, 75

Crenshaw, D. M., Kraemer, S. B., Gabel, J. R., et al. 2003a, ApJ, 594, 116

Crenshaw, D. M., Kraemer, S. B., & George, I. M. 2003b, ARA&A, 41, 117

Crenshaw, D. M., Kraemer, S. B., Schmitt, H. R., et al. 2009, ApJ, 698, 281

Croston, J. H., Hardcastle, M. J., Harris, D. E., et al. 2005, ApJ, 626, 733

Crummy, J., Fabian, A. C., Gallo, L., & Ross, R. R. 2006, MNRAS, 365, 1067

Czerny, B. & Elvis, M. 1987, ApJ, 321, 305

Czerny, B., Nikołajuk, M., Różańska, A., et al. 2003, A&A, 412, 317

Dauser, T., Garcia, J., Wilms, J., et al. 2013a, MNRAS, 430, 1694

Dauser, T., Garcia, J., Wilms, J., et al. 2013b, MNRAS, 430, 1694

De Marco, B., Ponti, G., Cappi, M., et al. 2013, MNRAS, 431, 2441

de Vaucouleurs, G., de Vaucouleurs, A., Corwin, Jr., H. G., et al. 1991, Third Reference Catalogue of Bright Galaxies. Volume I: Explanations and references. Volume II: Data for galaxies between 0^h and 12^h. Volume III: Data for galaxies between 12^h and 24^h.

Denney, K. D., Bentz, M. C., Peterson, B. M., et al. 2006, ApJ, 653, 152

Di Gesu, L., Costantini, E., Ebrero, J., et al. 2015, A&A, 579, A42

Di Matteo, T. 1998, MNRAS, 299, L15

Done, C., Davis, S. W., Jin, C., Blaes, O., & Ward, M. 2012, MNRAS, 420, 1848

Done, C. & Fabian, A. C. 1989, MNRAS, 240, 81

Done, C., Gierliński, M., Sobolewska, M., & Schurch, N. 2007, in Astronomical Society of the Pacific Conference Series, Vol. 373, The Central Engine of Active Galactic Nuclei, ed. L. C. Ho & J.-W. Wang, 121

Done, C. & Jin, C. 2016, MNRAS, 460, 1716

Done, C., Jin, C., Middleton, M., & Ward, M. 2013, MNRAS, 434, 1955

Dovčiak, M. & Done, C. 2015

Dovčiak, M. & Done, C. 2016, Astronomische Nachrichten, 337, 441

Dovčiak, M., Karas, V., & Yaqoob, T. 2004, ApJS, 153, 205

Dovčiak, M., Muleri, F., Goosmann, R. W., Karas, V., & Matt, G. 2011, ApJ, 731, 75

Du, P., Hu, C., Lu, K.-X., et al. 2014, ApJ, 782, 45

Ebrero, J., Kaastra, J. S., Kriss, G. A., de Vries, C. P., & Costantini, E. 2013, MNRAS, 435, 3028

Ebrero, J., Kaastra, J. S., Kriss, G. A., et al. 2016, A&A, 587, A129

Edelson, R. & Nandra, K. 1999, ApJ, 514, 682

Elitzur, M. & Ho, L. C. 2009, ApJL, 701, L91

Elitzur, M. & Shlosman, I. 2006, ApJL, 648, L101

Elliot, J. L. & Shapiro, S. L. 1974, ApJL, 192, L3

Elvis, M. 2000, ApJ, 545, 63

Elvis, M., Risaliti, G., Nicastro, F., et al. 2004, ApJL, 615, L25

Elvis, M., Wilkes, B. J., McDowell, J. C., et al. 1994, ApJS, 95, 1

Emmanoulopoulos, D., Papadakis, I. E., McHardy, I. M., et al. 2012, MNRAS, 424, 1327

Fabbiano, G. 1989, ARA&A, 27, 87

Fabian, A. C. 2006, in ESA Special Publication, Vol. 604, The X-ray Universe 2005, ed. A. Wilson, 463

Fabian, A. C., Iwasawa, K., Reynolds, C. S., & Young, A. J. 2000, PASP, 112, 1145

Fabian, A. C., Lohfink, A., Kara, E., et al. 2015, MNRAS, 451, 4375

Fabian, A. C., Rees, M. J., Stella, L., & White, N. E. 1989, MNRAS, 238, 729

Fabian, A. C., Vaughan, S., Nandra, K., et al. 2002, MNRAS, 335, L1

Fabian, A. C., Zoghbi, A., Ross, R. R., et al. 2009, Nature, 459, 540

Fabian, A. C., Zoghbi, A., Wilkins, D., et al. 2012, MNRAS, 419, 116

Fanaroff, B. L. & Riley, J. M. 1974, MNRAS, 167, 31P

Ferland, G. J., Porter, R. L., van Hoof, P. A. M., et al. 2013, RMxAA, 49, 137

Ferreira, J., Petrucci, P.-O., Henri, G., Saugé, L., & Pelletier, G. 2006, A&A, 447, 813

Francis, P. J. & Wills, B. J. 1999, in Astronomical Society of the Pacific Conference Series, Vol. 162, Quasars and Cosmology, ed. G. Ferland & J. Baldwin, 363

Frank, J., King, A., & Raine, D. J. 2002, Accretion Power in Astrophysics: Third Edition, 398

Fukumura, K. & Kazanas, D. 2007, ApJ, 664, 14

García, J., Dauser, T., Lohfink, A., et al. 2014, ApJ, 782, 76

García, J., Dauser, T., Reynolds, C. S., et al. 2013, ApJ, 768, 146

García, J. & Kallman, T. R. 2010, ApJ, 718, 695

George, I. M. & Fabian, A. C. 1991a, MNRAS, 249, 352

George, I. M. & Fabian, A. C. 1991b, MNRAS, 249, 352

Ghisellini, G., ed. 2013, Lecture Notes in Physics, Berlin Springer Verlag, Vol. 873, Radiative Processes in High Energy Astrophysics

Ghisellini, G. & Haardt, F. 1994, ApJL, 429, L53

Ghisellini, G., Haardt, F., & Matt, G. 1994, MNRAS, 267, 743

Ghisellini, G., Maraschi, L., & Treves, A. 1985, A&A, 146, 204

Gierliński, M. & Done, C. 2004, MNRAS, 349, L7

Gohil, R. & Ballantyne, D. R. 2015, MNRAS, 449, 1449

Grandi, P., Malaguti, G., & Fiocchi, M. 2006, ApJ, 642, 113

Grandi, S. A. 1982, ApJ, 255, 25

Grupe, D., Beuermann, K., Mannheim, K., & Thomas, H.-C. 1999, A&A, 350, 805

Grupe, D., Komossa, S., Gallo, L. C., et al. 2008, ApJ, 681, 982

Grupe, D., Komossa, S., Leighly, K. M., & Page, K. L. 2010, ApJS, 187, 64

Grupe, D. & Mathur, S. 2004, ApJL, 606, L41

Guainazzi, M., Perola, G. C., Matt, G., et al. 1999, A&A, 346, 407

Guilbert, P. W., Fabian, A. C., & Rees, M. J. 1983, MNRAS, 205, 593

Güver, T. & Özel, F. 2009, MNRAS, 400, 2050

Haardt, F. & Maraschi, L. 1991, ApJL, 380, L51

Haardt, F. & Maraschi, L. 1993, ApJ, 413, 507

Haardt, F., Maraschi, L., & Ghisellini, G. 1994, ApJL, 432, L95

Haardt, F., Maraschi, L., & Ghisellini, G. 1997, ApJ, 476, 620

Hamann, F. & Sabra, B. 2004, in Astronomical Society of the Pacific Conference Series, Vol. 311, AGN Physics with the Sloan Digital Sky Survey, ed. G. T. Richards & P. B. Hall, 203

Harrison, F. A., Craig, W. W., Christensen, F. E., et al. 2013, ApJ, 770, 103

Hazard, C., Mackey, M. B., & Shimmins, A. J. 1963, Nature, 197, 1037

Henri, G. & Petrucci, P. O. 1997, A&A, 326, 87

Ho, L. C. 2008, ARA&A, 46, 475

Ho, L. C. 2009, ApJ, 699, 626

Ishibashi, W. & Courvoisier, T. J.-L. 2012, A&A, 540, L2

Janiuk, A., Czerny, B., & Madejski, G. M. 2001, ApJ, 557, 408

Jin, C., Ward, M., & Done, C. 2012a, MNRAS, 422, 3268

Jin, C., Ward, M., & Done, C. 2012b, MNRAS, 425, 907

Jin, C., Ward, M., Done, C., & Gelbord, J. 2012c, MNRAS, 420, 1825

Kaastra, J. S., Detmers, R. G., Mehdipour, M., et al. 2012, A&A, 539, A117

Kaastra, J. S., Kriss, G. A., Cappi, M., et al. 2014, Science

Kaastra, J. S. & Mewe, R. 1993, A&AS, 97, 443

Kaastra, J. S., Mewe, R., Liedahl, D. A., Komossa, S., & Brinkman, A. C. 2000, A&A, 354, L83

Kaastra, J. S., Mewe, R., & Nieuwenhuijzen, H. 1996, in UV and X-ray Spectroscopy of Astrophysical and Laboratory Plasmas, ed. K. Yamashita & T. Watanabe, 411–414

Kaastra, J. S., Petrucci, P.-O., Cappi, M., et al. 2011, A&A, 534, A36

Kalberla, P. M. W., Burton, W. B., Hartmann, D., et al. 2005, A&A, 440, 775

Kallman, T. & Bautista, M. 2001, ApJS, 133, 221

Kellermann, K. I., Sramek, R., Schmidt, M., Shaffer, D. B., & Green, R. 1989, AJ, 98, 1195

Kendall, M. G. 1980, Multivariate analysis

King, A. & Pounds, K. 2015, ARA&A, 53, 115

Kirsch, M. G. F., Altieri, B., Chen, B., et al. 2004, in Society of Photo-Optical Instrumentation Engineers (SPIE) Conference Series, Vol. 5488, UV and Gamma-Ray Space Telescope Systems, ed. G. Hasinger & M. J. L. Turner, 103–114

Knigge, C., Scaringi, S., Goad, M. R., & Cottis, C. E. 2008, MNRAS, 386, 1426

Kollmeier, J. A., Onken, C. A., Kochanek, C. S., et al. 2006, ApJ, 648, 128

Kompaneets, A. 1957, Soviet Physics JETP, 4, 730

Kotov, O., Churazov, E., & Gilfanov, M. 2001, MNRAS, 327, 799

Krongold, Y., Nicastro, F., Elvis, M., et al. 2007, ApJ, 659, 1022

Landt, H., Padovani, P., Giommi, P., Perri, M., & Cheung, C. C. 2008, ApJ, 676, 87

Laor, A. 1991, ApJ, 376, 90

Liedahl, D. A. 1999, in Lecture Notes in Physics, Berlin Springer Verlag, Vol. 520, X-Ray Spectroscopy in Astrophysics, ed. J. van Paradijs & J. A. M. Bleeker, 189

Lightman, A. P. & White, T. R. 1988, ApJ, 335, 57

Liu, Y., Elvis, M., McHardy, I. M., et al. 2010, ApJ, 710, 1228

Lobban, A. P., Reeves, J. N., Porquet, D., et al. 2010, MNRAS, 408, 551

Lodders, K. 2003, ApJ, 591, 1220

Lohfink, A. M., Reynolds, C. S., Mushotzky, R. F., & Nowak, M. A. 2013, MemSAI, 84, 699

Lusso, E., Comastri, A., Vignali, C., et al. 2010, A&A, 512, A34

Magdziarz, P., Blaes, O. M., Zdziarski, A. A., Johnson, W. N., & Smith, D. A. 1998, MNRAS, 301, 179

Magdziarz, P. & Zdziarski, A. A. 1995, MNRAS, 273, 837

Makishima, K., Maejima, Y., Mitsuda, K., et al. 1986, ApJ, 308, 635

Malizia, A., Molina, M., Bassani, L., et al. 2014, ApJ, 782, L25

Malzac, J., Beloborodov, A. M., & Poutanen, J. 2001, MNRAS, 326, 417

Malzac, J. & Petrucci, P.-O. 2002, MNRAS, 336, 1209

Malzac, J., Petrucci, P. O., Jourdain, E., et al. 2006, A&A, 448, 1125

Marinucci, A., Matt, G., Bianchi, S., et al. 2015, MNRAS, 447, 160

Marinucci, A., Tortosa, A., & NuSTAR AGN Physics Working Group. 2016, Astronomische Nachrichten, 337, 490

Markoff, S., Nowak, M. A., & Wilms, J. 2005, ApJ, 635, 1203

Markowitz, A., Edelson, R., & Vaughan, S. 2003a, ApJ, 598, 935

Markowitz, A., Edelson, R., Vaughan, S., et al. 2003b, ApJ, 593, 96

Markowitz, A. G., Krumpe, M., & Nikutta, R. 2014, MNRAS, 439, 1403

Markowitz, A. G. & Reeves, J. N. 2009, ApJ, 705, 496

Marscher, A. P., Jorstad, S. G., Gómez, J.-L., et al. 2002, Nature, 417, 625

Martí-Vidal, I., Muller, S., Vlemmings, W., Horellou, C., & Aalto, S. 2015, Science, 348, 311

Martocchia, A., Karas, V., & Matt, G. 2000, MNRAS, 312, 817

Martocchia, A. & Matt, G. 1996, MNRAS, 282, L53

Martocchia, A., Matt, G., & Karas, V. 2002, A&A, 383, L23

Matt, G. 2002, Philosophical Transactions of the Royal Society of London Series A, 360, 2045

Matt, G., Baloković, M., Marinucci, A., et al. 2015, MNRAS, 447, 3029

Matt, G., Fabian, A. C., & Reynolds, C. S. 1997, MNRAS, 289, 175

Matt, G., Fabian, A. C., & Ross, R. R. 1993, MNRAS, 262, 179

Matt, G., Fabian, A. C., & Ross, R. R. 1996, MNRAS, 278, 1111

Matt, G., Guainazzi, M., & Maiolino, R. 2003, MNRAS, 342, 422

Matt, G., Marinucci, A., Guainazzi, M., et al. 2014, MNRAS, 439, 3016

Matt, G., Perola, G. C., & Piro, L. 1991, A&A, 247, 25

McHardy, I. M., Koerding, E., Knigge, C., Uttley, P., & Fender, R. P. 2006, Nature, 444, 730

McHardy, I. M., Papadakis, I. E., Uttley, P., Page, M. J., & Mason, K. O. 2004, MNRAS, 348, 783

Mehdipour, M., Branduardi-Raymont, G., Kaastra, J. S., et al. 2011, A&A, 534, A39

Mehdipour, M., Kaastra, J. S., Kriss, G. A., et al. 2016, A&A, 588, A139

Mehdipour, M., Kaastra, J. S., Kriss, G. A., et al. 2015, A&A, 575, A22

Merloni, A. & Fabian, A. C. 2002, MNRAS, 332, 165

Merloni, A., Heinz, S., & di Matteo, T. 2003, MNRAS, 345, 1057

Miller, L., Turner, T. J., & Reeves, J. N. 2008, A&A, 483, 437

Miller, L., Turner, T. J., Reeves, J. N., et al. 2007, A&A, 463, 131

Mineshige, S., Kawaguchi, T., Takeuchi, M., & Hayashida, K. 2000, PASJ, 52, 499

Miniutti, G. & Fabian, A. C. 2004, MNRAS, 349, 1435

Miniutti, G., Fabian, A. C., Anabuki, N., et al. 2007, PASJ, 59, 315

Miniutti, G., Sanfrutos, M., Beuchert, T., et al. 2014, MNRAS, 437, 1776

Misner, C. W., Thorne, K. S., & Wheeler, J. A. 1973, Gravitation

Mitsuda, K., Inoue, H., Koyama, K., et al. 1984, PASJ, 36, 741

Morgan, C. W., Hainline, L. J., Chen, B., et al. 2012, ApJ, 756, 52

Morgan, C. W., Kochanek, C. S., Morgan, N. D., & Falco, E. E. 2010, ApJ, 712, 1129

Murphy, K. D. & Yaqoob, T. 2009, MNRAS, 397, 1549

Murray, N., Chiang, J., Grossman, S. A., & Voit, G. M. 1995, ApJ, 451, 498

Mushotzky, R. F., Done, C., & Pounds, K. A. 1993, ARA&A, 31, 717

Nandra, K., Clavel, J., Edelson, R. A., et al. 1998, ApJ, 505, 594

Nandra, K., George, I. M., Mushotzky, R. F., Turner, T. J., & Yaqoob, T. 1997, ApJ, 476, 70

Nandra, K., O'Neill, P. M., George, I. M., & Reeves, J. N. 2007, MNRAS, 382, 194

Nandra, K. & Pounds, K. A. 1994, MNRAS, 268, 405

Narayan, R., Mahadevan, R., & Quataert, E. 1998, in Theory of Black Hole Accretion Disks, ed. M. A. Abramowicz, G. Björnsson, & J. E. Pringle, 148–182

Narayan, R. & Yi, I. 1994, ApJL, 428, L13

Narayan, R. & Yi, I. 1995, ApJ, 452, 710

Narayan, R., Yi, I., & Mahadevan, R. 1995, Nature, 374, 623

Nenkova, M., Sirocky, M. M., Nikutta, R., Ivezić, Ž., & Elitzur, M. 2008, ApJ, 685, 160

Netzer, H. 2006, in Lecture Notes in Physics, Berlin Springer Verlag, Vol. 693, Physics of Active Galactic Nuclei at all Scales, ed. D. Alloin, 1

Netzer, H. & Wills, B. J. 1983, ApJ, 275, 445

Nicastro, F. 2000, ApJL, 530, L65

Nicastro, F., Piro, L., De Rosa, A., et al. 2000, ApJ, 536, 718

Niedźwiecki, A., Zdziarski, A. A., & Szanecki, M. 2016, ApJL, 821, L1

Niedźwiecki, A. & Życki, P. T. 2008, MNRAS, 386, 759

Novikov, I. D. & Thorne, K. S. 1973, in Black Holes (Les Astres Occlus), ed. C. Dewitt & B. S. Dewitt, 343–450

Osterbrock, D. E. 1989, Astrophysics of gaseous nebulae and active galactic nuclei

Osterbrock, D. E. & Pogge, R. W. 1985, ApJ, 297, 166

Paczyńsky, B. & Wiita, P. J. 1980, A&A, 88, 23

Page, M. J., Brindle, C., Talavera, A., et al. 2012, MNRAS, 426, 903

Pancoast, A., Brewer, B. J., Treu, T., et al. 2014, MNRAS, 445, 3073

Panessa, F., Bassani, L., Cappi, M., et al. 2006, A&A, 455, 173

Papadakis, I. E., Nandra, K., & Kazanas, D. 2001, ApJL, 554, L133

Papadakis, I. E., Sobolewska, M., Arevalo, P., et al. 2009, A&A, 494, 905

Parker, M. L., Fabian, A. C., Matt, G., et al. 2015, MNRAS, 447, 72

Pereira-Santaella, M., Diamond-Stanic, A. M., Alonso-Herrero, A., & Rieke, G. H. 2010, ApJ, 725, 2270

Perola, G. C., Matt, G., Cappi, M., et al. 2002, A&A, 389, 802

Peterson, B. 2006, in Physics of Active Galactic Nuclei at all Scales (Springer), 77–100

Peterson, B. M., Ferrarese, L., Gilbert, K. M., et al. 2004, ApJ, 613, 682

Petrucci, P. O., Haardt, F., Maraschi, L., et al. 2001, ApJ, 556, 716

Petrucci, P. O., Haardt, F., Maraschi, L., et al. 2000, ApJ, 540, 131

Petrucci, P. O. & Henri, G. 1997, A&A, 326, 99

Petrucci, P.-O., Paltani, S., Malzac, J., et al. 2013, A&A, 549, A73

Phillips, M. M. 1979, ApJL, 227, L121

Piconcelli, E., Jimenez-Bailón, E., Guainazzi, M., et al. 2005, A&A, 432, 15

Pogge, R. W. 2011, in Narrow-Line Seyfert 1 Galaxies and their Place in the Universe, 2

Ponti, G., Miniutti, G., Cappi, M., et al. 2006, MNRAS, 368, 903

Ponti, G., Papadakis, I., Bianchi, S., et al. 2012, A&A, 542, A83

Pounds, K. A., Reeves, J. N., Page, K. L., et al. 2003, MNRAS, 341, 953

Poutanen, J. & Svensson, R. 1996, ApJ, 470, 249

Pozdnyakov, L. A., Sobol, I. M., & Syunyaev, R. A. 1983, Astrophysics and Space Physics Reviews, 2, 189

Pringle, J. E. & Rees, M. J. 1972, A&A, 21, 1

Proga, D. 2000, ApJ, 538, 684

Proga, D. 2003, ApJ, 585, 406

Proga, D. & Kallman, T. R. 2004, ApJ, 616, 688

Puccetti, S., Fiore, F., Risaliti, G., et al. 2007, MNRAS, 377, 607

Reeves, J., Done, C., Pounds, K., et al. 2008, MNRAS, 385, L108

Reeves, J. N. & Turner, M. J. L. 2000, MNRAS, 316, 234

Reis, R. C. & Miller, J. M. 2013, ApJ, 769, L7

Remillard, R. A. & McClintock, J. E. 2006, ARA&A, 44, 49

Reynolds, C. S. 1996, PhD thesis, University of Cambridge

Reynolds, C. S. 2013, Classical and Quantum Gravity, 30, 244004

Reynolds, C. S., Brenneman, L. W., Wilms, J., & Kaiser, M. E. 2004, MNRAS, 352, 205

Reynolds, C. S. & Nowak, M. A. 2003, Physics Reports, 377, 389

Risaliti, G., Elvis, M., & Nicastro, F. 2002, ApJ, 571, 234

Risaliti, G., Harrison, F. A., Madsen, K. K., et al. 2013, Nature, 494, 449

Risaliti, G., Miniutti, G., Elvis, M., et al. 2009, ApJ, 696, 160

Risaliti, G., Nardini, E., Salvati, M., et al. 2011, MNRAS, 410, 1027

Ross, R. R. & Fabian, A. C. 1993, MNRAS, 261, 74

Ross, R. R. & Fabian, A. C. 2005, MNRAS, 358, 211

Rowan-Robinson, M. 1977, ApJ, 213, 635

Różańska, A., Malzac, J., Belmont, R., Czerny, B., & Petrucci, P.-O. 2015, A&A, 580, A77

Rybicki, G. B. 2003, ApJ, 584, 528

Rybicki, G. B. & Lightman, A. P. 1979, Radiative processes in astrophysics

Santos-Lleo, M., Clavel, J., Barr, P., et al. 1995, MNRAS, 274, 1

Schmidt, M. 1963, Nature, 197, 1040

Seyfert, C. K. 1943, ApJ, 97, 28

Shakura, N. I. & Sunyaev, R. A. 1973, A&A, 24, 337

Sobolewska, M. A. & Papadakis, I. E. 2009, MNRAS, 399, 1597

Soldi, S., Beckmann, V., Baumgartner, W. H., et al. 2014, A&A, 563, A57

Starling, R. L. C., Page, M. J., Branduardi-Raymont, G., et al. 2005, MNRAS, 356, 727

Straumann, N. 2004, General relativity with applications to astrophysics

Strauss, M. A., Huchra, J. P., Davis, M., et al. 1992, ApJS, 83, 29

Sunyaev, R. A. & Titarchuk, L. G. 1980, A&A, 86, 121

Sunyaev, R. A. & Titarchuk, L. G. 1985, A&A, 143, 374

Tanaka, Y., Nandra, K., Fabian, A. C., et al. 1995, Nature, 375, 659

Thorne, K. S. 1974, ApJ, 191, 507

Titarchuk, L. 1994, ApJ, 434, 570

Tombesi, F., Cappi, M., Reeves, J. N., et al. 2013, MNRAS, 430, 1102

Tombesi, F., Cappi, M., Reeves, J. N., et al. 2010, A&A, 521, A57

Torricelli-Ciamponi, G., Pietrini, P., Risaliti, G., & Salvati, M. 2014, MNRAS, 442, 2116

Turner, A. K., Fabian, A. C., Vaughan, S., & Lee, J. C. 2003, MNRAS, 346, 833

Ulrich, M.-H., Maraschi, L., & Urry, C. M. 1997, ARA&A, 35, 445

Urry, C. M. & Padovani, P. 1995, PASP, 107, 803

Ursini, F., Boissay, R., Petrucci, P.-O., et al. 2015a, A&A, 577, A38

Ursini, F., Marinucci, A., Matt, G., et al. 2015b, MNRAS, 452, 3266

Ursini, F., Petrucci, P.-O., Matt, G., et al. 2016b, MNRAS, doi: 10.1093/mnras/stw2022

Ursini, F., Petrucci, P.-O., Matt, G., et al. 2016a, Astronomische Nachrichten, 337, 552

Vasudevan, R. V. & Fabian, A. C. 2009, MNRAS, 392, 1124

Vasudevan, R. V., Mushotzky, R. F., Reynolds, C. S., et al. 2014, ApJ, 785, 30

Vaughan, S., Fabian, A. C., & Nandra, K. 2003, MNRAS, 339, 1237

Veilleux, S. & Osterbrock, D. E. 1987, ApJS, 63, 295

Véron-Cetty, M.-P. & Véron, P. 2010, A&A, 518, A10

Wald, R. M. 1984, General relativity

Walter, R. & Fink, H. H. 1993, A&A, 274, 105

Walter, R., Lutovinov, A. A., Bozzo, E., & Tsygankov, S. S. 2015, A&ARv, 23, 2

Walton, D. J., Nardini, E., Fabian, A. C., Gallo, L. C., & Reis, R. C. 2013, MNRAS, 428, 2901

Walton, D. J., Risaliti, G., Harrison, F. A., et al. 2014, ApJ, 788, 76

Wandel, A., Peterson, B. M., & Malkan, M. A. 1999, ApJ, 526, 579

Weedman, D. W. 1976, QJRAS, 17, 227

Whewell, M., Branduardi-Raymont, G., Kaastra, J. S., et al. 2015, A&A, 581, A79

Wilkins, D. R. & Fabian, A. C. 2012, MNRAS, 424, 1284

Wilkins, D. R., Kara, E., Fabian, A. C., & Gallo, L. C. 2014, MNRAS, 443, 2746

Wills, B. J., Netzer, H., & Wills, D. 1985, ApJ, 288, 94

Woo, J.-H. & Urry, C. M. 2002, ApJ, 579, 530

Wu, C.-C., Boggess, A., & Gull, T. R. 1983, ApJ, 266, 28

Yaqoob, T. 2012, MNRAS, 423, 3360

Yu, Z., Yuan, F., & Ho, L. C. 2011, ApJ, 726, 87

Yuan, F. & Narayan, R. 2014, ARA&A, 52, 529

Zdziarski, A. A., Johnson, W. N., & Magdziarz, P. 1996, MNRAS, 283, 193

Zdziarski, A. A., Lubiński, P., Gilfanov, M., & Revnivtsev, M. 2003, MNRAS, 342, 355

Zoghbi, A., Fabian, A. C., Uttley, P., et al. 2010, MNRAS, 401, 2419

Życki, P. T., Done, C., & Smith, D. A. 1999, MNRAS, 309, 561

Zycki, P. T., Krolik, J. H., Zdziarski, A. A., & Kallman, T. R. 1994, ApJ, 437, 597

Résumé

Des trous noirs supermassifs de plusieurs centaines de millions de masses solaires résident au centre de la plupart des galaxies massives. Dans 90% des cas, ces trous noirs sont dans état quiescent, très peu lumineux. Cependant, dans les 10% restant, des processus extrêmement violents sont observés, avec la libération d'énorme quantités d'énergie notamment en UV, X et gamma. On observe aussi parfois des jets puissants de matière pouvant s'étendre sur plusieurs centaines de kpc. Le coeur de ces galaxies sont appelés Noyaux Actifs de Galaxie (NAG). Ce sont parmi les objets les plus lumineux de l'univers. L'accrétion de la matière environnante sur le trou noir supermassif central est unanimement reconnue comme la source d'énergie la plus plausible pour expliquer la puissance phénoménale observée. L'énergie gravitationelle serait ainsi en partie libérée dans un disque d'accrétion, sous forme de rayonnement thermique piquant dans l'optique/UV, et en partie rayonnée en X/gamma par une couronne de plasma chaud présente dans l'environnement proche du trou noir.

De nombreux phénomènes sont néanmoins encore très mal connus et beaucoup de questions n'ont toujours pas de réponses satisfaisantes: quelles sont la dynamique et la structure des flots d'accrétion et d'éjection dans les NAG? Quels sont les processus radiatifs produisant le rayonnement UV/X? Quelle est l'origine des différentes composantes spectrales présentes dans ces domaines d'énergie? Cette thèse a pour objectif d'apporter de nouvelles contraintes observationnelles pour meux répondre à ces questions. Son originalité réside dans le développement et l'utilisation de modèles réalistes de Comptonisation thermique permettant d'une part de mieux contraindre les propriétés physiques et géométriques des régions d'émission UV/X et d'autre part de mieux comprendre l'origine des différentes composantes spectrales observées. Nous nous sommes notamment intéressés, au cours de cette thèse, à l'excès d'émission X-mou (<2 keV), présent dans un grand nombre de NAG, et dont l'origine est toujours inconnue.

Ces travaux s'articulent autour de deux axes principaux. Le premier est l'étude spectrale détaillée de longues campagnes d'observation multi-longueur d'ondes de trois galaxies de Seyfert (NGC 5548, NGC 7213 et NGC 4593). La qualité des données ont ainsi permis de révéler les paramètres physiques (notamment la température et la profondeur optique) et géométriques de la couronne thermique à l'origine du continuum X. Le second axe porte sur l'analyse de données d'archives (en provenance du satellite XMM-Newton) d'un échantillon important de galaxies de Seyfert. Cela a permis d'apporter des contraintes plus générales sur les processus d'émission haute énergie observés dans ces objets. Ces deux approches ont notamment montré que l'exces d'émission X-mou pouvait provenir des couches supérieures chaudes du disque d'accrétion, suggérant un chauffage plus efficace en surface plutôt que dans les régions internes.

Abstract

Supermassive black holes of several hundred million solar masses lie at the centre of most massive galaxies. In 90% of cases, these black holes are in quiescent, very low luminous states. Nevertheless, in the remaining 10%, extremely violent processes are seen, with the liberation of huge amounts of energy especially in the UV, X-ray and gamma-ray bands. We also sometimes observe powerful jets, extending up to several hundred kpc scales. The cores of these galaxies are called Active Galactic Nuclei (AGNs). These are among the most luminous objects in the Universe. The accretion of surrounding matter onto the central supermassive black hole is generally considered as the most likely energy source to explain the extraordinary observed luminosity. The gravitational energy would be partly liberated into an accretion disc as thermal radiation peaking in the optical/UV band, and partly radiated in the X-ray/gamma-ray band by a corona of hot plasma lying in the environment close to the black hole.

However, several phenomena are still poorly understood and a number of questions lack satisfactory answers: what are the dynamics and the structure of the accretion and ejection flows in AGNs? What are the radiative processes producing the UV/X-ray radiation? What is the origin of the different spectral components present in those energy bands? The goal of this thesis is to derive new observational constraints to better answer to these questions. Its originality resides in the development and application of realistic models of thermal Comptonization, allowing us to better constrain the physical and geometrical properties of the UV and X-ray-emitting regions, and to better understand the origin of the different observed spectral components. In particular, we studied the excess of the soft (<2 keV) X-ray emission, seen in a great number of AGNs, and whose origin is still unknown.

This work is structured along two main branches. One is the detailed spectral analysis of long, multiwavelength observational campaigns on three Seyfert galaxies (NGC 5548, NGC 7213 and NGC 4593). The quality of the data permitted to reveal the geometrical and physical parameters (in particular the temperature and optical depth) of the thermal corona producing the X-ray continuum. The second branch is based on the analysis of archival data (from the XMM-newton satellite) of a large sample of Seyfert galaxies. This allowed us to derive more general constraints on the high-energy emission processes observed in these objects. These two approaches have shown, in particular, that the soft X-ray emission excess may arise in the warm upper layers of the accretion disc, suggesting a more effective heating of the surface rather than the inner regions.